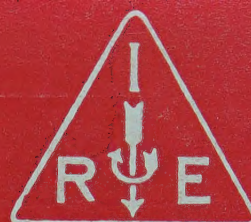


IRE Transactions



in Microwave Theory and Techniques

Volume MTT-9

NOVEMBER, 1961

Number 6

Published Bimonthly

In This Issue

- Parametric Limiting with Varactor Diodes
- Solid-State X-Band Power Limiter
- Spurious Outputs from Pulsed Microwave Tubes
- Wide-Band Degenerate Parametric Amplifiers
- Four-Frequency Parametric Devices
- Plasma Guide Microwave Selective Coupler
- High-Power Duplexers
- Quasi-Optical Surface Waveguide
- Isolators and Attenuators for Millimeter Wavelengths
- Measurement of the VSWR of Coaxial Connectors
- Hybrid-Ring Directional Coupler
- Coupled Strip-Line Configuration Using Printed-Circuit Construction
- Conductivity and Permittivity of Semiconductor Spheres
- Dominant Cutoff Wavelength of a Lunar Line
- Negative-Conductance Slot Amplifier

K7800
I23

PUBLISHED BY THE

Professional Group on Microwave Theory and Techniques

IRE PROFESSIONAL GROUP ON MICROWAVE THEORY AND TECHNIQUES

The Professional Group on Microwave Theory and Techniques is an association of IRE members with professional interest in the field of Microwave Theory and Techniques. All IRE members are eligible for membership and will receive all Group publications upon payment of the prescribed annual fee of \$3.00. Members of the American Physical Society and the Institution of Electrical Engineers of Great Britain may become affiliated with PGMTT and receive all Group publications upon payment of the Affiliate fee of \$7.50 per year.

Administrative Committee

Chairman

T. N. ANDERSON

Vice Chairman

S. B. COHN

Secretary-Treasurer

M. WIND

B. D. AARON

H. M. ALTSCHULER

R. W. BEATTY

A. C. BECK

R. C. HANSEN

W. W. MUMFORD

A. A. OLINER

R. A. RIVERS

S. W. ROSENTHAL

T. S. SAAD

R. D. WENGENROTH

R. F. SCHWARTZ

G. SHAPIRO

G. SINCLAIR

M. C. THOMPSON

K. TOMIYASU

Honorary Life Members

G. C. SOUTHWORTH

A. G. CLAVIER

Editor

DONALD D. KING

PGMTT Chapters

Albuquerque-Los Alamos
Baltimore
Boston
Buffalo-Niagara
Chicago
Columbus
Denver-Boulder
Long Island
Los Angeles
New York
Northern N. J.

R. A. Lincoln
Kenneth Claborn
P. A. Rizzi
E. L. Price, Jr.
R. D. Standley
G. J. Falkenbach
J. L. Dalke
Marc Chomet
W. G. Perry
Adolph Brenner
H. A. French

Omaha-Lincoln
Orange Belt
Orlando
Philadelphia
San Diego
San Francisco
Seattle
Schenectady
Syracuse
Tokyo, Japan
Washington, D.C.

W. G. Elwell
A. G. Holtum, Jr.
E. O. Houseman, Jr.
Frank Klawnsnik
W. F. Moore
P. H. Vartanian, Jr.
J. S. Yee
C. C. Allen
H. C. Rothenberg
Kiyoshi Morita
Frank Reggia

IRE TRANSACTIONS®

on Microwave Theory and Techniques

Published by The Institute of Radio Engineers, Inc., for the Professional Group on Microwave Theory and Techniques, at 1 East 79 Street, New York 21, N.Y. Responsibility for the contents rests upon the authors, and not upon the IRE, the Group, or its members. Individual copies of this issue and all available back issues may be purchased at the following prices: IRE members (one copy) \$2.25, libraries and colleges \$3.25, all others \$4.50. Annual subscription price: non-members, \$17.00; colleges and public libraries, \$12.75.

Address all manuscripts to Donald D. King, PGMTT Editor, Electronic Communications, Inc., 1830 York Road, Timonium, Md. Submission of three copies of manuscripts, including figures, will expedite the review.

COPYRIGHT ©1961—THE INSTITUTE OF RADIO ENGINEERS, INC.

Printed in U.S.A.

All rights, including translations, are reserved by the IRE. Requests for republication privileges should be addressed to the Institute of Radio Engineers, 1 E. 79 St., New York 21, N.Y.

IRE Transactions

on

Microwave Theory and Techniques

EDITORIAL BOARD

Editor

Donald D. King

Advertising Editor

Robert A. Rivers

Volume MTT-9

NOVEMBER, 1961

Published Bimonthly

Number 6

TABLE OF CONTENTS

1960 Microwave Prize— <i>Dr. A. F. Harvey</i>	458
---	-----

1961 NATIONAL SYMPOSIUM PAPERS

Passive Phase-Distortionless Parametric Limiting with Varactor Diodes.....	<i>I. T. Ho and A. E. Siegman</i>	459
Solid-State X-Band Power Limiter.....	<i>W. F. Krupke, T. S. Hartwick, and M. T. Weiss</i>	472
On Spurious Outputs from High-Power Pulsed Microwave Tubes, and Their Control.....	<i>K. Tomiyasu</i>	480
Practical Design and Performance of Nearly Optimum, Wide-Band Degenerate Parametric Amplifiers.....	<i>M. Gilden and G. L. Matthaei</i>	484
Transmission-Phase Relations of Four-Frequency Parametric Devices.....	<i>D. B. Anderson and J. C. Aukland</i>	491
A Plasma Guide Microwave Selective Coupler.....	<i>W. H. Steier and I. Kaufman</i>	499
High-Power Duplexers.....	<i>C. E. Muehe, Jr.</i>	506
Quasi-Optical Surface Waveguide and Other Components for the 100- to 300-Gc Region.....	<i>F. Sobel, F. L. Wentworth, and J. C. Wiltse</i>	512
Broad-Band Isolators and Variable Attenuators for Millimeter Wavelengths....	<i>C. E. Barnes</i>	519

CONTRIBUTIONS

A New High-Precision Method for the Measurement of the VSWR of Coaxial Connectors.....	<i>A. E. Sanderson</i>	524
Hybrid-Ring Directional Coupler for Arbitrary Power Divisions.....	<i>Chuck Y. Pon</i>	529
A Coupled Strip-Line Configuration Using Printed-Circuit Construction that Allows Very Close Coupling.....	<i>William J. Getsinger</i>	535
The Measurement of Conductivity and Permittivity of Semiconductor Spheres by an Extension of the Cavity Perturbation Method.....	<i>K. S. Champlin and R. R. Krongard</i>	545
The Dominant Cutoff Wavelength of a Lunar Line.....	<i>A. Y. Hu and A. Ishimaru</i>	552
The Negative-Conductance Slot Amplifier.....	<i>M. E. Pedinoff</i>	557

CORRESPONDENCE

Measurement of the Conversion Conductances of Esaki Mixer Diodes.....	<i>R. A. Pucel</i>	567
A Versatile Phase Measurement Method for Transmission-Line Networks.....	<i>Peter Lacy</i>	568
A VHF High-Power Y-Circulator.....	<i>G. V. Buehler and A. F. Eikenberg</i>	569
N-Terminal Power Divider.....	<i>R. W. Peterson</i>	571
10-DB X_L Cross Guide Coupler.....	<i>Richard Z. Gerlack</i>	571
Design Note on an L-Band Strip-Line Circulator.....	<i>W. S. Koop and A. K. Jordan</i>	571
A Stepped-Dielectric Transformer for Rectangular-to-Circular Waveguide.....	<i>B. Maher</i>	572
A Microwave Power Divider.....	<i>Richard J. Mohr</i>	573
On the Efficiency of Excitation of Surface Waves by Distributed Coupling.....	<i>Efraim Ravid-Weissberg</i>	573
Higher-Order Mode Resonances in Strip-Line Y-Junction Circulators.....	<i>Alvin Clavin</i>	575
A Proposed Design to Enhance Microwave-Power-Limiter Characteristics.....	<i>William H. Wright, Jr.</i>	575
A High-Power Coaxial Ferrite Phase Shifter.....	<i>A. S. Boxer, S. Hershenov, and E. F. Landry</i>	577
A Duplexer Using the Zero Permeability Characteristics of Ferrite.....	<i>L. K. Wilson, and G. J. Neumann</i>	578
A Series-Connected Traveling-Wave Parametric Amplifier.....	<i>Tuck Hop Lee</i>	578
1961 National Symposium.....		580
Contributors.....		582
Annual Index, 1961.....	<i>Follows page</i>	585

D. J. Angelakos
F. R. Arams
B. A. Auld
W. P. Ayres
R. W. Beatty
A. D. Berk
A. D. Bresler
H. E. Bussey
J. C. Cacharis
S. B. Cohn
P. D. Coleman
R. E. Collin
R. W. Damon
W. B. Day
M. P. Forrer
I. Goldstein
R. C. Hansen
E. M. T. Jones
R. W. Klopfenstein
P. A. Loth
R. V. Lowman
T. Moreno
S. P. Morgan
K. S. Packard, Jr.
J. Reed
F. Reggia
J. M. Richardson
P. A. Rizzi
S. D. Robertson
R. F. Schwartz
W. Sichak
D. C. Stinson
E. Strumwasser
L. Swern
P. H. Vartanian, Jr.
A. T. Villeneuve
R. D. Weglein
M. T. Weiss
G. J. Wheeler
R. F. Whitmer
J. C. Wiltse
L. Young
F. J. Zucker



Dr. A. F. Harvey
Recipient of the 1960 Microwave Prize



The Institute of Radio Engineers
Professional Group on Microwave Theory and Techniques
1960 Microwave Prize

to
Dr. A. F. Harvey

for a very significant contribution to the field of endeavor of the IRE-PCMT in his paper entitled "Periodic and Guiding Structures at Microwave Frequencies" published in the IRE TRANSACTIONS-MTT-8, No. 1, pp. 30-61, January 1960. The paper was an exceptionally well written and comprehensive survey.

May 16th, 1961



R. F. Monigahan
Chairman, PCMTT

W. N. Mumford
Chairman, PCMTT Awards Committee

Passive Phase-Distortionless Parametric Limiting with Varactor Diodes*

I. T. HO† AND A. E. SIEGMAN†, MEMBER, IRE

Summary—The theory of passive parametric limiting with a varactor diode as the nonlinear element is developed and verified experimentally. The limiting is found to be flat and phase-distortionless. Expressions are given for threshold level, dynamic range, bandwidth, and power dissipation. The transient phenomena, comprising leading- and trailing-edge leakage spikes, are studied theoretically and experimentally, and found to be small in typical instances. Experimental results reported upon include a simple waveguide limiter structure at S band; a lumped-circuit limiter at 126 Mc; and a strip-line limiter using a pill varactor at S band. The latter has an insertion loss of 2.5 db below threshold, a threshold level of 2 mw, a dynamic range in excess of 20 db, and less than 5° of phase distortion. Agreement between theory and experimental results is excellent.

INTRODUCTION

A METHOD of obtaining flat and phase-distortionless limiting in a passive parametric circuit was proposed some time ago by one of the authors [1]. Several experimental verifications of this idea, using varactor diodes as the parametric element, have since been reported [2], [3], [6]. In the present paper, we present a more detailed analysis of the diode type of passive parametric limiter, including both steady-state and transient behavior. We also present experimental results from several such limiters which closely confirm the theoretical predictions.

To describe the operation of this type of limiter, one may suppose that there is coupling between a signal frequency (ω) tank and a subharmonic frequency ($\omega/2$) tank through a nonlinear coupling element, as shown in Fig. 1. When the input signal power at ω is smaller than a certain threshold level P_{th} , the ω tank may be treated as an ordinary resonant circuit inserted between the input and the output. However, above this threshold level, which is the level just sufficient to excite the system into oscillation at the subharmonic frequency, a sharp limiting action occurs in the ω tank. Any further increase in the input signal above the threshold level does not appear in the output, but is partially transferred into the subharmonic oscillations and partially reflected back to the power source due to an increased impedance mismatch between the source and the ω tank. The general behavior is shown in Fig. 2.

The ideal output is limited abruptly and flatly beyond the threshold level until the input power increases

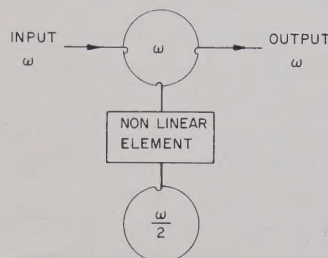


Fig. 1—Schematic of a passive parametric limiter.

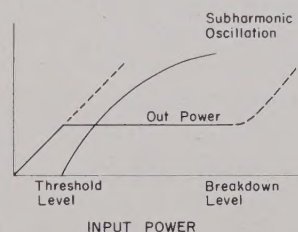


Fig. 2—General characteristics of a passive parametric limiter.

to some breakdown level P_{br} . The breakdown level for the varactor diode limiter occurs when the sum of the dc bias and the RF voltage is either larger than the reverse breakdown voltage of the varactor diode, or else is large enough to drive the varactor diode into its forward conduction region. In either case, this creates a more complicated situation, and the limiting action then generally deteriorates.

When a square-wave-modulated input signal whose amplitude is larger than the threshold level is applied to a parametric limiter, the output will be of fixed amplitude and phase-distortionless in the steady-state region, at least in the ideal case. However, the output signal will also show transient phenomena, including both a leading-edge leakage spike and a trailing-edge leakage spike. The leading-edge spike is formed because the subharmonic oscillations take time to build up from thermal noise, and the limiting action does not occur until the subharmonic oscillations have built up to a substantial value. The trailing-edge leakage spike is formed because energy stored in the subharmonic oscillation reconverts itself into the signal frequency when the input signal is turned off. In general, the leading-edge spike is found to represent more energy than the trailing-edge one.

In the ideal square-wave input case, the height of the leading-edge leakage spike is equal to the non-limited amplitude of the input signal, while the duration of the spike decreases as the input signal amplitude is in-

* Received by the PGMTT, May 1, 1961. The work reported in this paper was supported by the Wright Air Development Div. of the U. S. Air Force under Contract AF33(616)-6207, and is taken in large part from a Ph.D. dissertation submitted to the Dept. of Elec. Engrg., Stanford University, Stanford, Calif., by I. T. Ho.

† Stanford Electronics Laboratory, Stanford University, Stanford, Calif.

creased. Thus, as the input level is increased, the leakage spike gets higher but shorter, according to both theory and experiment. However, it is also found that when a realistic square-wave-modulated input signal with a finite rise time is applied to the limiter, the amplitude of the leading-edge spike does not increase indefinitely as input power increases, but rather approaches a saturation level.

In this paper: 1) the governing equations for the varactor diode parametric limiter are derived and solved in the steady-state case and design data for such limiters developed; 2) solutions of the governing equations in the transient case are summarized in order to show the nature and governing parameters of the initial and final leakage spikes; 3) this transient analysis is carried further in order to study the transient response to a finite rise time input, and to show the resulting saturation of the initial leakage spike; 4) experimental data are given for diode limiters operating in the VHF and microwave bands. Besides illustrating the possibilities of the parametric limiter as a useful device, these results also verify the theoretical analysis in detail.

It should be noted that essentially this same parametric limiting mechanism is responsible for the limiting action observed in ferrites and garnet-sphere devices at high power levels [4], [5], [14]. In these cases, various spin-wave modes play the role of the half-frequency tank. The analysis given here is thus also relevant to the ferrite case to some extent, with appropriate modifications. However, the ferrite case is generally somewhat more complicated because the spin waves furnish not one but many subharmonic resonant modes.

Comparison should be made between this work and the varactor diode parametric limiting results recently published by Olson and Wade [7], [16]. The two cases are, of course, quite different, the present limiter being an entirely passive "self-pumped" device, while Olson and Wade consider the signal-limiting properties of the standard parametric amplifier or frequency converter with the usual separate pumping signal. The best experimental results obtained by Olson and Wade considerably surpass the results obtained in this work at least in dynamic range, their limiter yielding a dynamic range of limiting in excess of 50 db in a two-stage limiter, as compared with ~ 20 db in our best one-stage limiter. In addition, their device has 10 db of gain below the limiting level as compared to $2\frac{1}{2}$ db of loss below threshold in our passive limiter, and the passive limiting threshold is considerably higher (although still in the milliwatt range). The passive device has a number of significant advantages, however. It is, of course, passive, requiring no pumping source, and also having none of the pump instability problems of other parametric devices. Its construction is much simpler with many fewer elements involved, and the setup and tuning is very simple, in contrast to the rather careful tuning and adjustment procedures which led to Olson and Wade's optimum results. The bandwidth of the passive limiter appears to be much wider. Finally, the dynamic range of the passive limiter can also be made substan-

tially larger than the results reported here, both by using two such limiters in cascade and also by using a varactor diode with a larger reverse breakdown voltage.

CIRCUIT MODEL AND GOVERNING EQUATIONS

When a reverse bias V_0 plus an RF voltage v is applied to a nonlinear capacitance diode, the instantaneous diode capacitance can be written in Taylor series form as $C(V) = C(V_0) + Dv + D_2v^2 + \text{higher-order terms}$. The negative bias is typically $V_0 = -2$ to -3 volts, and the RF voltage v is not larger than this if the diode is not driven into its forward conduction or reverse breakdown regions. Under these conditions, it can be shown that for typical $C(V)$ curves [9], the D_2v^2 term in the expansion is small compared to the Dv term, and we can drop the second and all higher-order terms.

From Fig. 1, the circuit model for a parametric limiter should consist of two resonant tanks plus a varactor diode. Fig. 3 shows the equivalent circuit used in this work. In this circuit,

L_1 and $L_{1/2}$ denote the inductances of the ω and $\omega/2$ tanks;

C_1 and $C_{1/2}$ denote the total capacitances in the ω and $\omega/2$ tanks, including the dc portion of the varactor diode capacitance in each case;

$G_{1/2}$ denotes the total internal loss conductance of the $\omega/2$ tank including losses due to the diode;

G_1 denotes the internal loss conductance of the ω tank including the diode losses, G_g and G_L denote the source and load conductances connected to this tank, and $G_T = G_1 + G_g + G_L$ denotes the total conductance in the ω tank;

and $C = Dv$ denotes the nonlinear portion of the varactor diode capacitance.

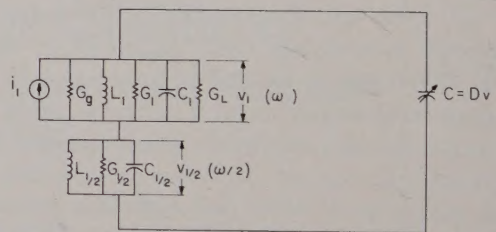


Fig. 3—Circuit model for a varactor diode parametric limiter.

We have followed the conventional practice in parametric analysis [7], [10] of including the dc portions of the diode admittance in the resonant tanks. The current source i_1 is the input signal source.

Assume that both the ω and $\omega/2$ tanks have Q 's much larger than unity. Then at the ω frequency, the $\omega/2$ tank will look like a short circuit while at $\omega/2$, the ω tank will also look like a short circuit. With this assumption, we write the usual integro-differential equations for the circuit, taking one additional differentiation to get rid of integral signs. The governing circuit equations for the ω and the $\omega/2$ frequencies are then

$$C_1 d^2 v_1 / dt^2 + G_T dv_1 / dt + \Gamma_1 v_1 = di_1 / dt - d^2(Cv) / dt^2$$

$$C_{1/2} d^2 v_{1/2} / dt^2 + G_{1/2} dv_{1/2} / dt + \Gamma_{1/2} v_{1/2} = -d^2(Cv) / dt^2, \quad (1)$$

where $v = v_1 + v_{1/2}$ is the total RF voltage at ω and $\omega/2$, $\Gamma = L^{-1}$, and only the appropriate frequency components from the $d^2(Cv)/dt^2$ term are to be included in each equation. The voltages at ω and $\omega/2$ are now written in terms of their assumed slowly varying phasor amplitudes as $v_1(t) = V_1(t) \exp(j\omega t) + V_1^*(t) \exp(-j\omega t)$ and $v_{1/2}(t) = V_{1/2}(t) \exp(j\omega t/2) + V_{1/2}^*(t) \exp(-j\omega t/2)$, and the driving current is written as $i_1(t) = I_1(t) \exp(j\omega t) + I_1^*(t) \exp(-j\omega t)$. Inserting these into (1) and neglecting certain terms on the assumption that $dV/dt \ll \omega V$ leads to the following equations for the slowly varying amplitude terms:

$$\frac{dV_1}{dt} + \frac{\omega}{2Q_T} V_1 + j \frac{\omega D}{2C_1} V_{1/2}^2 = \frac{I_1}{2C_1} + j \frac{1}{2\omega C_1} \frac{dI_1}{dt} \quad (2)$$

and

$$\frac{dV_{1/2}}{dt} + \frac{\omega}{4Q_{1/2}} V_{1/2} + j \frac{\omega D}{2C_{1/2}} V_{1/2}^* V_1 = 0, \quad (3)$$

where $Q_T = \omega C_1/G_T$ is the loaded Q of the ω tank, and $Q_{1/2} = \omega C_{1/2}/2G_{1/2}$ is the Q of the $\omega/2$ tank. These equations are for the case where ω is exactly on resonance. Additional reactive terms are present in both equations when ω is off resonance. Eqs. (2) and (3) are the basic equations for the analysis of the parametric limiter.

For simplicity, we have treated here only the degenerate case in which the subharmonic oscillation is at exactly half the signal frequency. The limiting mechanism is also operable with the subharmonic oscillation occurring simultaneously at two different lower frequencies which add up to the signal frequency, and such operation has been observed [6]. Limiter design and construction, as well as analysis, would seem to be simplest in the degenerate case, however.

STEADY-STATE SOLUTIONS AND DESIGN FORMULAS

Limiting Action and Threshold Level

The steady-state behavior of the limiter is obtained by setting the time derivatives in (2) and (3) to zero. Assuming for the moment an applied signal exactly on resonance, these equations can be manipulated to yield

$$V_1 = j \frac{G_{1/2}}{\omega D} \frac{V_{1/2}}{V_{1/2}^*} \quad (4)$$

and

$$V_{1/2}^2 = \frac{-j}{\omega D} (I_1 - G_T V_1). \quad (5)$$

Below threshold, there are no subharmonic oscillations, $V_{1/2}$ is zero, and hence (4) is indeterminate. Eq. (5), however, gives $I_1 = G_T V_1$, i.e., the ω tank is unaffected by the $\omega/2$ tank, and V_1 and I_1 are in phase. Above threshold it is immediately apparent from (4) that V_1 has a constant value independent of the magnitude of $V_{1/2}$ or, in other words, V_1 limits. Since, in the shunt model used, V_1 is the voltage across the load conductance G_L , the power output from the device also limits.

More precisely, above threshold we can write $V_{1/2} = |V_{1/2}| \exp(j\theta_{1/2})$. It is convenient to choose the origin of time such that $\theta_{1/2}$ has either of the values $-\pi/4$ or $+3\pi/4$. Substituting this into (4) then makes V_1 a real and positive quantity given by

$$V_1 = V_{th} = \frac{G_{1/2}}{\omega D} = \frac{V_d}{2Q_{1/2}}, \quad (6)$$

where it is convenient to introduce the parameter $V_d \equiv C_{1/2}/D$ which indicates the relative amount of non-linearity in the $\omega/2$ tank. When the varactor diode is strongly coupled to the microwave circuitry employed in the limiter (i.e., the "filling factor" is large, which is the optimum situation), $C_{1/2}$ will consist primarily of the dc capacitance of the varactor diode itself, and V_d will have a minimum value characteristic of the diode only. This, then, serves as a figure of merit for the varactor diode in parametric limiter applications. As an example, for a Microwave Associates MA4253 diode operated at -1 volt bias in a strip-line circuit, this quantity is $V_d \sim 40$ volts.

The two possible choices of phase for the subharmonic oscillations illustrate the well-known bistable phase condition for parametric subharmonic oscillations, as employed for example in the parametron computer element [12], [13]. With either choice, (5) can be rewritten as

$$|V_{1/2}|^2 = \frac{1}{\omega D} (I_1 - G_T V_{th}), \quad (7)$$

which shows how the subharmonic oscillations increase in amplitude as I_1 is raised above the threshold value I_{th} given by

$$I_{th} = G_T V_{th} = \frac{G_T V_d}{2Q_{1/2}}. \quad (8)$$

Note that both $|V_{1/2}|^2$ and V_{th} in (7) are purely real quantities, and therefore, I_1 must also be a purely real quantity. This indicates that I_1 and V_1 have the same phase above and below threshold, or in other words the limiting action is phase-distortionless, at least for signals applied exactly on resonance.

Finally, the input power level corresponding to the limiting threshold is given by

$$P_{th} = \frac{I_{th}^2}{2G_g}. \quad (9)$$

This quantity is given in a more useful form in the following section.

Insertion Gain, Input VSWR, and Power Distribution

The power insertion gain $L_0 (\leq 1)$ of the limiter below threshold is given by the standard expression for a transmission cavity, namely

$$L_0 = \frac{4Q_T^2}{Q_{e0}Q_{eL}} = \frac{4G_g G_L}{(G_g + G_1 + G_L)^2} \quad (10)$$

where Q_{eg} and Q_{eL} are the external Q 's of the input and output couplings from the ω tank, respectively. The threshold power level can be rewritten from (9) and (8) as

$$P_{th} = \frac{V_d^2}{8Q_{1/2}^2} \left[\frac{(G_g + G_1 + G_L)^2}{G_g} \right]. \quad (11)$$

If the source conductance is taken to be variable (*i.e.*, by varying the degree of coupling between the signal source and the ω tank), the insertion gain is found to be maximized and the threshold power level minimized by the same condition, namely that the source be matched to the limiter, or $G_g = G_1 + G_L$. If this condition is satisfied, the insertion loss becomes

$$L_0 = \frac{G_L}{G_1 + G_L} = \frac{Q_1}{Q_1 + Q_{eL}}. \quad (12)$$

This can be made close to unity by making $Q_{eL} \ll Q_1$, *i.e.*, by making the external loading heavy compared to the unloaded Q . The optimizing condition requires that the input coupling also be made heavy. With optimum input coupling, the threshold power can be thrown into the form

$$P_{th} = \frac{1}{1 - L_0} \frac{V_d^2 G_1}{2Q_{1/2}^2} = \frac{1}{1 - L_0} P_{th(min)}. \quad (13)$$

There is a minimum threshold power given by $P_{th(min)} = V_d^2 G_1 / 2Q_{1/2}^2$. If the diode is tightly coupled to the limiter circuitry, G_1 will consist primarily of the equivalent shunt conductance of the varactor diode itself, and $Q_{1/2}$ will be essentially equivalent to the Q of the varactor diode. Therefore, this minimum threshold power is essentially a property of the varactor diode only. As a typical example, the numbers involved might be $V_d = 40$ volts, $G_1 = 4 \times 10^{-3}$ mhos, and $Q_{1/2} = 100$, leading to a threshold power of 0.3 mw. Varactor diode limiters can thus have respectably low limiting levels.

Eq. (13) shows, however, that the actual threshold power is greater than this minimum value by an amount depending on how close the insertion gain is made to unity. Fig. 4 plots the ratio $P_{th}/P_{th(min)}$ in db as a function of the insertion gain in db. The quantity Q_1/Q_{eL} (or $Q_1/Q_{eg} = Q_1/Q_{eL} + 1$) is, of course, the parameter which moves one along this curve.

Above the threshold level, the effect of the $\omega/2$ tank and the subharmonic oscillations on the ω tank may be accounted for by introducing into the ω tank an additional effective conductance G_{add} which increases with input power in such a way as to keep V_1 constant at V_{th} when I_1 increases above I_{th} . This additional conductance is given by

$$\begin{aligned} G_{add} &= \frac{I_1}{V_1} - G_T \\ &= (I_1/I_{th} - 1)G_T \\ &= (n - 1)G_T, \end{aligned} \quad (14)$$

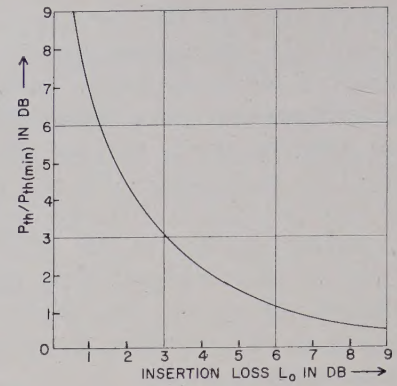


Fig. 4—Increase in threshold power above the minimum value, as a function of the below-threshold insertion loss L_0 .

where $n = I_1/I_{th}$ is a measure of how far the input power is increased above threshold. As a result of this additional conductance, the input impedance of the limiter as seen by the signal source changes. The signal source in most practical cases will probably be undercoupled to the limiter, since the Q of the limiter is generally limited by the diode Q and is not large. With this assumption, the magnitude of the reflection coefficient looking from the signal source towards the limiter above threshold can be written

$$\rho = \frac{G_1 + G_L + G_{add} - G_g}{G_1 + G_L + G_{add} + G_g} = \frac{\rho_0}{n} + \frac{n-1}{n}, \quad (15)$$

when ρ_0 is the reflection coefficient below the threshold level. The input voltage-standing-wave ratios above and below threshold, S and S_0 , are thus related by

$$S = nS_0 + (n-1). \quad (16)$$

Experimental verification of this equation will be given below.

The input power to the limiter above threshold is distributed among the following four outlets: 1) output power; 2) power losses in the ω tank; 3) power losses in the $\omega/2$ tank due to the subharmonic oscillations; and 4) power reflected from the limiter back to the signal source or to an isolator placed in the input line. Power losses 2) and 3) are dissipated chiefly by the diode in practical cases, since the diode losses generally predominate over copper losses if the diode is tightly coupled. If we assume for simplicity that the limiter input below threshold is matched, as required for optimum performance, then the powers into each of these four categories are given by the simple expressions

$$\begin{aligned} P_{out} &= 2V_{th}^2 G_L = L_0 P_{th}, \\ P_{loss}(\omega) &= 2V_{th}^2 G_1 = (1 - L_0) P_{th}, \\ P_{loss}(\omega/2) &= 2V_{th}^2 G_{add} = 2(n-1) P_{th}, \\ P_{reflected} &= \rho^2 P_{in} = (n-1)^2 P_{th}. \end{aligned} \quad (17)$$

These four powers are plotted in Fig. 5 as a function of the input power below and above threshold. It is appar

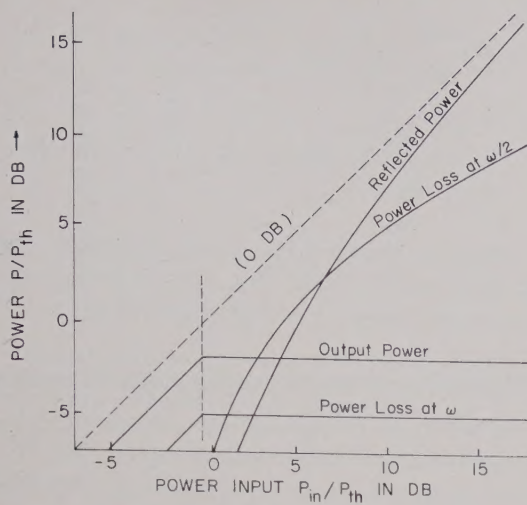


Fig. 5—Distribution of input power among various outlets, as a function of the input power level, assuming an insertion loss of 2.5 db below threshold.

ent that above the threshold, the largest amount of power is reflected, although the diode must also absorb some power at higher input power levels. This information is important in determining the maximum power input the limiter can withstand without damage to the varactor diode due to overload.

Dynamic Range

In the varactor diode limiter, the diode should not be driven either beyond its reverse breakdown voltage or into its forward conduction region, so that the sum of the dc bias and RF voltages must not go positive nor exceed the reverse breakdown voltage $-V_{br}$. The desirable reverse bias for the diode is thus $V_0 \approx -V_{br}/2$, and the total instantaneous RF voltage must then not exceed $V_{br}/2$. Although the total RF voltage is the sum of v_1 and $v_{1/2}$, it can be shown that $v_{1/2}$ is much the larger of the two when strong limiting action is occurring. Since the peak value of $v_{1/2}$ is $2|V_{1/2}|$, the condition for breakdown is

$$2|V_{1/2}| = \left[\frac{(n-1)2V_d V_d'}{Q_T Q_{1/2}} \right]^{1/2} \leq \frac{V_{br}}{2}, \quad (18)$$

where $V_d' \equiv C_1/D$ is a parameter of the same nature as $V_d \equiv C_{1/2}/D$. In fact, if the diode is very tightly coupled to the limiter circuitry, the situation will be $C_1 \approx C_{1/2} \approx$ the dc capacitance of the varactor diode. Eq. (18) can be reversed to give the maximum allowable value of n as

$$n_{\max} = \frac{Q_T Q_{1/2} V_{br}^2}{8V_d V_d'} + 1. \quad (19)$$

The dynamic range of the limiter from threshold to breakdown is, then,

$$\text{Dynamic range} = 20 \log_{10} n_{\max}. \quad (20)$$

Over this range, the limiting in a good limiter should be essentially flat and phase-distortionless. One can, of

course, drive the limiter even beyond this range, and limiting action will still be present. The limiting will not be ideal, however, and care must be taken that the diode is not damaged by excessive current or power dissipation.

Bandwidth

Assume now that the signal frequency ω is not exactly equal to the resonant frequency ω_0 of the signal tank. We then define

$$\begin{aligned} \Delta\omega &= \omega - \omega_0 & \Delta(\omega/2) &= (\omega/2) - (\omega_0/2) \\ \delta &= \Delta\omega/\omega_0 & \delta_{1/2} &= \Delta(\omega/2)/(\omega_0/2) = \delta. \end{aligned} \quad (21)$$

We will assume here that the subharmonic tank is tuned to exactly one-half the signal tank, and that, as mentioned before, the subharmonic oscillation occurs in degenerate fashion at $\omega/2$ rather than at any two other frequencies adding up to ω .

Eq. (4) must now be modified to

$$V_1(\omega) = j \frac{Y_{1/2}}{\omega D} \frac{V_{1/2}}{V_{1/2}^*}, \quad (22)$$

where

$$\begin{aligned} Y_{1/2} &= G_{1/2} + j(\omega C_{1/2}/2 - 2/\omega L_{1/2}) \\ &\approx G_{1/2}[1 + j2Q_{1/2}\delta]. \end{aligned} \quad (23)$$

Eq. (22) indicates that V_1 is still ideally limited even when the signal is off resonance. If we make the same assumption as previously about the phase of $V_{1/2}$, the threshold voltage as a function of frequency will be given by

$$V_{th}(\omega) = V_{th}(\omega_0)[1 + j2Q_{1/2}\delta], \quad (24)$$

and the limited output power level will be

$$P_{out}(\omega) = P_{out}(\omega_0) \cdot [1 + 4Q_{1/2}^2 \delta^2]. \quad (25)$$

The output power from the limiter operating above threshold has the form of an inverted resonance curve with Q value equal to the $Q_{1/2}$ of the subharmonic resonant circuit. Below threshold, of course, the limiter is simply a transmission cavity with power transmission given by the usual expression

$$L(\omega) = L_0 \frac{1}{1 + 4Q_T^2 \delta^2}. \quad (26)$$

Combining (25) and (26) leads to a set of curves of power output vs frequency at various input power levels of the form shown in Fig. 6 where the particular choice of parameters used is $Q_{1/2} = Q_T$.

For signals off resonance, the equivalent of (5) is

$$V_{1/2}^2 = \frac{-j}{\omega D} (I_1 - Y_1 V_1), \quad (27)$$

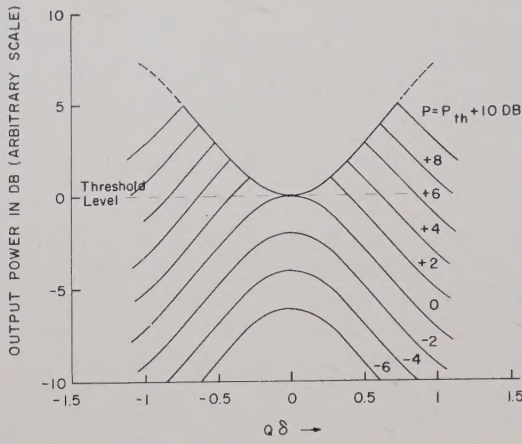


Fig. 6—Output power vs frequency for increasing power inputs (assuming $Q_T = Q_{1/2} = Q$).

where Y_1 is the admittance of the ω tank, approximately given by

$$Y_1 \approx G_T(1 + j2Q_T\delta). \quad (28)$$

The threshold value of I_1 off resonance is thus

$$\begin{aligned} I_{th}(\omega) &= Y_1(\omega)V_{th}(\omega) \\ &= I_{th}(\omega_0)[(1 + j2Q_T\delta)(I + j2Q_{1/2}\delta)], \end{aligned} \quad (29)$$

and the threshold input power off resonance is

$$P_{th}(\omega) = P_{th}(\omega_0) \cdot [(1 + 4Q_T^2\delta^2)(1 + 4Q_{1/2}^2\delta^2)]^{1/2}. \quad (30)$$

The threshold input power increases both because a larger voltage V_1 is required off resonance, and also because a larger power input is required to create this voltage off resonance.

Using the same choice as before for the origin of time or the phase of $V_{1/2}$ permits (27) to be put in the form

$$I_1(\omega) = Y_1(\omega)V_{th}(\omega) + \omega D |V_{1/2}|^2. \quad (31)$$

Below and at threshold the phase relationship between I_1 and V_1 is that appropriate to $Y_1(\omega)$. Above threshold, the phase relationship is determined by the preceding equation. It is apparent that as I_1 and $|V_{1/2}|$ increase above the threshold level, this phase relationship will be altered. Therefore, the limiting is no longer perfectly phase-distortionless off resonance; the amount of phase distortion increases with input level and with distance from resonance.

Second Order Effects

If the next higher order term D_2v^2 in the nonlinear capacitance expression is retained in the theory, it can be shown that the resulting steady-state equations analogous to (4) and (5) are

$$\begin{aligned} \frac{\omega}{4Q_{1/2}} V_{1/2} + j \frac{\omega D}{2C_1} V_{1/2}^* V_1 \\ = \frac{3D_2\omega^2}{4} [2|V_1|^2 + |V_{1/2}|^2] V_{1/2} \end{aligned} \quad (32)$$

$$\begin{aligned} \frac{\omega}{2Q_T} V_1 + j \frac{\omega D}{2C_1} V_{1/2}^2 \\ = \frac{I_1}{2C_1} + 3D_2\omega^2 [2|V_{1/2}|^2 + |V_1|^2] V_1. \end{aligned} \quad (33)$$

It can then be shown from these equations that the limiting is no longer ideally flat, the power out vs power in characteristic showing a slight upward tilt.

TRANSIENT SOLUTIONS AND LEAKAGE SPIKES

The ferrite type of parametric limiter exhibits relatively large and troublesome leakage spikes [4], [5], [14]. Such leakage spikes are not generally found to be nearly as troublesome in the varactor diode type of limiter. Nonetheless, detailed studies of the transient solutions to the governing equations (2) and (3) were carried out as part of this investigation, solutions being obtained both by numerical calculation and by deriving iterated piecewise analytical solutions. A very brief summary of these results is presented here. The detailed results can be found in the original report [2].

Nature of the Spikes

When an input signal pulse with a very steep leading edge is applied to the parametric limiter, the output at ω will at first build up very rapidly to the appropriate unlimited level, the rate of buildup being determined only by the usual energy buildup considerations for a resonant circuit. If the input signal is far above threshold, the output will, of course, far exceed the steady-state limiting level of the device. The subharmonic oscillations at the same time begin to build up from their thermal noise level towards their steady-state value. The subharmonic buildup is essentially exponential with time, except for a very brief initial period when the energy in the ω tank is still being established. The rate of rise of the $\omega/2$ oscillations is determined by the strength of the "pumping" done by the input signal, the rate of rise being faster the farther the input signal is above the limiting threshold. As soon as the subharmonic oscillations reach nearly to their steady-state value, the limiting action begins, and the signal level in the ω tank very rapidly drops to the steady-state limited value. The signal output thus exhibits an initial leakage spike whose height increases directly with input signal level and whose duration decreases with increasing input level.

If the input signal is suddenly turned off after the limiter has reached the steady-state condition, the device is left with a substantial amount of energy stored in the subharmonic resonant circuit. Some of this energy will be reconverted to the ω frequency and will appear as a trailing-edge spike of output at ω , following the signal turn-off.

Fig. 7 illustrates the general appearance of these leading- and trailing-edge leakage spikes.

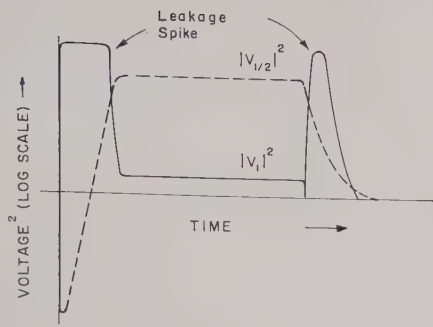


Fig. 7—Output power vs time for a rectangular input pulse, showing leading- and trailing-edge leakage spikes and the buildup of the subharmonic oscillations (dashed line).

Calculations

As part of the work (2) and (3) were solved by numerical forward integration using a large digital computer and small forward steps in time following the application of a signal pulse. Examination of (3) will show that no subharmonic voltage $V_{1/2}$ will ever be developed unless some initial excitation is present to be parametrically pumped up. The initial excitation in the physical case is, of course, thermal noise fluctuations, and these were represented in the calculations by putting in an initial amplitude of $V_{1/2}$ corresponding to the rms thermal noise voltage of the conductance in the $\omega/2$ tank. (The noise voltage was actually reduced by 3 db to account for the fact that only half of the noise energy would be in the proper phase to be pumped up, the other half being so phased as to be parametrically pumped down to zero.) Fig. 8 shows the observed behavior of the output voltage and the subharmonic voltage predicted by the numerical calculations for several different excitations above the threshold level. The input signal is assumed to be an ideal step function, and the numerical parameters are typical values for a varactor diode limiter. It is apparent that the leakage spikes are extremely brief, on the order of nanoseconds, since the pump-up of the subharmonic oscillations is very rapid. The leakage energies are correspondingly small, on the order of 10^{-9} joules.

The exponential nature of the subharmonic buildup has been pointed out in previous studies of parametron oscillators and ferrite limiters [5], [13], [14]. It can be readily derived by rewriting (3) in the form

$$\frac{d}{dt} |V_{1/2}| = -\frac{\omega}{4Q_{1/2}} |V_{1/2}| - j\frac{\omega}{2} \frac{|V_1|}{V_d} \exp[j(\theta_1 - 2\theta_{1/2})] |V_{1/2}|, \quad (34)$$

where θ_1 is the phase angle of V_1 and $\theta_{1/2}$ the phase angle of $V_{1/2}$. If $V_{1/2}$ is divided into two quadrature components with phase angles $\theta_{1/2} = \theta_1/2 + 135^\circ$ and $\theta_{1/2} = \theta_1/2 + 45^\circ$, the former will be parametrically amplified and the latter parametrically deamplified. If V_1 is assumed to very rapidly reach the nonlimited value given by $|V_1| = nV_{th} = nV_d/2Q_{1/2}$, then the subharmonic oscillation

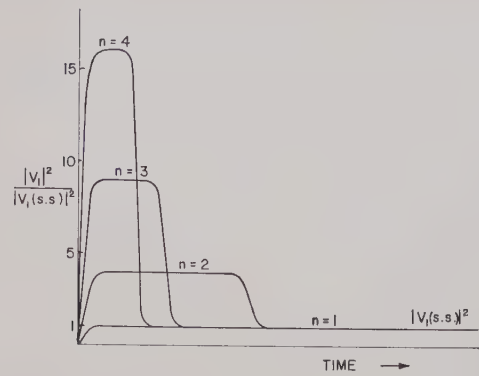


Fig. 8—Leading-edge leakage spikes in a varactor diode limiter for various inputs above the threshold level, as obtained from numerical computations. Parameters are: $f=3$ kMc; $Q_T=5$; $Q_{1/2}=50$; $C_1=C_{1/2}=2.8$ pf; $D=0.28$ pf/v. The input levels $n=2, 3$ and 4 correspond, respectively, to inputs which are 6, 9.6 and 12 db above the threshold level.

tion voltage grows as

$$|V_{1/2}| = |V_{1/2}(0)| \exp[(n-1)\omega t/4Q_{1/2}]. \quad (35)$$

The length of the initial leakage spikes is essentially the buildup time required for $V_{1/2}$ to grow from its initial noise value to the steady-state value given by (18). The initial noise value is given by $V_{1/2}^2 = 2kTB_{1/2}/G_{1/2}$ (halved because only growing components are included), and a reasonable value for $B_{1/2}$ would seem to be the bandwidth of the $\omega/2$ tank, $B_{1/2} = \omega/2Q_{1/2}$. With these assumptions, the buildup time or leakage spike length is given by

$$\tau = \frac{2Q_{1/2}}{(n-1)\omega} \ln \left[\frac{(n-1)C_{1/2}V_dV_d'}{4kTQ_TQ_{1/2}} \right]. \quad (36)$$

The argument of the logarithm is the ratio of the steady-state subharmonic oscillation power level to the thermal noise power level, which is a very large ratio, on the order of 120 db for typical values. Therefore, the logarithm is insensitive to the exact value of the thermal noise level, and changes of ± 20 db in the assumed thermal noise level have only a small effect on τ . Fig. 9 shows on a logarithmic scale a comparison between the exponential build-up of $V_{1/2}$ as given by (35) and the results for the same case as obtained from the numerical computer solutions. (The small difference at the initial level is due to different detailed assumptions about the noise level from which the oscillation grows.)

The $Q_{1/2}$ of the $\omega/2$ tank is apparently an important parameter in determining the length of the leakage spikes. This value is fairly low (~ 100) in the varactor diode case, which, coupled with a fairly strong degree of nonlinearity, leads to a short leakage spike. Ferrite and garnet limiters operating on this same principle are observed to have substantially longer leakage spikes. This is, in part, due to the relatively higher Q of the spin waves which play the role of the $\omega/2$ tank in the ferrite case.

In work by one of the authors [2], considerable attention is given to the details of the crossover region when

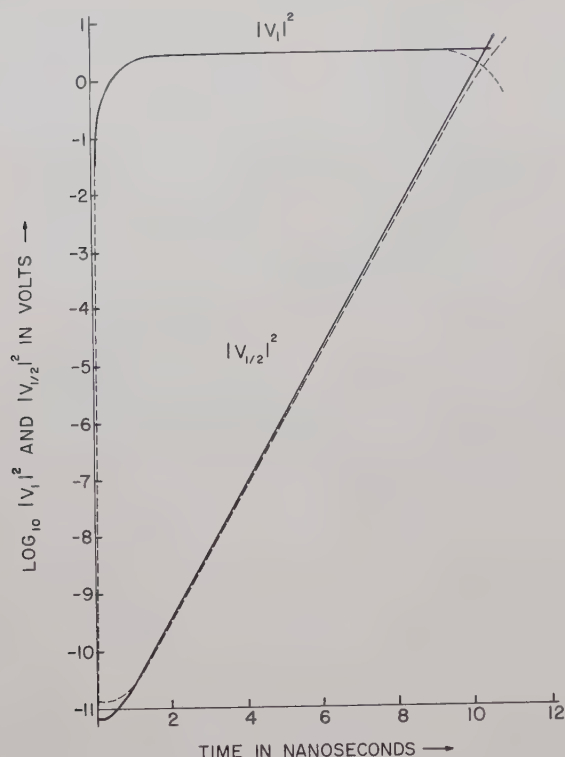


Fig. 9—Exponential buildup of the subharmonic oscillations during the leading-edge spike. Dashed line=computer solution; solid line=analytical solution. Numerical parameters are the same as in Fig. 8, with $n=16$ (24 db above threshold).

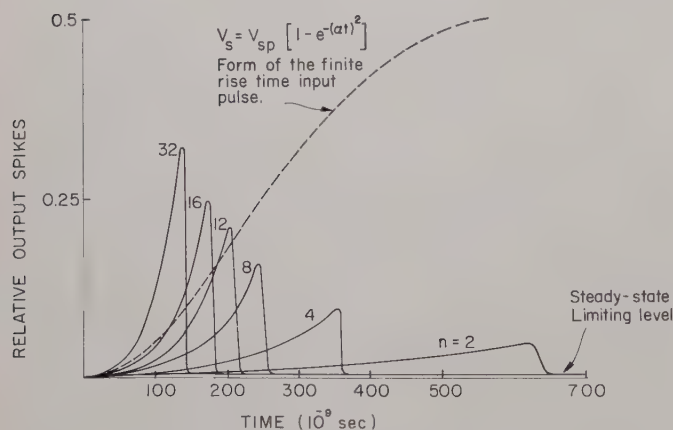


Fig. 11—Leading-edge leakage spikes in a varactor diode limiter for a finite rise time input signal. Numerical parameters are the same as in Fig. 8 with the exception of the input signal. Note difference in shape and length of leakage spikes from Fig. 8.

$V_{1/2}$ nears its steady-state value and the limiting action begins. Iterated piecewise analytic expressions are developed to study the behavior in this region. Fig. 10 shows some of the details of this region, with the numerical computer solution indicated by a dashed line, two successive analytical approximations indicated by solid curves I and II. In general, it can be said that there is a smooth and rapid transition from the initial buildup region to the steady-state limiting region, with

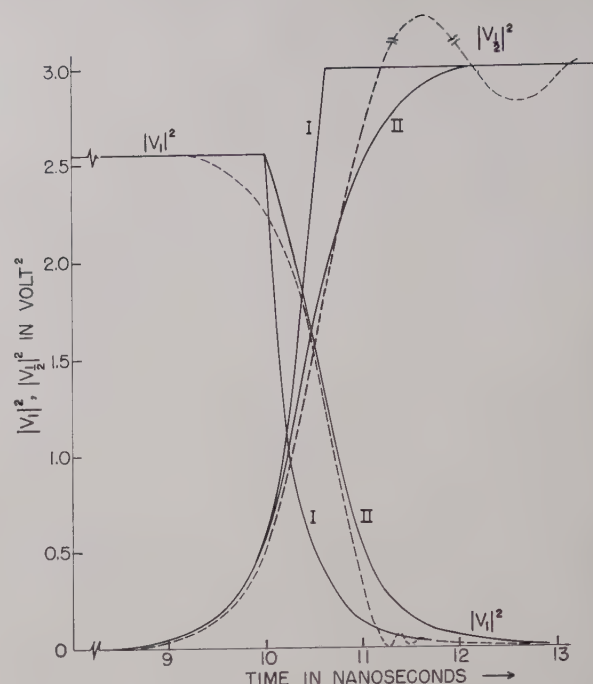


Fig. 10—Details of the limiter behavior in the crossover region from the leading-edge spike to the steady-state limiting condition. Dashed line=computer solution; solid lines I and II=two successive analytical approximations. Numerical parameters are the same as in Fig. 9.

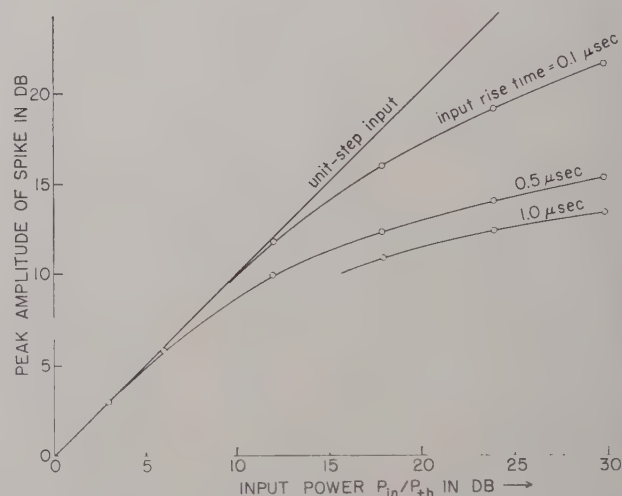


Fig. 12—Curves illustrating the "saturation" behavior of leakage spikes like those in Fig. 11 for input signals of different rise times. Obtained from computer solutions; numerical parameters same as previously.

only small overshoots and other extraneous effects.

The shortness of the initial leakage spikes in the varactor diode limiter, as compared to typical rise times for pulsed sources, led to consideration of the buildup and leakage spikes in the parametric limiter with finite-rise-time pulses applied. Fig. 11 illustrates the leakage spikes obtained from the computer solution for increasing input power levels when the input signal has a finite rise time. It is observed that the leakage spikes

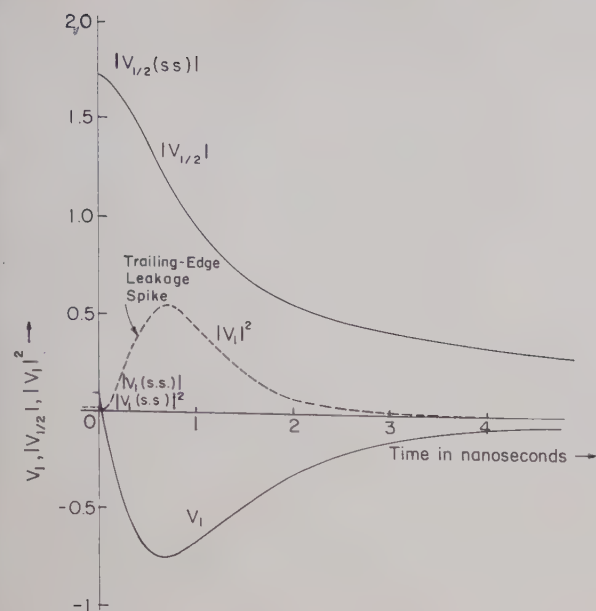


Fig. 13—Trailing-edge leakage spike as obtained from the numerical solutions. Numerical parameters same as in previous figures, with $n = 16$.

are shorter at higher input levels, as in the step-function input case, but the spike heights do not continue to rise as the input power is increased. For higher input powers, the subharmonic oscillations have built up to the limiting level before the input pulse is fully built up to its maximum level. The leakage spike height appears to “saturate” at higher input levels. Fig. 12 verifies this by showing the initial leakage-spike height as a function of input power above threshold for several different rise times and a typical set of varactor diode limiter parameters.

The Trailing-Edge Spike

The numerical computation method was also used to obtain the trailing-edge spike characteristics by using the steady-state limited values as initial conditions and solving (2) and (3) with the driving current I_1 set to zero. Fig. 13 shows the trailing-edge leakage spike for a typical case. Note that the subharmonic voltage is much larger than the limited signal voltage in the steady-state situation. Note also that the signal voltage amplitude V_1 drops to zero and then changes sign. This corresponds to V_1 changing from the driving to the driven quantity in the parametric circuit.

It should be noted that there can be an entirely independent source of leakage spikes in practical situations. If the frequency of the pulsed signal source changes during the rise and fall of the signal pulse, as may well be the case with some pulsed signal sources, this can also cause a significant leakage spike on the trailing edge of the limited pulse.

EXPERIMENTAL RESULTS

Three versions of parametric limiters using varactor diodes as nonlinear devices were built and tested during

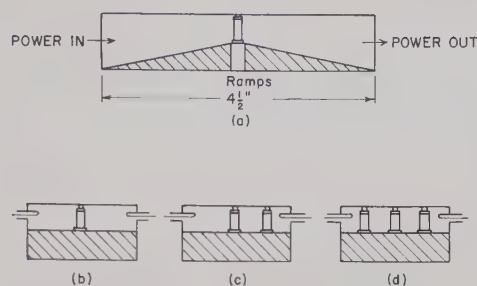


Fig. 14—S-band waveguide version of the parametric limiter. (a) Side view; (b), (c), (d) end views of models having one, two and three diodes. The loops are for monitoring the subharmonic resonance.

this work, and a fourth version using a YIG sphere as its nonlinear element was borrowed from the Watkins-Johnson Co. and tested. Each version served a different purpose in verifying the theoretical predictions given in the previous sections. These four versions [2] were:

- 1) An S-band waveguide version used for some initial experiments, characterized by no resonant tank at the ω frequency and employing several Microwave Associates, Inc., MA460 varactor diodes in parallel shunted across the waveguide.
- 2) An S-band YIG sphere version used for observing the leakage spikes, since these are too short to be readily seen in the S-band varactor diode-type limiter.
- 3) A VHF (126 Mc) lumped-circuit version again employing MA460 varactor diodes used to observe the leakage spikes by virtue of its lower signal frequency.
- 4) An S-band strip-line version employing a Microwave Associates Inc., MA4253 pill-type varactor diode with the twin virtues of low-series inductance and high-cutoff frequency, used for detailed comparisons with the steady-state theory given above.

S-Band Rectangular Waveguide Version

A parametric limiter with one or more MA 460 varactor diodes installed inside an S-band rectangular waveguide was first designed and built as shown in Fig. 14. The detection loops were for monitoring the $\omega/2$ oscillation. The important features of this design were:

a) There was no ω resonant tank. One, two, or three diodes were simply placed side by side across the waveguide, whose height was reduced by ramps before and after the diodes. The waveguide was propagating at the signal and all higher frequencies, but was well below cutoff at the subharmonic frequency.

b) A novel method was employed for obtaining the $\omega/2$ resonance. The imaginary characteristic impedance of the rectangular waveguide below cutoff, which for the TE₁₀ mode is inductive in nature, was resonated with the diode capacitance to create the subharmonic resonance at the $\omega/2$ frequency. This type of resonance is sometimes called a “ghost mode” [15]. The subharmonic resonance was tuned by varying the reverse bias, thus changing the dc capacitance of the diode.

Measurements of output limiting were conducted separately for the three diode arrangements shown in Fig. 14. They all yielded similar sharp limiting as predicted for a parametric limiter. However, the dynamic range of limiting increased considerably with more diodes.

	1 diode	2 diodes	3 diodes
Signal frequency	3040 Mc/sec	2878 Mc/sec	2738 Mc/sec
Dynamic range of limiting	3 db	7.5 db	16 db
Bias	-1.5 v	-1.5 v	-1.5 v
Threshold level	~10 mw	~10 mw	~10 mw

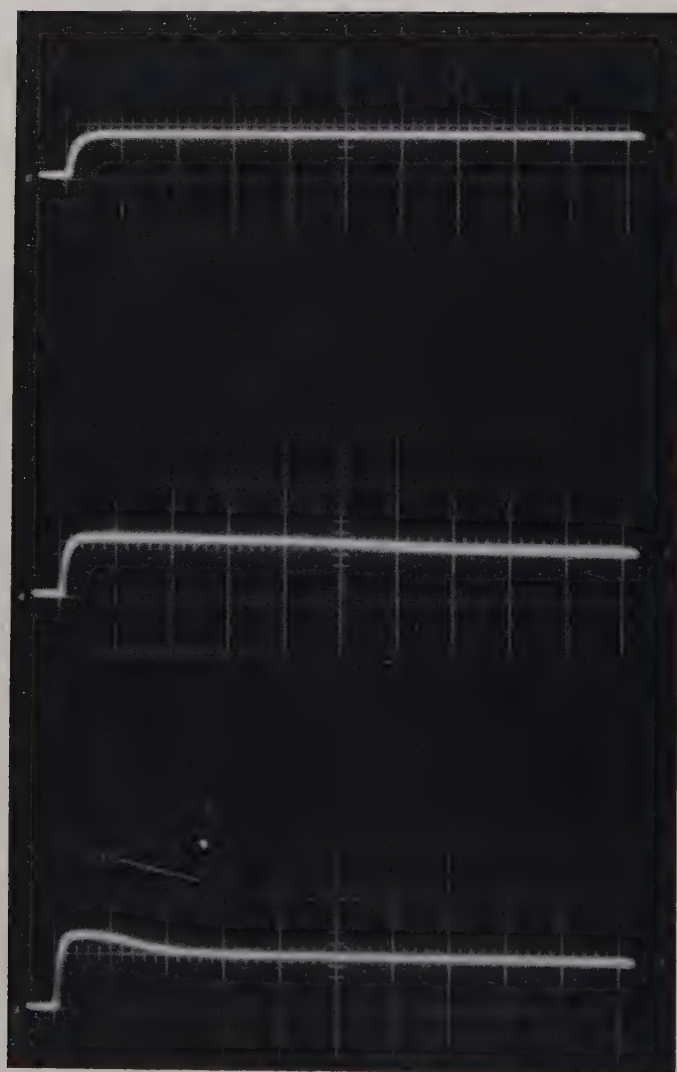
Approximately a ten per cent bandwidth was obtainable in the limiting of these three cases. Phase-distortion measurements showed that the phase distortion of the 3-diode limiter was less than $\pm 3^\circ$, which is the accuracy of the measurement, over the entire 16-db range of limiting. Insertion loss of the 3-diode limiter below threshold was approximately 10 db. This con-

figuration represents a particularly simple form for such a limiter and may merit further development.

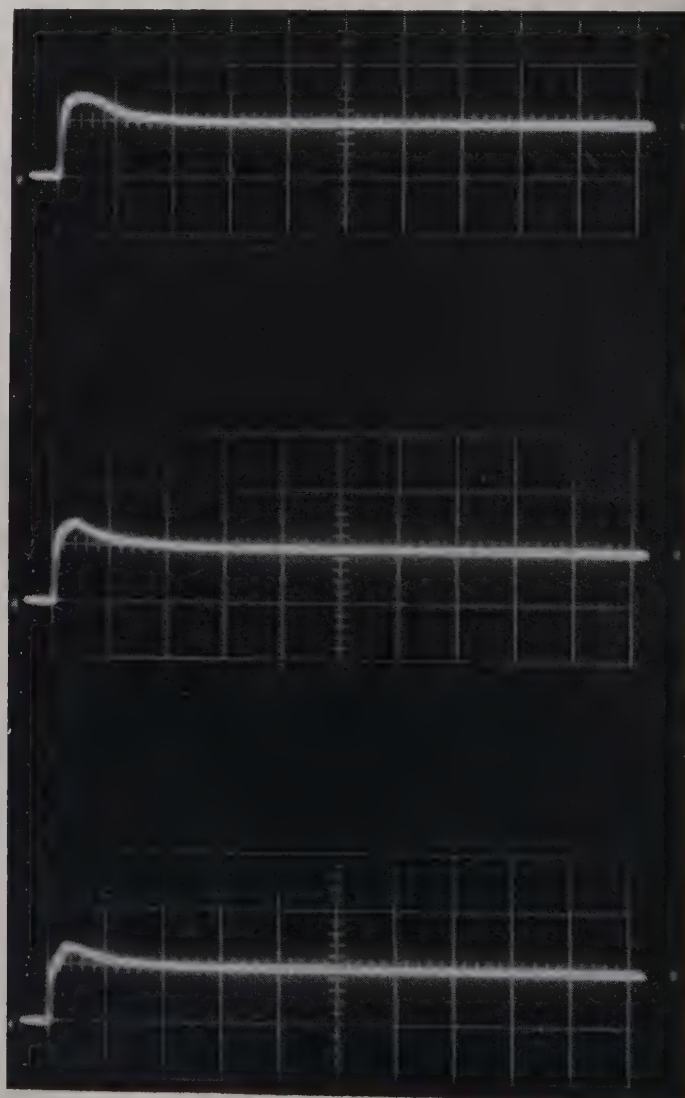
S-Band Yttrium Iron Garnet Sphere Version

Leakage spikes were too short to be readily seen in the previous S-band varactor diode limiter. The theoretical duration time of the leading-edge leakage spike is found to be on the order of 10^{-9} second when reasonable values for the parameters are substituted into (36). To make τ long enough to be easily observable, two alternatives were tried, one by using a YIG sphere limiter because of its higher $Q_{1/2}$, the other by using a VHF version (126 Mc) to lower the ω . The results of the YIG sphere version are shown in this section, and those of the VHF version are shown in the next section.

The leading-edge leakage spikes are shown in Fig. 15. The duration times of the leakage spikes become shorter as the input power increases. The peak amplitudes of the leakage spikes increase first and then saturate. The



(a)



(b)

Fig. 15—Leakage spikes observed in a garnet sphere form of parametric limiter. The behavior of the leakage spikes is in qualitative agreement with the theory.

qualitative behavior of the leading-edge leakage spikes at first agrees in general with the theoretical predictions, although detailed quantitative comparisons are not possible because the basic parameters for the garnet sphere limiter are not known. The insertion loss of this version was measured to be 5 db, and the dynamic range was over 20 db.

VHF Lumped Circuit Version

From (36) one realizes that a lower signal frequency ω will also make the duration time of the leading-edge leakage spike longer. A lower-frequency (126 Mc) limiter was therefore built by shunting three MA460 varactor diodes with a lumped circuit coil to form a $\omega/2$ tank and then placing band-pass filters at $f=126$ Mc on each side of this circuit. The $\omega/2$ tank was tuned to 126/2 Mc with a 1-v reverse bias applied on

the varactor diodes. The leading edges of the output waveforms are shown in Fig. 16, which were taken on a wideband oscilloscope without using a crystal detector. As in Fig. 15, the leading-edge leakage spikes saturate quite rapidly.

The insertion loss of this version is measured to be 3 db; its dynamic range is 10 db. The threshold level of this limiter was measured to be 2.4 db above a milliwatt, and a more than 5 per cent bandwidth was observed.

S-Band Stripline Version

The recently available pill-type varactor diode has the twin advantages of low series inductance and high-cutoff frequency. Its tiny size of $\frac{1}{8}$ in \times $\frac{1}{8}$ in fits a stripline configuration better than other microwave configurations, and hence a stripline limiter was designed. The pill varactor used in this work had a zero-bias

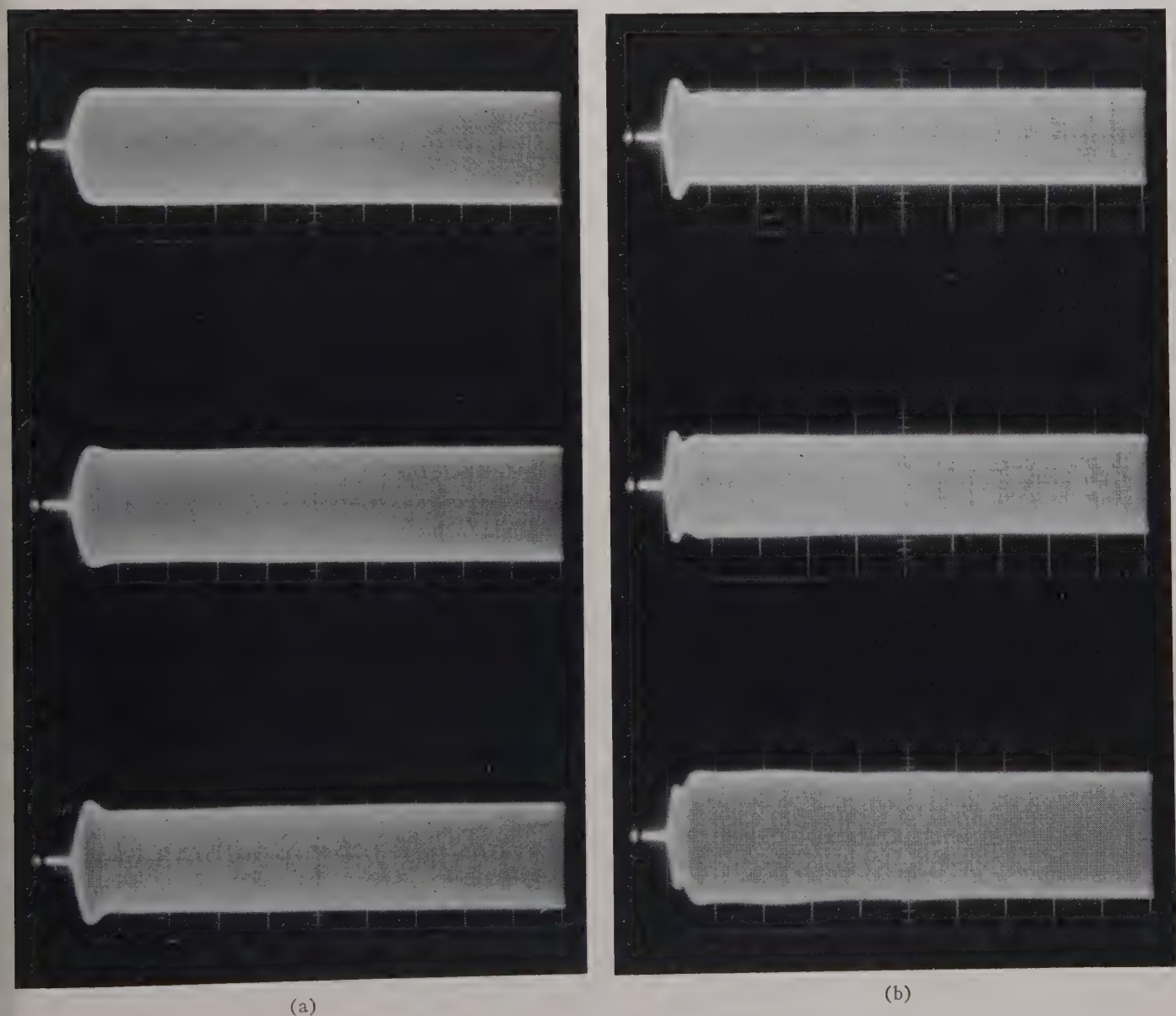


Fig. 16—Leakage spikes observed in a varactor diode limiter operating at 126 Mc. Again, there is qualitative agreement with the theory, at least at the lower power levels.

capacitance of 0.78 pf and a cutoff frequency of 126 kMc.

The pill varactor was mounted between the center conductor and one of the ground planes of the strip-line. Two movable shorts, one on each end of the strip-line, together with the change in varactor dc capacitance with change in bias voltage, served to adjust the resonant frequencies of this device. Fig. 17(a) shows a side view of the limiter, and Fig. 17(b) shows the electric field distributions for the ω and $\omega/2$ resonant modes employed. Signal power was coupled into and out of the ω tank by two loops located at a position where the magnetic field of the ω mode was maximum while that of the $\omega/2$ mode was minimum. A pair of monitoring loops was also placed at a position where the magnetic field of the ω mode was zero in order to monitor the subharmonic oscillations and perform tuning adjustments at $\omega/2$. Diode dc isolation and RF bypass were obtained by placing below the pill varactor a capacitor formed by 1" diameter copper disk with a 5-mil thick teflon dielectric. The lower-ground plane was countersunk to a depth such that the top of the copper disk was flush with the remaining surface of the lower-ground plane. Fig. 18 shows photographs of this limiter assembled and disassembled.

With this limiter, essentially flat limiting over a range of 20 db above a threshold level of ~ 1 mw was observed, as shown in Fig. 19. Insertion loss below threshold was ~ 2.5 db. The phase distortion was measured both below and above the threshold level with the results shown in Fig. 20. Over the entire input power range, the phase distortion is within $\pm 5^\circ$, the accuracy of measurement being approximately $\pm 3^\circ$.

Comparison with Theory

The strip-line limiter operated at a reverse bias of 1.0 v had the following characteristics, as determined from the known diode characteristics plus careful measurements of the below-threshold characteristics of the resonant modes at ω and $\omega/2$:

$$\omega_0 = 2382 \text{ Mc}$$

$$Q_T = 41$$

$$Q_{1/2} = 117$$

$$\text{Input VSWR} = 1.2$$

$$G_L = G_g = 20 \times 10^{-3} \text{ mhos}$$

$$G_T = G_1 + 2G_g \approx 44 \times 10^{-3} \text{ mhos}$$

$$V_d = V_d' \approx 40 \text{ v}$$

$$V_{br} = 5.5 \text{ v}$$

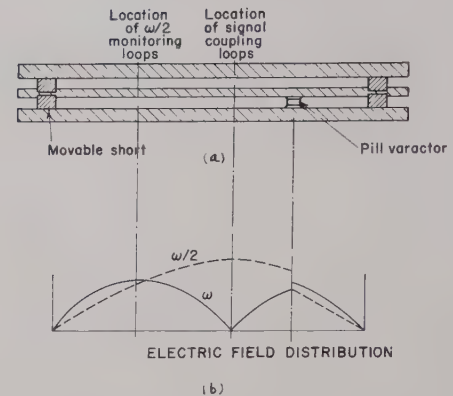


Fig. 17—Side view of the strip-line varactor diode limiter, and mode patterns of the resonant modes at ω and $\omega/2$.

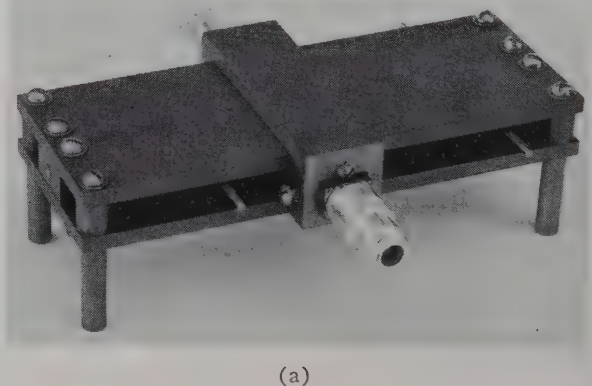


Fig. 18—Assembled and exploded view of the strip line limiter ($\omega/2$ coupling loops not shown).

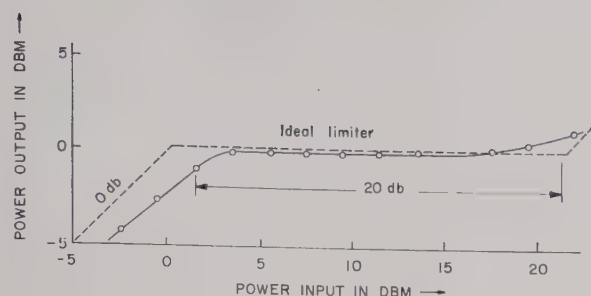


Fig. 19—Limiting characteristic of the strip-line varactor diode limiter showing a 2-mw threshold level and a 20-db dynamic range.

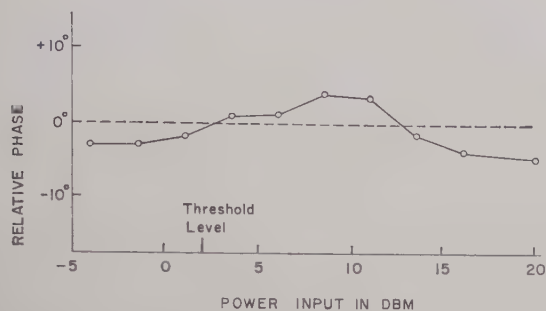


Fig. 20—Relative phase of the limiter output compared to limiter input as a function of input power level, showing the phase-distortionless nature of the parametric limiting.

One can substitute these parameters into the various theoretical expressions given above and compare them with the experimental results. The following comparisons will show the excellent agreement obtained:

a) *Threshold level*: Use of the above numbers in (8) and (9) gives a predicted threshold level of 1.25 mw. The measured value is approximately 2 mw.

b) *Phase distortion*: As shown in Fig. 20, the phase distortion is very small, nearly within the error of measurement, in agreement with theoretical predictions.

c) *Input VSWR above threshold*: Eq. (16) relates the input VSWR above threshold to the value below threshold and the value of n . Fig. 21 shows the comparison between this equation and the experimental results obtained on the stripline limiter. A similar input VSWR curve given by Wolf and Pippin [3] was also compared with (16), and good agreement was again obtained.

d) *Dynamic range*: From (19) and (20), the predicted dynamic range is $n_{\max} = 12.4$ or a dynamic range of 22 db. The measured value, as determined by the point at which the power output curve of Fig. 19 begins to rise, is approximately 20 db.

e) *Bandwidth*: The power output vs frequency characteristics of the limiter at different input power levels were studied with the aid of a swept-frequency RF source, leading to the oscilloscope traces of detected output vs frequency shown in Fig. 22. Since the output of the swept-frequency source was not leveled and various mismatches are present in the system, detailed com-

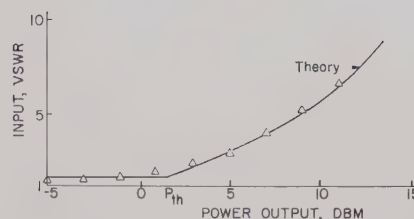
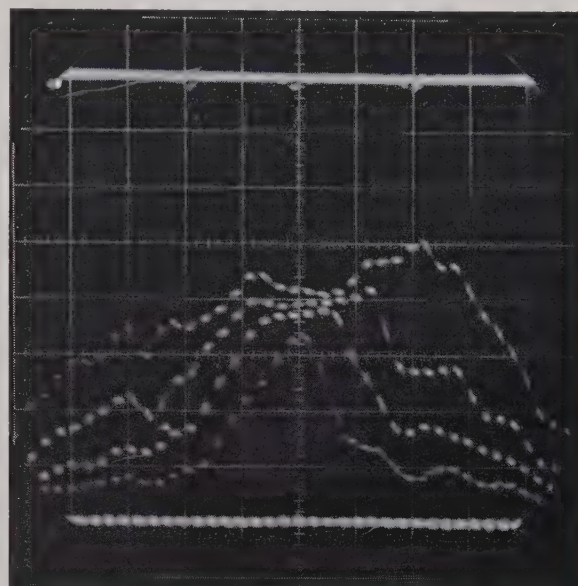
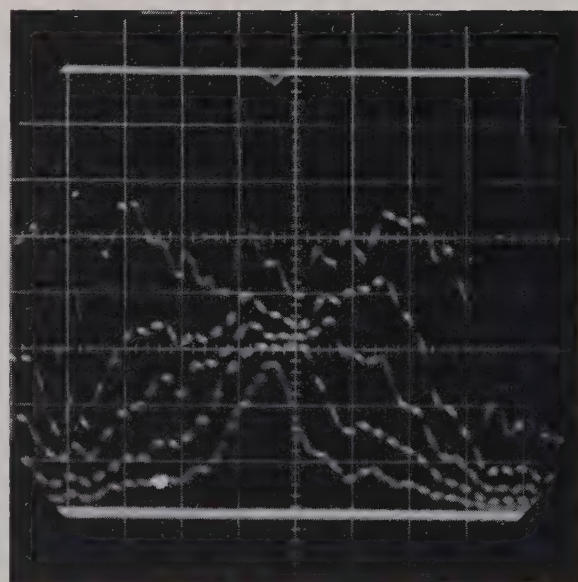


Fig. 21—Input VSWR to the limiter as a function of input power level, compared to the theoretical expression of (16).



(a)



(b)

Fig. 22—Strip-line limiter power output vs frequency for various input powers, using a nonleveled swept signal generator, for comparison with Fig. 6.

parison of these results with the theoretical curves of Fig. 6 is not possible, but it can be seen that the general nature of the curves agrees well with the theoretical predictions. There appears to be a slight drift of the center frequency of the limiter with increasing power level, which is attributed to a shift in the dc capacitance due to second-order effects, since the amount of this shift was dependent on the stiffness of the dc bias supply.

In general, it seems fair to conclude that excellent agreement is obtained between these measurements and the theoretical formulas developed earlier in this paper.

CONCLUSIONS

The passive parametric limiter offers several features, including, a) a sharp limiting threshold; b) flat power output for a substantial dynamic range above the threshold; c) little or no phase distortion; d) conveniently low-threshold power levels; and e) simple construction, with no auxiliary pumps, power supplies, or equipment (other than a simple dc bias supply) being required. Such limiters can be built at essentially any frequency from the audio to the microwave range, and may find employment either in protective applications or in signal-processing applications, particularly those where the phase-distortionless feature is essential. The present work has presented design equations and data for parametric limiters employing varactor diodes, together with experimental results at VHF and microwave frequencies which indicate the performance characteristics of such limiters. The excellent agreement between theory and experiment gives substantial confidence in the accuracy of the design equations.

REFERENCES

- [1] A. E. Siegman, "Phase-distortionless limiting by a parametric method," *Proc. IRE*, vol. 47, pp. 447-448; March, 1959.
- [2] I. T. Ho, "Passive Phase-Distortionless Parametric Limiter," Stanford Electronics Labs., Stanford, Calif., Tech. Rept. 157-2; April, 1961; also Ph.D. dissertation, Dept. of Elec. Engrg., Stanford Univ., Stanford, Calif.; April, 1961.
- [3] A. A. Wolf and J. E. Pippin, "A passive parametric limiter," 1960 Internatl. Solid State Circuits Conf. Digest of Tech. Papers, Philadelphia, Pa., pp. 90-91; February, 1960.
- [4] R. W. Degrasse, "Low-loss gyromagnetic coupling through single crystal garnets," *J. Appl. Phys.*, vol. 30, pp. 155S-156S; April, 1959.
- [5] G. S. Uebele, "Characteristics of ferrite microwave limiters," *IRE TRANS. ON MICROWAVE THEORY AND TECHNIQUES*, vol. MTT-7, pp. 18-23; January, 1959.
- [6] A. D. Sutherland and D. E. Countiss, "Parametric phase-distortionless L-band limiter," *Proc. IRE*, vol. 48, p. 938; May, 1960.
- [7] F. A. Olson, *et al.*, "Parametric devices tested for phase-distortionless limiting," *Proc. IRE*, vol. 47, pp. 587-588; April, 1959.
- [8] W. Shockley, "Theory of p-n junctions in semiconductors and p-n junction transistors," *Bell Sys. Tech. J.*, vol. 28, pp. 436-489; July, 1949.
- [9] A. Uhler, Jr., "Varactors," Microwave Associates, Inc., Burlington, Mass., Brochure 59V; February, 1959.
- [10] H. Heffner and G. Wade, "Gain, bandwidth, and noise characteristics of the variable-parameter amplifier," *J. Appl. Phys.*, vol. 29, pp. 1321-1331; September, 1958.
- [11] J. M. Manley and H. E. Rowe, "Some general properties of nonlinear elements—Part I: General energy relation," *Proc. IRE*, vol. 44, pp. 904-913; July, 1956.
- [12] J. Von Neumann, "Nonlinear capacitance or inductance switching, amplifier, and memory organs," U. S. Patent No. 2,815,488; December 3, 1957.
- [13] E. Goto, "The parametron, a digital computing element which utilized parametric oscillation," *Proc. IRE*, vol. 47, pp. 1304-1316; August, 1959.
- [14] "X-band ferrite limiter," Hughes Aircraft Co., Component Div., Culver City, Calif. Interim Engrg. Repts. I-IV; September, 1959-June, 1960.
- [15] E. T. Jaynes, "Ghost modes in imperfect waveguides," *Proc. IRE*, vol. 46, pp. 416-418; February, 1958.
- [16] F. A. Olson and G. Wade, "A cavity-type parametric circuit as a phase-distortionless limiter," *IRE TRANS. ON MICROWAVE THEORY AND TECHNIQUES*, vol. MTT-9, pp. 153-157; March, 1961.

Solid-State X-Band Power Limiter*

W. F. KRUPKE†, T. S. HARTWICK‡, AND M. T. WEISS‡, SENIOR MEMBER, IRE

Summary—An X-band solid-state power limiter has been designed and built to protect receiver crystals from high-power microwave pulses in the kilowatt region. This passive and reliable crystal protection has been achieved by utilizing the nonlinear properties of

both ferrites and semiconductor diodes. An understanding of the ferrite nonlinear mechanism, which gives rise to the characteristically large leakage spike, has been achieved and quantitatively described. This formulation resulted in an essentially optimized high-power ferrite limiter, whose mode of operation is qualitatively understood. Use of this ferrite limiter for crystal protection requires a fast response, lower threshold secondary-limiting unit, which was developed by using semiconductor diodes for power limiting in a reactive mode of operation. The ferrite and diode limiters were combined in a single device with an over-all insertion loss of 2.0 db and a 200-Mc operating "bandwidth."

* Received by the PGMTT, May 15, 1961; revised manuscript received, June 29, 1961. This paper is based on work performed at Hughes Aircraft Co., Culver City, Calif., and supported by the Bureau of Ships, Dept. of the Navy, under Contract NObS-77605.

† Aeronautical Div., Minneapolis-Honeywell Co., Los Angeles, Calif.

‡ Electronics Lab., Aerospace Corp., El Segundo, Calif.

INTRODUCTION

THERE has been a long standing need in radar systems for a passive solid-state power limiter capable of providing protection for sensitive receiver crystals from high-power microwave pulses. Although present-day gaseous TR tubes perform adequately in many systems applications, their poor recovery time, somewhat questionable reliability, and relatively poor performance under high average power conditions limits their effectiveness in many of the newer radar systems. To determine whether a practical solid-state limiter is possible, extensive investigations have been conducted using both ferrites and microwave diodes as limiters.

A practical limiter must pass low-level signals through the limiter essentially unattenuated and attenuate high-power signals such that no more than approximately a half erg of spike energy and a half watt maximum of flat leakage reach the crystals. In addition, quick recovery time, high-power handling capability, broad-band operation, and reasonable size are important. In this paper, the study of nonlinear properties of ferrites and diodes has resulted in a power limiter which combines the attractive features of each nonlinear element. Though this ferrite-diode limiter does not yet meet all of the requirements of a practical device, the feasibility of constructing such a limiter has been established.

FERRITE LIMITER

Subsidiary resonance absorption in ferrites, first observed by Damon¹ and later explained by Suhl,² was first utilized for power limiting by Scovil.³ An extensive study of this limiter was made by Uebele⁴ who pointed out two problems which prevented a practical limiter design. First, a high amplitude spike resulted on the leading edge of the "limited" pulse and, second, the threshold power for limiting was too high for crystal protection. In all other respects the subsidiary resonance limiter is satisfactory and it would be a useful device if the two basic problems were solved. DeGrasse⁵ has shown that ferrite instabilities at the main ferromagnetic resonance can also be used for limiting. The ferrite resonator is utilized as a band-pass filter; at low power the Q is high and a low insertion loss results. At high power, spin-wave excitation drastically lowers the resonator Q resulting in high loss. At S -band frequencies,

the threshold power is low because subsidiary resonance and main resonance coincide, and these limiters have been effective as low-power limiters. Since Uebele's limiter has the greater potential for a high-power limiter, it was studied in detail and the result is a greatly improved limiter design.

The Leading Edge Spike Problem

The equations of ferrite behavior at high RF power levels, although complicated, present a clear-cut circuit analog. The uniform precession resonant circuit is coupled through a nonlinear reactance to the spin-wave resonant circuits. The reactance presents a negative resistance to the spin waves and amplification results. When the negative resistance exceeds the positive resistance, the spin waves of low (thermal) excitation rise in amplitude exponentially with time, creating a substantial loss to the uniform precession. The equation for this exponential rise is given by Suhl as

$$a_k = a_t e^{j\omega_k t} e^{(|\rho_k| |a_0| - \eta) t}, \quad (1)$$

where

- a_k = amplitude of k th spin wave,
- a_t = measure of thermal level of the spin waves,
- a_0 = uniform precession amplitude,
- ρ_k = coupling terms from uniform precession to k th spin wave,
- η = spin wave damping term.

This equation shows that if the uniform precession amplitude becomes large enough so that $|\rho_k| |a_0| > \eta$ (the threshold condition), then the spin-wave amplitude will increase exponentially with time. This increase would continue indefinitely were it not for the reaction of the spin wave back on the uniform precession. Therefore, the variation of the uniform precession can be described as follows: suppose a microwave pulse, of sufficient amplitude to be above the threshold value, is applied to the sample of ferrite. The uniform precession will tend to build up to the value given by the usual low-power theory within a time of order $1/\gamma\Delta H$ or about 10^{-8} sec and, initially, the precession angle is given by the conventional theory. Eventually the spin waves increase in amplitude, reducing a_0 and causing a decline of the exponential rate of increase of the spin waves. Finally, no further increase in the spin-wave level can take place and the steady state is attained with a_0 reduced to a value just below threshold. Fig. 1 gives a qualitative picture of the increase of the spin-wave amplitude and the decrease in output power at the signal frequency.

An exact transient analysis of the loss to the signal circuit would be very difficult to compute. However, by analysis of the beginning of the exponential rise of the spin waves, valuable information can be obtained about the time required for the initiation of loss to the signal

¹ R. W. Damon, "Relaxation effects in the ferromagnetic resonance," *Rev. Mod. Phys.*, vol. 25, pp. 239-245; January, 1953.

² H. Suhl, "The nonlinear behavior of ferrites at high microwave signal levels," *PROC. IRE*, vol. 44, pp. 1270-1284; October, 1956.

³ H. E. D. Scovil, private communication.

⁴ G. S. Uebele, "Characteristics of ferrite microwave limiters," *IRE TRANS. ON MICROWAVE THEORY AND TECHNIQUES*, vol. MTT-7, pp. 18-23; January, 1959.

⁵ R. W. DeGrasse, "Low-loss gyromagnetic coupling through single crystal garnets," *J. Appl. Phys.*, suppl. to vol. 30, pp. 1555-1656; April, 1959.

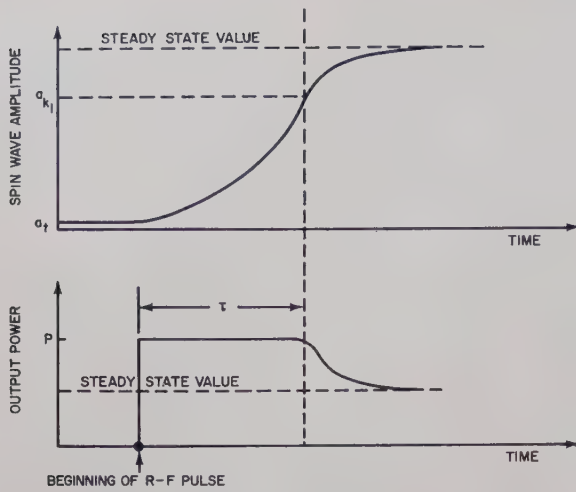


Fig. 1—Build-up of spin-wave amplitude and its effect on ferrite limiter output pulse.

circuit and the factors which enter into the amplitude and duration of the "spike."

Assume that the loss to the signal circuit will become evident when the spin waves reach an amplitude given by a_{k1} as shown in Fig. 1. The time taken to reach this amplitude is τ if (1) is valid during this time. The logarithm of (1) gives

$$\ln \left| \frac{a_{k1}}{a_i} \right| = (|\rho_k| |a_0| - \eta)\tau = L, \quad (2)$$

where L is a constant equal to the logarithm of $|a_{k1}/a_i|$. Since $|a_0|^2$ is proportional to the input power P ,

$$|\rho_k| |a_0| = K\sqrt{P}, \quad (3)$$

where K is a proportionality constant which depends on ρ_k , a materials parameter, and on the conversion from power to field, a ferrite geometry parameter. Eq. (2) can therefore be rewritten as follows:

$$\frac{1}{\tau} = \left(\frac{K}{L} \right) \sqrt{P} - \left(\frac{\eta}{L} \right). \quad (4)$$

The above equation assumes, of course, that the RF input pulse rises to its peak value much more rapidly than τ . The spike will be of the same amplitude as the input pulse and its duration will be given by (4).

An experimental verification of (4) is more difficult than might be anticipated because of the frequency modulation occurring at the leading edge of the usual magnetron pulse. In order to avoid this difficulty, an X-band CW magnetron was used as a power source in conjunction with a ferrite modulator. In this way, it became possible to eliminate frequency modulation and to obtain long pulse lengths ($>10 \mu\text{sec}$) which are necessary for the evaluation of the constants K/L and η/L . Data were obtained for a Ferramic R-4 ferrite slab, and the plot of $\sqrt{P_i}$ versus $1/\tau$ (see Fig. 2) showed the expected straight-line dependence.

If the RF input pulse rises more slowly than τ , as shown in Fig. 3, then the above analysis must be modi-

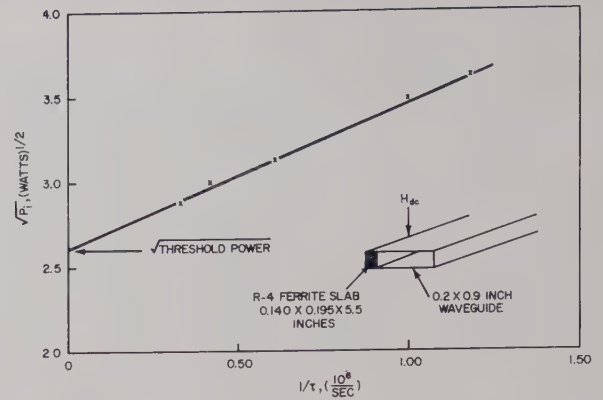


Fig. 2—This graph indicates the dependence of the spin-wave rise-time on the incident power for the slab structure shown.

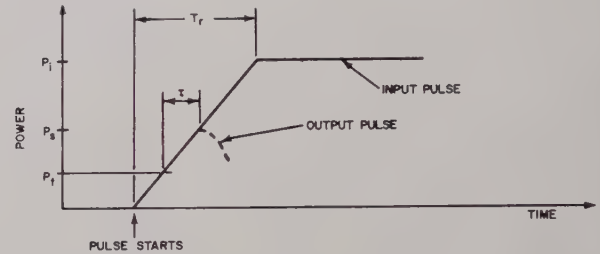


Fig. 3—Formation of the spike for an RF pulse of finite rise-time.

fied. Here the spike amplitude P_s is no longer equal to the input-pulse amplitude but is smaller and is given by a cubic equation. This equation simplifies into the following:

$$P_s = \left(\frac{L}{K} \right)^2 \left[\frac{1}{\tau} + \frac{\eta}{L} \right]^2, \quad (5)$$

$$P_i = \left(\frac{T_r}{\tau} \right) \left[P_s - \left(\frac{L}{K} \right)^2 \times \left(\frac{\eta}{L} \right)^2 \right], \quad (6)$$

where the threshold power is given by

$$P_t = \left(\frac{\eta}{K} \right)^2. \quad (7)$$

One can easily show that $dP_s/dP_i = 0$ for large P_i . Keeping in mind that $P_s = P_i$ until $\tau = T_r$, a graph of P_s vs P_i is produced much like the CW power response of a long thin slab, *i.e.*, the spike has a "threshold" value of power and ultimately becomes limited. The spike amplitude P_s was actually measured for the Ferramic R-4 slab of Fig. 2 as P_i was increased to the maximum available from the CW magnetron source. Good qualitative agreement was obtained with (5) and (6) (see Fig. 4), and a modification of the equations using the true pulse shape, instead of the ideal linear rise, gave quantitative agreement.

The four parameters, T_r , L , K and η can be varied to eliminate or suppress the leakage spike. Taken in order, we note first that the pulse rise time, T_r , strongly affects the spike amplitude. Thus, as T_r is decreased, the spike amplitude should increase; in particular, the spike

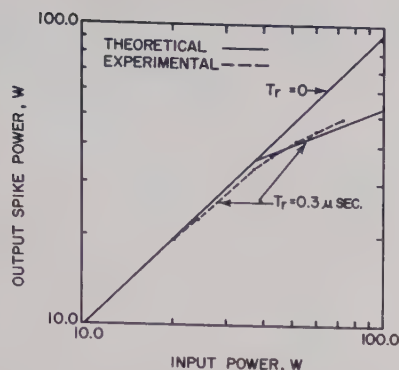


Fig. 4—Variation of spike amplitude with incident power for a spike of finite rise-time.

threshold power should rise as T_r is decreased. It is easy to alter the input pulse rise time, keeping L , K , and η constant, by placing various microwave filters with different Q_{ext} before the ferrite. For the Ferramic R-4 slab structure of Fig. 2, pulses with $T_r = 0.50 \mu\text{sec}$ and $T_r = 0.03 \mu\text{sec}$ yielded spike threshold power values of $P_i = 20 \text{ w}$ and $P_i = 200 \text{ w}$, respectively. Simple calculations show good qualitative agreement with (5) and (6). However, the reduction of T_r in a practical device is probably not possible, since most radar systems employ RF pulses with sharp rise-times.

The effect of decreasing the quantity L , the logarithmic ratio of a_{k1} to a_t , is to reduce P_s . Physically, this is equivalent to raising the ferrite spin temperature a_t or pre-exciting the spin waves. It is actually possible to pre-excite the spin waves by using a "primer-pulse" which, in addition to the signal, also excites subsidiary resonance. The following experiment⁶ was performed to show the effectiveness of this pre-pulsing scheme. The pulsed outputs of two X-band magnetrons were synchronized so that a 2.5- μsec pre-pulse would envelope a 0.5- μsec signal pulse. Fig. 5 illustrates the observed output wave shapes with (a) only the signal pulse applied and (b) both the signal pulse and the pre-pulse applied. A decrease in signal spike amplitude can be observed in case (b). Ideally, both pulses should be at the same frequency for optimum effect since then the subharmonic spin-wave frequencies are identical, *i.e.*, the same spin wave is being amplified by both pulses. For different pre-pulse frequencies, more pre-pulse power is expected, and this behavior is borne out by the data plotted in Fig. 6. This pre-pulsing technique demonstrates the decrease expected of P_s with decrease in L , but obviously is not a practical method for spike suppression.

Thus, it appears that only η , the spin-wave damping parameter and K , a measure of geometric RF "field peaking" can conveniently be altered. The parameter η is selected according to which ferrite is used. What effect this selection will produce on the spike amplitude depends on the relative magnitudes of η/L and $1/\tau$ as can

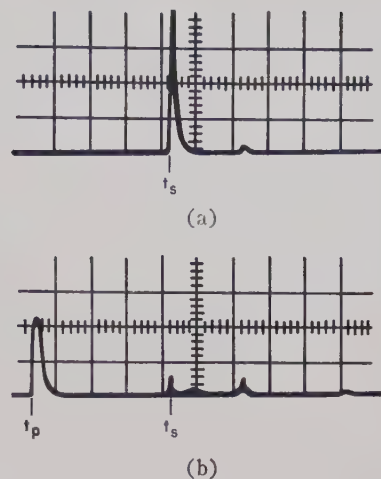


Fig. 5—Effect of spike of applying pre-pulse; t_p = start of prepulse, t_s = start of signal pulse, time scale = $0.25 \mu\text{sec/cm}$. (a) Without prepulse. (b) With prepulse.

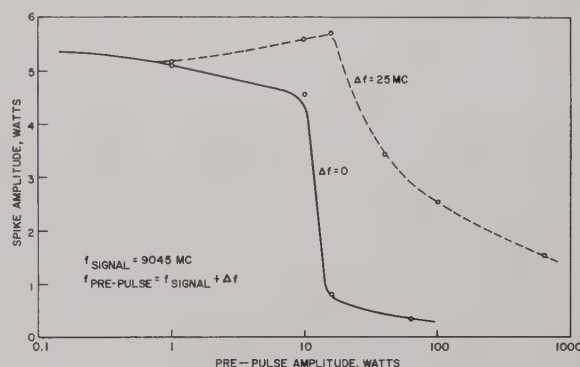


Fig. 6—Dependence of signal pulse spike on frequency and amplitude of prepulse. The signal pulse amplitude is 12 w.

be seen in (5). If $\eta/L \gg 1/\tau$, then the spike amplitude is sensitive to changes in η , and at the same time the spike amplitude and the threshold power will be relatively large. On the other hand, if $\eta/L \ll 1/\tau$, the spike amplitude is insensitive to lowering η/L , and the selection of a better ferrite (lower η/L) will not appreciably affect the spike. From the equations, it can be noticed that increasing K always has a decisive effect on spike amplitude and threshold power level. Therefore, the greatest improvement in the spike response of the slab-type limiter can be achieved by selecting experimentally a material with the lowest threshold for instability in a given configuration and by then concentrating on field peaking techniques.

Selection of Ferrite Material and Geometric Configuration

The first step in ferrite limiter design is to select the proper material. A suitable material must exhibit low loss at low-power levels, a low instability threshold, and high loss at high-power levels. Accordingly, threshold power and loss data were taken on ferrite slabs in waveguides and on spheres in a microwave cavity. The result is that for a subsidiary resonance limiter, General Ceramic's Ferramic R-4 was superior to all com-

mercial and experimental ferrites examined. Since a figure of merit would be difficult to define, we state simply that this material exhibits a low-power loss comparable to Ferramic R-1 (the material used by Uebele), but a threshold power an order of magnitude lower than R-1. It should be noted that R-4 ferrite possesses the lowest threshold power measured. On the basis of Suhl's approximation for the spin-wave damping, $\eta = \gamma \Delta H / 2$, the lowest line-width material should exhibit the lowest threshold power and this is not consistent with the broad ($\Delta H > 250$ gauss) line-width of R-4 ferrite. This behavior must be due to an effect produced by the unusual polycrystalline structure of the ferrite.

Typical of the thin-slab data is that shown in Fig. 7 of an 0.080-in R-4-slab 4 inches long placed against the side wall of standard X-band waveguide. The insertion loss was only 0.05 db and no deterioration of performance was noticed at large average power levels. For these reasons, such a configuration could be utilized as a "prelimiter," useful for dissipating the brunt of the average power in a large incident signal.

A low impedance microwave circuit must be selected which will produce a large K value and a reasonably low insertion loss. These requirements tend to be mutually exclusive since the ferrite always contributes a linear loss term. A low impedance circuit with excellent characteristics consists of the tapered ferrite slab, shown in Fig. 8, in reduced height X-band waveguide. Uebele showed that the threshold power for this structure was lowered by an order of magnitude over the threshold power for a thin slab at only a slight compromise in insertion loss. Therefore, this structure was studied further and was utilized in all of the main limiter designs.

Some insight into the operation of Uebele's limiter configuration can be gained by noting two important facts. First, experiments indicate that as the thickness of a thin slab is increased, the threshold power decreases. Second, at an input power just above threshold, Uebele's limiter produced a plateau power output less than the threshold power level, an effect that is hard to reconcile with the absorption mechanism involved. Both of these facts suggest that a transition occurs from a TE_{10} mode to a different mode in the ferrite-loaded waveguide section.

A perturbed TE_{10} mode propagates when H_{dc} is set to subsidiary resonance in a thin slab against the side wall of rectangular waveguide. It has been shown that for thick slabs,⁷ appropriately biased with an H_{dc} , a surface mode (or ferrite-dielectric mode) can propagate. The RF field intensity becomes quite large at the ferrite-air interface for this low impedance mode. Thus, one might expect the tapered slab to support some combination of both modes and to actually furnish a gradual transition

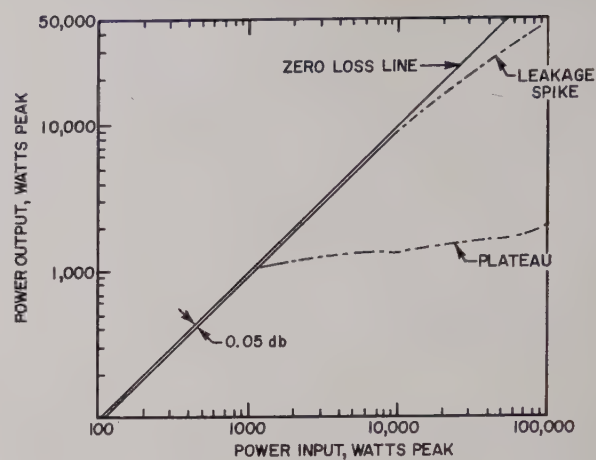


Fig. 7—Power response of a Ferramic R-4 thin-slab limiter.

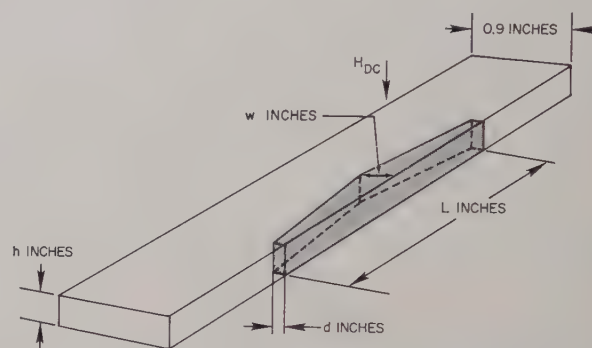


Fig. 8—Limiter geometry showing tapered ferrite-slab structure.

from TE_{10} mode at the slab ends to the surface mode at the slab center. Precisely this behavior was experimentally observed by probing the electric field in the slab-loaded waveguide section, and plotting the transverse variation of intensity as the length of the slab was traversed. Additional support for the moding effect is furnished by probing the RF field at high power. One expects the central portion of the slab, where the RF magnetic field is most intense, to become unstable first as the power is raised. For a power level just above threshold, the pulse shape is rectangular at the input end of the slab and remains so as the probe is traversed along the length of the slab, until, at the slab center the pulse becomes distorted to a spike and plateau.

An analytical solution to the tapered-slab problem is difficult even in the absence of high-power effects and is probably insoluble if loss is included. Although the above reasoning is qualitative, the arguments are strongly supported by experiment and provide information to guide the design of the ferrite-waveguide structure.

Ferrite Limiter Construction

Several limiters were constructed using Ferramic R-4 ferrite and the limiter shape of Fig. 8. The limiter dimensions were systematically varied to obtain the lowest value of threshold power for an arbitrary insertion-

⁷ K. J. Button and B. Lax, "Theory of ferrites in rectangular waveguides," IRE TRANS. ON ANTENNAS AND PROPAGATION, vol. AP-4, pp. 531-537; July, 1956.

loss value, usually taken as 1 db. Limiters resulted with an insertion loss of 1 db and a threshold power which varied from about 20 w ($h=0.400$ in) down to 5 w ($h=0.050$ in). Shown in Fig. 9 is the response curve of a typical limiter with dimensions $L=4.0$ in, $h=0.050$ in, $w=0.160$ in, and $d=0.080$ in. The insertion loss is less than 0.9 db over a 300-Mc band and the threshold power is less than 10 w over the same bandwidth.

Although variation of any one dimension affects all parameters specifying the limiter response, certain dependences are noticed. Thus, the main effect of decreasing the waveguide height is to lower the threshold power. The w and d dimensions primarily affect the insertion loss, since the match between modes is altered; small variations about $w=0.150$ in and $d=0.090$ in were generally found to provide a suitable insertion-loss value. The transverse dc magnetic field adjustment is not extremely critical, but large variations affect both the insertion loss and the threshold power.

It is clear that the limiter with the response of Fig. 9 cannot protect crystals over any power range. Even if the threshold power were lowered below the 1-w level, the leakage spike would prevent crystal protection. Since the microwave circuit design has been considerably improved, and is hopefully nearly optimized, it is natural to inquire whether a better ferrite material might aid in suppressing the spike. Eqs. (5) and (6), with the experimental constants $T_r=0.03$ μsec and $\eta/L=3.1$ (μsec) $^{-1}$, taken from Fig. 2, yield the result that $\eta/L \ll 1/\tau$ and so it follows that the spike cannot be reduced by using a more nonlinear material. Hence, the slab-type subsidiary resonance limiter is useful for crystal protection only if it is followed by a secondary limiter which will eliminate the leakage spike.

Since the output power of the slab-type limiter is relatively low, one is encouraged to re-inspect single crystal garnet limiters. However, YIG single crystal limiters operating at both subsidiary resonance and main resonance can be ruled out as secondary limiters. At subsidiary resonance the high Q cavity, necessary to obtain a low threshold, creates a high insertion loss and severely reduces the bandwidth. The main resonance limiter, useful at S band where the coincidence of main and subsidiary resonance instabilities creates an extremely low threshold, requires a microwave cavity at X band and is narrow band. In addition, a large spike is observed on the output pulse thus making this type of device unsuitable as a secondary limiter.

DIODE LIMITERS

It has been realized for some time that the nonlinear properties of diodes can be used for passive power limiting at low power levels where diode power dissipation is low. An investigation was therefore undertaken to determine if a diode could handle a ferrite limiter spike in the 100 erg region and a flat leakage of 20 w and thus serve as a secondary limiter.

One type of diode limiter makes use of the diode non-

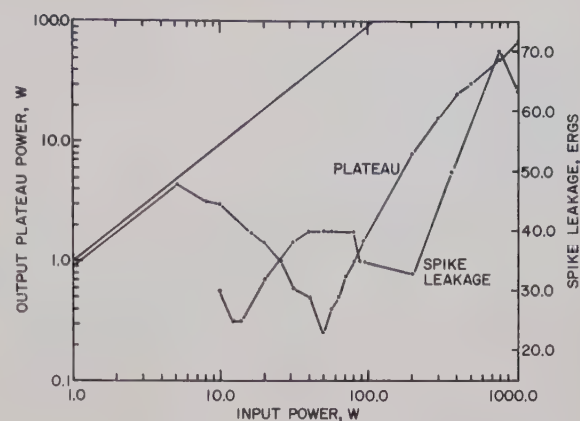


Fig. 9—Power response of Ferramic R-4 tapered-slab limiter.

linearity to convert signal power, above a threshold level, into subharmonic oscillations^{8,9} as in the ferrite case. This type of device is narrow band and generally is restricted to limiting power levels below 1 w. A second scheme, better suited to our purposes, utilizes the diode nonlinearity to change the admittance presented to the RF wave, as was shown by Garver and Tseng.¹⁰ The essential advantage of this technique is that the admittance change can be used to switch the high power into a load resulting in little power dissipation in the diode itself. To predict the admittance of a diode as a function of the applied RF power, that is, the limiting characteristic, the equivalent circuit of the diode and mount is needed. Although substantial efforts have been made to determine the equivalent circuit,¹¹ an accurate model of the diode plus mount has not yet been given.

Diode Limiter Configurations

In order to study in more detail the possible limiter circuits and diode limiter spike response, a 1N263 diode limiter was constructed. The diode was mounted across the waveguide at the E -field maximum with the diode axis parallel to the narrow waveguide wall. The diode mount introduced little capacitance and provided a way to apply a dc bias voltage to the diode. A matched load terminated the diode mount and the admittance of the diode plus matched load was measured as a function of RF power. The results, shown on the Smith chart (Fig. 10), clearly demonstrate the power-switching technique. Thus, for input powers below 0.2 mw an extremely large VSWR is presented to the RF wave resulting in nearly total reflection; above this power level

⁸ A. A. Wolf and J. E. Pippin, "A passive parametric limiter," *Digest of Tech. Papers, Solid-State Circuits Conf.*, Philadelphia, Pa., pp. 90-91; February, 1960.

⁹ A. E. Siegman, "Phase-distortionless limiting by a parametric method," *PROC. IRE*, vol. 47, pp. 447-448; March, 1959.

¹⁰ R. V. Garver and D. Y. Tseng, "X-band diode limiting," *IRE TRANS. ON MICROWAVE THEORY AND TECHNIQUES* (Correspondence), vol. MTT-9, p. 202; March, 1961.

¹¹ R. V. Garver and J. A. Rosado, "Microwave diode cartridge impedance," *IRE TRANS. ON MICROWAVE THEORY AND TECHNIQUES*, vol. MTT-8, pp. 104-107; January, 1960.

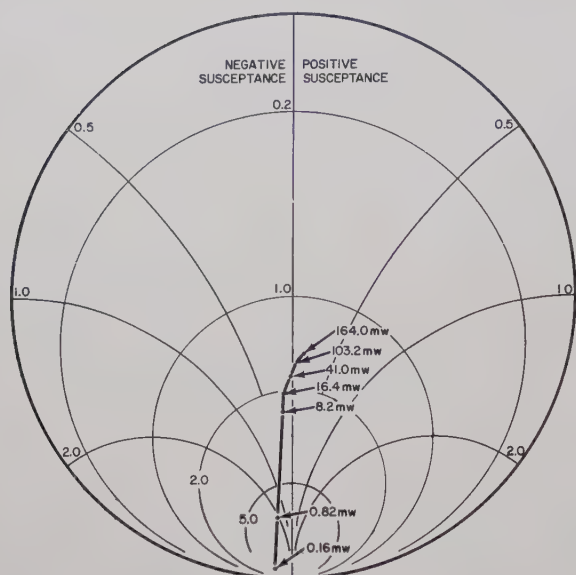


Fig. 10—Variation of admittance with RF power for 1N263 diode and mount.

both the conductance and susceptance change rapidly with power, little power is reflected, and the remainder is split between the diode and matched load. Since the diode conductance is much smaller than the load conductance, and the diode susceptance is also small, most of the incident power is dissipated in the load. This behavior is ideal for power limiting because of the low power dissipation in the diode.

In an actual reflection-type limiter model, means must be provided for separation of input and output signals. This may be accomplished by connecting two diode mounts, terminated in matched loads, to a 3-db broad-band hybrid.¹⁰ The input signal splits at the junction with a 90° relative phase shift, half of the power going to each diode section. At low signal level most of the power incident on each diode is reflected, and the phases are such that the reflected signals add in the hybrid output arm and cancel in the hybrid input arm. At high signal levels the power is largely transmitted to the load and the signal at the hybrid output port is correspondingly reduced. This hybrid limiter was constructed and effectively limited 2.5- μ sec signal pulses for up to 5 w amplitude with a threshold power of 1.0 mw and an insertion loss of 0.6 db. Two improvements were made in this design which left the insertion loss unchanged, but increased the power-handling capacity to 15 w. First, a dual-diode mount was built by placing two 1N263 diodes side-by-side in the transverse plane; second, 10-kilohm resistors were placed in the diode dc-return to limit the current flow. Both improvements decrease the current flow across the diode junction and, in this way, less power is dissipated per diode.

This hybrid diode limiter is useful only if it can limit the sharply rising leakage spike, produced by the ferrite limiter. By using the ferrite power limiter as a spike

signal source, the spike-limiting response was obtained. The results prove the diode limiter can limit a leakage spike of 0.020- μ sec width for as much as 100-w amplitude (20 erg). However, at more than a 10-erg input a gradual diode deterioration was noticed for long exposure times (several minutes). This effect restricts the application of the limiter as a secondary limiter, and points out the need for a limiter diode with a larger power-handling capacity.

Varactor Diode Limiter

Mesa-type varactor diodes possess a large contact area and are able to dissipate a larger amount of power, without diode deterioration, than the 1N263 point-contact type of construction. Accordingly, several varactor diodes, including MA460A, MA460E, MA460F, MA450A, MA450F, and some experimental diodes, were evaluated; only the double-ended MA450F diode, back biased to -5 volts, offered the desired characteristics. At input powers below 500 mw the reflection loss was a low 0.2 db, and the reflection loss increased to 10 db for an input power above 500 mw. This behavior, ideal for constructing a secondary limiter, is probably due to the rapid decrease in resistance associated with the avalanche breakdown. By contrast, the other diodes exhibited very little change in admittance as the power was varied, and were generally lossier.

It is significant that the diode-rectifying structures in the MA460 and MA450 series are electrically equivalent, and that their microwave response differs only because they are enclosed in different types of packages. The MA460 series of diodes which uses a single-ended cartridge package proved to be ineffective for limiting. In contrast, the MA450 diodes with a double-ended package (similar to the 1N263 package) gave consistently better results. The performance difference between the MA450F and the MA450A is due to the change in diode cutoff frequency which probably tunes the diode series resonance.

An experimental limiter was constructed using four MA450F diodes biased to -5 volts, in conjunction with a hybrid section, as discussed earlier. The dc external loading resistors used here, however, were 470 kilohms. It was also found possible to position a tuning screw a distance $\lambda g/2$ behind the diodes and greatly enhance the amount of isolation. This resulted in the power response curve shown in Fig. 11. The low-power insertion loss of this device is 0.4 db, with a threshold power level of 1 w; these values are constant over a 200-Mc band centered about 9300 Mc. For this limiter, the leading edge spike has a width less than 10 nsec. If the avalanche breakdown mechanism is principally responsible for the diode admittance change, then the spike data is not inconsistent with the relatively long time constants appropriate to the avalanche. Since the spike rapidly becomes narrower as power increases, and is also even-

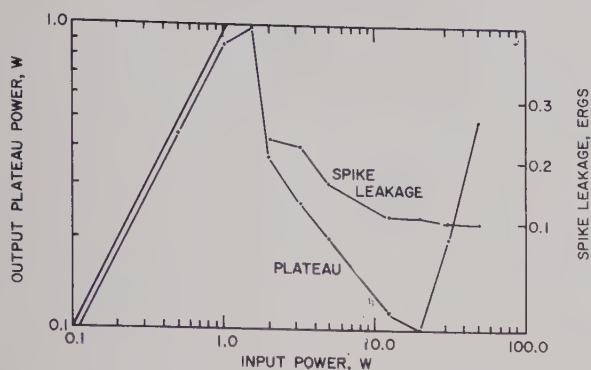


Fig. 11—Power response of MA450F hybrid limiter.

tually limited, its presence does not abort the limiter's effectiveness as a secondary limiter. Again using the ferrite limiter as a spike source, over 15 db of spike limiting was measured for input-leakage spike amplitudes of 1500 w (300 ergs) with no noticeable deterioration of the MA450F diodes.

A three-port circulator for the separation of the input signal from the output signal provides a simple method of obtaining a threshold power just one half that of the hybrid limiter. Here the input signal, incident on the diode section, is either reflected into the output port or transmitted to the load, depending on the signal level. Such a device was built and it exhibited less than 0.4-db insertion loss, and over 10 db of isolation for input powers above 500 mw.

These two limiter configurations provide the secondary limiter characteristics needed to build a passive solid-state limiter useful for crystal protection.

SOLID-STATE LIMITER

Since the diode and ferrite limiters have been constructed with the desired individual characteristics, the problem has been reduced to combining the individual units into a workable solid-state limiter. In doing this, emphasis has been placed on demonstrating the feasibility of eventually constructing a model which will be useful in radar sets. Therefore, the procedure has not been to redesign compatible limiter stages, but rather to adjust the characteristics of the existing limiters so as to obtain limiting over a wide power range with a reasonably low insertion loss, taken here as 2 db.

Accordingly, a four-stage limiter was constructed consisting of a ferrite prelimiter, a ferrite main limiter and two stages of diode limiting. The completed limiter model is shown in Fig. 12. The ferrite prelimiter consists of a tapered slab of ferrite in 0.200-in high X-band waveguide similar to that shown in Fig. 8. For an insertion loss of only 0.3 db, a threshold power of 100 w was obtained.

The main ferrite limiter, which was previously discussed, exhibits the limiting response shown in Fig. 9. At the design frequency of 9300 Mc, the insertion loss

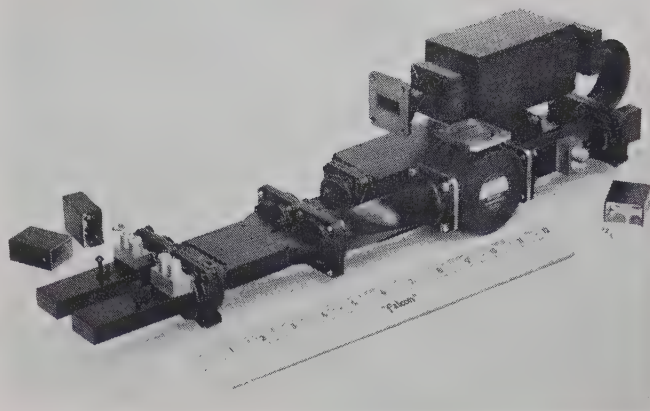


Fig. 12—Photograph of four-section solid-state limiter.

is 0.8 db. By combining the prelimiter and main limiter, a plateau power output less than 20 w was obtained. However, upon combining the two limiters, a double leading edge spike resulted and some care had to be exercised in adjusting the magnetic field to minimize this effect.

Following the two ferrite limiters, both a hybrid MA450F diode limiter and a circulator MA450F diode limiter were used in order to reduce the spike and plateau level to a value sufficiently low to provide complete crystal protection. The characteristics of these diode limiters have been described in detail in a previous section. Briefly, these two diode limiters in tandem have an insertion loss less than 1 db over a bandwidth greater than 200 Mc and a threshold power of 500 mw.

In combining the various stages of this limiter, a variety of adjustments are required in order to match the individual characteristics to obtain an optimum device. These adjustments were most easily accomplished by duplexing a low-power signal modulated at 1000 cycles together with the high pulsed signal. Thus, the effect of any adjustments on both low- and high-power performance could readily be determined.

The performance characteristics of this complete power limiter are as follows:

- Center frequency—9300 Mc,
- Insertion loss—2 db,
- Maximum input power (for complete crystal protection)—5000 w,
- Bandwidth (over which crystal protection is provided)—200 Mc,
- Spike leakage—less than 0.6 erg.

The complete power response is plotted in Fig. 13. In addition to the above measurements, the effectiveness of the limiter in protecting a balanced mixer using 1N23E crystals was tested. No deterioration of the 8.8-db-mixer noise figure could be measured after the limiter-mixer combination was subjected to a 5-kw peak input signal. This test clearly demonstrates the effectiveness of the limiter for crystal protection.

CONCLUSION

The X-band limiter described in this paper indicates the feasibility of building an all solid-state device capable of complete crystal protection. Obviously, a substantial engineering effort is still required before this type of limiter can become practical for system use. Thus, a reduction in size, weight, cost and insertion loss is vital in order for this device to compete successfully with presently available TR tubes. Nevertheless, such improvements will undoubtedly come, particularly in those systems where the present TR tubes are not satisfactory.

ACKNOWLEDGMENT

The authors would like to thank D. L. Snyder and S. W. Scott for their technical assistance and Dr. A. D. Berk for his helpful discussions and suggestions in connection with this work.

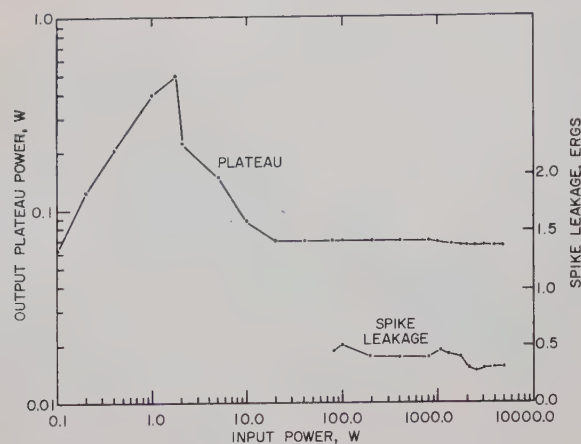


Fig. 13—Power response of four-section solid-state limiter.

On Spurious Outputs from High-Power Pulsed Microwave Tubes and Their Control*

K. TOMIYASU†, SENIOR MEMBER, IRE

Summary—Excessive spurious outputs from high-power pulsed magnetrons, klystrons and traveling-wave tubes can cause intolerable radiation interference and deleterious effects in a high-power microwave system. The harmonic output from a klystron may vary appreciably with changes in operating conditions. Harmonic outputs from tubes cannot be eliminated but their radiation can be significantly reduced by using filters. If the parasitic or spurious oscillations are very strong, adverse effects such as amplitude and phase instability of the fundamental frequency output may occur. Some of the spurious outputs may be reduced or eliminated by redesign of the tube or its modulator.

INTRODUCTION

THE emission of spurious outputs from microwave tubes has been known for a long time. Spurious outputs are defined as those frequency components other than the fundamental frequency with its normal sideband modulation components.

With steady increase in transmitter power level, receiver sensitivity, and density of radiating equipment, the problem of spurious outputs has taken on greater significance in terms of radiation interference [1], [2].

As the power levels of high-power tubes have increased so have the spurious output power levels. In a microwave system, the presence of spurious power may have deleterious effects such as arcing in chokes, arcing at flanges and undesired leakage through ionized duplexers. In addition, if a large amount of spurious power is generated, the tube efficiency may be decreased; it may cause other harmful effects to the tube and an objectionable amount of amplitude and phase instability may be added to the fundamental frequency output.

The presence of spurious frequencies usually can be detected at the tube output, provided that the spurious frequency is above cutoff of the output transmission line. If the spurious frequency is below cutoff and the spurious signal amplitude is sufficiently large, its presence may be inferred from any phase and amplitude instability of the fundamental frequency output. This instability may adversely affect the system of which the tube is a part without interfering with other nearby systems.

Although the frequencies can be measured with relative ease, the power levels are much more difficult to ascertain [3]–[6]. Spurious outputs other than harmonics are often quite erratic. Since a methodical redesign study of a high-power tube is generally costly,

* Received by the PGM-TT, May 4, 1961; revised manuscript received, July 24, 1961.

† General Engrg. Lab., General Electric Co., Schenectady, N. Y.

time consuming, and frequently inconclusive, the amount of progress made in suppressing these outputs has been limited.

This paper briefly summarizes the spurious outputs from high-power pulsed magnetrons, klystrons, and traveling-wave tubes. Some control methods are also discussed. Tubes which are designed for long pulse and continuous (CW) output operation may also generate spurious signals caused by ion oscillations [7]–[10]. These signals may modulate the amplitude of the beam, and the frequency may range from a few kc to a few Mc. Ion oscillations will not be discussed further in this paper.

MAGNETRON

Besides harmonics from pulsed magnetrons, anharmonic frequencies are occasionally generated which are due to moding within the RF structure of the magnetron. Although harmonic generation cannot be prevented due to the nature of the electron cloud within the magnetron, anharmonic frequencies can be controlled to a certain extent by appropriate design of the magnetron and its modulator. The second harmonic power may be about 40 db below the fundamental but the third harmonic can be as strong as 20 db below [4]. Filtering has been found successful in reducing the radiation of harmonics [11], [12] as well as anharmonic [13] frequencies. Additional spurious outputs from magnetrons may be due to space-charge effects [14], [15].

KLYSTRON

There are several possible types of spurious outputs from a pulsed klystron, for instance, harmonics, diode oscillation, drift tunnel oscillation and others. The amount of spurious frequency power depends on many factors, but most heavily upon tube design, manufacturing tolerances and operating parameters.

Harmonics

Harmonic frequency components are usually present on the electron beam in a high-efficiency, high-power klystron. Measurements made on one klystron using multiple probe techniques have shown the second harmonic power may be 35 db below the fundamental frequency power and the third may be 40 db below [16]. There are many operating parameters on a klystron which will affect the harmonic power output, such as pulse length, frequency within band, detuned cavities, magnetic field, input RF drive power level, saturated power output, beam voltage and output load impedances at the spurious frequencies.

Fig. 1 illustrates the variation in second harmonic power radiated from a VA-87B klystron as a function of frequency within the design band [16]; it is to be noted that the power is a minimum near midband. Fig. 2 illustrates the variation in second harmonic power as a function of beam voltage. At the recommended beam voltage of 90 kv, the second harmonic power is a mini-

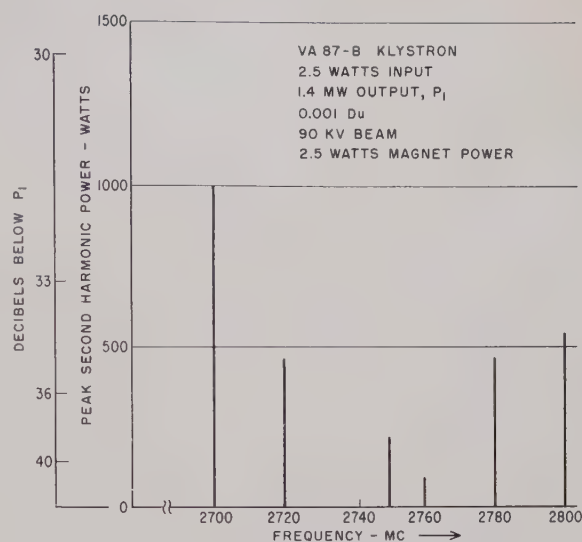


Fig. 1—VA 87-B klystron harmonic output as a function of frequency.

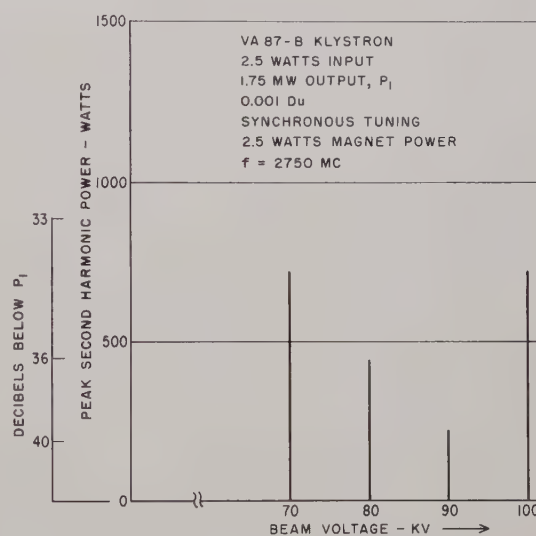


Fig. 2—VA 87-B klystron harmonic output as a function of beam voltage.

um. Additional measurements were taken and the results showed the large dependence of harmonic power on operating parameters. It should be mentioned that these data were obtained on a specific tube under specific operating conditions and that these are not necessarily representative of all klystrons.

As for a control method, it is difficult to eliminate completely the harmonic components on the beam. An alternate method is to design cavities which would present low circuit impedances at the harmonic frequencies. Considerable work has been carried out on this approach at Cornell University with encouraging results [17]. For expediency, the use of filters has been found effective in reducing the amount of radiated power at the harmonic frequencies.

Diode Oscillation

Under certain operating conditions, Llewellyn shows

that high-frequency oscillations are possible between a planar cathode and anode in the appropriate geometry [18]. These are called diode oscillations and this type of oscillation can sometimes be found in the electron gun of a high-voltage klystron. Diode-oscillation frequencies may be below, within, and even above the design frequency band of the tube.

The conditions required to cause these oscillations are

- 1) A dc beam transit angle of about $n + \frac{1}{4}$ RF cycle at frequency f is needed to generate a negative resistance across the diode, where n is any integer. The magnitude of this resistance must be sufficiently large to overcome the circuit losses.
- 2) An electromagnetic circuit with sufficiently high Q is resonant at frequency f .
- 3) Sufficient coupling exists between resonant circuit and electron beam.

On a particular S-band multimewatt klystron which had erratic diode oscillations, probing techniques showed that two of the resonant electromagnetic modes associated with the diode oscillations were localized in the annular region between the cathode and anode housing [19]. These two resonant modes had a Q in excess of 1000, and the modes were identified as the TE_{41} and TE_{61} modes in a coaxial line. Although the fields of the resonant modes were not in close proximity with the negative-resistance electron beam, there was sufficient coupling to drive the circuit into oscillation. The erratic oscillations had approximate frequencies of 1400, 2500 and 3650 Mc; these frequencies agree very closely with calculated values.

The geometry of the electron gun has a profound influence on the frequencies and on the likelihood of diode oscillations. The oscillations can be prevented by failing to satisfy the three conditions listed above, *e.g.*, by lowering the Q of the resonant circuit [20]. Filters can prevent radiating these spurious frequencies; however, if the oscillation is sufficiently severe, it may cause a detrimental amount of amplitude and phase instability of the fundamental frequency output. The latter adverse interdependent effect is a result of the electron beam which couples to both the diode oscillation and amplifying circuits. Unfortunately, this adverse effect cannot be eliminated by using a simple filter.

Drift Tunnel Oscillation

Based on the report of spurious output from a Stanford University klystron [21], an analysis was made on the possibility of TE_{0n} -mode oscillations in the circular drift tunnels between cavities [22]. The calculated frequency agrees very closely with the reported spurious frequency of 5770 Mc. The conditions for oscillation are the same as those listed above for diode oscillation, with the exception that the transit angle refers to transit through the tunnel. The transverse electric field in the resonant circuit displaces the beam

transversally. The displaced beam provides the coupling between beam and circuit, and it converts some of the kinetic energy of the beam to a negative RF resistance in the circuit. The latter is a consequence of beam deceleration from an antiphased longitudinal component of the fringing microwave field at the emergent end of the drift tunnel [23].

If drift tunnel oscillations occur, the frequencies may be two or three times higher than the design frequency band of the klystron. These spurious frequencies must be above cutoff of the TE_{0n} mode in the circular drift tunnel and this cutoff frequency f_c is given by [24]

$$f_c D = 6917 \text{ Mc} \cdot \text{inch}$$

where D = tunnel diameter in inches.

Very little can be stated at present as to control since the erratic oscillation behavior has generally prevented a systematic study of it. Undoubtedly a strong magnetic focusing field would reduce the amount of transverse-beam displacement, and hence, the possibility of oscillation.¹ Also, a smaller beam diameter may reduce the coupling. Filters could prevent radiation of this spurious signal, but if severe, an objectionable amount of phase and amplitude instability of the fundamental frequency output may occur.

Monotron Oscillation

Within a single cavity, an oscillation may occur which is called monotron oscillation [25]–[29]. The conditions for oscillation and the means for its suppression are the same as for diode oscillations.

Other Spurious Outputs

Other spurious signals may be generated due to unintentional feedback either external or internal to the tube.

TRAVELING-WAVE TUBE

Some of the spurious outputs from a high-power pulsed traveling tube are similar to those from a high-power klystron, while others are not. The tube design, manufacturing tolerances and operating parameters have large effects on the power level of the spurious outputs.

Harmonics

Harmonic frequency components are usually present on the electron beam in a high-efficiency, high-power traveling-wave tube. Limited measurements [16], [30] show that the second harmonic power may be 20 to 40 db below the fundamental frequency power. The operating parameters affect the harmonic power levels the same way they affect the klystron. Filters have been

¹ Beam diameter enlargement and asymmetry may be caused by the magnetic field of the heater current. See A. S. Gilmour, Jr., "Effect of filament magnetic field on the electron beam from a Pierce gun," *PROC. IRE* (Correspondence), vol. 49, p. 976; May, 1961.

found effective in absorbing the undesired harmonic power.

Diode Oscillation

There is basically no difference in the design of electron guns for klystron and traveling-wave tube for the same power level. Hence, the cause and adverse effects of diode oscillations and redesign methods to eliminate these oscillations are the same as for the klystron.

Band-Edge Oscillation

When traveling-wave tubes are pulsed, "band-edge" or "rabbit-ears" oscillations are sometimes detected in the output [31], [32]. These extremely short pulses occur at the beginning and at the end of the beam current pulse. The frequency is approximately equal to the high-frequency end of the pass band of the tube structure, hence the name, band-edge oscillation. The frequency-time relationship of these oscillations is shown graphically in Fig. 3.

The mechanism for generating band-edge oscillation can be explained by referring to Fig. 4 which shows an ω - β plot of a traveling-wave tube. The slope of the line passing through the origin is equal to the velocity of the

electron. At the rated beam voltage, the electron velocity is equal to the circuit phase velocity.

When the electron velocity starts from zero, as under pulsed operation, the line passing through the origin will start with a small slope which progressively increases as the beam voltage increases. Prior to reaching the rated voltage, the line will pass through point A on the first pass band ω - β curve. It is at this brief instant of time when a backward-wave oscillation occurs within the tube.

Band-edge oscillations may be eliminated if the rise and fall in beam voltage can be made sufficiently fast. They can also be eliminated in a tube which employs a control grid or modulating anode. Filters can prevent radiating these spurious outputs.

Second Pass-Band Oscillation

Depending on its structure and operating parameters, a traveling-wave tube while amplifying a signal whose frequency is in the first pass band sometimes may oscillate simultaneously at a higher frequency in the second pass band. Since this spurious oscillation is quite rare, very little is known of techniques for its suppression. While filters may prevent the radiating of the second pass band oscillation, a severe oscillation in the tube may cause adverse amounts of phase and amplitude instabilities in the signal being amplified. It is conceivable that oscillations may occur at frequencies in pass bands higher than the second.

Other Spurious Outputs

Other spurious outputs in a traveling-wave tube that are associated with higher-order asymmetrical electromagnetic modes within the slow-wave structure, and generated by rotationally asymmetrical components of the beam current may be possible.

CONCLUSION

Several types of spurious outputs from high-power pulsed microwave tubes have been discussed. At least three of the spurious outputs, *viz.*, diode, drift tunnel and monotron oscillations, are caused by negative resistances generated from beam transit time effects. Some control methods are mentioned.

Filters are useful in suppressing the radiation of many spurious frequencies, notably harmonics, generated by high-power microwave tubes. Severe spurious oscillations may cause objectionable phase and amplitude instabilities of the output at the fundamental frequency. Further study is required to eliminate all spurious outputs from high-power tubes.

ACKNOWLEDGMENT

Some of the results reported herein were obtained by V. G. Price, J. P. Rooney, C. Milazzo, R. H. Stone and G. Novick. The author is indebted to T. G. Mihran, D. A. Wilbur and S. P. Yu for their contributions.

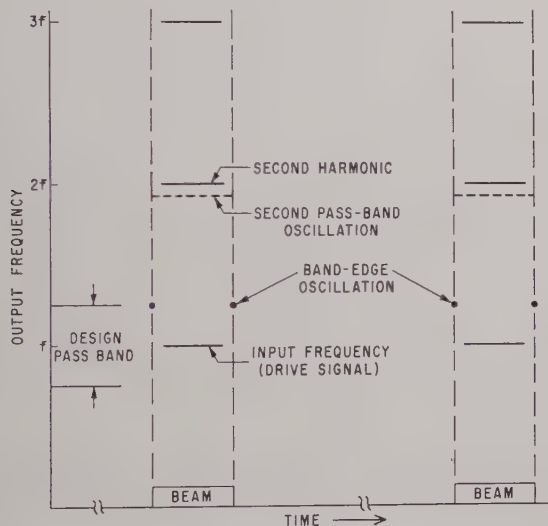


Fig. 3—Spurious output from traveling-wave tube.

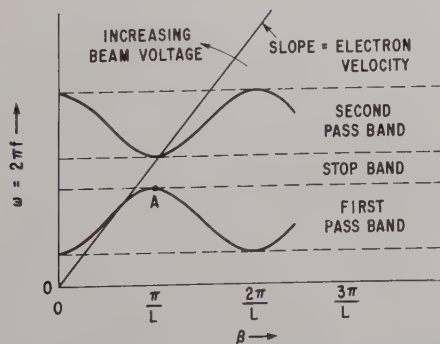


Fig. 4— ω - β diagram for traveling-wave tube.

REFERENCES

- [1] R. D. Campbell, "Radar interference to microwave communication services," *Elec. Engrg.*, vol. 77, pp. 916-921; October, 1958.
- [2] A. H. Ryan, "Control of microwave interference," IRE TRANS. ON RADIO FREQUENCY INTERFERENCE, vol. RFI-1, pp. 1-10; May, 1959.
- [3] M. P. Forrer and K. Tomiyasu, "Effects and measurements of harmonics in high-power waveguide systems," 1957 IRE NATIONAL CONVENTION RECORD, pt. 1, pp. 263-269.
- [4] —, "Determination of higher order propagating modes in waveguide systems," *J. Appl. Phys.*, vol. 29, pp. 1040-1045; July, 1958.
- [5] D. J. Lewis, "Mode couplers and multimode measurement techniques," IRE TRANS. ON MICROWAVE THEORY AND TECHNIQUES, vol. MTT-7, pp. 110-116; January, 1959.
- [6] V. G. Price, "Measurement of harmonic power generated by microwave transmitters," IRE TRANS. ON MICROWAVE THEORY AND TECHNIQUES, vol. MTT-7, pp. 116-120; January, 1959.
- [7] C. C. Cutler, "Spurious modulation of electron beams," PROC. IRE, vol. 44, pp. 61-64; January, 1956.
- [8] R. L. Jepsen, "Ion oscillations in electron beam tubes; ion motion and energy transfer," PROC. IRE, vol. 45, pp. 1069-1080; August, 1957.
- [9] A. D. Sutherland, "Relaxation instabilities in high-perveance electron beams," IRE TRANS. ON ELECTRON DEVICES, vol. ED-7, pp. 268-273; October, 1960.
- [10] Y. Koike and Y. Kumagai, "An experiment of ion relaxation oscillation in electron beams," PROC. IRE, vol. 49, pp. 525-526; February, 1961.
- [11] V. Met, "Absorptive filters for microwave harmonic power," PROC. IRE, vol. 47, pp. 1762-1769; October, 1959.
- [12] V. G. Price, *et al.*, "Harmonic suppression by leaky-wall waveguide filter," 1959 IRE WESCON CONVENTION RECORD, pt. 1, pp. 112-118.
- [13] H. A. Wheeler and H. L. Bachman, "Evacuated waveguide filter for suppressing spurious transmission from high power S-band radar," IRE TRANS. ON MICROWAVE THEORY AND TECHNIQUES, vol. MTT-7, pp. 154-162; January, 1959.
- [14] O. Doehler, "Space charge effects in traveling-wave tubes using crossed electric and magnetic fields," *Proc. Symp. on Modern Advances in Microwave Techniques*, Brooklyn, N. Y., November 8-19, 1954. Polytech. Inst. of Brooklyn, N. Y., vol. 4, pp. 101-121; 1955. See especially pp. 115-119.
- [15] R. W. Gould, "Space charge effects in beam-type magnetrons," *J. Appl. Phys.*, vol. 28, pp. 599-605; May, 1957.
- [16] G. Novick and V. G. Price, "Measurement and Control of Harmonic and Spurious Microwave Energy," General Electric Microwave Lab., Palo Alto, Calif., Final Rept., Phase III, Contract AF30(602)1670, ASTIA Document No. AD-214430; May 15, 1959.
- [17] L. A. MacKenzie, "Klystron Cavities for Minimum Spurious Output Power," Cornell University, School of Elec. Engrg., Ithaca, N. Y., Res. Rept. No. EE418; January 31, 1959.
- [18] F. B. Llewellyn, "Electron-Inertia Effects," Cambridge University Press, London, England, 2nd ed., chs. 3, 5; 1943.
- [19] K. Tomiyasu and M. P. Forrer, "Diode oscillation in high-voltage klystrons," IRE TRANS. ON ELECTRON DEVICES, vol. ED-8, pp. 381-386; September, 1961.
- [20] T. D. Sege, "Electron beam forming apparatus," U. S. Patent No. 2,916,659; December 8, 1959.
- [21] M. Chodorow, *et al.*, "Design and performance of a high-power pulsed klystron," PROC. IRE, vol. 41, pp. 1584-1602; November, 1953. See especially p. 1601.
- [22] K. Tomiyasu, "On the possibility of drift-tunnel oscillations in high power klystrons," PROC. IRE, vol. 49, pp. 1207-1208; July, 1961.
- [23] B. Fank, "Investigation of the Transverse-Field Klystron," Stanford Electronics Labs., Stanford University, Stanford, Calif., Tech. Rept. No. 305-1; March 10, 1958.
- [24] K. Tomiyasu, "Table for determining cutoff frequencies for circular waveguide," to appear in *Microwave J.*
- [25] D. R. Hamilton, "Summary of microwave tube types and functions," in "Klystrons and Microwave Triodes," M.I.T. Rad. Lab. Ser., D. R. Hamilton, Ed., McGraw-Hill Book Co., Inc., New York, N. Y., vol. 7, ch. 2; 1948. See especially p. 30.
- [26] J. Marcum, "Interchange of energy between an electron beam and an oscillating electric field," *J. Appl. Phys.*, vol. 17, pp. 4-11; January, 1946.
- [27] T. Wessel-Berg, "A General Theory of Klystrons with Arbitrary Extended Interaction Fields," Microwave Lab., Stanford University, Stanford, Calif., M.L. Rept. No. 376; ONR Contract N6 onr 25123 (NR 373 361); March, 1957.
- [28] —, "Large-Signal Analysis of Monotron Oscillators with Constant RF Field," Norwegian Def. Res. Establ., Bergen, Norway, Tech. Note No. 1, June, 1960; Rome Air Dev. Ctr., Contract No. AF 61(052)-264 (RADCN 60-179), June, 1960.
- [29] K. Bløtekjaer and B. Grung, "Optimum RF Field Distribution of Monotron Cavities," Norwegian Def. Res. Establ., Bergen, Norway, Tech. Note No. 2, September, 1960; Rome Air Dev. Ctr., Contract No. AF 61(052)-264 (RADCN 61-14), September, 1960.
- [30] J. A. Ruetz and W. H. Yocum, "High-power traveling-wave tubes for radar systems," IRE TRANS. ON MILITARY ELECTRONICS, vol. MIL-5, pp. 39-45; April, 1961.
- [31] D. G. Dow, "Behavior of traveling-wave tubes near circuit cutoff," IRE TRANS. ON ELECTRON DEVICES, vol. ED-7, pp. 123-131; July, 1960.
- [32] R. M. Bevensee, "A unified theory of electron beam interaction with slow wave structures, with application to cutoff conditions," *J. Electronics and Control*, vol. 9, pp. 401-437; December, 1960.

Practical Design and Performance of Nearly Optimum Wide-Band Degenerate Parametric Amplifiers*

M. GILDEN†, MEMBER, IRE, AND G. L. MATTHAEI‡, MEMBER, IRE

Summary—The design of a two-resonator single-diode degenerate parametric amplifier is described, which incorporates features that give it nearly optimum wide-band performance. These features include the use of almost lumped circuit elements, a sepa-

rate pump resonator which is very lightly coupled to the diode and pump circuits, and a diode resonated in series rather than in shunt, from which several advantages accrue. A bandwidth of 21 per cent with 15-db midband gain (double channel) is obtained at 1 Gc using two resonators, as compared with 8 per cent using one resonator. Both measured responses are found to be in excellent agreement with theoretical responses obtained with a digital computer. The measured double-channel noise figure was 1 db. Theoretical and experimental results are presented which show this type of amplifier to be remarkably insensitive to tuning errors. Good results were also obtained using two identical amplifiers in balanced operation with a 3-db coupler so as to eliminate the need for a circulator.

* Received by the PGMTT, May 1, 1961; revised manuscript received, July 24, 1961. The research was sponsored by the Wright Air Dev. Div., Wright-Patterson AFB, under Contract No. AF 33(616)-5803.

† Microwave Associates, Burlington, Mass. Formerly with Stanford Research Institute, Menlo Park, Calif.

‡ Stanford Research Institute, Menlo Park, Calif.

INTRODUCTION

SINGLE-diode parametric amplifiers with increased bandwidth can be obtained by using properly designed multiresonator coupling circuits instead of single-resonator circuits. Such increases in bandwidth were first demonstrated by Seidel and Herrmann¹ for the case of degenerate parametric amplifiers. In their analysis the parameters of the resonators are fixed by forcing the frequency derivatives of the gain function to be zero at midband. More recently Matthaei^{2,3} has shown that multiresonator coupling circuits can be designed to give relatively large bandwidths for either degenerate or nondegenerate parametric amplifiers as well as for up-converters. His analysis is based on a filter-theory viewpoint.

A single-diode degenerate parametric amplifier was designed and constructed to verify part of the design theory of Matthaei and to ascertain what practical difficulties might arise. Included in the device were several special features which helped to fulfill the objectives of the theory for optimum design.^{2,3} A brief discussion of an experimental verification has previously been given by the authors.⁴ In this paper (and in two SRI reports⁵) the single-diode degenerate amplifier is discussed in more detail, including the sensitivity of such amplifiers to mistuning and their operation in balanced and cascaded configurations using 3-db directional couplers.

DESCRIPTION OF THE SINGLE-DIODE AMPLIFIER

The equivalent circuit of the two-resonator amplifier (as operated with a circulator) is shown in Fig. 1. The variable-capacitance diode is represented by a series circuit, where C_0^s is the series average value of the diode capacitance, C_1^s is the series time-varying component of capacitance, L_d is the diode parasitic inductance, and R_s is the diode loss resistor.^{2,3} Capacitance C_0^s and L_d along with some additional inductance make up the series resonator indicated by X_1 in the figure. The second resonator in shunt, indicated by B_2 , is included in order to obtain greater bandwidth. The pump power is supplied to the diode through the pump resonator, which is loosely coupled to the series resonator and pump generator.

A drawing of the strip-line realization of the equivalent circuit in Fig. 1 is shown in Fig. 2, and a photograph of the completed amplifier with its cover plate removed is shown in Fig. 3. A Hughes 1N896 diode is used which has a computer-type package. This diode has 0.020-inch-diameter wire leads which, because of their high characteristic impedance in the structure, provide the additional series inductance required to make the series circuit resonant at the signal frequency $f_0 = 1$ kMc. The shunt resonator is formed using a small, short-circuited stub to provide the inductance, and a metal block insulated with dielectric material to form the capacitance. The capacitor block was designed so that it would become resonant at the pump frequency

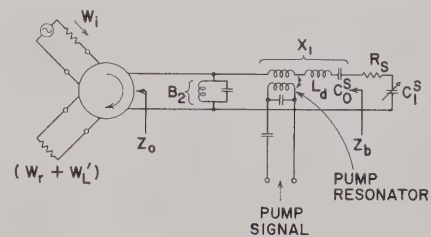


Fig. 1—Equivalent circuit of double-resonator degenerate parametric amplifier.

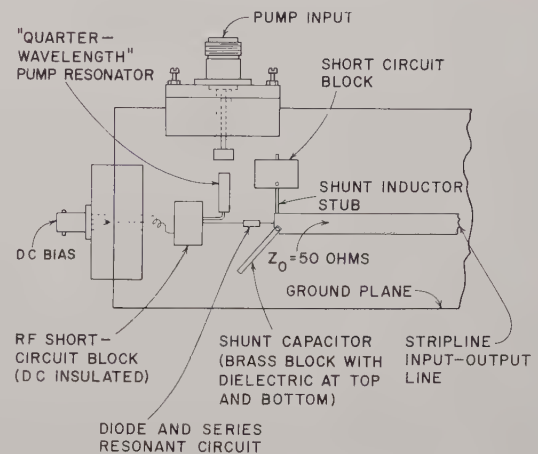


Fig. 2—Construction details of double-resonator degenerate parametric amplifier.

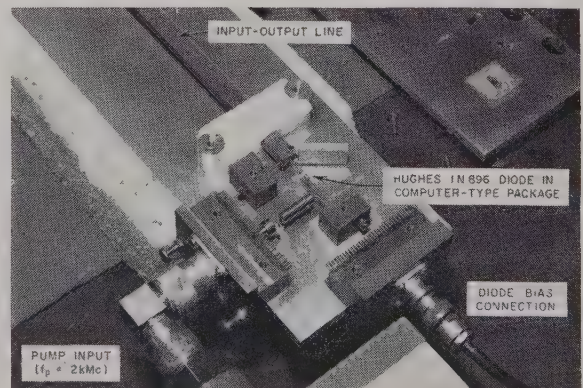


Fig. 3—Photograph of double-resonator degenerate parametric amplifier (cover plate removed).

¹ H. Seidel and G. F. Herrmann, "Circuit aspects of parametric amplifiers," 1959 IRE WESCON CONVENTION RECORD, pt. 2, pp. 83-90.

² C. W. Barnes, G. L. Matthaei, and R. C. Honey, "Applications of New Techniques to Low-Noise Reception," Stanford Res. Inst., Menlo Park, Calif., Quart. Progress Rept. No. 7, Sec. 3-A, SRI Project No. 2550, Contract No. 33(616)-5803; March, 1960. See also Quart. Progress Rept. No. 8.

³ G. L. Matthaei, "A study of the optimum design of wideband parametric amplifiers and up-converters," IRE TRANS. ON MICROWAVE THEORY AND TECHNIQUES, vol. MTT-9, pp. 23-28; January, 1961.

⁴ M. Gilden and G. L. Matthaei, "A nearly optimum wideband degenerate parametric amplifier," Proc. IRE (Correspondence), vol. 49, pp. 833-834; April, 1961.

⁵ M. C. Pease, et al., "Application of New Techniques to Low Noise Reception," Stanford Res. Inst., Menlo Park, Calif., Quart. Progress Rept. No. 10, Sec. 3-A, SRI Project No. 2550, Contract No. AF 33(616)-5803; December, 1960. See also Final Rept. of February, 1961.

$f_p = 2f_0$ and thus provide a short circuit across the input-output line at that frequency. The pump resonator consists of a nominally quarter-wavelength resonator which is inductively coupled to the diode resonator and capacitively coupled to the pump generator line. The short-circuit end of the pump resonator also provides its mechanical support. DC bias is applied to the diode using an external battery.

The design of the circuit elements included a number of design features which made possible nearly optimum performance of a two-resonator amplifier. The diode was resonated in series so that its internal inductance L_d merely contributes to the total inductance required for the series resonant circuit and does not degrade the performance (when operating below the self-resonant frequency of the diode). In an amplifier with the diode resonated in shunt, diode self resonance can have a very serious effect on bandwidth if the diode self-resonant frequency is at all near the operating frequency. The circuit elements were also made as nearly lumped as possible so that the multiple resonances which occur in any distributed elements would be far removed from the signal frequency. Such multiple resonances tend to increase the reactance or susceptance slope of the diode resonance at the operating frequency and as a result tend to narrow the bandwidth. The pump resonator was lightly coupled at both input and output so that it had little effect on the diode circuit at other frequencies, but it would still give efficient power transfer to the diode at the pump frequency. About 6 mw of incident power was required to drive the diode over its full range of capacitance.

There is another advantage in resonating the diode in series in this particular amplifier. For the desired input frequency and 50-ohm input impedance level, the required diode is conveniently of a size ($2.2 \mu\text{mf}$ zero-bias capacitance) which allows the use of higher Q diodes. If the diode had been resonated in shunt and the same input impedance level was used, a diode with much larger capacitance would have been required, and the Q 's for such diodes are considerably lower. The series diode arrangement used also keeps stray capacitance across the diode barrier junction to a minimum and thus prevents degradation of the effective diode C_1/C_0 ratio.⁶ (Keeping this ratio large is very important for obtaining large bandwidth.)^{2,3} Also, to keep C_1/C_0 large the diode was pumped as hard as possible consistent with good noise figure.

By making the distance from the RF short-circuit block (see Fig. 2) to the diode about a quarter wavelength at the upper-sideband frequency $f_0 + f_p = 3 \text{ kMc}$,

the diode is made to see a large reactance at that frequency and also at the second harmonic of pump, $2f_p = 4 \text{ kMc}$. In this manner, dissipation of power at these frequencies is prevented.

EXPERIMENTAL RESULTS

Single-Diode Degenerate Parametric Amplifier

A negative-resistance amplifier requires a circulator in order to obtain best performance with a single amplifier unit.⁷ Since currently no 1-Gc circulators with adequate bandwidth appear to be available, the amplifier was tested using a 3-db directional coupler to give separate input and output ports as shown in the block diagram (Fig. 4.) The precision directional coupler was fabricated using an interleaving printed circuit construction developed at SRI on another program.⁸ It had a residual VSWR less than 1.05 and an isolation in excess of 30 db across the frequency band of interest. The frequency response, corresponding to operation with an ideal circulator, was obtained using the circuit of Fig. 4 in which a reference output level was established with a short circuit in place of the amplifier. In this circuit a short circuit would correspond to an amplifier with a gain of unity. Since a broad-band detector was used and the input signal was modulated, the output power represents the sum of both signal and idler power.

The measured and computed response of the amplifier with and without the shunt resonator is shown in Fig. 5. The value of C_0^* and R_s used in computing the response was established by measurements, the L_d value was as suggested by the diode manufacturer, and the C_1^* value was the value required to give 15-db midband gain (as determined by computation). The other circuit-element values were fixed by the prototype filter used in the amplifier. The agreement between the computed and measured results gives very encouraging verification of the previously developed theory.^{2,3} The computed 3-db bandwidth of the single-resonator design is seen to be 81 Mc while the measured bandwidth is practically the same. The 3-db bandwidth of the computed double-resonator response is about 221 Mc, while the corresponding measured bandwidth is about 210 Mc giving a fractional bandwidth of 21 per cent. These values of bandwidth correspond to a C_1/C_0 value of about 0.32.

The noise figure of the parametric amplifier was measured using a circuit shown in the block diagram of Fig. 6. The pads and the tuners were included to insure that the amplifier would be well matched and would see identical impedance when the noise source was on and

⁶ The C_0 and C_1 referred to here are the conventional parallel-equivalent average and time-varying capacitance coefficients as defined by the Fourier series $C(t) = C_0 + 2C_1 \cos(2\pi f_p t) + \dots$. The computation of the series coefficients, C_0^* and C_1^* in Fig. 1, is discussed elsewhere,^{2,3} but $C_0^*/C_1^* = C_1/C_0$ where C_0^* is roughly equal to C_0 .

⁷ Of course, using two identical amplifier units in a balanced circuit with a 3-db directional coupler can give an equivalent performance, as is shown by results given later in this section.

⁸ W. J. Getsinger, S. B. Cohn, and J. K. Shimizu, "Design Criteria for Microwave Filters and Coupling Structures," Stanford Res. Inst., Menlo Park, Calif., Tech. Rept. No. 10, Sec. 2, SRI Project No. 2326, Contract No. DA 36-039 SC-74862; July, 1960.

off. Care was also taken to reduce the leakage of local-oscillator power and excess noise from the receiver to the parametric amplifier. The image response of the receiver was also suppressed. With the filters and tuners required for a reliable measurement it was convenient to make a noise measurement only at the midband frequency. In the measurement the signal and idler frequencies were adjusted to be close enough together so that both passed through the receiver IF amplifier. The procedure included obtaining a noise-figure measurement F_A with the circuit as shown in Fig. 6 and also obtaining a measurement F_B with the noise source placed at Point B and a matched load at Point A. With this noise measurement the actual noise figure of the parametric amplifier is given by the expression

$$F = \frac{F_A}{L_{AB}} - \frac{F_B - 1}{G}$$

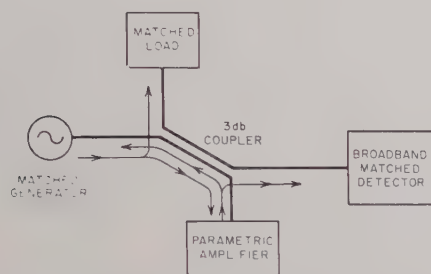


Fig. 4—Block diagram of circuit used in measuring the amplifier frequency response.

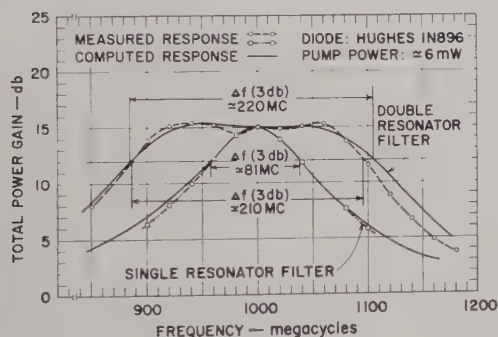


Fig. 5—Frequency response of the single- and double-resonator parametric amplifier.

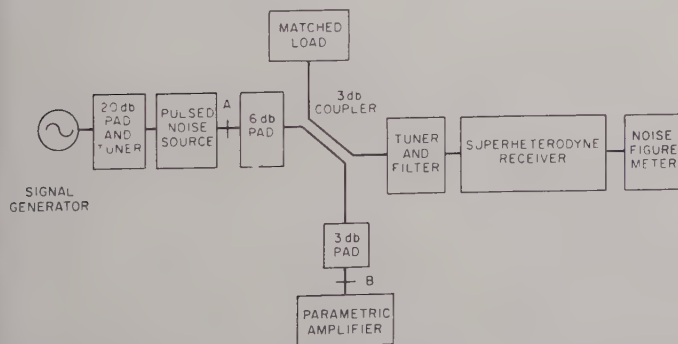


Fig. 6—Block diagram of apparatus for measuring noise figure.

where

- F is the parametric-amplifier double-channel noise figure.
- G is the power-gain *ratio* of the parametric amplifier.
- L_{AB} is the power-loss *ratio* from A to B ($L_{AB} > 1$) including the 3-db loss of the directional coupler.

The noise figure F obtained by this procedure is a double-channel noise figure and is the noise figure which would be obtained if the device were operated with an ideal circulator. The computed value of double-channel noise figure for this amplifier was about 0.5 db as compared with measured values which ranged closely about 1.0 db. Considering the manufacturer's tolerances on the excess noise of the noise tube, the tolerances on the noise-figure meter accuracy, and the possible experimental error, the total possible error would be in excess of ± 0.5 db. Under these conditions the 1.0-db measured noise figure appears to be in satisfactory agreement with the 0.5-db theoretical figure.

Uncritical Nature of Degenerate-Amplifier Tuning

In the course of these experiments, it was found that the amplifier-tuning adjustment was not as critical as expected. This was subsequently further verified by examining the analytical expressions and by computing responses for improperly tuned amplifiers. The midband frequency of the amplifier, regardless of the tuning of the two resonators, is found to be always coincident with one-half the pump frequency. This is shown by the single-resonator computed responses in Fig. 7(a) for the same amplifier parameters used for Fig. 5, but with several different pump frequencies. The gain varied because the level of pumping was held fixed (*i.e.*, C_1/C_0 was fixed at 0.316); however, moving the pump frequency from 2.000 Gc to 1.820 Gc, the change in gain was small in the case of the single-resonator amplifier. In the case of the two-resonator amplifier responses shown in Fig. 7(b), the midband gain went up as a result of the effect of the second resonator on the impedance presented to the diode. If the pump power had been reduced (*i.e.*, if C_1/C_0 had been made smaller) for this case the response would probably have had a flatter top.

A related effect is the uncritical nature of the adjustment of the series resonant circuit. As shown by the single-resonator amplifier computed responses in Fig. 8, the midband frequency is not altered by rather large changes in the length of the inductive element and consequently the resonant frequency f_0 of the series circuit. However, to maintain the same value of midband gain, the C_1/C_0 ratio for the diode was adjusted in each case as indicated in the figure. It is interesting to note in the figure that in order to maintain 15-db gain the diode must be pumped somewhat harder (*i.e.*, C_1/C_0 must be larger) when the diode resonator is detuned. The de-

tuned cases requiring larger C_1/C_0 values are seen to be accompanied by a somewhat larger bandwidth.

Of practical interest, too, in these amplifiers is the degree to which the diodes, with their spread of values, can be interchanged in a particular unit. To verify this under controlled conditions a set of frequency responses of a two-resonator amplifier (the same as for Fig. 5) were computed for a range of values of average capaci-

ties. As shown in Fig. 9, only the bandwidth and the ripple amplitude of the response vary; the midband frequency remains fixed. The change in bandwidth is not large, and should not be a serious problem. Note that if C_0 is smaller than its design value, the amplifier requires less pump power (*i.e.*, a smaller C_1/C_0 value) for the same midband gain than when C_0 has its proper value. However, if C_0 is larger, C_1/C_0 must be increased to maintain the same gain.

The reason for the relatively uncritical nature of the degenerate parametric amplifier tuning can be seen by examining the power-gain expression. For this discussion, diode loss resistance R_s may be neglected, so the expression for power gain is simply^{2,3}

$$|\Gamma|^2 = \frac{|Z_b Z_b' + X_{12} X_{21}|^2}{|Z_b Z_b'^* - X_{12} X_{21}|^2}, \quad (1)$$

where Z_b is the impedance seen looking back into the input filter as shown in Fig. 1 and Γ is the voltage reflection coefficient between the circulator and the amplifier. The asterisk indicates that the conjugate is to be taken. In (1), Z_b is evaluated at the signal frequency f , while Z_b' is the same impedance evaluated at the idler frequency $f' = f_p - f$, where f_p is the pump frequency. The quantity $X_{12} X_{21}$ in (1) is $1/[(2\pi C_1)^2 ff']$.

The power gain $|\Gamma|^2$ is most sensitive to variations in the difference expression in the denominator of (1). Study of the denominator shows that to a first approximation the imaginary part of the quantity within the magnitude signs will be unaffected by moderate mistuning of the diode resonator, while the real part will be only slightly affected.⁵ Further, the expression obtained shows that the small change in the real part can be compensated for by a small increase in C_1/C_0 . These results are consistent with the computed results in Figs. 7 to 9 and with our experimental observations.

Balanced Amplifiers

The single-diode parametric amplifier becomes a useful device when separate input and output ports can be provided. Amplifier bandwidths of the order of 20 per cent exclude the use of currently available circulators operating in the vicinity of 1 Gc, but an alternative is to use a pair of single-diode amplifiers with a 3-db directional coupler as shown in Fig. 10. This circuit, unlike one using a circulator, is bilateral, since it can amplify equally well in both directions. To prevent distortion of the frequency response it is required that the individual amplifier units have nearly identical impedance characteristics and that each work into a well matched load. This requirement means that the directional coupler and the terminations at *both* input and output ports must not produce an appreciable VSWR at the amplifier unit. The signal-frequency components will automatically add at the output port and cancel at the input port of the 3-db directional coupler if the input impedances of the two amplifiers are identical; however,

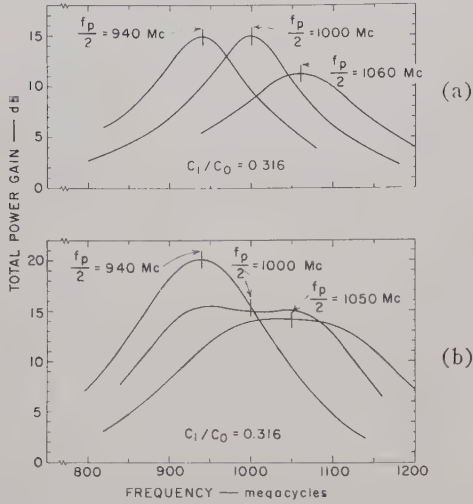


Fig. 7—Frequency-response dependence on pump frequency (computed results). (a) Single-resonator amplifier. (b) Double-resonator amplifier.

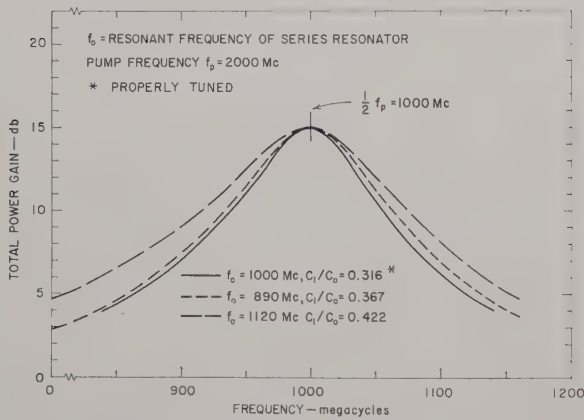


Fig. 8—Frequency-response dependence on the inductive element in the series resonant circuit (computed results).

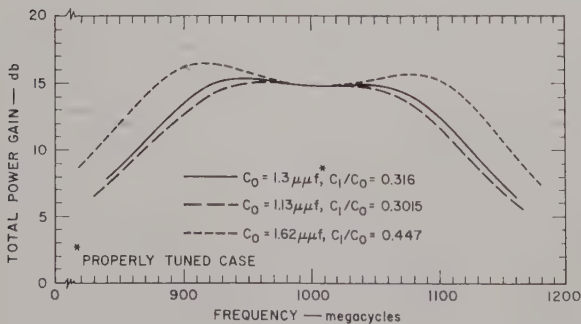


Fig. 9—Frequency-response dependence on the average diode capacitance in two-resonator amplifier (computed results).

for the idler-frequency signals the relative phases of the pump signals must be adjusted to make the idler outputs add at the output port. Making this adjustment at one frequency will provide proper idler phases at all frequencies.

The feasibility of the balanced operation is demonstrated by the experimental frequency response in Fig. 11 for the balanced amplifier shown in Fig. 10. A second amplifier unit identical to the one discussed above was used together with the precision 3-db directional coupler mentioned earlier. Both the transmission-power gain, which is the useful output, and the reflection-power gain are shown. The reflection-power gain (the db ratio of power reflected to power incident at the input of the balanced amplifier) is indicative of the balance between the two single-diode units. The transmission-power gain with a bandwidth of 210 Mc (i.e., 21-per cent bandwidth) is a good replica of the single-amplifier frequency response (see Fig. 5), and the reflection power gain, except within a narrow band of frequencies, is always less than 0 db, indicating a satisfactory balance between amplifiers. The power gain in-

cludes both signal and idler outputs, since both carry the signal modulation.

Cascaded Balanced Amplifier

The operating characteristics of the balanced amplifier being satisfactory, it seemed worth while to try to obtain even greater bandwidth by cascading several balanced amplifiers which are adjusted so that the individual pass bands are contiguous as shown in Fig. 12. To understand this circuit, note that the minimum value of gain of a degenerate amplifier is unity outside the pass band because the reflection from the amplifier corresponds to that of a pure reactance. Thus, when the first balanced amplifier doesn't amplify it merely passes the power on to the second amplifier. To obtain stable operation, the design gain must not be too large in order to provide a safety margin against distorting the response of the individual units and against reflections which could lead to oscillations.

A two-stage cascaded balanced amplifier was assembled and tested. The first stage was the balanced amplifier described earlier with a midband frequency of 1 Gc and the second stage was of similar construction but scaled for operation at 1320 Mc. Unfortunately, the 3-db directional couplers had not originally been in-

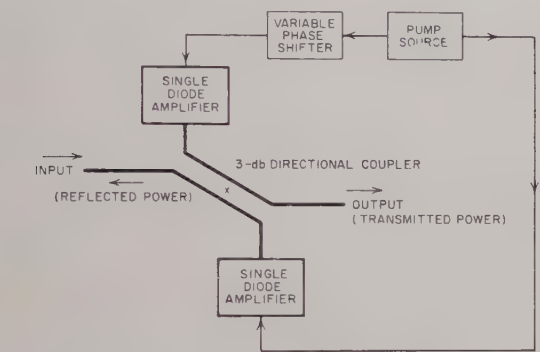


Fig. 10—Block diagram of two-port balanced amplifier.

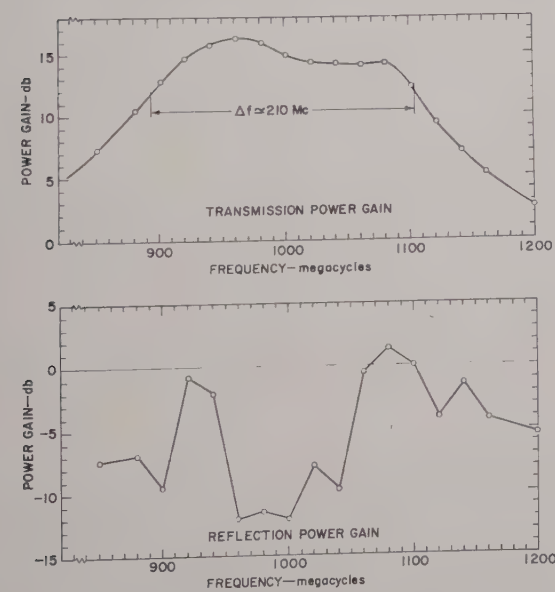


Fig. 11—Frequency response of balanced amplifier.

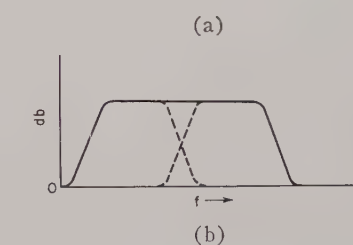
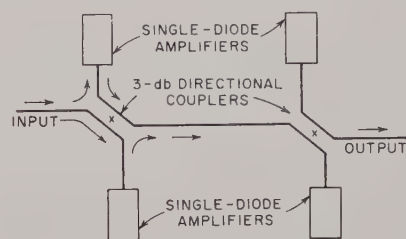


Fig. 12—Cascaded balanced amplifiers. (a) Balanced amplifier and tandem connection. (b) Composite frequency response.

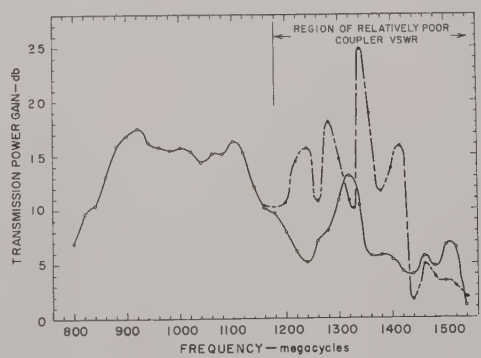


Fig. 13—Frequency response of cascaded balanced amplifiers.

tended for use up into the frequency range covered by the second amplifier. Therefore, because of reflections from the directional couplers, the frequency response of the second amplifier did not attain the flat broad-band shape of the first amplifier.

The measured frequency response of the cascaded amplifier is shown in Fig. 13. The heavy solid line represents the initial response after adjusting each balanced amplifier separately. Note that the shape of the response in the range of the well-matched 1000-Mc stage is a fair replica of the single-balanced-amplifier response in Fig. 5. The response in the range of the second stage is erratic because of the reflections from the directional couplers. An attempt to compensate for these reflections in the 1320-Mc second stage by adjusting the diode bias and the pump amplitude and phase finally resulted in the response at the higher end shown by the dashed line. The usable bandwidth, say for which the gain is over 10 db, extends from 850 Mc to 1420 Mc, which is approximately a 50-per cent bandwidth.

Discussion

This work has shown that practical, nearly optimum, single-diode degenerate amplifiers can be designed according to previously developed theory.^{2,3} The construction used for the particular example had a number of significant features which are particularly advantageous for frequencies up to the self-resonant frequency of the diode. The excellent agreement between theory and experiment gave strong evidence of the validity and practical usefulness of the design methods which were used.

It was found that the C_1/C_0 ratio for practical diodes can be 0.32 or slightly larger. The measured and computed responses corresponded to a C_1/C_0 ratio of this value. Pumping the diode harder (which makes C_1/C_0 larger), made it possible to raise the midband gain as high as 20 db; however, above about 16-db midband gain the noise figure began to increase. Thus, $C_1/C_0 = 0.32$ appears to be about the maximum practical value for low-noise operation, at least for the case of Hughes 1N896 diodes. As was previously mentioned, making C_1/C_0 as large as permissible is necessary in order to obtain maximum bandwidth.

The investigations made of the performance of improperly tuned degenerate amplifiers showed that there

is a tendency for detuning effects to cancel out. Because of this, if such amplifiers are designed so that the prototype design does not require quite all of the pump power that the diode can take, some latitude in diode parameters can be tolerated which would only require a readjustment of the pump power in order to obtain the desired midband gain. For a related reason, since the amplifier response always tends to center at exactly half the pump frequency, small adjustments in the midband frequency can be made by shifting the pump frequency.

Balanced operation of amplifiers giving separate input and output terminals was shown to be practical, although most commercial 3-db couplers would have too large a VSWR to be satisfactory for such purposes. It is, nevertheless, possible to build couplers with an adequately low VSWR, as is proved by the one fabricated for this particular application. Balanced operation using two amplifiers and a well matched 3-db coupler was seen to give wideband performance comparable to what would be obtained by a single amplifier with a very well matched, wideband circulator having very low loss. Until such circulators are available for all frequency bands of interest, the balanced amplifier appears to provide an attractive alternative. The chief limitation of this form of amplifier is that only well matched terminations can be used at both its input and output terminal. This condition is required not only to prevent oscillations due to multiple reflections but also to insure that each amplifier unit itself sees a well matched load so that its frequency response will not become distorted.

The results from the cascaded balanced amplifiers showed that this scheme does present a useful way for obtaining extremely wide bandwidth. Although the response at the higher end of the band was erratic due to the coupler VSWR with couplers which are well matched over the entire frequency band the response should be as desired. This type of amplifier has some advantages over the traveling-wave types of amplifiers in that it will give reasonably good gain with very wide bandwidth while using relatively few diodes. With this type of amplifier care must be taken, however, that the reflections of the terminations and the couplers are not too large, since this will distort the response and might cause oscillation.

Transmission-Phase Relations of Four-Frequency Parametric Devices*

D. B. ANDERSON†, MEMBER, IRE, AND J. C. AUKLAND‡, MEMBER, IRE

Summary—The gain, bandwidth, and excess noise temperature properties of parametric amplifiers are generally known. However, a knowledge of their transmission-phase properties is also essential for the effective application of parametric amplifiers to angular detection systems, such as monopulse radars and interferometers. These angle detection systems derive even, odd, and quadrupolar spatial components of the antenna diffraction patterns. The differential amplitude and differential phase between these signal components contain the spatial information of position, extent, and shape of the target. Consequently, to employ parametric transducers in certain systems requires an understanding of the transmission phase properties which are delineated in this paper.

The analysis follows the matrix representation of a nonlinear capacitive susceptance, four-frequency transducer wherein due note is taken of the phases. The transmission-phase relations are written which include the effects of nonzero port susceptance and nonlinear reactance element losses. At midband without losses, the relations reduce to easily remembered equations which are significant to the application of parametric transducers in phase-sensitive systems. Some applications and experimental results are cited.

I. INTRODUCTION

LOW-NOISE parametric amplification is now a reality, and its application to receiver systems is being seriously considered. The gain, bandwidth, and excess noise temperature properties of parametric amplifiers are generally known. However, a knowledge of the transmission-phase property of parametric amplifiers is also essential to their effective application in certain types of phase-sensitive systems. The transmission-phase relations are the phase shifts associated with the transmission coefficient of the transition between the various ports of a transducer.¹

For example, a monopulse angle-detection radar employs an antenna and a hybrid-junction labyrinth which derives even, odd, and quadrupolar spatial components of the antenna diffraction pattern. The source signal or target echo differential amplitude and differential phase between labyrinth ports contain spatial information of target position, extent, and shape.² Consequently, to employ parametric transducers for low-noise amplification, or to implement the phase-detection function in monopulse systems, requires a knowledge of their transmission-phase properties.

The gain, bandwidth, and noise properties for the various operational modes of four-frequency parametric devices have been considered previously.³⁻⁸

The authors' intent is to delineate the transmission-phase properties of four-frequency parametric devices.

The signal phases in each permitted port are interrelated through the pump phase by the mixing process which occurs in the nonlinear element. Four-frequency parametric transducers (signal, pump, upper sideband, and lower sideband) are considered because they encompass both the negative conductance and the frequency conversion mechanisms of amplification which individually appear in the three-frequency difference and sum spectral modes, respectively. As the signal frequencies in the three-frequency difference mode converge to the two-frequency degenerate mode, the amplification of the single unique frequency (one-half the pump frequency) is sensitive to the relative pump phase. The four-frequency transmission-phase relations will be developed; from these the relations for three- and two-frequency devices are obvious.

In this report the method of analysis uses the well-known matrix representation for a nonlinear capacitive-susceptance four-frequency parametric transducer wherein due note is taken of the phases. A lossy nonlinear reactive element and the effects of nonzero port susceptances are considered, removing the midband restrictions on the transmission-phase relations written previously.⁹ Use of the transmission-phase relations will be illustrated by their application to several non-

* E. M. T. Jones and J. S. Honda, "A low-noise up-converter parametric amplifier," 1959 IRE WESCON CONVENTION RECORD, pt. 1, pp. 99-107.

† D. K. Adams, "An analysis of four-frequency nonlinear reactance circuits," IRE TRANS. ON MICROWAVE THEORY AND TECHNIQUES, vol. MTT-8, pp. 274-283; May, 1960.

‡ D. B. Anderson and J. C. Aukland, "A general catalog of gain, bandwidth, and noise temperature expressions for four-frequency parametric devices," submitted for publication, IRE TRANS. ON MICROWAVE THEORY AND TECHNIQUES.

§ C. Blake, "Review of Reactance Amplifier Circuit Theory," Lincoln Lab., Mass. Inst. Tech., Lexington, Rept. No. 46G-004; July 7, 1960.

|| C. R. Boyd, "A general approach to the evaluation of n -frequency parametric mixers," *Proc. NEC*, vol. 16, pp. 472-479; October, 1960.

¶ J. A. Luksch, E. Q. Matthews, and G. A. VerWys, "Design and operation of four-frequency parametric up-converters," IRE TRANS. ON MICROWAVE THEORY AND TECHNIQUES, vol. MTT-9, pp. 44-52; January, 1961.

|| D. B. Anderson and J. C. Aukland, "The midband phase relations in four-frequency parametric amplifiers," Symp. on the Application of Low-Noise Receivers to Radar and Allied Equipment, Lincoln Lab., October 24-28, 1960; Mass. Inst. Tech., Lexington, vol. 3, pp. 165-175; November 22, 1960.

* Received by the PGMTT, May 16, 1961; revised manuscript received, July 31, 1961.

† Autonetics Div., N. American Aviation, Inc., Anaheim, Calif.

‡ "IRE Standards on Antennas and Waveguides," *Proc. IRE*, vol. 47, pp. 568-582; April, 1959.

§ D. B. Anderson and D. R. Wells, "Some Further Notes on the Spatial Information available from Monopulse Radar," presented at 5th MIL-E-CON Natl. Convention on Military Electronics, Washington, D. C.; June 26-28, 1961.

reciprocal and unilateral parametric transducers. A discussion follows of some wideband transmission-phase-measurement techniques and their experimental results for several operational modes. The transmission-phase relations developed should not be confused with the interrelations of propagation constants that have been defined for travelling wave structures.

II. DEVELOPMENT OF TRANSMISSION-PHASE RELATIONS

In the following cursory analysis the four-frequency parametric transducer considered is represented by Fig. 1.

For small signal conditions, the current components in the time-varying susceptance are represented in matrix notation as

$$[I_n] = [B][V_n] \quad (1)$$

for each port at frequency ω_n , where the nonlinear susceptance is represented by the admittance matrix $[B]$, and the current and the voltage at each port are described by matrices $[I_n]$ and $[V_n]$, respectively. The capacitive susceptance realized in a back-biased semiconductor diode is considered because of its general acceptance for low-noise applications. A single large periodic pump voltage $V_p(t)$ causes the capacitance to vary as

$$C[V_p(t)] = C_0 + \frac{C_1}{2} + \frac{C_1^*}{2} \\ = C_0 + |C_1|e^{j(\omega_p t + \phi_p)} + |C_1|^*e^{-j(\omega_p t + \phi_p)}. \quad (2)$$

The asterisk (*) denotes C_1^* as the conjugate of C_1 , where C_0 is the capacitance due to the fixed bias, and C_1 is the time variation of capacitance about C_0 caused by the pumping voltage $V_p(t)$.

In the microwave region the back-biased semiconductor diode only approaches the ideal nonlinear capacity because the spreading resistance R_s is in series with the barrier capacity. Using the admittance representation of the diode, the equivalent conductance is written as

$$G_{dn} = \frac{\omega_n^2 C_0^2 R_s}{1 + \omega_n^2 C_0^2 R_s^2}, \quad (3)$$

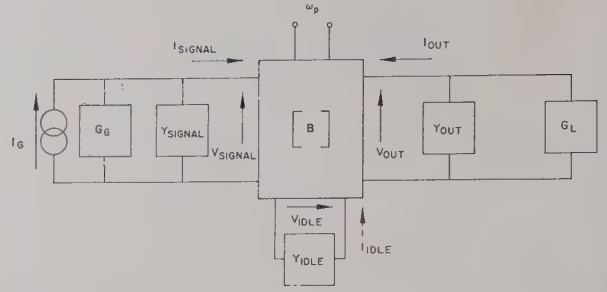


Fig. 1—General four-frequency parametric transducer.

and the equivalent capacitive susceptance is written as

$$B_{dn} = \frac{\omega_n C_0}{1 + \omega_n^2 C_0^2 R_s^2} \quad (4)$$

at the ports $n=1, 2, 3$. Practical microwave varactors have a high Q where the diode Q at each frequency ω_n is

$$Q_{dn} = \frac{1}{\omega_n C_0 R_s}, \quad (5)$$

so that a simplification of the equivalent conductance and susceptance is valid, and (3) and (4) become

$$G_{dn} = \omega_n^2 C_0^2 R_s \quad (6)$$

and

$$B_{dn} = \omega_n C_0. \quad (7)$$

The nomenclature for the four-frequencies which shall be allowed to exist in the external ports will be described as

$$\omega_1 < \omega_2 = \omega_p - \omega_1 < \omega_p < \omega_3 = \omega_p + \omega_1. \quad (8)$$

There are certain frequencies greater than ω_3 which are generated by the nonlinear reactance, but power at these frequencies is not permitted to exist in the external ports. The matrix equation (1), when written for the four frequencies specified in (8), where the effective diode loss at each frequency ω_n from (6) has been included in the diagonal term, is

$$\begin{bmatrix} I_1 \\ I_2^* \\ I_3 \end{bmatrix} = \begin{bmatrix} \omega_1^2 C_0^2 R_s + j\omega_1 C_0 & j\frac{\omega_1 C_1}{2} & j\frac{\omega_1 C_1^*}{2} \\ -j\frac{\omega_2 C_1^*}{2} & \omega_2^2 C_0^2 R_s - j\omega_2 C_0 & 0 \\ j\frac{\omega_3 C_1}{2} & 0 & \omega_3^2 C_0^2 R_s + j\omega_3 C_0 \end{bmatrix} \begin{bmatrix} V_1 \\ V_2^* \\ V_3 \end{bmatrix}. \quad (9)$$

The preceding equation fully describes the mixing process that occurs in the nonlinear element. The Kirchhoff current equations for each port of the nonlinear reactance, neglecting the generator current, are written as

$$I_1 = -V_1 Y_1 = -V_1(G_1 - jB_1) \quad (10)$$

$$I_2^* = -V_2^* Y_2 = -V_2^*(G_2 + jB_2) \quad (11)$$

$$I_3 = -V_3 Y_3 = -V_3(G_3 - jB_3), \quad (12)$$

where $(G_n \pm jB_n)$ represents the Y_n admittance associated with each port for which the susceptance term B_n cancels the diode susceptance $\omega_n C_0$ at the midband frequency line $\omega_n = \omega_{n0}$ of the mode spectrum.

The transmission-phase relations may now be determined where the phase dependencies of the voltage in (9)–(12) are included. As an example, consider a four-frequency operational mode spectrum with the input at ω_1 , the output at ω_2 , and the idle at ω_3 . The output current from (9) is given by

$$I_2^* = (\omega_2^2 C_0^2 R_s - j\omega_2 C_0) V_2^* - j \frac{\omega_2 C_1^*}{2} V_1, \quad (13)$$

which will be equated to (11). Collecting real and imaginary terms after including the pump dependency of (2), the expression has the form of

$$K_r e^{j(\omega_2 t + \phi_2)} + K_i e^{j(\omega_2 t + \phi_2 + \pi/2)} = K_t e^{j(\omega_2 t + \phi_p - \phi_1 - \pi/2)}, \quad (14)$$

where ϕ_n is the phase of the voltage V_n , and the phasor magnitudes are given as

$$K_r = (G_2 + \omega_2^2 C_0^2 R_s) V_2 \quad (15)$$

$$K_i = (\omega_2 C_0 - B_2) V_2 \quad (16)$$

$$K_t = \frac{\omega_2 C_1}{2} V_1. \quad (17)$$

Eq. (14) has a graphical interpretation as phasors in Fig. 2.

Inspection of Fig. 2 readily yields the transmission phase at the output due to the signal input and the pumping of the nonlinear reactance as

$$\phi_2 = \phi_p - \phi_1 - \frac{\pi}{2} - \tan^{-1} \left(\frac{K_i}{K_r} \right). \quad (18)$$

Defining $\omega_n = \omega_{n0}(1 + \delta_n)$ for each port, where ω_{n0} is the midband resonant frequency of the external port, and δ_n is the fractional deviation from resonance, (18) becomes

$$\phi_2 = \phi_p - \phi_1 - \frac{\pi}{2} - \tan^{-1} \left\{ \frac{\omega_{20}^2 L_2 C_0 (1 + \delta_2)^2 - 1}{L_2 G_2 \omega_{20} (1 + \delta_2) \left[1 + \frac{\omega_{20}^2 (1 + \delta_2)^2 C_0^2 R_s}{G_2} \right]} \right\}, \quad (19)$$

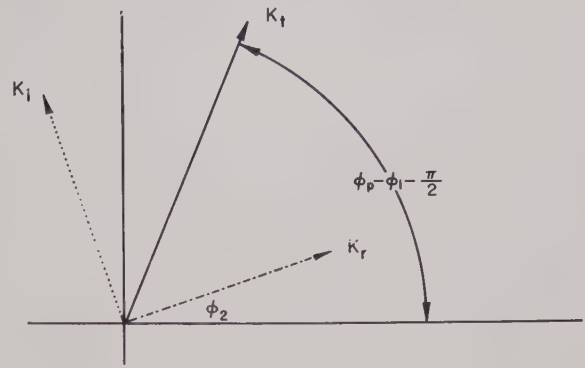


Fig. 2—Graphical interpretation of transmission phase.

where the external susceptance B_n has been assumed to be $1/\omega_n L_n$. For simple resonant cavities where its $Q = 1/\omega_n L_n G_n$, (19) becomes

$$\phi_2 = \phi_p - \phi_1 - \frac{\pi}{2} - \tan^{-1} \left[\frac{2Q_2 \delta_2}{1 + \frac{1}{Q_{d2}^2 G_2 R_s}} \right], \quad (20)$$

where $\delta_n \ll 1$.

The arctangent term in (20) accounts for the varactor losses and detuning or off-center frequency operation of the output cavity. The constant $\pi/2$ in the phase relation (20) is reminiscent of the phase shift in a quarter-wave transformer. It should be noted that the phase of the input voltage in (20) is that at the input port or the nonlinear reactance and may not be the signal voltage phase applied to an input lossy cavity. The additional transmission phase shift through the input passive cavity may be accounted for in the conventional manner.

Now consider a four-frequency operational mode spectrum, where the input is at ω_1 , the output is at ω_3 , and the idle at ω_2 ; an argument analogous to the previous case yields the relation

$$\phi_3 = \phi_p + \phi_1 - \frac{\pi}{2} - \tan^{-1} \left[\frac{2Q_3 \delta_3}{1 + \frac{1}{Q_{d1}^2 G_3 R_s}} \right], \quad (21)$$

where $\delta_n \ll 1$.

The results of (20) and (21) are distinguished by the difference in sign of ϕ_1 .

Now consider the four-frequency operational mode, where the input is at ω_2 , the output is at ω_1 , and the idle is at ω_3 .

$$I_1 = (\omega_1^2 C_0^2 R_s + j\omega_1 C_0) V_1 + j \frac{\omega_1 C_1}{2} V_2^* + j \frac{\omega_1 C_1^*}{2} V_3, \quad (22)$$

which is equated to (10). From (9) and (12) V_3 is written in terms of V_1 and collecting the terms as before yields the relation

$$\phi_1 = \phi_p - \phi_2 - \frac{\pi}{2}$$

$$- \tan^{-1} \left[\frac{\frac{2Q_1\delta_1}{1 + \frac{1}{Q_{d1}^2 R_s G_1}} - \frac{2a_{31}Q_3\delta_3}{1 + \frac{1}{Q_{d3}^2 R_s G_3}}}{1 + a_{31}} \right], \quad (23)$$

where $\delta_n \ll 1$

$$a_{31} = \frac{\omega_1 \omega_3 |C_1|^2}{4(G_1 + \omega_1^2 C_0^2 R_s)(G_3 + \omega_3^2 C_0^2 R_s)}. \quad (24)$$

The parameter a_{mn} is a measure of the coupling from the ω_m to ω_n port due to a pumping of a nonlinear reactance.

Similarly, for the four-frequency operational mode with the input at ω_3 , the output at ω_1 , and the idle at ω_2 , the transmission-phase relation is

$$\phi_1 = \phi_3 - \phi_p - \frac{\pi}{2}$$

$$- \tan^{-1} \left[\frac{\frac{2Q_1\delta_1}{1 + \frac{1}{Q_{d1}G_1R_s}} - \frac{2a_{21}Q_2\delta_2}{1 + \frac{1}{Q_{d2}^2G_2R_s}}}{1 - a_{21}} \right], \quad (25)$$

where $\delta_n \ll 1$

$$a_{21} = \frac{\omega_1 \omega_2 |C_1|^2}{4(G_1 + \omega_1^2 C_0^2 R_s)(G_2 + \omega_2^2 C_0^2 R_s)}. \quad (26)$$

Note that the form of (23) and (25) is similar, except that in (25) the pump and signal phase terms are interchanged. This is to be expected since the role of ω_p and ω_3 in the down-conversion mechanism from the sum frequency ω_3 acts like the difference-frequency mechanism, insofar as energy transfer is concerned. In both (23) and (25) the parametric coupling parameter a_{mn} shows how the idle cavity influences the transmission-phase properties.

Now, with the transmission-phase relations between ports of different frequencies (20), (21), (23), and (25), the phase properties of one-port parametric transducers (employing ferrite circulators to separate input and output ports at a single frequency) may be deduced by noting the transmission-phase conversion into the idle loading, then by noting the reflection at the idle port, and then by writing these in the transmission phase relation back to the original port.

The arctangent term of (20), (21), (23), and (25) expresses the effect of cavity detuning in the external ports and the diode losses on the phase. Note that at midband $\delta_n = 0$ the varactor loss does not influence the phase. The midband transmission-phase relations are more useful in the cursory analysis of phase-sensitive instrumentation, so by inspection the midband relations for various operational modes are tabulated as

Input to Output

Phase Relation

$$\omega_1 \rightarrow \omega_2 \quad \phi_2 = \phi_p - \phi_1 - \frac{\pi}{2} \quad (27)$$

$$\omega_1 \rightarrow \omega_3 \quad \phi_3 = \phi_p + \phi_1 - \frac{\pi}{2} \quad (28)$$

$$\omega_2 \rightarrow \omega_1 \quad \phi_1 = \phi_p - \phi_2 - \frac{\pi}{2} \quad (29)$$

$$\omega_3 \rightarrow \omega_1 \quad \phi_1 = \phi_3 - \phi_p - \frac{\pi}{2} \quad (30)$$

$$\omega_2 \rightarrow \omega_3 \quad \phi_3 = 2\phi_p - \phi_2 - \pi \quad (31)$$

$$\omega_3 \rightarrow \omega_2 \quad \phi_2 = 2\phi_p - \phi_3. \quad (32)$$

The four-output transmission-phase relations (27)–(30) are easily remembered by noting the symmetry whereby the phases combine in the same manner as the frequencies combine, the result being in quadrature with the output phase, where the quadrature sign is determined by the nonlinear reactance. From these four basic relations, a simple manipulation yields (31) and (32) for conversion between the pump sidebands. These six equations may be applied for any type of nonlinear mixing elements by using the appropriate radian constant—negative constants for capacitive, positive constants for inductive, and no constants for resistive nonlinear elements.

The transmission-phase relations are also valid for the three-frequency case, wherein one of the pump sidebands is made nonexistent by setting $G_{idle} = \infty$ so $a_{mn} = 0$. A three-frequency difference transducer, wherein ω_1 and ω_2 are both coupled to the same port, is said to be degenerate, because, for the single unique frequency (one-half the pump $\phi_1 = \phi_2$) and from (29), the pump phase is

$$\phi_p = 2\phi_1 + \frac{\pi}{2} \quad (33)$$

to realize amplification.

III. SOME APPLICATIONS OF TRANSMISSION-PHASE RELATIONS

Phase-sensitive systems measure the differential phase between the signals received in separate channels. Parametric devices used to amplify or process the signals must preserve the phase coherence between the channels. This requirement dictates the following:

- 1) A single-pump oscillator must be common to all channels.
- 2) Like parametric operation, modes must be used to preserve the signal-spectrum order.
- 3) The signal-selectivity bandwidth and transmission-line (signal and pump) electrical length must be similar for each channel to prevent signal dispersion.

When parametric devices are used in monopulse systems, the transmission-phase relations have proven use-

ful in system analysis in the same manner as the transmission phase rules have distinguished difference between the various microwave hybrid-junction types used in the design of monopulse labyrinths. The phase relations may also be used to conceive nonreciprocal or unilateral parametric devices. Some applications will be illustrated by applying the phase relations to two parametric devices described in the literature. The block diagram and mode spectrum of a nonreciprocal device¹⁰ is illustrated in Fig. 3.

This device employs an up-converter followed by a down-converter, both pumped from a common source but in phase quadrature. From (28) and (30) the phase at each point for each direction of propagation is indicated in Fig. 3. It is clear that the device's phase length depends upon the direction of propagation because of the manner in which the pump is applied. Thus, when surrounded with two hybrid junctions, the device functions as a four-port circulator.

Adams⁴ and Blake⁶ have described a five-frequency parametric amplifier which has positive input-output conductances, unlimited conversion gain, and may be unilateral. The pump harmonic is employed as the fifth frequency. The principles which they employ combine two operational modes. If the modes are separated into individual parametric transducers of equal gain between two hybrid junctions and pumped coherently, then a four-port circulator is obtained, as illustrated in Fig. 4.

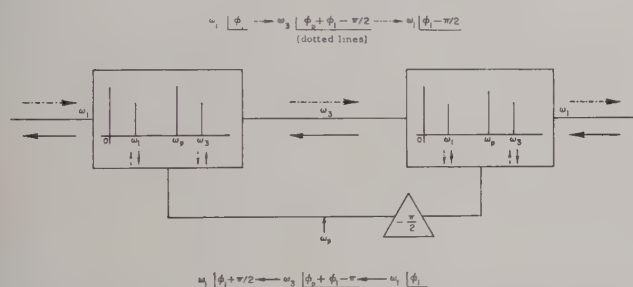


Fig. 3—A parametric nonreciprocal transducer.

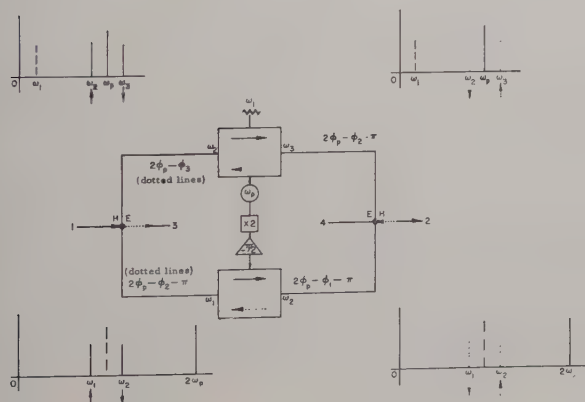


Fig. 4—A parametric 4-port circulator.

One amplifier functions in the three-frequency mode with respect to the ω_{2p} pump, where ω_{2p} is the second harmonic of ω_p . The other amplifier functions as a four-frequency device with respect to the ω_p pump, where ω_1 idles. From (27), (29), (30), and (32), the phase at each port for each direction of propagation is illustrated in Fig. 4. The frequencies on the opposite sides of the circulator are related as $\omega_2 = \omega_1'$ and $\omega_3 = \omega_2'$, where the primes signify the frequencies from the device pumped by ω_{2p} . It is clear that the signal will circulate as $1 \rightarrow 2 \rightarrow 3 \rightarrow 4 \rightarrow 1$, where both the signal frequencies and signal levels alternate between ports.

IV. EXPERIMENTAL PHASE MEASUREMENTS

Several experiments have been performed to verify some of the stated transmission-phase relations and to determine the application feasibility of parametric transducers in phase-sensitive instrumentation such as monopulse systems. The block diagram of instrumentation used to simultaneously measure the transmission gain and phase of a parametric amplifier over a wide frequency band is illustrated in Fig. 5. The frequencies in each leg of the phase bridge are separated by 1000 cps, and the total length of each leg is approximately 1700 wavelengths. The phase measurements are independent of signal amplitude over a 30-db dynamic range. Provisions are also included to measure the effective input noise temperature. A three-frequency difference parametric amplifier, operating in a quasi-degenerate mode with a pump of 17.0 Gc was used for the phase experiments. The parametric amplifier was designed for flexibility rather than wideband and low-noise temperature, although a 1.9 Gc gain-bandwidth product and 110°K radiometric noise temperature have been observed. The amplifier was designed to study the quasi-degenerate four-frequency operation and to accept a wide variety of varactor diodes with self-resonant frequencies both above and below the degenerate point.

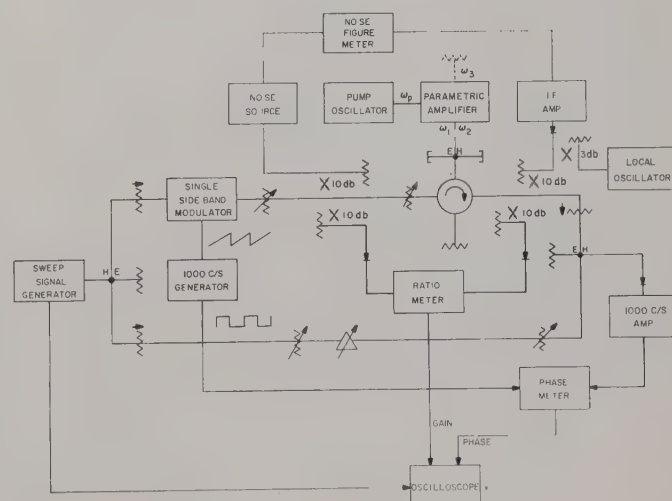
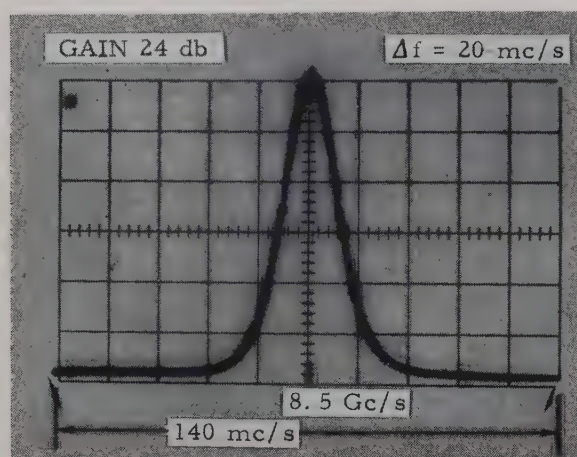


Fig. 5—Gain and phase instrumentation.

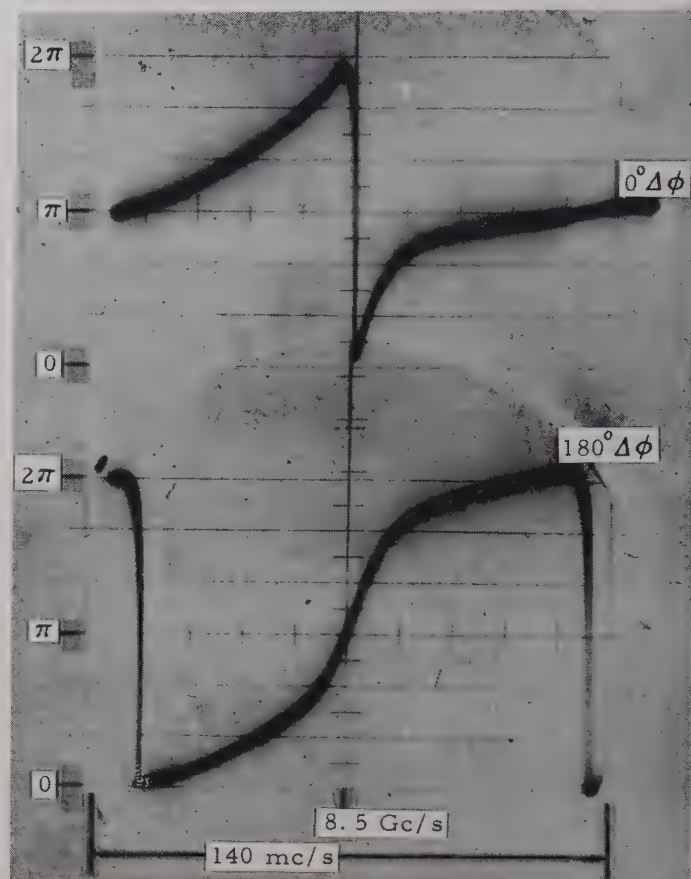
¹⁰ A. K. Kamal, "A parametric device as a nonreciprocal element," *Proc. IRE*, vol. 48, pp. 1424-1430; August, 1960.

The observed experimental transmission gain and phase properties for a variety of operating conditions are illustrated in Figs. 6–11 (pp. 496–498). Relative power gain and differential phase 0 to 2π is displayed as a function of frequency for the conditions indicated.

Some explanation of the phase data displayed is prudent here for proper interpretation. A phase function is a continuous circular function which has been recorded herein on a rectilinear system; therefore, when the phase meter and oscillogram indicators reach 0 or 2π , the indicator rapidly traverses the scale and continues the phase function. The transmission-phase data of a degenerate parametric amplifier is shown in Fig. 6 for 0 and π positions of the phase shifter in the opposite leg of the phase bridge. Both curves are identical phase functions, but the upper curve has the scale traversal positioned at the amplifier midband.

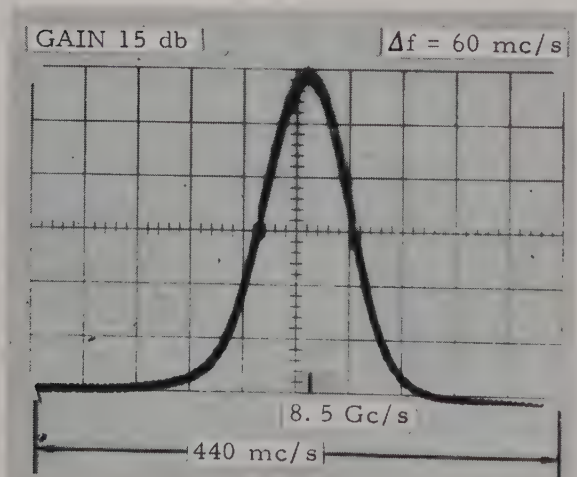


(a)

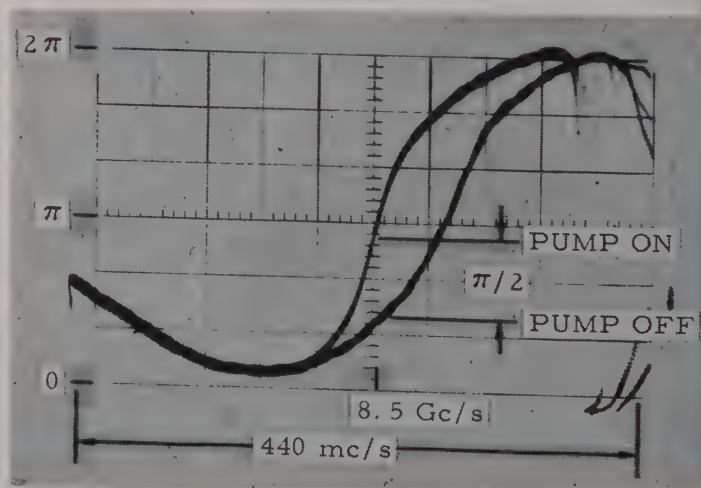


(b)

Fig. 6—Transmission gain and phase as a function of frequency for a degenerate parametric amplifier. (a) Gain. (b) Phase

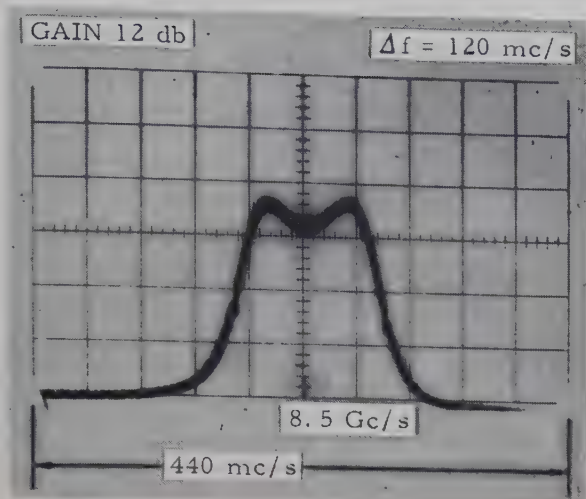


(a)

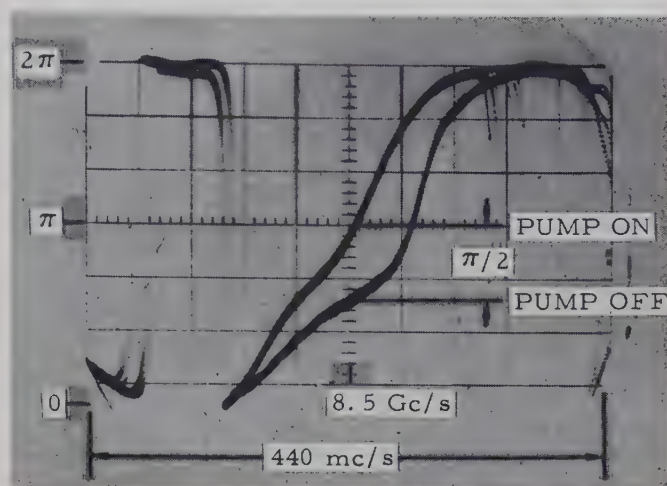


(b)

Fig. 7—Transmission gain and phase as a function of frequency for a degenerate parametric amplifier, pump on and pump off. (a) Gain. (b) Phase.



(a)



(b)

Fig. 8—Transmission gain and phase as a function of frequency for a wideband degenerate parametric amplifier, pump on and pump off. (a) Gain. (b) Phase.

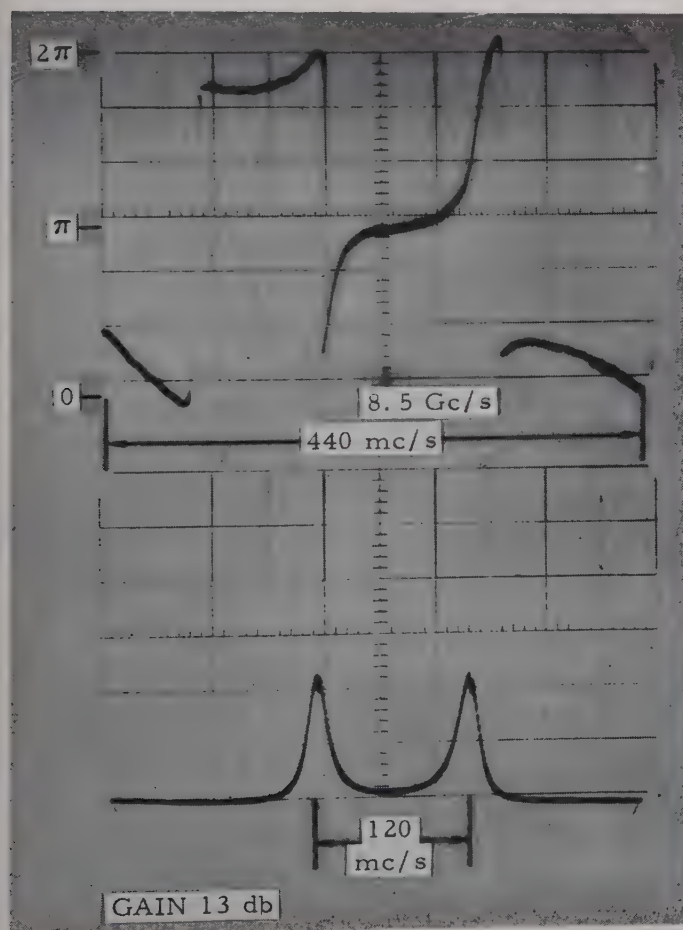


Fig. 9—Transmission gain and phase as a function of frequency for a nondegenerate parametric amplifier.

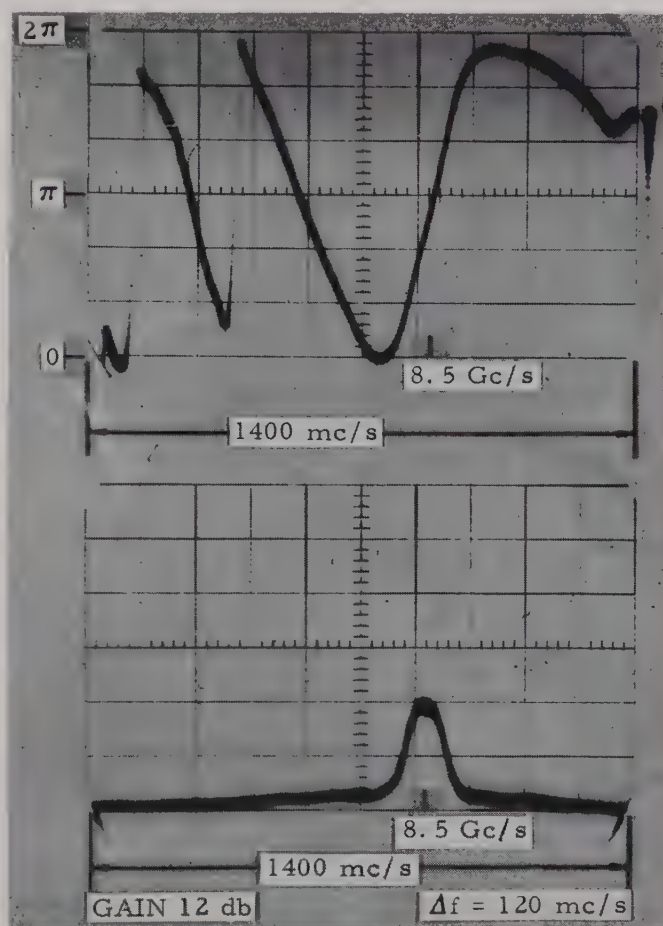


Fig. 10—Transmission gain and phase as a function of frequency of a wideband parametric amplifier showing the phase bridge dispersion properties over a wide band.

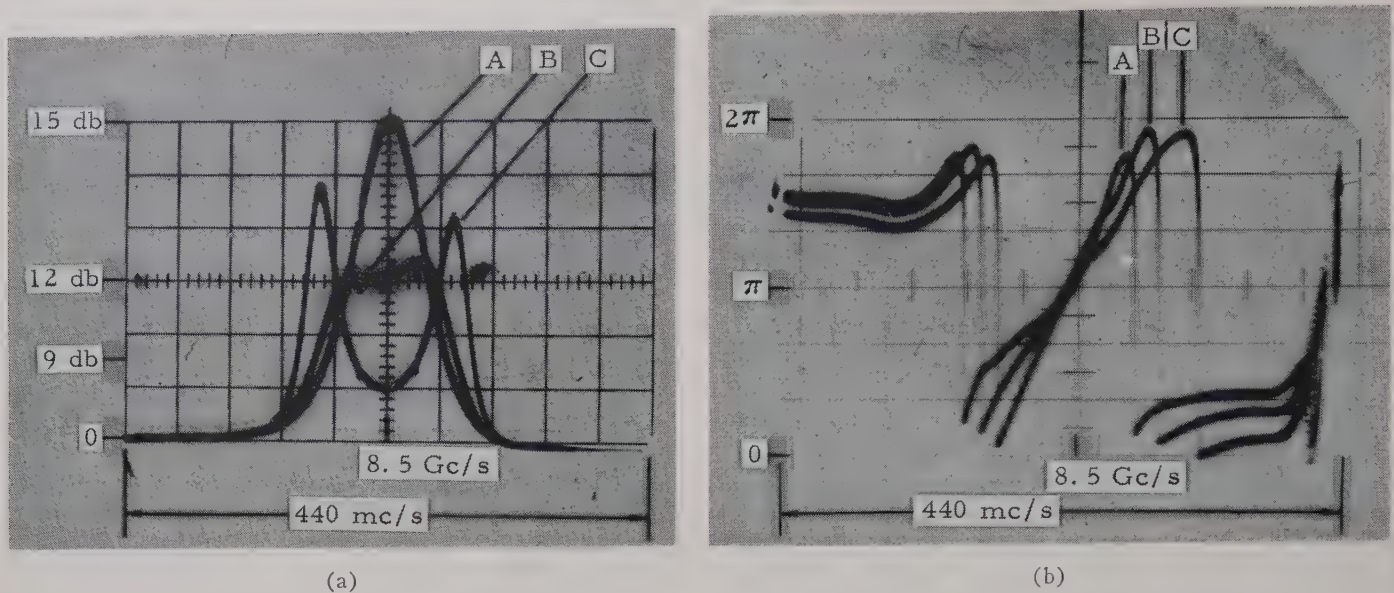


Fig. 11—Transmission gain and phase as a function of frequency for three conditions of input coupling. (a) Gain. (b) Phase.

In Figs. 7 and 8 the upper phase curve is associated with the functioning amplifier, while the lower phase curve is for the transducer's cavity response without pump power. Note the $\pi/2$ shift at midband, which is to be expected from (27) and (29). The amplifier gain response in Fig. 8 for approximate critical coupling between ω_1 and ω_2 circuits is shown again in Fig. 10 with a sweep display width of 1.4 Gc. The two left scale traversals show the dispersion in the phase bridge which is the result of only crude compensation of coaxial components and helix in the TWT single sideband modulator. In Fig. 9 the amplifier shows separate responses for ω_1 and ω_2 , and the corresponding phase curve unfortunately has the scale traversals aligned with the amplifier response. The gain and phase response for three successive degrees of coupling are shown in Fig. 11 in which the phases remain unchanged at $\delta_n = 0$. Similar results are observed when the ω_3 loading is altered.

The short-time stability of the phase-measuring system shown in Fig. 5 was observed to be less than one degree. No particular effort was made to stabilize the pump frequency, the signal frequency, or the TWT frequency translator.

When the conditions for coherent phase measurements are fulfilled in a monopulse receiver, the unpredictable variations of the differential phase stability between parametric transducers is inherently so small as to be unmeasurable.

V. CONCLUSION

The transmission-phase relations have been written for four-frequency parametric transducers for various modes including the effects of varactor losses and cavity detuning. Four-frequency parametric transducers were considered because they encompass both the negative-conductance and frequency-conversion mechanisms of parametric amplification. These relations are also valid for the three- and two-frequency modes. At midband these relations reduce to simple, easily remembered equations which are valid for any type of nonlinear pumped circuit element.

The application of parametric transducers to monopulse systems because of their low-noise properties has been emphasized. There are other properties of parametric transducers that can be effectively applied to phase-sensitive systems. For example, if coherence between information channels is maintained by fulfilling the stated conditions, an array of radiators and parametric transducers may be scanned by appropriate phasing in the pump distribution.

A wideband differential phase bridge has been used to investigate the transmission phase properties of various parametric transducer modes. Midband transmission-phase relations have proved useful in the analysis of phase-sensitive instrumentation. The observed results vary in the manner predicted. The experimental results suggest that parametric transducers are ideally suited for phase-sensitive systems.

A Plasma Guide Microwave Selective Coupler*

W. H. STEIER† AND I. KAUFMAN‡, MEMBER, IRE

Summary—A new type of microwave coupler has been investigated in the X-band and S-band ranges. In this coupler, a gas discharge tube passes through two rectangular waveguides that are separated by some distance. A metal cylinder surrounds the discharge tube in the separation space. The coupling of microwave power via this plasma guide coupler can be varied electronically over a range greater than 30 db. Pulsed power levels of more than 100 w can be handled. When operated as a switch, a switching time of from 2 to 5 μ sec has been observed. This paper describes some of the operating characteristics that have been observed, an approximate theory of operation, and measurements pertinent to a complete description of the coupler.

I. INTRODUCTION

THE use of gas discharges as switching and attenuating elements has been investigated in detail in the development of TR tubes for radar applications.¹ In the main, these devices depend on a gas discharge struck across a waveguide to effectively short it; or if the system is coaxial, a discharge is struck across a gap in the center conductor.²⁻⁴ Another type of device that was investigated earlier depends on the fact that a hollow waveguide containing a plasma has a higher cutoff frequency than in the absence of the plasma; so that the plasma can be used to control the cutoff frequency, and thereby the transmission, of the waveguide.^{5,6} Both types of devices are two-port elements, in which the input microwave power is either reflected from or transmitted through the region containing the discharge. The plasma guide coupler described here is different from this class of devices, in that the microwave energy is first coupled out of an input waveguide onto a coupling waveguide containing a plasma column. The energy propagates along the plasma column to a second, output waveguide. Unlike the hollow wave-

guide, the coupling guide depends on the presence of the plasma column to transmit energy. The wave propagating properties of the plasma column are dependent on the plasma density. Since the plasma density is easily controlled by dc or pulsed circuitry, the amount of power coupled from input to output is readily controlled by external means. Although it is possible to further control the propagating characteristics by a variable magnetic field, this method will not be discussed in this paper. Because input and output waveguides are physically separated, very high isolation between input and output is possible when the plasma guide is in the nonpropagating condition. This paper presents results of an exploratory investigation of plasma guide couplers.

Since the plasma guide coupler employs the unique cutoff properties of the space-charge waves on a plasma column to selectively couple microwave energy, some of the basic properties of the plasma guide modes are described before considering the device itself.

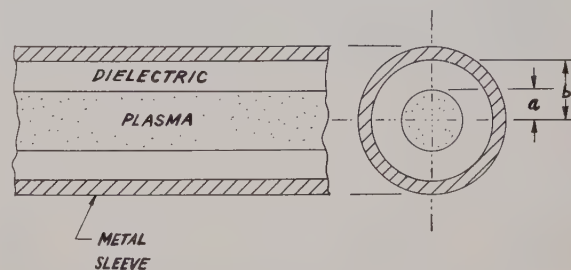


Fig. 1—Plasma guide transmission line.

II. PLASMA GUIDE MODES

The wave-propagating properties of a stationary plasma column have been investigated by Trivelpiece and Gould.⁷ They have shown that a plasma column surrounded by concentric dielectric and metal sleeves (as in Fig. 1) can propagate electromagnetic energy provided the plasma density is sufficiently high. The modes of propagation considered are electromechanical in nature and are quite different from the modes of a hollow circular waveguide perturbed by a plasma column. These plasma guide modes are space-charge waves, in which the electron density within the plasma column or on its surface is modulated as the wave passes.

In the absence of any dc magnetic fields, the plasma guide modes are essentially surface waves and can exhibit slow wave properties. In the analysis it is assumed

* Received by the PGMTT, May 1, 1961; revised manuscript received, September 5, 1961.

† Consultant to Space Technology Labs., Inc., Canoga Pk., Calif. Present address: Ultramicrowave Group, Dept. of Elec. Engrg., University of Illinois, Urbana, Ill.

‡ Space Technology Labs., Inc., Canoga Pk., Calif.

¹ For an example, see L. N. Ridenour, "Radar System Engineering," McGraw-Hill Book Co., Inc., New York, N. Y., pp. 407-411; 1947.

² L. Goldstein and N. L. Cohen, "Radiofrequency conductivity of gas-discharge plasmas in the microwave region," *Phys. Rev.*, vol. 73, p. 83; January, 1948.

³ P. Rosen, "The propagation of electromagnetic waves in a tube containing a coaxial d.c. discharge," *J. Appl. Phys.*, vol. 20, pp. 868-877; September, 1949.

⁴ D. Kerr, S. C. Brown, and W. P. Kern, "Microwave studies of the dielectric properties of arcs," *Phys. Rev.*, vol. 71, p. 480; April 1, 1947.

⁵ L. Goldstein and N. L. Cohen, "Behavior of gas discharge plasmas in high frequency electromagnetic fields," *Elec. Commun.*, vol. 28, pp. 305-321; December, 1951.

⁶ D. H. Pringle and E. M. Bradley, "Some new microwave control valves employing the negative glow discharge," *J. Electronics*, vol. 1, pp. 389-404; January, 1956.

⁷ A. W. Trivelpiece and R. W. Gould, "Space charge waves in cylindrical plasma columns," *J. Appl. Phys.*, vol. 30, pp. 1784-1793; November, 1959.

that the collision frequency ν_c is zero. The modes exist therefore only when the operating frequency $\omega \gg \nu_c$. Because propagation is at a phase velocity less than the velocity of light, the fields inside the plasma are described by modified Bessel functions of the first kind:⁸

$$E, H \propto I_n(\gamma r) e^{in\phi} e^{j(\omega t - \beta z)}. \quad (1)$$

In the dielectric region, the fields are given by a sum of modified Bessel functions of the first and second kinds:

$$E, H \propto [AI_n(\gamma_0 r) + BK_n(\gamma_0 r)] e^{in\phi} e^{j(\omega t - \beta z)}. \quad (2)$$

Here,

$$\begin{aligned} \gamma_0^2 &= \beta^2 - \omega^2 \mu_0 \epsilon_0 K_e \\ \gamma^2 &= \beta^2 - \omega^2 \mu_0 \epsilon_0 + \omega_p^2 \mu_0 \epsilon_0; \end{aligned} \quad (3)$$

μ_0, ϵ_0 = constants of free space,

ω_p = plasma angular frequency— $\omega_p = 5.6 \times 10^4 \times (\text{number of electrons/cc})^{1/2}$,

K_e = dielectric constant of the dielectric sleeve,

A, B = constants determined from the characteristic equation, and

ω = operating frequency.

Propagation can take place in both symmetric modes and in modes with angular variation. Trivelpiece and Gould have computed the frequency-phase ($\omega - \beta$) characteristics of the E -mode solution for circularly symmetric waves. To demonstrate the property of density-controlled propagation characteristics, the $\omega - \beta$ plot of Fig. 2 has been repeated from their paper. Fig. 2 corresponds to the axially symmetric E -mode solution for a plasma column of radius a in an infinite vacuum dielectric; c is the velocity of light. It is seen that a cutoff frequency, at which βa approaches infinity, exists for each value of the plasma frequency ω_p . Above this frequency, no wave propagation in the manner of the plasma guide can take place. Conversely, in order to achieve propagation at a particular frequency ω , it is necessary to raise the plasma frequency (by increasing the plasma density) above a cutoff level. As the plasma density is raised to extremely high values, propagation occurs at the velocity of light; so that the plasma guide behaves as an unloaded coaxial line.

In addition to the axially symmetric mode, it is possible to achieve propagation in modes with angular variation. It is, indeed, the mode of one angular variation which chiefly concerns us in this paper. Here, as in most dielectrically-loaded structures, the nonsymmetric modes are hybrid, *i.e.*, both E_z and H_z are required to satisfy the boundary conditions. Because of this property, the propagation constant and the field distribution become difficult to evaluate and no numerical computations have been done.

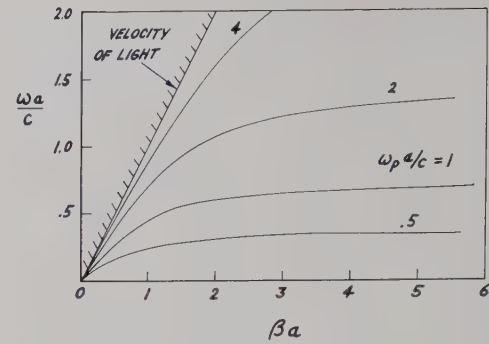


Fig. 2—Phase characteristics for axially symmetric mode; $b/a = \infty$ (after Trivelpiece and Gould).

By using the large argument approximations for the Bessel functions, Trivelpiece has shown that this cutoff plasma frequency for both the symmetric and non-symmetric modes is given by⁹

$$\omega_p = \omega [1 + K_e]^{1/2}. \quad (4)$$

The space-charge waves can propagate for densities greater than the above; for lower densities the modes are cut off. In practice, the plasma guide transmission line need not have the dielectric tube completely filling the metal sleeve, but an air region can exist between dielectric and metal cylinders. The cutoff plasma frequency for this configuration is also given by (4), since for very large values of βa the field exists chiefly in the vicinity of the plasma-dielectric interface.

In the above discussion of the loss-free plasma, we have seen the possibility of either propagation or reactive attenuation. We are also interested in resistive attenuation. This is due to loss of the coherent energy imparted to the plasma electrons by collisions with other particles and with the walls.

This attenuation is of greatest importance in the propagating region near cutoff. For a general transmission system, the attenuation constant is given by

$$\alpha = \frac{W_L}{2Uv_g}, \quad (5)$$

where

W_L = average power lost per unit length,

U = energy stored per unit length, and

v_g = group velocity.

Since W_L and U both vary approximately as the square of the field intensity, α varies inversely with group velocity. Thus, since the group velocity is very small near cutoff, and since it can be varied by change of the ratio ω/ω_p , the plasma coupler can be used as a variable attenuator.

In summary, therefore, we can state that the cutoff frequency of a given plasma guide is affected by the

⁸ S. Ramo and J. R. Whinnery, "Fields and Waves in Modern Radio," John Wiley and Sons, Inc., New York, N. Y., 2nd ed., pp. 412-413; 1953.

⁹ A. W. Trivelpiece, "Slow Wave Propagation in Plasma Waveguides," California Inst. of Tech., Pasadena, Nonr 220(13) Tech. Rept. No. 7; May, 1958.

plasma density in the plasma column. Since this plasma density can be changed by external electronic methods, the plasma guide has the property of possessing a cut-off frequency controllable by external electronic apparatus. It is this property that is employed in the plasma guide coupler to make an electronically-controlled microwave variable attenuator or switch.

III. PLASMA GUIDE SELECTIVE COUPLER

A. Description

The construction of a typical coupler is shown in Fig. 3. The discharge tube passes through the two narrow walls of each waveguide. The center section, which is the plasma guide, is surrounded by a metal sleeve. Coupling occurs between waveguides when the plasma density in the column exceeds the critical density, given in terms of the plasma frequency approximately by (4).

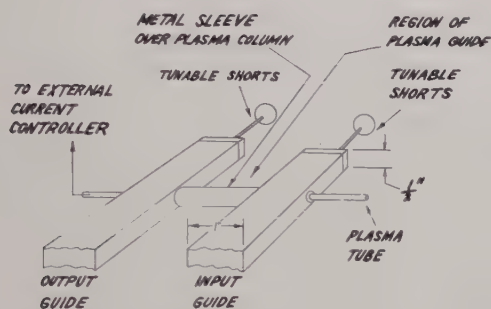


Fig. 3—Plasma guide microwave selective coupler.

In the majority of the experiments, the discharge tube used a mercury pool cathode of the type described by Dattner.¹⁰ In more recent experiments, a thyratron-type hot-cathode tube has given satisfactory results at S band. The plasma tube was made of quartz. Tubes of both 8 mm O.D., 6 mm I.D., and 7 mm O.D., 5 mm I.D. were used. The tubes were approximately 250 mm long. The spacing between input and output guides was not critical; distances from 0.7 to 4.5 in were found satisfactory.

As the plasma density gets very large, the properties of the plasma guide approach those of a coaxial line. If efficient high density coupling is to be obtained, the diameter of the metal outer sleeve must therefore be chosen so that the appropriate coaxial mode can propagate. This is true in spite of the fact that cutoff for the plasma guide is given by (4), which contains no dimension.

If the symmetric plasma guide mode is excited, there is no dimensional restriction, just as in TEM mode propagation along a coaxial line. For the couplers described here, however, a mode with one angular variation is excited, and hence the outer dimension must be large enough to allow for the coaxial TE₁₁ mode. Furthermore, if no low current coupling is desired, the di-

ameter of the outer sleeve chosen must also be small enough to prevent propagation in the circular waveguide TE₁₁ mode.

The pressure of mercury in the discharge tube is controlled by the temperatures of the pool cathode and of the discharge tube. By measurements of these temperatures, this pressure was found to be approximately 0.08 mm Hg during the conditions of coupling reported on here.

B. Coupling

A composite CRO trace of the coupled microwave power vs plasma density, or discharge current, is shown in Fig. 4. The display was obtained by sweeping the plasma tube current with a 60-cycle supply, in series with the dc supply of the tube, from 0.1 to about 2.0 a. The input 8.35-Gc microwave power was square-wave modulated to give the base line trace in each display. The metal sleeve around the discharge tube was made tight fitting, so that no hollow waveguide modes could propagate between the guides at the operating frequency.

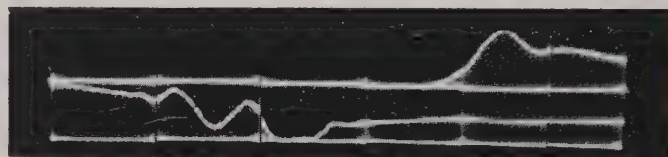


Fig. 4—Display of coupled power (top) and power transmitted past plasma in input guide (bottom) vs plasma current. Minimum current = 0.1 a; maximum current = 2.0 a.

The top of Fig. 4 is a display of the power coupled to the output waveguide. In the transition region, where the plasma guide is beginning to conduct, the device can be used as a variable attenuator with a dynamic range exceeding 30 db by electronically varying the discharge current. By operating at two discrete densities, one above and one below cutoff, the device can be used as a microwave switch.

The bottom trace of Fig. 4 is a display of power transmitted past the plasma tube in the input guide. Here the tunable short of Fig. 3 was replaced by a crystal detector. The resultant spectrum is a display of the Tonks-Dattner dips,^{10,11} that are associated with plasma resonance and are discussed below. It is of interest to note that power transmission along the plasma guide occurs only at currents exceeding those at the plasma resonance dips.

A number of workers have observed oscillations in a plasma column, that have characteristic frequencies of 100 kc to 1 Mc. For the currents used in the X-band coupler, none of these plasma oscillations were observed. They were, however, evident at lower currents.

The insertion loss of the coupler in the X-band range,

¹⁰ A. Dattner, "The plasma resonator," *Ericsson Technics (Stockholm)*, vol. 13, no. 2, pp. 310-350; 1957.

¹¹ L. Tonks, "The high frequency behavior of a plasma," *Phys. Rev.*, vol. 37, pp. 1458-1483; June 1, 1931.

when the plasma was in its state of maximum coupling, was on the order of 12 to 15 db when no attempts at impedance matching were made. It appears that this relatively high insertion loss is due to poor coupling of the microwave elements, not to attenuation along the plasma column, since no appreciable attenuation of this type was found in field measurements along the column. The use of matching vanes in the input and output guides reduced the insertion loss to 8.5 db. A further reduction is probably possible with still better impedance matching.

In an alternate method of coupling between two guides, which has been observed earlier,¹² the plasma column is inserted through the broad walls of the guides. The variation of coupled power with discharge current in this arrangement is essentially the same as Fig. 4. The minimum insertion loss for this type of structure, however, could not be reduced below 15 db, even with the use of ridged waveguides for impedance matching.

The S-band coupler exhibited essentially the same coupling variation as the X-band device. The maximum coupling observed with no impedance matching vanes was -11 db.

The field measurements indicated that very little attenuation exists along the plasma column when it is in a state of high coupling. It would be of interest to see if this was to be expected from data of collisions in the plasma. Trivelpiece⁹ has suggested that the attenuation constant α is given, approximately, by

$$\alpha \simeq \frac{\nu_c}{v_g}, \quad (6)$$

where ν_c is an effective collision frequency, and v_g is the group velocity. This collision frequency is given, approximately, by the sum of collision frequencies of electrons with neutral molecules (ν_{eo}), with ions (ν_{ei}), and with the walls of the container (ν_{ew}).

Based on temperature measurements of mercury pool (76°C) and coupling tube (157°C), the following results were found for an X-band coupler while in a state of high coupling:¹³

Gas pressure: 0.08 mm Hg

Electron temperature: 2×10^4 °K

Ion density: $2 \times 10^{13}/\text{cm}^3$

Neutral molecule density: $2 \times 10^{15}/\text{cm}^3$

ν_{eo} : 1160 Mc

ν_{ei} : 110 Mc.

The electron wall collision frequency was estimated

as the ratio of average electron thermal velocity to discharge tube diameter. This results in

$$\nu_{ew} \simeq 160 \text{ Mc.}$$

It is seen that under these conditions electron-molecule collisions dominate.

Based on these calculations, and from (6), the attenuation constant is 0.4 db/cm, so that the attenuation in a 2-in length coupler should be 2 db. These results indicate that a short coupling tube at high densities should indeed exhibit low attenuation as observed.

C. Cutoff Plasma Density Measurements

Eq. (4) predicts the cutoff plasma frequency, or plasma density for coupling, at a given frequency. To verify that the space-charge modes are the mechanism of coupling, measurements of the cutoff plasma density were made, using the Tonks-Dattner dips mentioned above. Boyd¹⁴ has demonstrated this to be a satisfactory method of measuring the average plasma density, by correlation with other techniques.

The physical arrangement for making these measurements is shown in Fig. 5. The input guide, on the left, was supplied with X-band power at the signal frequency. The cylindrical section is the plasma guide and the center waveguide is the output. The probe shown inserted in the cylinder was used for measurements of the angular distribution of the fields as discussed below. The third rectangular waveguide was supplied with power from a second microwave source at the probing frequency. The probing frequency was tuned until the main Tonks-Dattner dip occurred at the same discharge current as the onset of coupling to the output guide at the signal frequency.

The plasma frequency was then calculated from the measured Tonks-Dattner frequency by

$$f_p = [1 + K_{\text{eff}}]^{1/2} f_{T-D}. \quad (7)$$

For the geometry of Fig. 6 a quasi-static analysis yields¹⁵

$$K_{\text{eff}} = K_e \left\{ \left(\frac{b}{a} \right)^2 \left[K_e + 1 - \left(\frac{b}{d} \right)^2 (K_e - 1) \right] - \left[K_e - 1 - \left(\frac{b}{d} \right)^2 (K_e + 1) \right] \right\} \cdot \left\{ \left(\frac{b}{a} \right)^2 \left[K_e + 1 - \left(\frac{b}{d} \right)^2 (K_e - 1) \right] + \left[K_e - 1 - \left(\frac{b}{d} \right)^2 (K_e + 1) \right] \right\}^{-1}, \quad (8)$$

¹² T. Sekiguchi and R. C. Herndon, "Thermal conductivity of an electron gas in a gaseous plasma," *Phys. Rev.*, vol. 112, pp. 1-10; October 1, 1958.

¹³ Collision cross sections were obtained from "The American Institute of Physics Handbook," "Handbuch der Physik," McGraw-Hill Book Co., Inc., New York, N. Y., 1957; and from Band XXII, Springer-Verlag, Berlin, Germany, 1956.

¹⁴ G. D. Boyd, "Experiments on the Interaction of a Modulated Electron Beam with a Plasma," California Inst. of Tech., Pasadena, Nonr 220(13) Tech. Rept. No. 11; May, 1959.

¹⁵ R. W. Gould, private communication.



Fig. 5—Plasma coupler, with third waveguide for probing plasma density.

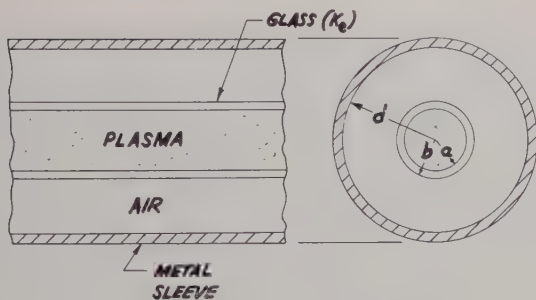


Fig. 6—Three-region cross section.

where

- K_e = relative dielectric constant of the discharge tube,
- a = plasma radius,
- b = plasma tube outer radius, and
- d = metal tube inner radius.

The upper and lower waveguide walls will exert nearly the same influence on the resonance as the outer metal cylinder of Fig. 6. In using (7) to determine f_p by the measurement of f_{T-D} , the geometric mean of the values of $[1 + K_{eff}]^{1/2}$ computed from (8) for the two cases of $d = \infty$ and $d = 5$ mm was therefore used.

The experimental points are plotted in Fig. 7. They cluster about the dashed straight line that lies considerably below the theoretical line computed from (4). This discrepancy between measured and theoretical plasma frequencies at cutoff has also been observed by Trivelpiece,⁹ who explained it on the basis of a radial density variation in the plasma. A density variation introduces an error because the cutoff frequency is determined by the density at the edge of the plasma, while f_{T-D} measurements are of the average plasma density.

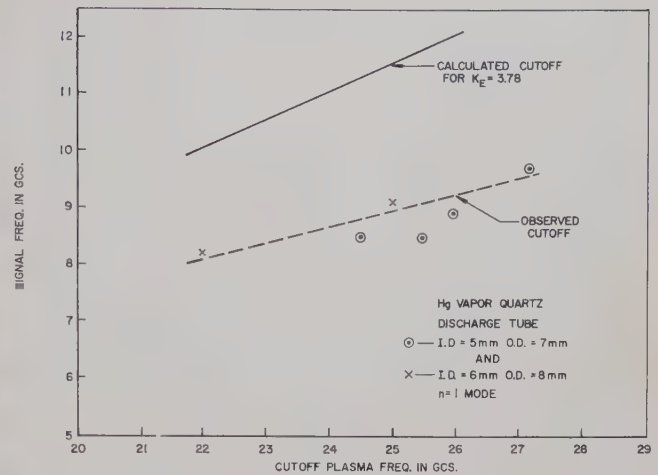


Fig. 7—Cutoff plasma frequency vs signal frequency.

The scatter of points about the dashed line is probably due to the limits on experimental accuracy imposed by the width of the main dip and the temperature fluctuations along the tube.

It should be pointed out that because no attempts were made to accurately control the temperature along the plasma tube, there are definite limitations on the experimental accuracy. The results do, however, correlate with the space-charge wave theory sufficiently to verify the mode of operation of the plasma guide coupler.

D. Wavelength Measurements

Trivelpiece and Gould show that the plasma guide modes have slow wave properties. For plasma densities just above cutoff, the guide wavelength should be very small; at high densities, propagation approaches that in a metal rod coaxial guide. As a further verification of the space-charge wave theory of operation of the coupler, wavelength measurements were made along the plasma at various discharge currents or plasma densities.

For wavelength measurements, the output guide was removed and a movable coaxial metal plunger was inserted in the air region between the quartz tube and the metal outer conductor. A fixed probe was inserted through this outer conductor between input guide and plunger to measure the radial electric field. The readings of the fixed probe plotted against the plunger position give the wavelength at a given discharge current.

Fig. 8 shows the wavelengths as measured on the 5 mm I.D., 7 mm O.D. quartz tube with 25.3 mm I.D. outer conductor. As shown in Section III-E, the mode excited has one angular variation. The data were taken at a fixed signal frequency of 8.50 Gc.

The results behave in the manner predicted by the space-charge wave theory. At high currents the wavelength approaches that for the TE_{11} mode on a coaxial line as expected. At lower densities the wavelength de-

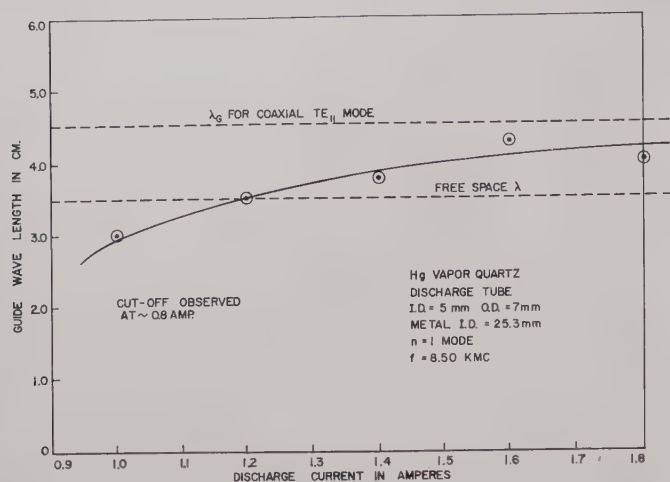


Fig. 8—Measured wavelengths along the plasma column as a function of the discharge current.

creases, showing the slow wave properties near cutoff. Unfortunately, it was not possible to obtain wavelength measurements any nearer to cutoff because of the high attenuation along the plasma guide in this region.

E. Angular Distribution

From the field pattern of the rectangular waveguide, it is to be expected that when the plasma tube is inserted through the narrow walls, the principal mode excited on the plasma coupler should have one angular variation. This was indeed found to be the case. Measurements were made at X band with the probe shown in Fig. 5 as the metal sleeve into which it was inserted was rotated.

Contrary to expectations, a mode with one angular variation was also excited when the plasma column was passed through the broad walls of the rectangular guide. This is apparently because negligible power passes beyond the plasma tube in the exciting guide during conditions of strong coupling. The method of excitation is then shown in Fig. 9(a), so that the plane of maximum transverse E field should be as shown in Fig. 9(b). Results of the probe measurements, in Fig. 9(c), show this to be the case. The slight asymmetry in the field pattern is perhaps due to imperfect alignment, or to the presence of other modes that were also excited.

F. Operation as Microwave Circuit Element

1) *Pulsed Operation*: The coupler was operated as a microwave switch by holding the discharge current at a quiescent value below cutoff. A pulse of voltage was then applied to the discharge tube to increase the plasma density and turn the switch on. Fig. 10 shows the results of applying a 2- μ sec, 44-v pulse to the anode of the X-band coupler. Here the top trace is the voltage supplied by the pulser, the center trace the discharge pulse current (2 a), and the bottom trace the microwave power in the output guide. The switching time is about 5 μ sec. A switching time of 2 μ sec was observed in the

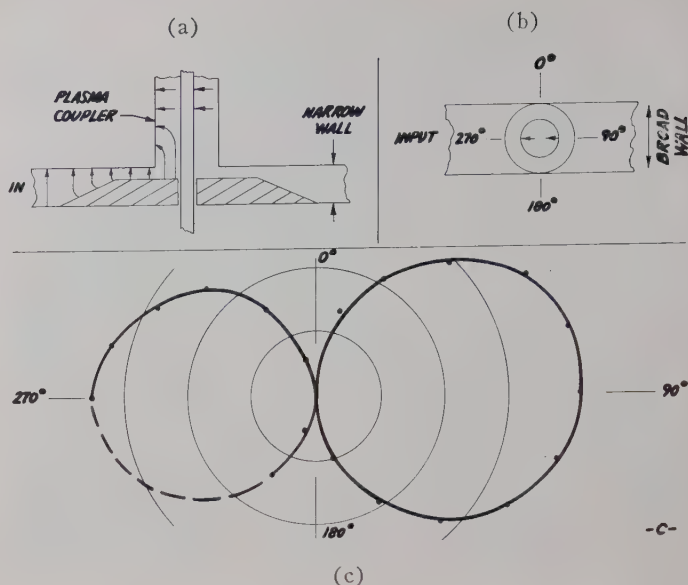


Fig. 9—Angular field distribution for coupling through broad wall. (a) Origin of fields in coupler. (b) Orientation. (c) Field pattern.

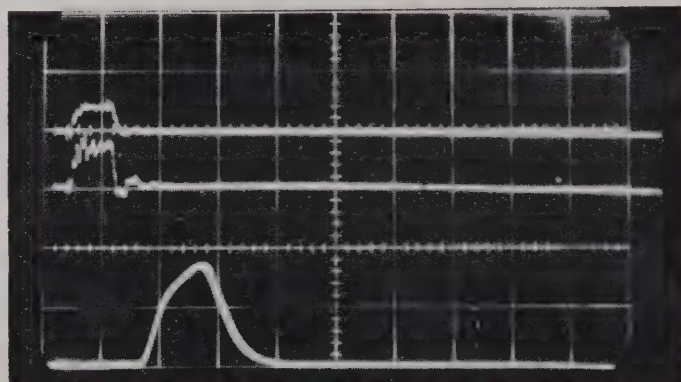


Fig. 10—Response of plasma coupler to 2- μ sec voltage pulse. Top trace: voltage pulse (44 v), center: current pulse (2 a), bottom: detected microwave pulse in output guide, frequency, 8.2 Gc; quiescent discharge current, 0.31 a; time scale, 2 μ sec/div.

S-band coupler, using a hot cathode tube.

2) *Power-Handling Capability*: The microwave-power-handling capabilities of the variable coupler are limited by the ionization caused by the incident microwave power. If too large an amount of microwave power is fed into the input, it can cause an increase in plasma density sufficient for continuous conduction. The CW operation of the coupler was at the milliwatt level, which caused no problem. In a test of operation as a switch, it was found that 128 w of pulsed X-band power could be handled with 30 db of isolation. The power-handling ability could be increased somewhat by operating at a lower quiescent discharge current, but then more switching power was required.

3) *Bandwidth*: No attempt has yet been made to investigate the bandwidth characteristics of the plasma guide coupler in detail. However, the individual couplers have been operated over a considerable portion of the X- and S-band ranges, although in each case

tuner adjustment was required across the band for maximum output. The final bandwidth of the device will be largely determined by the frequency sensitivity of the impedance match from the rectangular guide to the plasma guide.

IV. ON-OFF-ON OPERATION

In a second method of operation, the plasma guide coupler can be made to alternately couple, attenuate, and couple power as the discharge current is monotonically increased. In this case, the metal sleeve around the plasma column is made large enough in diameter so that the TE_{11} circular hollow metal waveguide mode can propagate. At very low densities, power is coupled between the input and output guides via this TE_{11} mode. As the density is increased, the cutoff frequency of this mode is increased, similar to that of a plasma-filled rectangular waveguide.^{5,6} When this cutoff frequency passes beyond the operating frequency, propagation ceases and the guides are decoupled. In this transition region the plasma coupler again becomes an electronically-controlled attenuator or switch. As the discharge current is increased still further, the plasma column will again start propagating, but now in the space-charge modes described earlier. If the current is increased still further, the guides will continue to be coupled via these plasma guide modes.

This mode of operation was observed at 9.3 Gc when the diameter of the metal sleeve was made 2.16 cm.

V. HIGH-POWER DETECTION OF MICROWAVES

The properties of the plasma guide can be demonstrated further in connection with a nonlinear plasma property. By observing the pulsed voltage across a resistor in series with the plasma tube, the system becomes a high-level detector of pulsed microwaves,¹⁶ the sensitivity of which is related to the plasma guide properties. Detection is due to the increased ionization caused by the microwave power absorbed in the plasma. This extra ionization causes an increase in the discharge current with a resultant voltage pulse on the series resistor.

Fig. 11 shows a series of oscilloscope displays of detected pulses at various quiescent discharge currents for the X-band detector, with constant pulsed 35-w input power of 2- μ sec duration. The characteristic 100-kc to 1-Mc plasma oscillations mentioned earlier are evident in the 0.1 to 0.3-a range. The detection sensitivity is summarized in the plot of detected output voltage vs discharge current (Fig. 12). In another test with different levels of power, the minimum detected power was 2 w; the maximum 1.2 kw.

The sensitivity of the detector is a function of the volume of plasma into which the microwave power can penetrate. In the region above plasma guide cutoff,

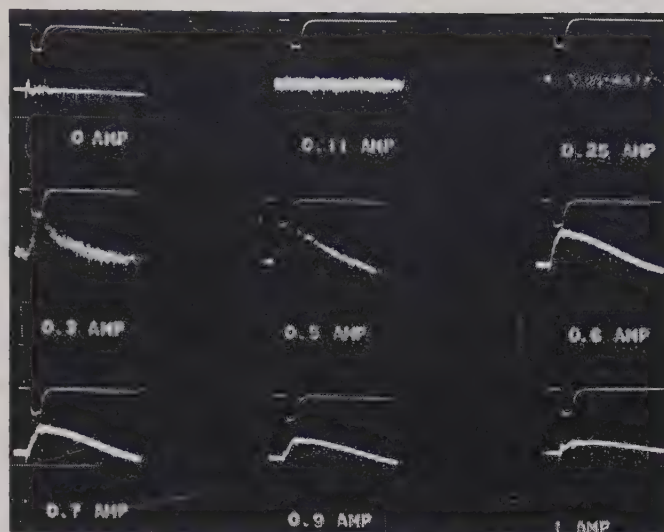


Fig. 11—Input microwave power pulse (top traces) and detected voltage pulse at several values of discharge current.

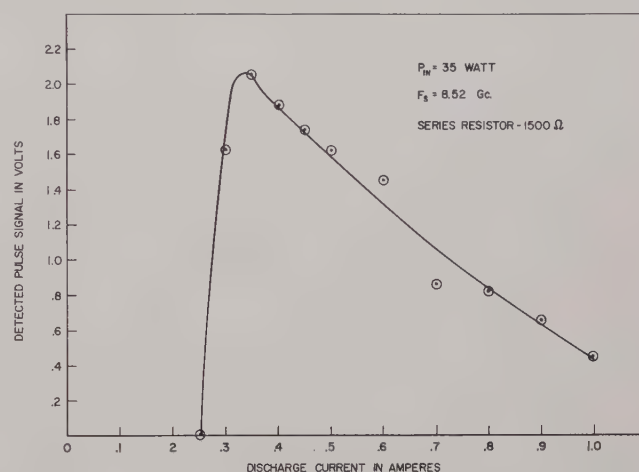


Fig. 12—Detector sensitivity as a function of discharge current.

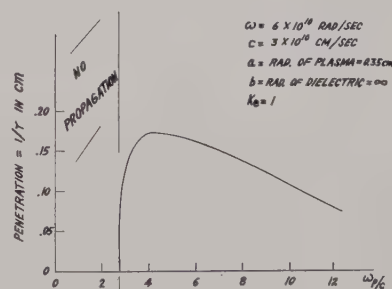


Fig. 13—The variation in radial penetration of the microwave fields into the plasma for a typical plasma guide.

where the energy can propagate along the plasma tube, this volume is determined by the radial penetration of the microwave fields. Fig. 13 shows the radial penetration as calculated from the space charge wave theory for a typical plasma guide. The shape of the curve agrees well with the observed variation in detector sensitivity.

¹⁶ See also, for example, B. J. Udelsion, "Effect of microwave signals incident upon different regions of a d.c. hydrogen glow discharge," *J. Appl. Phys.*, vol. 28, pp. 380-381; March, 1957.

VI. CONCLUSIONS

The use of plasma waveguides for coupling microwave energy from one rectangular waveguide to another has been demonstrated. These plasma guides require no dc magnetic field. Since their propagating characteristics may be altered by a change of plasma density, the coupling system becomes an electronically-controllable attenuator or switch. The operation has been demonstrated over a considerable portion of the X - and S -band ranges. The principles of this operation have been verified by measurements of both linear and nonlinear behavior. In operation as a fast microwave switch, switching times of the order of 2 to 5 μsec have been found.

During conditions of no coupling, very high isolation between waveguides exists. Minimum insertion loss during the condition of high coupling found to date has been 8.5 db. Additional work is therefore required on the circuit aspect of effecting broad-band, efficient coupling between rectangular and plasma waveguides. The

use of gases with lower collision frequencies than mercury should be considered, to reduce any losses along the plasma guide. Since this coupler operates in the transition region between the slow wave plasma modes and the coaxial metal waveguide, additional theoretical work on the propagating properties of plasma guides in this transition region is also required.

Finally, additional effort should be aimed at the production of plasmas whose densities can be controlled fairly accurately, if this type of coupler or switch is to find wide application. These can be gas discharge plasmas for the lower microwave frequencies and semiconductor plasmas for the higher ranges.

ACKNOWLEDGMENT

It is a pleasure to acknowledge helpful discussions with Dr. R. F. Wuerker, Dr. W. D. Hershberger, Dr. R. W. Gould, C. Leiby, and Dr. R. W. Fredricks. The assistance of R. P. Kemp in the laboratory is also very much appreciated.

High-Power Duplexers*

C. E. MUEHE, JR.†

Summary—The various circuit arrangements used in duplexers are analyzed in terms of their power-handling ability in two situations: first, where the bandwidth is narrow so that insertion loss determines maximum Q , and second, where large bandwidths are required and the maximum Q is determined by available Q bandwidth products. In both cases the ATR duplexer has an advantage. Arc loss was measured for folded cylinder TR tubes. At medium current densities the results agree well with experimental measurements in dc positive columns. At high current densities a constant conductivity is reached. Graphs of power-handling ability for a unity coupler duplexer using different methods of cooling are presented. It is shown that the requirements for easy firing and long life limit the achievable recovery time.

TWO recent survey articles^{1,2} discuss advances in microwave duplexer design that provide circuits with less low-level insertion loss and greater bandwidth and that provide TR tubes with lower-arc loss, less leakage to the receiver, faster recovery and longer

life. We will direct our attention to a problem that continues to plague duplexer designers—that of switching higher and higher powers while still meeting the requirements on insertion loss, bandwidth and recovery time. This problem concerns mainly the switching tubes (*i.e.*, the ones nearest the source of high power). It will be assumed that an adequate number of TR gaps or attenuators of one form or another follow the switching tubes in order to lower the leakage to an acceptable level.

We will first discuss the circuits in which the switching tubes are used, then arc-loss measurements and their interpretation, and finally, the effect of gas fill and geometry on gas breakdown and recovery time.

CIRCUITS

Fig. 1 shows a version of the common branched duplexer which consists of two cavities shunt-mounted on a transmission line. On transmit, gas in the gaps becomes ionized, the cavities are detuned and the transmitter power proceeds to the antenna with a small amount leaking through to the receiver. The equivalent circuit (see Fig. 1) shows that the cavity may be adequately represented by a certain (R/Q) value. The resistors R_1 represent the input and output impedances transformed

* Received by the PGM-TT, May 12, 1961; revised manuscript received, September 5, 1961.

† Lincoln Lab., Massachusetts Institute of Technology (with support from the U. S. Army, Navy and Air Force), Lexington, Mass.

¹ A. F. Harvey, "Duplexing systems at microwave frequencies," IRE TRANS. ON MICROWAVE THEORY AND TECHNIQUES, vol. MTT-8, pp. 415-431; July, 1960.

² A. M. Starik, "Principal directions in the development of antenna TR-switches," *Radiotekh. Elektron.*, vol. 5, pp. 1035-1051; July, 1960.

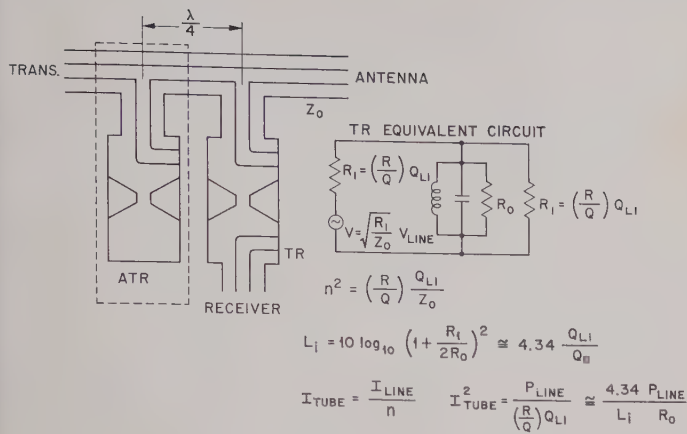


Fig. 1—Typical branched duplexer.

to the center of the cavity. When the discharge forms, represented by shorting the capacitor, a current I_{tube} flows through the discharge. The square of the tube current is inversely proportional to the (R/Q) value and the loaded Q_{L1} of the cavity. This fact emphasizes the first principle of high-power duplexer design: to reduce TR-tube current, with its consequent heating, place the discharge in as high Q structure as other system requirements will allow.

The square of the tube current may also be written (Fig. 1) as being inversely proportional to the allowable insertion loss on receive L_i and to the cavity-shunt-loss resistance R_0 . Therefore, for a narrow-band system, narrower than the bandwidth of the single cavities used, a compromise may be made between insertion loss on receive and tube dissipation on transmit.

On receive, the return signals pass from the antenna through the TR cavity into the receiver. The purpose of the ATR is to reflect any return signal that goes down the transmitter line. The quarter-wavelength spacing shown is necessary so that an open circuit will be presented by the transmitter line at the junction of the TR cavity and the main line. It can easily be verified that four times as much of the received energy incident on the ATR will be lost in the ATR cavity as compared to an identical TR cavity. However, since in this arrangement only one-fourth of the return signal is incident on the ATR, equal losses will be sustained in both TR and ATR cavity. (The foregoing statements assume that the transmitter presents a match or an open circuit at the junction of the ATR cavity and the main line.)

Fig. 2 shows most of the circuits used in present-day duplexers. The boxes labeled TR represent band-pass filters, which usually consist of one or more resonant elements in cascade either directly coupled or quarter-wave coupled. In the transmit condition these TR structures break down at their high-voltage points and the band-pass filter turns into a good reflecting structure. The boxes labeled ATR consist of a number of resonant cavities coupled to the transmission line at regular intervals. The ATR structures act as good reflectors on re-

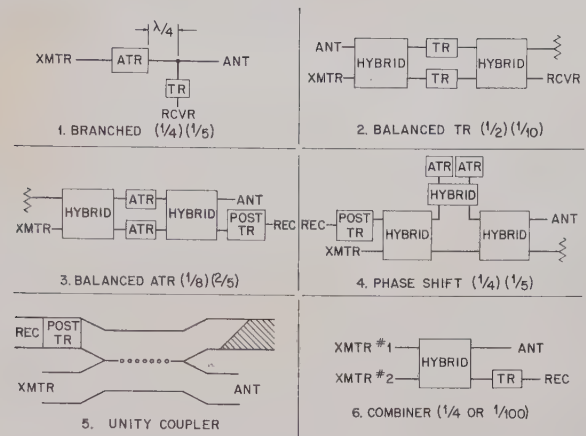


Fig. 2—Circuit arrangements for most duplexers in use at the present time.

ceive and as good transmission structures on transmit. The boxes marked "hybrid" are 3-db directional couplers.

The branched duplexer with single-cavity ATR and TR structures is illustrated in Fig. 1. Notice that on transmit, when the gap is discharged only one-fourth of the line power is incident on each cavity, since the wave incident on each cavity plus its reflection must add to the total line voltage at the junction on the main transmission line. The first bracketed term (one-fourth) states the portion of the line-power incident on the cavities making up the TR or ATR structure.

In the balanced TR³ duplexer the high power from the transmitter, after being divided in two by the first hybrid, is reflected directly off the TR cavities so that the first bracketed term is (one-half). For the balanced ATR⁴ case the transmitter power is first divided in two by a hybrid, then by one-fourth at the junction of the cavities with the main line, giving a first bracketed term of (one-eighth).

The unity coupler duplexers,⁵ constructed by putting TR tubes in the coupling aperture of a unity coupler, requires that the TR tubes carry the full current in the guide walls. It will not be compared with the other forms of duplexers.

Sometimes two transmitters are combined,⁶ as shown in the last duplexer circuit of Fig. 2. If the transmitters are well balanced in phase and amplitude, somewhat less than 1/100 of the line power will be incident upon the TR. However, in the event of failure of one of the transmitter tubes, the TR will have to handle one-fourth the line power, so it should be designed to stand this

³ L. D. Smullin and C. G. Montgomery, "Microwave Duplexers," M.I.T. Rad. Lab. Ser., McGraw-Hill Book Co., Inc., New York, N. Y., vol. 14; 1948.

⁴ C. W. Jones, "Broad-band balanced duplexers," IRE TRANS. ON MICROWAVE THEORY AND TECHNIQUES, vol. MTT-5, pp. 4-12; January, 1957.

⁵ L. Milosevic, "High-power duplexers," *Le Vide*, vol. 12, pp. 109-116; January/February, 1957.

⁶ K. Eakin and R. Rapiano, "A hybrid duplexer," *Microwave J.*, vol. 4, pp. 47-49; January, 1961.

power for at least a short length of time until the situation can be corrected.

COMPARISON FOR NARROW-BAND SYSTEM

The second bracketed term in each figure gives the fractional loss of the receive signal for each structure, assuming that all TR and ATR structures consist of single identical cavities with the same loaded and unloaded Q 's and that each TR cavity loses one-tenth of the signal passing through it. Thus, in the case of the balanced TR duplexer, the return signal splits in two in the hybrid and a tenth of each half is lost in each TR cavity, so that the total loss is one-tenth of the incoming signal. The interesting result is that the product of the incident power (first bracketed fraction) times the insertion loss on receive (second bracketed term) is the same for the first four duplexers. But, if we assume that the power-handling capacity and the insertion loss vary directly with the loaded Q of the cavities, so that if we readjust the Q 's of the various circuits to give equal insertion losses, then the power-handling capacity of all the structures will be the same. The assumption that power-handling capacity and insertion loss vary directly with the loaded Q is rigorously true for high Q cavities and approximately true for resonant windows.

This analysis is perhaps an oversimplification because it assumes single-cavity TR and ATR structures. With the ATR structures, however, it is possible to put two identical cavities a half-wavelength apart. Their conductances (resistances in series on the main line if they are series mounted) are thus in parallel on the main line so that the insertion loss on receive is halved. The total heat generated on transmit is doubled, of course, but it is distributed over twice the area.

COMPARISON FOR WIDE-BAND SYSTEMS

The balanced TR, balanced ATR and unity coupler duplexers are recommended for systems requiring wide instantaneous bandwidth. These duplexers take advantage of symmetry to avoid the necessity of using frequency-sensitive line lengths as in the branched and phase-shift duplexers. Since the TR structure is simply a band-pass filter on receive, filter theory may be employed to determine its characteristics. Fig. 3 shows the Q bandwidth products one can achieve. Belevitch⁷ assumes a Tchebycheff response function with as many points of perfect match as there are tuned circuits. Fano⁸ assumes no matched points in the pass band. The insertion losses are all reactive; any resistive-type insertion loss must be added to them.

The responses of several ATR structures are given by Jones.⁴ He considered cavities with typical resistive losses spaced at quarter- and half-wavelength intervals

along a waveguide. A simpler analysis has been carried out by the author wherein the equivalent low-frequency, lumped-constant circuits are considered. The analysis thus neglects the effect of the variation of phase angle between the cavities on the resulting insertion loss. It also neglects any resistive losses in the cavities. The results are presented in Fig. 4.

One mode of operation is to place the cavities a half-wavelength apart along the transmission line. The circuit then acts like a number of parallel resonant circuits in series with one another. They must all be tuned synchronously or, according to Foster's reactance theorem, there will appear points of zero impedance between the resonances. The insertion loss is a monotonically increasing function of frequency off resonance.

Alternatively the cavities may be spaced at quarter-wavelength intervals, in which case the equivalent circuit has alternate parallel resonant circuits in series with the line and series resonant circuits in parallel with the line. The best bandwidth is achieved by stagger-tuning the circuits. The power-loss ratio can be set equal to one plus a Tchebycheff function squared. In the two-cavity case, the cavities are tuned to $f_0(1 \pm B/2\sqrt{2})$, where f_0 is the center frequency and B is the fractional bandwidth. In the three-cavity case, the center Q is half the end cavity Q 's and is given by the Q_{L1} in Fig. 4. The

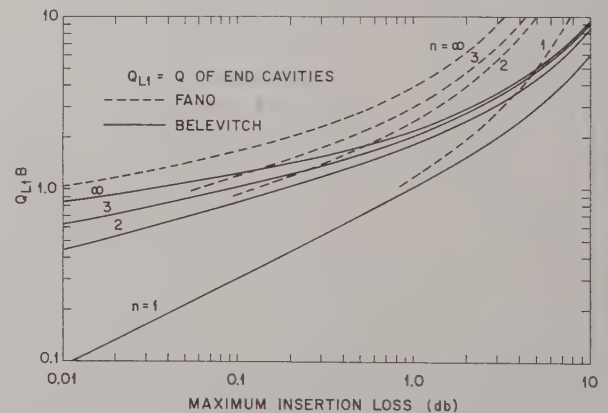


Fig. 3— Q -bandwidth products for TR structures with n -tuned circuits.

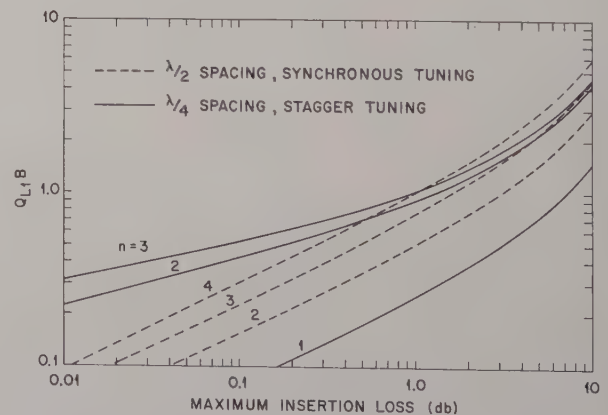


Fig. 4— Q -bandwidth products for ATR structures with n -tuned circuits.

⁷ V. Belevitch, "Tchebychev filters and amplifier networks," *Wireless Engr.*, vol. 29, pp. 106-110; April, 1952.

⁸ R. M. Fano, "Theoretical limitations of the broadband matching of arbitrary impedances," *J. Franklin Inst.*, vol. 249, pp. 139-154; January, 1950.

center cavity is tuned to f_0 and the end cavities to $f_0(1 \pm \sqrt{3}/4B)$.

In quarter-wavelength spacing, each cavity is more or less providing the reflection required in any one part of the band so that the resistive loss of one cavity must be added to the insertion losses of Fig. 4. When half-wavelength spacing is used, the resistive loss is that of one cavity divided by the number of cavities used.

A comparison of Figs. 3 and 4 shows that for two- and three-cavity structures, the ATR structure requires half the Q of the TR structure for the same bandwidth and insertion loss. However, since the incident power on the ATR cavities is only one-fourth that incident on the TR cavities, the former will still be able to handle twice the line power. A careful examination shows that the same total power is being dissipated, but it is spread out over more cavities by using the ATR structures.

DETERMINATION OF ARC LOSS

The two most commonly used high-power switch tubes are shown in cross section¹ in Fig. 5. Current is capacitively coupled from the metal frame through the dielectric into the discharge. One reason for this construction is the elimination of all metal from areas adjacent to the discharge. In high-power discharges, metal is sputtered over the inside of the tube and quickly destroys its usefulness. The encapsulated window consists of a glass enclosure for the gas, one side of which is bonded to a kovar frame. In the folded cylinder TR tube the discharge takes place in the annular space between two concentric dielectric cylinders. In both cases the discharge has the electrical conductivity of a poor metal.

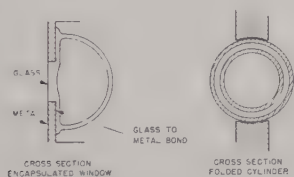


Fig. 5—Encapsulated window and folded cylinder TR tubes shown in cross section.

Arc loss may be measured using the apparatus shown in Fig. 6. The discharge tube is mounted so that the discharge completes the end of a multiple quarter-wavelength stub on a coaxial line. The resonant choke is used to confine the discharge to the desired region. In its absence the discharge would fill the entire TR tube, making computation of the discharge impedance difficult. The slotted line and directional coupler are used to measure the high-power standing-wave ratio and the magnitude of the power incident on the TR tube. Because the geometry of the discharge is well known, these readings are easily converted to the skin resistance and linear current density of the discharge. The component of the electric field in phase with the current is given by the product of skin resistance times linear cur-

rent density. A typical set of curves taken at 425 Mc is shown in Fig. 7. For low current densities the skin resistance is inversely proportional to linear current density, a fact that indicates a constant sustaining field. At a current density slightly above that at which the skin depth in the plasma equals the spacing in the tube, the skin resistance departs from a straight line. This is caused by the shielding action of the discharge.

The variation of electric field with current density is shown in Fig. 8. For medium current densities there are sufficient electron-electron collisions to insure a Maxwellian velocity distribution among the electrons. The electrons are produced by direct impact of high-energy electrons on gas molecules and are lost by diffusion to the walls. The conductivity of the plasma is directly proportional to the electron density. At higher densities where shielding occurs to give a nonuniform electric field, electron production is higher in regions of high

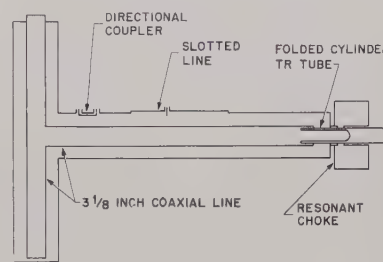


Fig. 6—Apparatus used to measure arc loss.

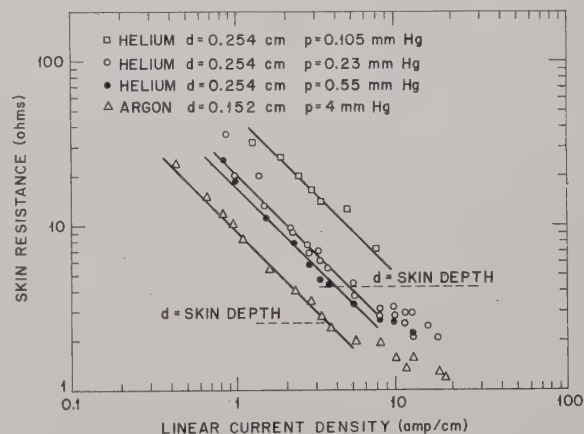


Fig. 7—Measured skin resistance as a function of linear current density for folded cylinders with spacing d and pressure p measured at 425 Mc.

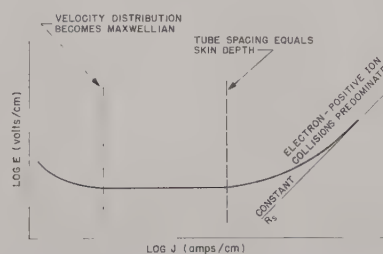


Fig. 8—Variation of the sustaining field with current in a folded cylinder TR tube.

field adjacent to one of the walls of the tube. Electrons are lost more easily by diffusion, which results in a higher sustaining field.

At still higher electron densities, the electron-positive ion collisions determine the conductivity of the plasma. The limiting value of conductivity (approached usually when the fractional ionization is between 10^{-3} and 10^{-2}) is that of a fully ionized gas.⁹ The conductivity depends on the ratio of electron charge density to collision frequency. The collision cross section for positive ions is much larger than for gas molecules; moreover, since the number of positive ions equals the number of electrons in the plasma, the ratio of electron charge density to collision frequency at high electron density will be a constant and thus will give a conductivity of about 2000 mho/m. (For comparison, copper has a conductivity of 6×10^7 mho/m.)

COMPARISON WITH DC DATA FOR MEDIUM CURRENT DENSITIES

Except for the shielding effect in the RF discharge, the conditions prevailing in the folded cylinder are exactly those existing in the positive column of a dc discharge at low pressure, for which considerable theoretical and experimental^{10,11} work has been done. The electric fields derived from the straight-line portions of the curves of Fig. 7 are compared with the measured fields in the dc-positive column in Fig. 9. The agreement is very good. In comparing the data for helium, Klarfeld states that at pressures slightly below the low-pressure end of his curves the sustaining field rises very rapidly, in agreement with the RF data.

Examination of dc data can now be used to determine the dissipation in the discharge when moderate current densities are involved. Notice that no polyatomic gases are shown in Fig. 9 because their sustaining fields are all above those of helium. In fact, it has been observed that even a trace of polyatomic gas in an inert gas discharge will increase the arc loss. One part in 10^8 of oxygen in argon has been found to double the arc loss. The reason for this is that polyatomic molecules have vibrational and rotational energy levels which are excited by electron collision, so that energy dissipation is higher than in the monatomic gases. For inert gases, dc data indicates that the heavier the molecules, the lower the sustaining field, and that some of the metal vapors, particularly mercury, look very promising. This is especially true in the case of tubes using diffusion as a recovery mechanism, since the pressure must be kept low where the problem of gas clean-up in inert-gas tubes is severe. Mercury offers what is an essentially infinite gas reservoir.

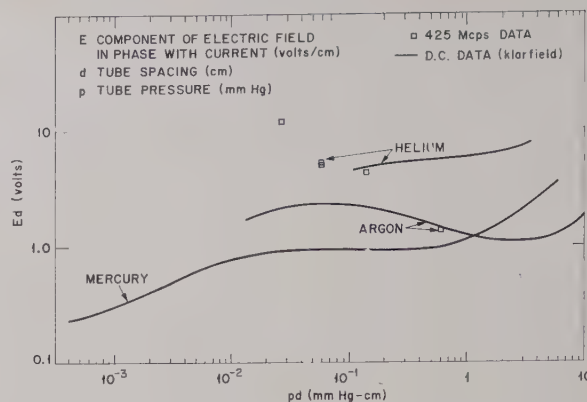


Fig. 9—Comparison between the sustaining field in an RF discharge and that in the positive column of a dc discharge.

POWER-HANDLING ABILITY FOR HIGH CURRENT DENSITIES

The lowest percentage arc loss occurs at high-power levels where the conductivity approaches a constant value, that of a fully ionized gas. Consider a rectangular waveguide of a 2:1 dimension ratio operating at a frequency where the guide wavelength is twice the width of the guide. A window (Fig. 10) is mounted in a long aperture made by cutting away the side wall of the guide. The window thickness is assumed to be one tenth the height of the guide and to make good thermal contact with the guide at its edges. Behind the window, just outside the guide, is a plasma with the conductivity of a fully ionized gas. The nature of the gas is not important except that lower pressures and gases which have lower sustaining fields will approach the fully ionized conductivity at lower current densities. The currents in the plasma are the same as in the guide wall.

Under these conditions, it is an easy task to calculate the heat dissipated in the plasma for a given power in the main guide. The power-handling capacity of such an arrangement depends on the method of heat transfer out of the discharge and the maximum allowable temperature rise. Results are presented (Fig. 10) for various types of surface cooling (solid lines) and for conduction cooling through the dielectric to the guide (dashed lines). Surface cooling means removal of heat from the surface of the window by forced air, radiation, or a liquid flowing across the surface of the window. Conduction cooling refers to transfer of heat out of the discharge by passage through the dielectric material of the window to the waveguide which is assumed to be held at room temperature. The peak window temperature was assumed to be 400° to 500°C because at these temperatures either the window material fails (glass deforms) or the loss tangent increases rapidly making the insertion loss on receive too large. The high power-handling capacity when aluminum oxide and beryllium oxide dielectrics are used is a reflection of their relatively higher heat conductivities.

It is to be emphasized that this graph applies to very wide-band duplexers operating at high peak power

⁹ L. Spitzer, "Physics of Fully Ionized Gases," Interscience Publishers, Inc., New York, N. Y., p. 81; 1956.

¹⁰ A. von Engel, "Ionized Gases," Oxford University Press, London, Eng., p. 209; 1955.

¹¹ B. Klarfeld, "The potential gradient in the positive column," *J. Tech. Phys. USSR*, vol. 5, pp. 725-740; September, 1938.

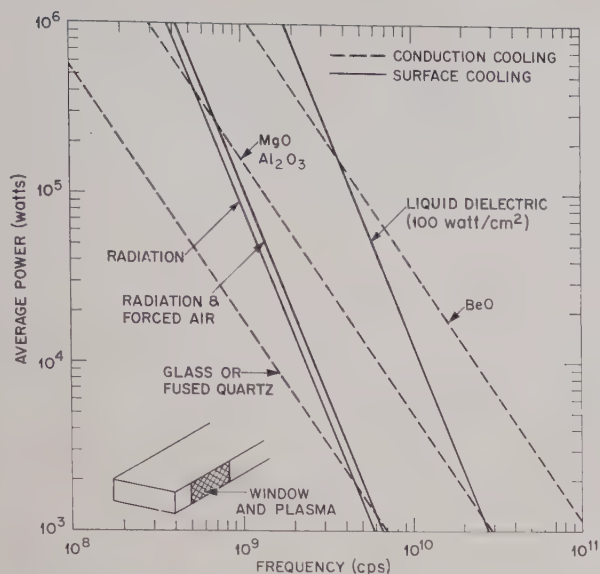


Fig. 10—Calculated power-handling capacity of a full size TR tube mounted in the side of a rectangular waveguide carrying the TE_{01} mode.

levels, such as the unity coupler duplexer. The power-handling of existing duplexers of this type agrees quite well with Fig. 10.

Two methods can be used to increase the power-handling capacity over that shown in Fig. 10. The first is to decrease the height of the window and/or increase its thickness but still mount it in the guide wall. This procedure raises the dashed lines of Fig. 10 but at the same time increases the loaded Q . The second method involves placing the window at the center of a cavity. This reduces the current in the tube, but again raises the Q of the circuit. Notice that both methods achieve increased power-handling ability by an increase in Q and thus a decrease in bandwidth of the duplexer.

OTHER CONSIDERATIONS IN DUPLEXER DESIGN

More often than not, the actual geometry and gas fill of a TR tube are chosen for reasons other than the optimization of its power-handling capacity. The choice is usually made on the basis of easy firing, adequate recovery time and long life. Fig. 11 illustrates the interrelation between breakdown voltage and recovery time for hydrogen gas and parallel-plate geometry. Similar graphs for other geometries and gas fills would have similar contours but would be somewhat different in magnitude and position. The graphs of breakdown voltage show that a very steep gradient exists starting at the left of the graph at d/λ equals 0.0025 and proceeding to lower values of d/λ as the pressure is raised. This gradient occurs because at tube spacings smaller than this value, all of the electrons can be swept out of the discharge space in half a cycle by fields smaller than those required for breakdown.¹²

Modern high-power switching tubes do not use at-

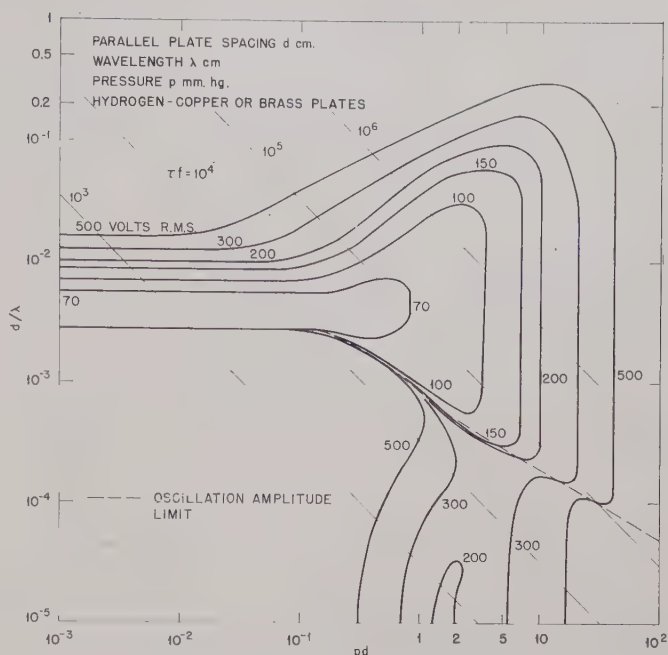


Fig. 11—Contours of constant breakdown voltage with lines of constant frequency recovery time products superimposed.

taching gases (those which cause electron disappearance by the formation of negative ions), because they cause a large increase in arc loss. Recovery is achieved by diffusion (electrons diffuse to the walls where they recombine with positive ions) or volume recombination (usually dissociative recombination). Diffusion-controlled recovery is preferred because the electron density decays with time in an exponential manner instead of inversely with time, as in recombination. This means that the duplexer is fully recovered at about one and one-half 3-db recovery times, whereas recombination-controlled recovery allows a fraction of a decibel loss at several times the 3-db recovery period. For both types of recovery, the recovery time is practically independent of power level and pulse length, but it depends directly on loaded Q for recombination while it is independent of Q for diffusion.

Recovery is controlled by recombination at high pressures and by diffusion in the low-pressure region where the arc loss tends to be least. The product of recovery time τ (sec) for diffusion-controlled recovery multiplied by frequency f (cps) is plotted on Fig. 11.

Examination of this graph shows that a good operating point falls at $d/\lambda = 0.003$ and at as low a pressure as possible to give quick recovery. It is found, however, that when the pressure is reduced too far, the arc loss goes up precipitously as shown in Fig. 9 for helium. Another problem associated with low-pressure operation is that of gas clean-up. It is found that even in the absence of sputtering, gas is lost into the walls by the action of the discharge. Lower pressures may be used when a large reservoir for gas is provided.¹³

¹² S. C. Brown, "Basic Data of Plasma Physics," John Wiley and Sons, Inc., New York, N. Y., p. 142; 1959.

¹³ D. W. Downton, "Measurement of clean-up in gas discharge tubes using radioactive krypton," *Proc. IEE*, vol. 105, pt. B (suppl.), pp. 485-487; November, 1958.

As an example, a folded cylinder for use at L band should have a spacing between cylinders of 0.030 in. At a pressure of 1 mm Hg of argon, the recovery time will be about 60 μ sec. This spacing is still about twice the skin depth in a fully ionized plasma.

CONCLUSIONS

There is no reason why gas tube duplexers cannot be designed so as to handle extremely high powers and still meet other system requirements. The power-handling ability of a duplexer may be increased by using pure inert gases, by using tube materials with high heat con-

ductivity, such as beryllium oxide, by narrowing the height of the window, or by putting the TR tube at the center of a high- Q cavity. An ATR duplexer may be used to spread the heat dissipation over a larger area. The actual tube spacing and fill are usually determined by considerations of easy firing, recovery time and tube life.

ACKNOWLEDGMENT

The author wishes to thank C. W. Jones and Dr. R. J. Carbone for many helpful discussions during the preparation of this paper.

Quasi-Optical Surface Waveguide and Other Components for the 100- to 300-Gc Region*

F. SOBEL†, F. L. WENTWORTH†, MEMBER, IRE, AND J. C. WILTSE†, SENIOR MEMBER, IRE

Summary—Components and techniques for the generation, transmission, and detection of energy in the 100- to 300-Gc frequency region were investigated theoretically and experimentally. The design and construction of fundamental components, such as harmonic generators and detectors, were necessary since many items are not available commercially. A detailed theoretical analysis was performed for the propagation characteristics of single-conductor transmission lines, and attenuation calculations were made for several dielectric image lines. Experimental measurements were made at 105 and 140 Gc on these two types of surface waveguides. Attenuation of these lines is compared with that of dominant-mode rectangular waveguide. An analysis of phase-correcting Fresnel zone plates was carried out, and several zone plates were designed, constructed and successfully tested at frequencies of 140, 210, and 280 Gc. Zone plates were used at several frequencies to make relatively long path transmission measurements and were also used in a specially designed Michelson interferometer. The frequency stability of the source klystron and the dielectric properties of a number of plastic materials were determined by measurements made with the interferometer. A method of frequency filtering by focal isolation was demonstrated with this equipment.

I. INTRODUCTION

AN investigation is being conducted to develop new components and techniques for use at wavelengths shorter than 3 mm. Much of the work completed to date has dealt with special rectangular

waveguide devices, surface waveguides (dielectric image lines and coated or uncoated single-conductor transmission lines), and devices of an optical nature.¹ The basic instrumentation consisted of adaptations of conventional rectangular waveguide components. Signal power was provided by crystal harmonic generators driven with a few tens of milliwatts of power at a fundamental frequency of either 35 or 70 Gc. Experimental measurements were made at 105, 140, 210, and 280 Gc. Video detection with silicon crystals resulted in output signal levels with a dynamic range of about 45 db above noise, except at 280 Gc, where the range was somewhat less. For some sets of measurements at 140 Gc, a range of 55 db was available.

At the time the program was started there was a scarcity of commercial components for frequencies above 100 Gc, and it was therefore necessary to design and construct various waveguide items such as detectors, harmonic generators, horn antennas, and filter sections.² Coin-silver waveguide with a cross section of 0.0325- by 0.065-in ID (RG-136/U) was chosen because the guide has a TE_{10} -mode cutoff frequency of 90.8 Gc and propagates only the dominant mode at frequencies below about 180 Gc.³ (The slightly larger size RG-138/U

* Received by the PGMTT, May 26, 1961; revised manuscript received, September 5, 1961. The research reported in this paper has been sponsored by the Electronics Research Directorate of the AF Cambridge Res. Labs., Office of Aerospace Research, U. S. Air Force, under Contract No. AF 19(604)-5475.

† Res. Div., Electronic Communications, Inc., Timonium, Md.

¹ M. J. King, *et al.*, "Quasi-Optical Components and Surface Waveguides for the 100 to 300 kMc Frequency Range," Electronic Communications, Inc., Timonium, Md., Rept. No. 2 on AFCLRL Contract No. AF 19(604)-5475; November, 1960.

² *Ibid.*; design details are given in this report.

³ The harmonic generators use RG-96/U or RG-98/U waveguide inputs.

guide was not chosen, even though some commercial components were available in this size, because this guide has a TE₁₀-mode cutoff frequency of 73.8 Gc and this is too close to the operating region of typical klystron sources in the 4-mm wavelength region.) Waveguide "squeeze" section filters were built to provide suppression of 105- or 140-Gc harmonic signals when operating at higher frequencies. Suppression of 140-Gc and 210-Gc harmonic frequencies was also accomplished by the focal isolation technique described below.

Another phase of the program has been concerned with improving the efficiency of the point contact diodes mounted in harmonic generators and video detectors. Experimental diodes have been formed with some of the recently developed III-V compounds, such as gallium arsenide, indium arsenide, and indium antimonide. Both tungsten and phosphor-bronze whiskers have been used. To date these diodes have not shown any valuable improvement over the silicon-crystal, tungsten-whisker combination. The only encouraging results noted thus far have been obtained with an indium-arsenide polycrystal and a phosphor-bronze whisker in a detector mount. After considerable searching of the crystal surface with the whisker several points were found which gave approximately 10 db more sensitivity than the silicon-tungsten combination. Further work seems warranted with indium arsenide in single crystal rather than polycrystalline form.

II. TRANSMISSION METHODS FOR SHORT MILLIMETER WAVELENGTHS

At frequencies above 70-Gc dominant-mode, hollow metal waveguide is unsatisfactory for many applications because of very high attenuation. This is illustrated in Fig. 1, which shows calculated attenuation values for several standard waveguides (see also Table I). Meas-

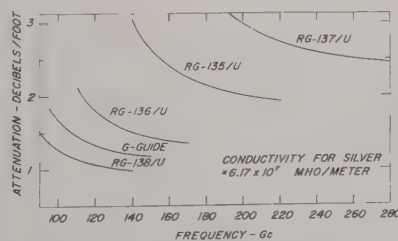


Fig. 1—Theoretical attenuation (TE₁₀ mode) in rectangular waveguides of coin silver.

TABLE I
RECTANGULAR WAVEGUIDE DATA

Designation	Size (ID)	TE ₁₀ -Mode Cutoff
RG-138/U	0.080×0.040 in	73.8 Gc
G-guide	0.075×0.034 in	78.7 Gc
RG-136/U	0.065×0.0325 in	90.8 Gc
RG-135/U	0.051×0.0255 in	115.8 Gc
RG-137/U	0.043×0.0215 in	137.5 Gc

ured values would be even larger because of losses at junctions and surface irregularities. The calculated values are based on the assumption of a perfectly smooth metal surface, but for these frequencies, where the skin depth is from 5 to 10 micro-inches, the surface roughness is usually many times the skin depth for most types of finishes. The attenuation was measured at 210 Gc for two different lengths of rectangular waveguide (having inside dimensions of 0.049 in×0.0245 in) and was found to be greater than twice the calculated value (in decibels per foot).

Certain other types of waveguides may be designed to have low-loss characteristics at these frequencies. Examples are surface-wave structures, hollow circular waveguide propagating the TE₀₁ mode, and oversize rectangular or circular waveguide propagating the lowest-order mode. For technical or economic reasons the use of optical transmission techniques also may be useful. (This category includes the beam waveguide recently described by Goubau.⁴) Surface-waveguide and optical transmission methods were used in this study because of their simplicity and low cost.

III. MEASURED AND CALCULATED RESULTS FOR SURFACE WAVEGUIDES

A. Dielectric Image Lines

The dielectric image line is simply a strip of low-loss dielectric material centered on a high conductivity metal plane. Because of its ease of construction and support and its low-loss transmission characteristics, this line recently has received much attention. For the image line, both conduction loss in the image plane and dielectric loss contribute to the total attenuation factor. Conduction loss is reduced by the use of higher conductivity metals (such as copper or silver). To obtain low dielectric loss and single-mode operation at millimeter wavelengths, the dielectric material must be small in cross section and must have a low loss tangent and a low dielectric constant.⁵ Typical materials which are satisfactory are polystyrene foam (which has been processed to have small cell sizes and uniform density) or Teflon, which can be purchased in thin, narrow tape form with a very thin pressure-sensitive adhesive backing.

The attenuation for the dominant HE₁₁ mode on an image line having a semicircular dielectric cross section may be calculated by the use of the following relationship:⁶

$$\alpha = 27.3(\phi\epsilon/\lambda)R + 69.5(R_s R'/\lambda\eta)$$

⁴ G. Goubau and F. Schwing, "On the guided propagation of electromagnetic wave beams," IRE TRANS. ON ANTENNAS AND PROPAGATION, vol. AP-9, pp. 248-256; May, 1961.

⁵ J. C. Wiltse, "Some characteristics of dielectric image lines at millimeter wavelengths," IRE TRANS. ON MICROWAVE THEORY AND TECHNIQUES, vol. MTT-7, pp. 65-69; January, 1959.

⁶ S. P. Schlesinger and D. D. King, "Dielectric image lines," IRE TRANS. ON MICROWAVE THEORY AND TECHNIQUES, vol. MTT-6, pp. 291-299; July, 1958.

where

- α = attenuation per unit length
- ϕ = loss tangent of the dielectric rod
- ϵ = relative dielectric constant of the rod
- λ = free-space wavelength (meters)
- η = intrinsic impedance of free space
- R_s = surface resistivity of the image plane.

The quantities R and R' are complicated functions of the dielectric constant and diameter (in free-space wavelengths) of the dielectric rod.⁶

About the smallest convenient diameter to which a polystyrene foam rod of semicircular cross section may be cut is an eighth of an inch (3.17 mm). The calculated attenuation of such a rod mounted on a copper image plane is shown in Fig. 2, where a relative dielectric con-

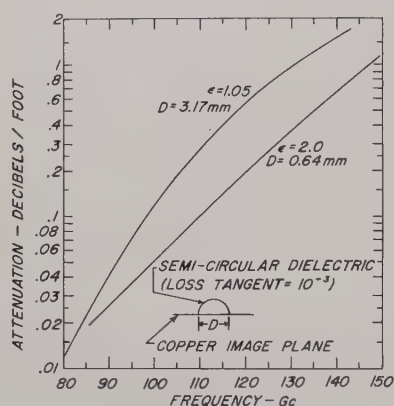


Fig. 2—Calculated attenuation (including dielectric and copper losses) for two dielectric image lines.

stant of 1.05 was assumed for the foam. A second curve is shown for a dielectric constant of 2.0 (Teflon) and a rod diameter of 0.025 in (0.64 mm). (This size was chosen because a semicircular cross section with this diameter has the same area as a tape 0.002 by $\frac{1}{8}$ in.) For each of the curves in Fig. 2 the loss tangent of the dielectric was assumed to be 10^{-3} and the conductivity of copper was taken as 5.8×10^7 mhos/m. Since the dielectrics are already very small, further reduction of attenuation by reduction of dielectric cross section has only limited possibilities. It has been found, however, that lower attenuation may be obtained by using a "flattened" cross section (*i.e.*, rectangular or semi-elliptical) with the longer transverse dimension parallel to the image plane.

A theoretical analysis of wave propagation on dielectric rods of elliptic cross section was carried out during the present investigation.⁷ Certain modes were found to exist in the elliptic rod which do not exist in the circular

rod. However, of all the modes investigated, only the one corresponding to the dominant circular HE_{11} mode has zero cutoff frequency. Furthermore, as the eccentricity of the rod tends toward unity ("flat" ellipse) the cutoff frequencies of the other modes (for an ellipse of finite width) tend toward higher values. A thin dielectric tape line (Teflon 0.002 in thick) was chosen for the experimental tests since it is a good approximation of the limit for the very flat ellipse and only the HE_{11} mode is present. The use of the metal image plane lying along the major axis further excludes the "even" type modes where the tangential component E_z is represented by functions with even periodicity.

The image planes used for experimental loss measurements were made of copper 4 in wide, in lengths of 5, 12, and 20 feet. The copper was first cleaned and polished to insure a minimum of scratches and other imperfections which could contribute unknown losses to the measurements. The dielectric (pressure-sensitive Teflon tape) was then very carefully laid in a straight line on the center of the plane and pressed to make good contact with the plane. For each tape size the measurements were made on image lines of identical construction except for length; hence, all other losses were constants and the attenuation due to the increase in the length of image line was readily determined. (Further details are given by King, *et al.*¹) The results of these measurements along with the theoretical loss for a semicircular dielectric cross section of the same area are shown in Table II.

TABLE II

Frequency	Tape Size	Average Measured Line Loss	Theoretical Loss (Semicircle)
105 Gc	$0.002 \times \frac{1}{8}$ in	0.14 db/ft	0.63 db/ft
140 Gc	$0.002 \times \frac{3}{8}$ in	0.43 db/ft	0.7 db/ft
140 Gc	$0.002 \times \frac{1}{4}$ in	0.98 db/ft	3.2 db/ft

The average measured loss is computed from at least five different measurements. The loss calculated for a semicircular dielectric cross section equal in area to that for a given tape is seen to be from 1.5 to 4 times greater than that measured for the tape line. Measurements were made at 105 Gc with a $\frac{1}{8}$ -in tape, but the fields extended beyond the edge of the image plane and this caused errors in the loss measurements. An attempt was made to measure the loss for a tape $\frac{3}{8}$ in wide but irregularities in the tape width gave a spread in results which was too large to be useful.

B. Single-Conductor Wire Lines

Surface-wave propagation on a coated or uncoated cylindrical conductor was described some years ago for frequencies as high as 10 Gc,⁸ but extrapolation of these

⁷ M. J. King and J. C. Wiltse, "Surface-Wave Propagation on a Dielectric Rod of Elliptic Cross-Section," Electronic Communications, Inc., Timonium, Md., Sci. Rept. No. 1 on AFCRL Contract No. AF 19(604)-5475; August, 1960.

⁸ G. Goubau, "Surface waves and their application to transmission lines," *J. Appl. Phys.*, vol. 21, pp. 1119-1128; November, 1950.

results to frequencies above 100 Gc leads to errors⁹ with conductor sizes which provide low-loss propagation. A new analysis was made for TM_{01} -wave propagation on coated or uncoated conductors at millimeter wavelengths.¹ (Modes other than the TM_{01} are highly attenuated and are not significant except near the launcher.) The low loss and reasonable field extent of the cylindrical-conductor transmission line offer an advantage over dominant-mode rectangular waveguide, in which the attenuation may be one or two orders of magnitude greater. The power-handling ability is also much greater for the single-conductor line than for rectangular waveguide. Wide ranges of attenuation and field extent are available from various combinations of wire size, material, and/or dielectric coating. These lines do have the disadvantage common to surface-wave lines in that they lack shielding (although shields can be provided). A further disadvantage is the necessity for physical supports which may increase the loss.

Measurements of attenuation were carried out at frequencies of 105 and 140 Gc for uncoated copper wires of circular cross section. Experimental transmission lines of several different diameters were built, and special launching horns were designed and constructed to generate the TM_{01} mode (see Fig. 3). The equipment used

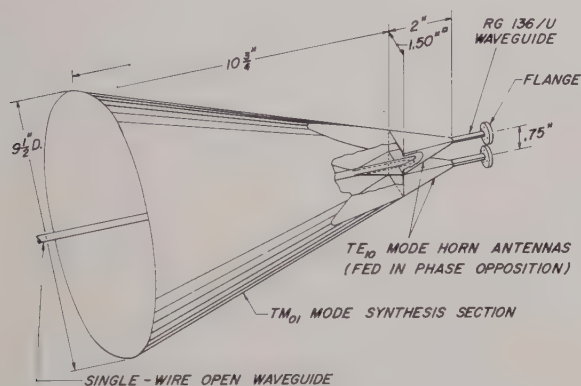


Fig. 3— TM_{01} -mode launcher for single-wire line.

to make attenuation measurements consisted of an open wire line 60 feet long with the transmitter and launcher at one end. The pick-up probe (a 28-db horn), a video detector, and an indicator were mounted on a wheeled cart which was moved along the wire in such a manner that the horn was maintained a constant distance from the wire. The smaller wires (0.080- and 0.128-in diameters) were copper-clad steel and were held in place by tension without danger of stretching the wire, as might

be the case if solid copper were used. In order to eliminate sag, which is present when the wire is held by tension alone, nylon monofilament (0.008-in diameter) was used to help support the wire. The larger diameter wires (0.375 and 0.500 in) were hard drawn copper tubing and were supported by nylon monofilament placed approximately every 8 feet along the wire.

The results of the measurements and the calculated values of attenuation are given in Table III. It may be seen that the measured attenuation is 2 to $2\frac{1}{2}$ times higher than the calculated values for the smaller wires (0.080- and 0.128-in diameter) and is approximately 3 to 6 times higher than the calculated values for the larger wires.

TABLE III
ATTENUATION OF SINGLE-WIRE TRANSMISSION LINES

Wire Diameter Inches	Frequency Gc	Calculated Attenuation	Measured Attenuation
0.080	105	0.07 db/ft	0.14 db/ft
0.128	105	0.05 db/ft	0.10 db/ft
0.375	105	0.02 db/ft	0.12 db/ft
0.500	105	0.015 db/ft	0.10 db/ft
0.080	140	0.08 db/ft	0.20 db/ft
0.128	140	0.06 db/ft	0.11 db/ft
0.375	140	0.03 db/ft	0.10 db/ft
0.500	140	0.02 db/ft	0.08 db/ft

The excess loss is attributed mainly to copper and radiation losses at surface imperfections, irregularities, and bends and supports along the wires. This is particularly true with the large-diameter wires as the wave is very loosely bound and irregularities along the wire can cause large (percentage) increases in the low-attenuation factors. That is, when the attenuation factor is very low, a small increase in the absolute value of the loss (a few hundredths of a decibel per foot) appears as a large percentage increase. Although the wires were cleaned immediately before making the attenuation measurements, surface oxidation of the copper also contributed a loss term which was not considered in the calculated values. Nonetheless, the measured attenuation for the single-wire line in this frequency range is much lower than that for conventional dominant-mode rectangular waveguide, which has an attenuation greater than 1 db/ft at 105 or 140 Gc.

For the wires possessing lowest losses, the "stability" of the wave (*i.e.*, the degree of "tightness of binding" to the wire) is poor; hence to obtain the lowest losses the wire line must be quite straight and uniform. Because the propagating wave is loosely bound to the wire line, one must use special techniques to go around bends. The wave may be more tightly bound (by the use of a dielectric coating, for example) or plane reflectors may be used (by analogy with optical techniques). Both of these approaches have also been used previously with dielectric image lines.

⁹ P. D. Coleman and R. C. Becker, "Present state of the millimeter wave generation and technique art—1958," IRE TRANS. ON MICROWAVE THEORY AND TECHNIQUES, vol. MTT-7, pp. 42–61; January, 1959. The attenuation values given therein (Fig. 7) are in error.

IV. QUASI-OPTICAL COMPONENTS

A. Fresnel Zone Plates

Quantitative measurements of phenomena involving interference and diffraction are generally much easier to perform in the millimeter wavelength region than at optical frequencies. In fact, some optical devices which have remained essentially laboratory curiosities have analogs in the millimeter wavelength range which can be used as practical system components. One such device is the phase-corrected Fresnel zone plate.

The simplest Fresnel zone plate consists of a set of plane concentric annular rings which are alternately transparent and opaque. The successive radii of these zones are so chosen that the distance from a selected point on the central axis increases by one-half wavelength in going from the inner to the outer radius of any ring. Therefore, if a plane wave is normally incident on the zone plate, the portions of the radiation which pass through various parts of the transparent zones all reach the selected point with phases which differ by less than one half-period. (The integral number of whole-period phase differences may be neglected for this development.) The superposition of these portions of the original plane wave results in an intensity at the selected axial point which may be much greater than that which would result from the unobstructed wave. Thus, the zone plate acts like a lens, producing a focusing action on the radiation it transmits.

The opaque half-period zones may be replaced by zones which transmit the radiation but introduce a 180° phase shift relative to the portions of the plane wave transmitted by the adjacent zones. This may be accomplished in practice by cutting into a dielectric plate circular grooves of the correct dimensions. In this way, all the half-period zones contribute to increasing the intensity at the focus.

Obviously, it is possible to divide each half-period zone into some number of subzones for each of which the phase correction is appropriately determined. If the process is continued, using a dielectric plate for the physical construction, the form of the phase-corrected zone plate approaches more and more closely that of a Fresnel lens, with its annular rings each having a smoothly curved surface. It can be shown that the intensity at the focus of a quarter-period zone plate is only 1 db below the intensity produced by a Fresnel lens of the same diameter and focal length.

For visible light, the limitations of wavelength make it difficult to produce half-period zone plates with large diameters and short focal lengths; a speed of $f/20$ is about as great as can be secured readily with photographic techniques. The fabrication of optical zone plates having subzones with controlled phase corrections requires great skill and effort.¹⁰ On the other hand,

phase-reversing plates and quarter-period phase-corrected plates for the millimeter wavelength spectrum are readily produced by common machine shop techniques, and speeds in excess of $f/1$ are quite easy to achieve.

Pairs of $f/1$ phase-reversing zone plates were designed and constructed for use at 140 Gc and at 210 Gc. The plates were machined from polystyrene sheet stock about 0.5 cm thick and 20 cm in diameter. The focusing action of the 140-Gc plates is equivalent to that which would be produced by a plano-convex polystyrene lens (hyperboloidal surface) about 4 cm thick. Fig. 4 shows a section view of one of the plates and the equivalent lens.

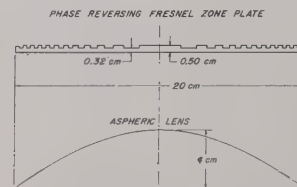


Fig. 4—140-Gc zone plate and equivalent lens.

The measured performance of the zone plates was found to agree very well with the predictions of Kirchhoff's theory. For example, using a small 15-db gain horn as a "point" source of radiation, the measured spread (between 3-db points) of the image, perpendicular to the optical axis, was found to be ± 0.3 cm. According to the diffraction theory, the radius of the Airy disk should be $1.22f\lambda/a = 0.26$ cm. In this formula, f is the focal length (20 cm), λ is the wavelength of the radiation (0.214 cm), and a is the aperture diameter (20 cm).

The half-power band-pass of the system composed of a transmitting horn, transmitting half-period zone plate, receiving zone plate, and receiving horn was found to be in approximate agreement with the theoretical value of 7 per cent of the center frequency. Smaller quarter-period plates (see Section IV-C) have a calculated pass band of 20 per cent. The behavior of a phase-correcting Fresnel zone plate as a function of frequency exhibits rather complicated changes over a large frequency interval. The effective gain, the focal length, the diameter (or number of zones), and the depth of the phase-correcting grooves are all interrelated. Adjustment of these parameters permits considerable control over both the frequency bandwidth and the number of secondary maxima and minima in the gain-vs-frequency characteristic. Detailed analysis of this problem is presently underway and will be reported in the near future.

B. Optical Transmission Methods

The feasibility of using phase-reversing zone plates as components for transmission systems has been demonstrated at 140 Gc and at 210 Gc. By using plates with diameters which are large relative to the wavelength, the Fresnel region can be made to extend to rather great

¹⁰ Phase-reversing zone plates were constructed by R. W. Wood. See R. W. Wood, "Physical Optics," The Macmillan Co., New York, N. Y., 3rd ed., pp. 38-39, 1934.

distances from the aperture. Within this region, radiation from the aperture is not attenuated in accordance with the inverse square law, but at a much smaller rate.¹¹ The Fresnel diffraction region may be considered as extending from near the aperture plane out to about one-half of the Rayleigh distance R defined by the equation $R = a^2/\lambda$. The Fraunhofer region, in which an inverse square law of attenuation is to be expected, "begins" in the range of 1 to 2 times R and extends to all greater distances. The results of transmission measurements at 210 Gc are shown in Fig. 5. Within the Fresnel region, the relative signal falls off at a rate of about 0.02 db/ft. At distances somewhat greater than R , an inverse square law approximates the measured curve quite well.

H -plane patterns were measured at 140 Gc by using identical horn and zone plate combinations as transmitting and receiving antennas. The receiving combination was placed at distances of 12 feet, 78 feet and 172 feet from the transmitter and rotated about a vertical axis passing through the center of its zone plate. The 12-foot distance corresponds to $0.2R$ and is well within the Fresnel region. The pattern is labeled "Fresnel region" in Fig. 6. Measurements at 78 feet ($1.3R$) and at 172 feet ($2.8R$) gave identical results, shown in the figure by the curve labeled "far field."

Numerous side lobes were found in both the H plane and E plane far-field patterns. For example, in the H plane a total of about 45 lobes was found; of these, 35 are within $\pm 45^\circ$ of the forward direction and 10 within $\pm 20^\circ$ of the backward direction. All of these were at

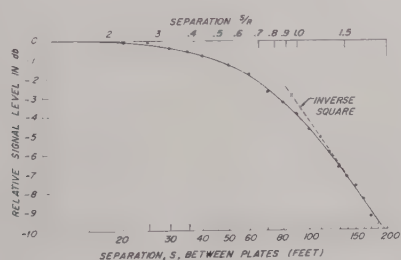


Fig. 5—Optical beam transmission at 210 Gc.

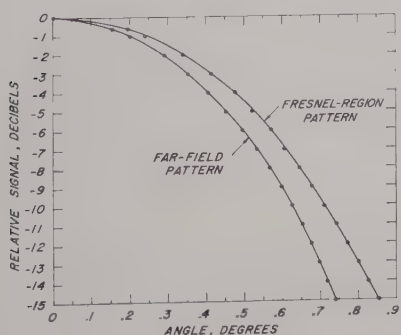


Fig. 6—Main lobe in H -plane pattern of 140-Gc zone plate.

¹¹ S. Silver, *et al.*, "Microwave Antenna Theory and Design," M.I.T. Rad. Lab. Ser., McGraw-Hill Book Co., Inc., New York, N. Y., p. 349 *et seq.*, vol. 12; 1949.

least 30 db below the main lobe. No attempt has been made to calculate theoretically this detailed radiation pattern.

C. Michelson Interferometer

To facilitate the development of quasi-optical components for millimeter waves and to permit the measurement of various properties of materials at frequencies from 100 to 300 Gc, a millimeter-wave Michelson interferometer was designed and constructed. (Culshaw has described a Michelson interferometer¹² and a Fabry-Perot interferometer¹³ for millimeter wavelengths.) The most common form of this interferometer employs an extended source of (optical) radiation. However, radiation at millimeter wavelengths is most conveniently emitted from a horn, which behaves essentially like a point source. Also, for visible light, the eye serves as an image-forming device to view the interference fringes, but at millimeter wavelengths the crystal video detector which is used acts like a point receiver. It is thus necessary to use a modification of the Michelson interferometer (first introduced by Twyman and Green) which uses collimated radiation. Phase-corrected Fresnel zone plates were found to be well suited to this application.

Fig. 7 is a photograph of two 7 cm $f/1$ zone plates constructed for the interferometer. The plate at the left in the photograph is phase-reversing, *i.e.*, it is a half-period zone plate. The other is a quarter-period zone plate in which successive rings introduce phase changes of $\pi/2$, π , $3\pi/2$, and $2\pi(=0)$ radians. Two quarter-period plates are used in the interferometer because of their greater collimating efficiency. (Direct measurement confirms the theoretical signal improvement of 6 db over the simpler half-period zone plates.) The other components of the Michelson interferometer, shown in Fig. 8, are exactly like their optical counterparts, with the exception of the beam divider. Rather than a semi-transparent mirror, the instrument utilizes a dielectric sheet (polystyrene) of the proper thickness to yield approximately equal net transmission and reflection for the wavelength at which the measurements are made. The position of the movable mirror can be set repeatedly within 0.0004 cm, and the received signal level at the interference minima is 30 db below that at the maxima.

The frequency stability of the klystron tube (Raytheon QK 369, operating at 70 Gc) was investigated by using the millimeter-wave Michelson interferometer to measure time fluctuations of wavelength. The path lengths of two interfering beams (of equal signal strength) were made to differ by approximately 60 wavelengths, and the respective signals were adjusted to be out of phase (null condition) at the detector. The varia-

¹² W. Culshaw, "The Michelson interferometer at millimetre wavelengths," *Proc. Phys. Soc. (London) B*, vol. 63, pp. 939-954; November, 1950.

¹³ W. Culshaw, "The Fabry-Perot interferometer at millimetre wavelengths," *Proc. Phys. Soc. (London) B*, vol. 66, pp. 597-608; July, 1953.

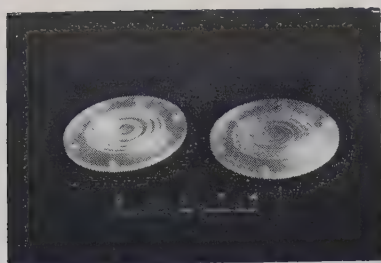


Fig. 7—Half-period and quarter-period zone plates for 140 Gc. (Scale is in inches.)

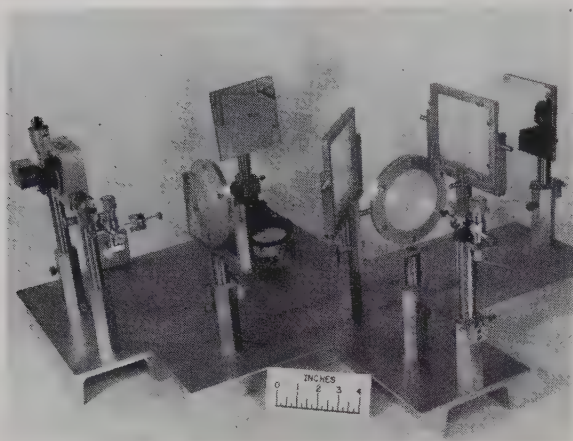


Fig. 8—Millimeter-wave Michelson interferometer.

tions of the detected signal level, representing changes in the amount of cancellation caused by changes in frequency, were recorded for an extended period of time, and corresponding frequency changes were then computed from them. The measured random frequency fluctuation was found to be less than ± 10 parts per million over periods of a few minutes and about ± 30 parts per million over a period of an hour. Frequency stability is apparently limited primarily by temperature fluctuations of the klystron.

The dielectric constants of a number of plastics have been measured with the interferometer. Actually, the product of magnetic permeability and dielectric constant $\mu\epsilon$ was measured, but for these materials it is known that $\mu=1$. Approximate values for the loss tangents of the materials at 140 Gc were determined by inserting sheet samples in a properly polarized collimated beam with the angle of incidence set at the Brewster angle, $\phi = \tan^{-1}\sqrt{\epsilon}$, at which the reflection coefficient is zero. In practice, this measurement is difficult to perform with good precision, and the values of loss tangents presented in Table IV are probably reliable only within a factor of two.

Experimental tests have been made on an optical technique of frequency filtering at millimeter wavelengths. Suppression of the second harmonic (140 Gc) can be accomplished by using the 210-Gc Fresnel zone plates instead of the conventional "squeeze-section"

TABLE IV
DIELECTRIC PROPERTIES OF SEVERAL MATERIALS

Material	Dielectric Constant		Loss Tangent 140 Gc
	140 Gc	210 Gc	
Polystyrene	2.52 ± 0.01	2.53 ± 0.01	0.002
Rexolite	2.47 ± 0.01	2.50 ± 0.06	0.002
Teflon	2.05 ± 0.01	2.08 ± 0.03	0.003
Lucite	2.56 ± 0.10	2.58 ± 0.10	—
Mylar	3.35	—	0.01
Ethylcellulose	3.71	—	0.1

waveguide filter. If a waveguide filter is not inserted between the crystal multiplier and the transmitting horn, both the second and third harmonics are present in the radiation from the horn, the lower frequency having a greater intensity. However, if the Fresnel zone plates designed for the higher frequency are inserted at the proper distances from the transmitting and receiving horns, the amount of 140-Gc radiation reaching the receiver is greatly reduced by what may be regarded as a defocusing action. Measurements with the Michelson interferometer show that the distance between the regularly spaced interference minima corresponds to half the wavelength of the 210-Gc radiation ($\lambda = 0.141$ cm). The presence of a small amount of the lower frequency results in a standing wave pattern having three different null depths which recur repetitively over a distance containing three of the shorter half-wavelengths and two of the longer half-wavelengths. Quarter-period zone plates designed for 280 Gc were used in the interferometer and the presence of this signal frequency was detected. A waveguide squeeze section removed the 140-Gc harmonic and the zone plates themselves defocused the 210-Gc radiation.

The Fresnel zone plates, whose action is wavelength-dependent, thus constitute a frequency filter and produce results quite analogous to those obtained by the method of focal isolation which was devised by Ruebens and Wood¹⁴ for work in the far infrared spectrum. The filtering action of the quartz lenses used by Ruebens and Wood arose from the dispersion of the quartz. In the case of the zone plates described here, the action is similar to that of a focusing diffraction grating. This method of frequency filtering by optical techniques should prove to be of considerable utility in the millimeter and submillimeter wavelength regions where construction of waveguide filters is very difficult or impracticable.

ACKNOWLEDGMENT

The authors wish to express their appreciation to J. Rodgers, who contributed many valuable ideas and made all the measurements, and to Mrs. M. King for her assistance with analysis and computation.

¹⁴ R. W. Wood, "Physical Optics," The Macmillan Co., Inc., New York, N. Y., 3rd ed., p. 523; 1934.

Broad-Band Isolators and Variable Attenuators for Millimeter Wavelengths*

C. E. BARNES†

Summary—A longitudinally magnetized rod of ferrite has been used as a dielectric waveguide which provides Faraday rotation independent of frequency in the band from 50 to 60 kMc. This rotator has been incorporated into broad-band isolators with forward losses of 1 db and reverse losses greater than 30 db with return losses of approximately 20 db over this band. It has also been used in a variable attenuator with a minimum loss of 1 db and a maximum loss greater than 30 db which is essentially constant over the band.

Advantages of this type of rotator at millimeter wavelengths include bandwidths in excess of 20 per cent, low field requirements (25–50 oe), relatively large dimensions, the use of common ferrites, and the absence of conducting waveguide walls which permits rapid switching of the control field.

The last feature has been utilized in an automatic power leveling system capable of removing variations of several kc frequency content from the swept output of a millimeter wave BWO.

A BROAD-BAND Faraday rotation isolator and variable attenuator have been developed to operate in the millimeter wave region of 50 to 60 kMc. These devices utilize the rather old but unexploited concept of a dielectric rod waveguide composed entirely of ferrite to give the following typical device characteristics:

Isolator

Forward loss	< 1 db
Reverse loss	> 30 db
Return loss	~20 db
Field required	~30 oe.

Variable Attenuator

Minimum loss	~ 1 db
Maximum loss	> 30 db
Return loss	~20 db
Field required for maximum loss	~30 oe.

The bandwidth of these devices exceeds that of any other isolator or attenuator known to the author to operate at these frequencies, while the high, low and return loss values are comparable with other such devices. Notable features of these devices include the use of a common ferrite, a low (25–50 oe) longitudinal field, and the absence of conducting waveguide walls, which makes the field readily switchable.

DEVICE DESCRIPTION

The isolator, which is very similar to the attenuator in appearance, is pictured in Fig. 1. Input and output

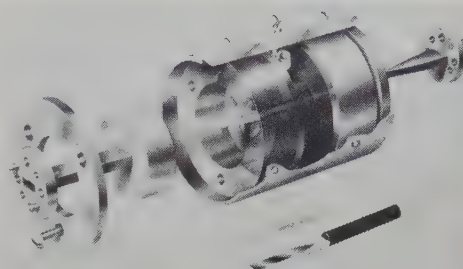


Fig. 1—A broad-band 50 to 60 kMc isolator utilizing a dielectric waveguide rotator.

ports for the devices are rectangular waveguides with the planes of polarization for the dominant modes in the two guides oriented at 0° to one another for the variable attenuator and at 45° to one another for the isolator. The rotator section between the input and output is a dielectric waveguide suspended in a nonconducting cylinder by means of plastic supports and coupled to the rectangular waveguides by simple tapers in the dielectric guide which protrude into the rectangular guides. The attenuator films which provide the reverse loss in the isolator and the variable loss in the attenuator are deposited metal films sandwiched into each end of the dielectric waveguide. Shielding from ambient fields is provided by μ -metal cylinders which encircle the devices over their entire length. The magnetic field is applied by means of an adjustable permanent magnet or a low-inductance solenoid coil as the application demands.

Figs. 2 and 3 show the performance of typical attenuators and isolators of this type. The dashed curves superimposed on the curves of Fig. 3 indicate, for comparison, the performance of a "conventional" Faraday rotation isolator (built at Bell Telephone Laboratories) utilizing a 0.030-in rod of ferrite in a 0.200-in diameter metallic waveguide. In each case the magnetizing field has been held constant and the losses plotted as functions of frequency. The reverse loss of Faraday rotation isolators is greatly dependent upon the angle of rotation. Thus, the frequency dependence of the angle of rotation for the "conventional" rotator is indicated by the sharp peaking of the reverse loss (dashed curves of Fig. 3). Similar peaking would occur in the maximum loss for a "conventional" Faraday rotation attenuator. Contrast this peaking with the nearly constant, high maximum loss of the dielectric waveguide attenuator (Fig. 2) and

* Received by the PGMTT, May 31, 1961; revised manuscript received, September 7, 1961.

† Bell Telephone Laboratories, Inc., Murray Hill, N. J.

reverse loss of the dielectric waveguide isolator (solid curves of Fig. 3). Comparing bandwidths on the basis of reverse loss, we see that the "conventional" rotator has a 30 db bandwidth of only 1 kMc while the 30 db bandwidth of the dielectric guide isolator exceeds 10 kMc. Note that the forward losses are comparable for the two isolators so that the reverse loss comparison is truly indicative of their relative bandwidths.

Return loss data was not available for the "conventional" Faraday rotation isolator. The return losses for the dielectric guide devices as indicated in Figs. 2 and 3 fluctuate some, but stay greater than 20 db over much of the band. A discussion of some of the sources and remedies for the remaining mismatch is included in the text.

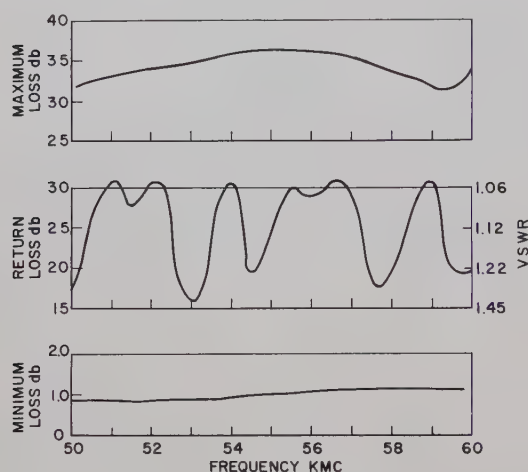


Fig. 2—Typical loss characteristics of a broad-band 50-60 kMc variable attenuator. The minimum loss is obtained with a 0 applied field and the maximum loss with a constant 30 oe applied field.

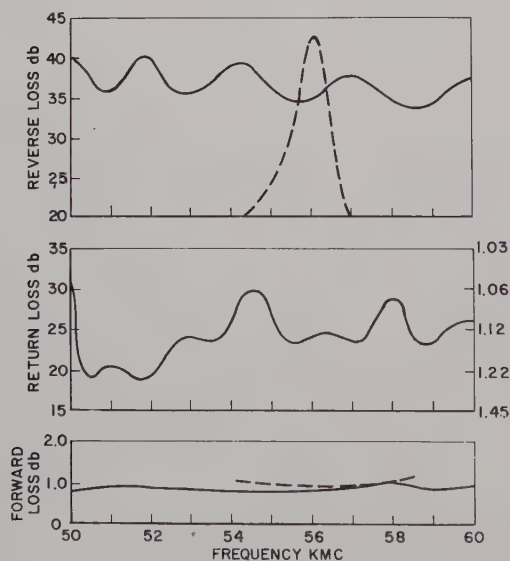


Fig. 3—Typical loss characteristics of a broad-band 50 to 60 kMc isolator (solid curves) with the characteristics of a "conventional" Faraday rotation isolator (dashed curves) for comparison. In each case the applied field was held constant over the frequency band.

DESIGN CONSIDERATIONS

Broadbanding

Southworth¹ published the set of curves shown in Figs. 4 and 5 which indicate the relative phase velocity v/v_0 and the ratio of the energies w_i/w_0 inside and outside of dielectric rods excited in the hybrid HE_{11} mode, which is the mode utilized in these devices. The curves are plotted as functions of the diameter $2a/\lambda_0$ for rods of dielectric constant 10 and 2.5. The curves for $\epsilon = 10$ are of special interest, because this is approximately the dielectric constant of a number of ferrites. Note that for $\epsilon = 10$ in the region $0.15 < 2a/\lambda_0 < 0.4$, the phase velocity rapidly changes from that for free space to near that for an infinite dielectric medium. Note also that in this same transition area the percentage of the total energy within the rod goes from near 0 per cent at $2a/\lambda_0 = 0.15$ to 95 per cent at $2a/\lambda_0 = 0.4$. Hence, for $2a/\lambda_0 > 0.4$, the dielectric rod has very nearly the characteristics of the infinite medium. It has been shown² that Faraday rotation in an infinite ferrite medium is independent of frequency subject to the restriction that the magnetizing field is much less than that required for gyromagnetic resonance

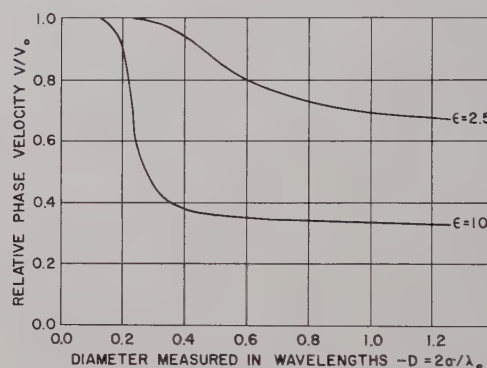


Fig. 4—The relative phase velocity, V/V_0 , for the HE_{11} mode in dielectric rod waveguides (from Southworth¹).

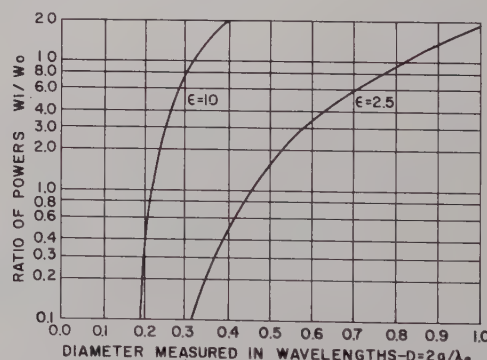


Fig. 5—The ratio of internal to external power, W_i/W_0 , for the HE_{11} mode in dielectric rod waveguides (from Southworth¹).

¹ G. C. Southworth, "Principles and Applications of Waveguide Transmission," D. Van Nostrand Co., Inc., New York, N. Y., pp. 130-131; 1950.

² C. L. Hogan, "The ferromagnetic Faraday effect at microwave frequencies and its applications," *Rev. Mod. Phys.*, vol. 25, pp. 253-261; January, 1953.

($H \ll H_0$). The rotation per unit length is given by

$$\theta/l = 4\pi M\gamma\sqrt{\epsilon}/c,$$

where

$\theta/l \equiv$ rotation per unit length

$M \equiv$ ferrite magnetization

$\gamma \equiv$ gyromagnetic ratio

$c \equiv$ velocity of light.

One should also expect rotation to be essentially independent of frequency, subject to the above restriction, for a longitudinally magnetized ferrite dielectric waveguide of diameter $2a/\lambda_0 > 0.4$. (This assumes $\epsilon = 10$. A higher value for ϵ would reduce the diameter required.) In the transition region, the Faraday rotation in a solid rod of ferrite is very frequency dependent, increasing rapidly with increasing frequency. It is interesting to note in passing that there is a similar transition region for ferrite rods in metallic guide. When a ferrite rod diameter is selected which is large enough to provide a good response to the applied field and small enough to avoid the onset of multimoding, it falls into this transition region. This accounts for the frequency dependence of the "conventional" Faraday rotator.

The broad-band rotators described here were designed to be sufficiently large in diameter to provide frequency independent rotation and to be readily machined by standard means, without making the diameter so large as to cause unnecessary losses or to be incompatible with the connecting waveguide. The ferrite diameter used was 0.070 in, which gives $2a/\lambda_0 \cong 0.3$ at 50 kMc. This reduction in diameter from $2a/\lambda_0 = 0.4$ to $2a/\lambda_0 = 0.3$ was permissible because the dielectric constant of the ferrite used was somewhat greater than 10.

Matching

Elsasser³ pointed out that the HE_{11} mode is readily excited by inserting the end of a dielectric rod into a rectangular waveguide. Indeed, a simple flat or conical taper of the dielectric rod provides a very reasonable broad-band match as indicated in Figs. 2 and 3.

In these devices the tapered dielectric-waveguide transitions serve both as housings for the loss films and as matching sections between the metallic and dielectric waveguides. Faraday rotation in the region of the loss films would degrade the characteristics of the devices; therefore, this part of the dielectric guide must be made of a magnetically inert material. The dielectric constant of this material should, insofar as possible, equal the dielectric constant of the ferrite in order to minimize the mismatch at the ferrite-dielectric interface. A high density alumina was selected because it is a ceramic with many of the mechanical properties of ferrite, has a relatively low loss tangent of ~ 0.0001 , and has a dielectric constant of ~ 9 which approaches that of the ferrite.

Indications are that the discrepancy between the dielectric constants of the ferrite, 10–15, and the dielectric constant of the alumina, 9, is the major contributor to the remaining mismatch of present devices. To achieve better matches in the absence of a more suitable dielectric material for the tapered transitions, it will probably be necessary to adjust the relative diameters of the ferrite and dielectric parts to compensate for the difference in dielectric constants or to step the diameter of one or the other so as to form a step transformer. Ideally the external match should be obtained without resorting to internal mismatches (e.g., step transformers), not only because of bandwidth considerations but also because of the effect of internal mismatches on insertion loss which will be discussed in the next section.

Losses

The minimum insertion loss for these devices is determined by the dielectric losses of the ferrite, wall losses in the connecting metallic guide, losses due to reflection including radiation caused by internal mismatches, and, in the isolator, the departure from the 45° operating rotation. An attempt was made to minimize the dielectric losses by selecting materials with low loss tangents and by keeping the length of the dielectric guide as short as possible. The magnetic losses are probably not very serious since both the saturation magnetization of the ferrite (5000 gauss) and the operating fields are far below the field required for gyromagnetic resonance ($\sim 18,000$ oe). Experimentally, dielectric guides of solid ferrite exhibit only slightly greater loss than similar guides made of low loss nonmagnetic alumina.

The wall loss quoted by manufacturers for coin silver waveguide of ID 0.074×0.148 in is about 0.04 db per inch in the 50 to 60 kMc band and each device includes 2 or 3 inches of this guide plus two flanges. The metallic guide and flanges on the device actually contribute about 0.20 db to the minimum loss.

When considering losses due to mismatches one must not only take into account the energy reflected from the device, but must also consider radiation from the dielectric waveguide caused by mismatches within the dielectric guide. When solid rods of ferrite or alumina are placed in these devices in place of the composite ferrite and alumina structures the insertion losses are invariably several tenths of a db less than for a composite device of equivalent length. The improvement in the external match can account for no more than a few hundredths of a db. The remainder of the improvement is attributed to the reduction in radiation due to the elimination of the ferrite-dielectric interfaces which are felt to be the major sources of internal mismatch.

Finally the departure from the desired angle of rotation must be considered as a source of forward loss in the isolator. This loss is given in db by

$$L_\theta = -10 \log_{10} \cos^2 (45^\circ - \theta),$$

³ W. M. Elsasser, "Attenuation in a dielectric circular rod," *J. Appl. Phys.*, vol. 20, pp. 1193–1196; December, 1949.

where θ is the angle of rotation. It can be seen that L_θ is quite insensitive to small departures from $\theta = 45^\circ$, and the rotation in these devices is so nearly independent of frequency that this source of loss can be neglected if the magnetic field is adjusted to give a 45° rotation at any frequency in the band.

The principal source of the reverse loss in the isolator and the variable loss in the attenuator is absorption in the loss films in the dielectric taper sections. While the resistivity of the film is not critical, experience has shown 100 ohms per square to be a satisfactory value for use in devices at all microwave frequencies. A metallized mica film was chosen because it was available in very thin (0.001 in thick) sheets and was readily cut to the dimensions needed. It would be preferable to deposit the film directly upon the dielectric material of the tapers and eliminate the mica, but this has not yet been done. Assuming efficient loss films, these losses are limited by the departure of the angle of rotation from the optimum angle, the degree to which linear polarization can be maintained, and in the isolator, the mismatch at the interface between the ferrite and alumina. The dependence of the maximum loss of the variable attenuator and the reverse loss of the isolator on the angle of rotation can be written as

$$L_\theta = 10 \log_{10} \csc^2 \Delta\theta,$$

where $\Delta\theta$ is the departure from the optimum angle (45° for the isolator and 90° for the variable attenuator). Isolators with greater than 35 db minimum reverse loss have been built. From the above equation it can be seen that this requires that the rotation be within $\pm 0.5^\circ$ of 45° . Since the interface mismatch and departure from linear polarization both tend to reduce the reverse loss, the rotation must actually be constant to somewhat less than $\pm 0.5^\circ$. This high reverse loss also requires that the linear polarization be kept to a rather high degree.

The dependence of the reverse loss in the isolator upon the interface mismatch comes about in the following way. A reverse wave enters the isolator and undergoes a 45° rotation in travelling to the far end interface where it is partially transmitted and partially reflected. The transmitted wave is absorbed in the far end loss film while the reflected wave undergoes an additional 45° rotation in travelling back toward the near end interface where it is partially transmitted and partially reflected. Once again the transmitted wave is absorbed, and the reflected wave is rotated an additional 45° in travelling back toward the far end. On this pass the reflected wave arrives at the far end polarized perpendicular to the loss film, and the portion transmitted beyond the interface is coupled out into the metallic waveguide. Neglecting the ferrite losses and reflection and radiation losses this transmitted wave is attenuated by just twice the return loss of the ferrite dielectric interface. Thus if the return loss of the interface were 15 db, the maximum reverse loss in the isolator would

be only slightly greater than 30 db. Thus it is important to match the interface as well as possible in order to optimize both the forward and the reverse losses of the isolator.

The Dielectric Waveguide Housing

The dielectric guide was housed in a nonconducting housing for two reasons. First, if a conducting cylinder were placed about the dielectric guide, the resulting waveguide would support several modes which would degrade the device characteristics. Second, a conducting cylinder would support eddy currents which slow the response of the device to a changing control field, and a fast response is essential to many variable-attenuator applications. In order to prevent communication between waves internal and external to the dielectric waveguide, a semiconducting carbon loaded phenol fibre was used for the housing. This material is lossy to the microwaves and presents a high resistance to the low frequency eddy currents. The contribution of this RF lossy housing to the minimum insertion loss of the devices is negligible providing its inner diameter is greater than twice the dielectric guide diameter, because over 95 per cent of the microwave energy is confined to the dielectric guide, and the RF fields outside the dielectric guide decay essentially exponentially. An equally satisfactory housing for devices which do not have to be "switched" is a metal cylinder lined with a 0.100 in thick RF lossy cylinder with the above restriction on the internal diameter. The lossy liner alters the boundary conditions at the conducting cylinder wall so as to prevent the propagation of higher modes.

Supporting the Dielectric Guide

The dielectric waveguide must be suspended upon the axis of its housing with its tapers protruding into the rectangular input and output guides. The support should have a dielectric constant much less than that of the dielectric guide so as to minimize its effect on the distribution of energy in the dielectric waveguide, and it should have low losses at millimeter wavelengths. Plastic foams are often employed in devices built to operate at lower frequencies, but they become difficult to work with in the millimeter wave range because of the small dimensions. In these devices, two 0.015 in thick wafers of a low loss plastic of dielectric constant ~ 2.5 which goes under the trade names of Stycast 0005 and Rexolite were used. These wafers are made in the form of circular washers and are placed in metal cups which are attached to each end of the dielectric waveguide housing, and the dielectric waveguide is suspended between them. The supporting wafers are recessed into depressions in the cups which are concentric with the housing and also concentric with machined receptacles for the flanges of the rectangular waveguides. Axial motion of the dielectric waveguide in its supports is prevented by the application of a spot of adhesive at each support.

Magnetic Field Requirements

Unlike gyromagnetic resonance which requires fields of 18 to 20 thousand oersteds at these frequencies, Faraday Rotation occurs for fields between 0 and those required for saturation of the ferrite. The field requirement is minimized by selecting a high saturation ferrite. In this case one need not worry about the saturation being so high as to cause low field losses, because the field required for resonance is three or four times as great as the saturation magnetization of the highest saturation ferrite. A nickel-zinc ferrite of 5000 gauss saturation was chosen and the length of the ferrite was adjusted so that the devices operated with ~ 30 oe applied field. The resulting ferrite lengths were 0.300 in for the isolator (45° rotation) and 0.500 in for the variable attenuator (0° to 90° rotation). The 30 oe field can be obtained with ~ 0.25 amps in a solenoid coil of 120 turns over a length of 0.50 in for the attenuator. For the isolator the field required can be obtained with a magnetized rod of Indiana Steel's Alnico V 0.300 long by 0.125 in in diameter brought to within ~ 0.200 in of the ferrite. In practice both the distance from the ferrite and the angular orientation of the magnet with respect to the axis of the ferrite are made adjustable to provide for a fine adjustment of the field so that the isolator's reverse loss can be optimized.

Magnetic Shielding

Since these devices operate at low fields (30 oe) and are critically dependent upon the operating field, they have been encased in $1/32$ in thick μ -metal cylinders which extend over the entire length of the dielectric guides including the tapers and which shield the ferrite from external magnetic fields.

THE VARIABLE ATTENUATOR AS A POWER LEVELER

No attempt will be made to itemize the various applications for these two devices, but there is one application of the variable attenuator which should be of considerable interest to anyone engaged in millimeter wave work. The variable attenuator is especially suited for use in an automatic power level control circuit for leveling the output of a backward wave oscillator, for example. In this application the variable attenuator is placed in tandem with the microwave generator. The power out of the attenuator is sampled by means of a directional coupler and a detector, and this level is compared with a reference level. The error between the power level and the reference level is translated into a correction current which is applied to the windings of the variable attenuator. This automatically adjusts the output power level toward the reference level. Several such leveler circuits have been put into operation by this author, A. W. Anderson, and R. V. Goordman, who designed the necessary reference circuits and differential current amplifiers. These circuits have been capable of removing variations of several kc frequency content

from the output of BWO's swept over the 50 to 60 kMc band. Fig. 6 shows the effect of leveling on the output of a BWO swept between 50 and 60 kMc.

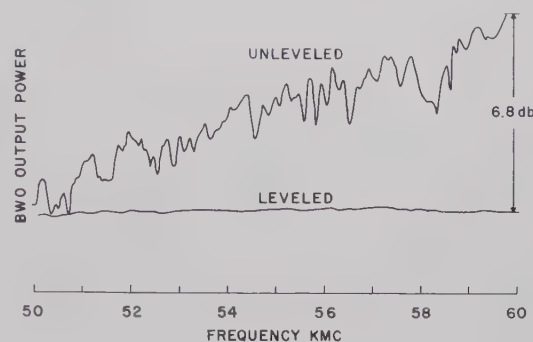


Fig. 6—Millimeter wave power leveling. A comparison of the leveled and unleveled output of a BWO swept from 50 to 60 kMc.

EXTENSION OF THE DESIGN

There is no apparent reason why the dielectric waveguide rotator should not be readily incorporated into any of the well-known Faraday rotation devices. This type of variable attenuator with similar characteristics has been built at 5.5 kMc and at X band which points up the fact that this design is applicable at any frequency subject to limitations on materials and dimensions. At the lower frequencies one may choose from other excellent broadband rotators such as the dielectrically compensated rotator described by Ohm⁴ and the ridged waveguide rotator described by Chait and Sakiotis.⁵ However, the simplicity of the dielectric waveguide rotator and the relatively large dimensions of its components tend to make it the most practical for millimeter wave applications.

ACKNOWLEDGMENT

A special commendation goes to A. W. Anderson who carried out the assembly and testing of these devices and their predecessors. His skill and imagination in solving the many mechanical and electrical problems which arose in connection with this effort have been of great value. J. A. Weiss contributed greatly to the development through numerous discussions and suggestions.

Thanks also go to the men in our model shop under A. W. Koenig who prepared the sometimes complicated and always small ferrite and alumina parts.

The author is also indebted to R. V. Goordman for his design of the leveler amplifier which has not only increased the utility of the devices but has increased the facility with which future development work can be carried out.

⁴ E. A. Ohm, "A broad-band microwave circulator," IRE TRANS. ON MICROWAVE THEORY AND TECHNIQUES, vol. MTT-4, pp. 210-217; October, 1956.

⁵ H. N. Chait and N. G. Sakiotis, "Broad-band ferrite rotators using quadruply-ridged circular waveguide," IRE TRANS. ON MICROWAVE THEORY AND TECHNIQUES, vol. MTT-7, pp. 38-51; January, 1959.

A New High-Precision Method for the Measurement of the VSWR of Coaxial Connectors*

A. E. SANDERSON†, MEMBER, IRE

Summary—A substitution method of measuring the very small reflections due to a pair of precision coaxial connectors has been developed. The connectors under test are mounted on a section of precision air line which serves as the impedance reference standard. The electrical length of this line, including connectors, is a multiple of one-half wavelength at the frequency of measurement.

A slotted line and a termination, both having the same type connectors as those under test, are required. With the aid of an auxiliary slide-screw tuner, the slotted line and the termination are matched to each other. The output of the slotted line is then plotted by a graphic level recorder having an expanded-scale presentation and a mechanical linkage between the chart drive and the probe on the slotted line.

The section of air line fitted with the connectors under test is then placed between the slotted line and the termination, and a second curve is recorded. The slotted line and termination errors still cancel each other, and any errors due to variations in probe coupling along the line also cancel out. The difference between the initial curve and the second curve represents the mismatch of the connectors under test with respect to the precision air line. With a recorder having a scale expansion of 2 per cent full scale, VSWR's as low as 1.001 are easily discernible.

INTRODUCTION

MEASUREMENT of the VSWR or reflection coefficient of a pair of coaxial connectors has always been difficult because it is hard to separate the reflections due to the connectors from those due to the termination and from errors in the slotted line. In the following substitution method, the difference between the two successive measurements represents very closely the VSWR of a pair of connectors with respect to a section of precision air line that serves as the impedance reference standard. The most troublesome sources of error in the usual direct method, such as termination VSWR, residual VSWR in the slotted line, probe reflections, and variation in probe coupling are present in both substitution measurements to the same degree, and therefore cancel out in the final results to a first approximation. This technique has proved most useful in the development of new connectors. Its use has made possible the development of a new, high-precision connector for use from dc to 9 Gc with reflections an order of magnitude lower than those of any previous connector. Partly because of the lack of suitable measurement techniques, the nominal design of most widely-used coaxial connectors is far from optimum. Many commercially available connectors could be improved substantially without tighter tolerances, simply by changes in the nominal dimensions.

The basic tools of this method are a slotted line and a graphic level recorder. These have been combined into one instrument, which presents a strip-chart recording of the standing-wave pattern on the slotted line. The chart drive is synchronized with the probe-carriage drive so that several different standing-wave patterns on the slotted line may be recorded on the same section of chart. The section of chart can then be removed and analyzed graphically to determine the magnitude and phase of the standing-wave patterns.

Such a "slotted-line-with-a-memory" is capable of much greater accuracy than the slotted line alone when used in the substitution method. Without the memory feature, the lack of flatness in the slotted line interferes with accurate determination of the position of the minimum and amplitude of the standing-wave pattern. At very low VSWR's, lack of flatness can prevent any measurement from being made because the sine wave variations that represent the desired signal are obscured by the variations in output owing to variations in probe coupling. However, these variations in coupling do repeat on successive passes of the probe carriage along the slotted line, and if the two curves of the substitution method are recorded, it is possible to subtract the curves graphically and obtain a good-looking sine wave when neither of the original curves resembles a sine wave at all. Therefore, the amplitude and phase of the difference curve, which are the quantities of interest in the substitution method, can be determined accurately by this method under circumstances that ordinarily would make a measurement impossible.

DESCRIPTION OF METHOD

The measuring apparatus is illustrated in Fig. 1. The electrical length of the test section (reference air line plus unknown connectors) is a multiple of a half wavelength. This condition is obtained by adjusting the frequency until the positions of minima for a short-circuit termination are the same with and without the test section in place. For the initial adjustment, the termination is connected directly to the slotted line. The auxiliary slide-screw tuner, which in practice may be part of either the slotted line or the termination, is used to match one to the other, *i.e.*, to eliminate sinusoidal variations in the output of the slotted line. The probe is driven along the slotted line, and an initial curve (curve 1 of Fig. 2) is recorded on the strip chart. This curve would be a straight line but for variations in probe coupling.

Next, a short circuit is placed at the reference plane and the probe is driven along the line again, producing a

* Received by the PGMTT, June 26, 1961; revised manuscript received, July 20, 1961.

† General Radio Company, West Concord, Mass.

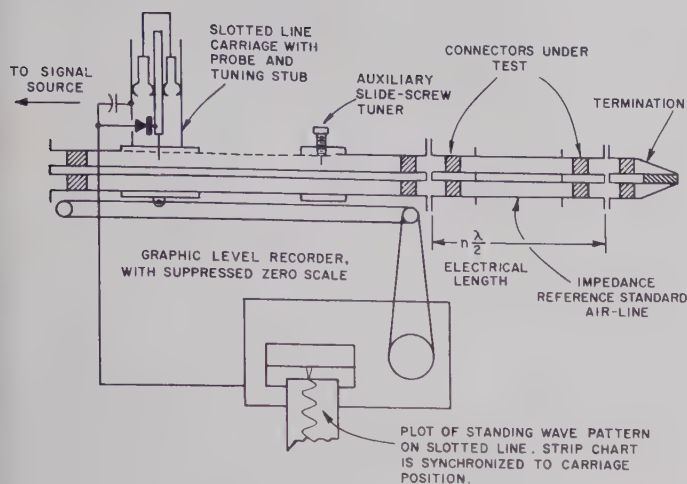


Fig. 1—Block diagram of measuring apparatus.

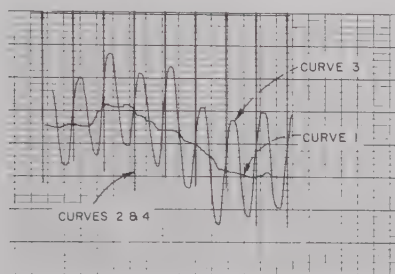


Fig. 2—Typical chart record taken at 8 Gc. Horizontal scale is 1 cm per division, vertical scale is 2 per cent full scale. Curve 1 is the initial condition; the difference between curves 1 and 3 is the VSWR of the connectors. Curves 2 and 4 are taken with a short circuit at the reference plane.

record of wavelength and position of minima on the slotted line. Connectors whose inner and outer conductors do not lie in one plane pose no special problem. The short circuit may be physically located at a distance from the junction of the two connectors. Then the positions of minima on the chart record are corrected by the distance between the physical short-circuit and the desired reference plane.

The test section is placed next between the slotted line and the termination, and a third curve is recorded. As a check on the fact that the electrical length of the test section is one-half wavelength, a fourth curve should be taken with the short circuit placed at the output end of the test section. The position of minima should be the same as before. The strip-chart record is now complete and may be removed for graphical analysis.

With a square-law detector and a linear recorder, the difference between curves 1 and 3 in Fig. 2 is sinusoidal, and the corresponding reflection coefficient may be plotted as a point on the Smith chart. As is shown in the Appendix, this point represents the reflection coefficient of the pair of connectors under test with respect to the characteristic impedance of the reference air line, and referred to the plane of the short circuit. This may be justified intuitively if one considers that the insertion of a reflectionless one-half wavelength section of transmission line of any constant characteristic

impedance would, theoretically, cause no change in the standing-wave pattern. Therefore, any difference between the two curves can arise only if the connectors do not match the air line and thus cause internal reflections within the test section.

DISCUSSION OF ERRORS

The result of this measurement is an approximation, of course, but the degree of approximation is quite good. If the slide-screw tuner is associated with the slotted line, the error in the measured value of the reflection coefficient of the connectors due to these approximations depends on the reflection coefficient of the termination. If the tuner is part of the termination, the error depends on the reflection coefficient of the slotted line.

With the tuner part of the slotted line

$$0 \leq |\Delta\Gamma| \leq 4|\Gamma_t|(|\Gamma_x| + |\Gamma_y|),$$

where

Γ_x, Γ_y = reflection coefficients of unknown connectors

$\Delta\Gamma$ = error

Γ_t = Γ of termination.

With the tuner part of the termination

$$0 \leq |\Delta\Gamma| \leq 4|\Gamma_m|(|\Gamma_x| + |\Gamma_y|),$$

Γ_m = Γ of measuring instrument.

The maximum error is a constant percentage of $|\Gamma_x| + |\Gamma_y|$, and with reasonably low-reflection components, is negligible. For example, a slotted line with $\Gamma_m = 0.01$ (residual VSWR ≈ 1.02) and connectors having $\Gamma_x = \Gamma_y = 0.01$, could cause the measured reflection coefficient to be in error by a maximum of 0.0008.

Attenuation in the test section may cause some error in the measurement if the termination has a finite reflection coefficient. Between the first and the second measurements, the apparent reflection coefficient of the termination as seen by the slotted line is reduced by twice the amount of the attenuation in the test section. Thus, even if the connectors were perfect, there would be a reflection-coefficient reading with the test section in place. If the attenuation of the test section is A db, then the error in the measurement is given by

$$\Delta\Gamma \approx .23A\Gamma_t.$$

Since the test section can be quite short, on the order of a few half-wavelengths at the test frequency, the attenuation of the test section can easily be kept below 0.1 db, corresponding to an error less than 2.3 per cent of Γ_t .

The reflections within the test section can cause an error in setting the frequency to obtain an even multiple of one-half wavelength in the test section. The maximum angular error in radians in setting the electrical length, assuming the worst phase relationship between Γ_x and Γ_y , is

$$\Delta\theta = 2(|\Gamma_x| + |\Gamma_y|).$$

This angular error causes the phase of Γ_l to be rotated from the phase at which it cancelled the slotted-line error. It can be shown that the maximum resulting error is

$$0 \leq |\Delta\Gamma| \leq 4|\Gamma_l|(|\Gamma_x| + |\Gamma_y|).$$

The same sort of error arises if the test section is not set exactly to $n\lambda/2$ for any other reason. In order to estimate the accuracy with which this setting must be made, the following formula is given:

$$\Delta\Gamma = 2\Delta\theta\Gamma_l = 4\pi \frac{\Delta x}{\lambda} \Gamma_l,$$

where Δx is the deviation in the length from $n\lambda/2$. Note that this is an absolute error, and not a percentage error, so the setting is most critical when measuring low-reflection connectors, with a termination having a significant Γ_l .

In general it is better practice to make the tuner a part of the termination rather than of the slotted line, since the slotted-line residual reflection is usually smaller than the termination reflection. The initial tuning adjustment then ensures that the termination is as good as the slotted line, and minimizes the possible errors due to all of the above-mentioned causes.

The lowest VSWR that can be measured depends on the detector noise level. The noise level can be minimized by use of a good mixer crystal and a low-noise amplifier with high selectivity. With these precautions, the noise can be brought down to a level corresponding to a VSWR of 1.0001 to 1.0003, so that a VSWR of 1.001 is well above the noise level.

RESULTS

The above method can be used to measure both coaxial and waveguide connectors. The following results were measured on a newly-developed coaxial connector having a Teflon bead support. The diameter of the outer conductor is 0.5625 inch, imposing an upper-frequency limit of about 9.3 Gc. Using a 15-cm test section, the connectors can be measured every 1 Gc up to 9 Gc. Fig. 2 is a typical chart record taken at 8 Gc. The results for a frequency run on a single pair of connectors over the range of 1 to 9 Gc are shown in Fig. 3. They are plotted both as points on an expanded Smith Chart and as a VSWR-vs-frequency run.

From the Smith Chart plot it is possible to determine that the behavior of this pair of connectors is correct theoretically. In this particular case, both connectors of the mated pair were identical, and the reference plane was chosen to be the centerline of a mated pair. Under these conditions the discontinuities are disposed symmetrically about the reference plane, and all the measured points should lie along the imaginary axis of the Smith Chart. From the distribution of points on the Smith Chart, it is possible to calculate what is wrong

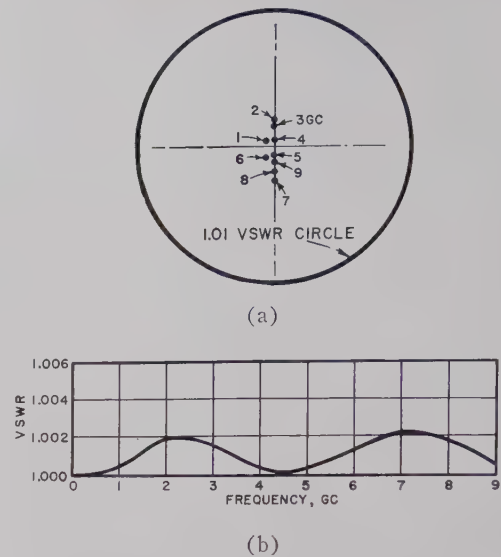


Fig. 3—Test data taken on a pair of precision coaxial connectors. (a) Smith Chart plot of data. (b) Same data plotted as VSWR vs frequency.

with a pair of connectors. In this particular case, the characteristic impedance of the connectors was too high by 0.1 per cent over an electrical length of 3.2 cm. This could have been corrected by an increase of 0.0002 inch in the diameter of the inner conductor over the corresponding physical length. Note that the phase information of the Smith Chart plot is essential to deriving this important design information. VSWR information alone is quite useless in trying to converge on a optimum design in the face of several independent variables such as are present in a coaxial connector with a bead support.

A noteworthy advantage of this technique is that a single slotted line and a single termination can be used over the entire frequency range of the connectors. At each frequency the auxiliary tuner must be set to match the slotted line to the termination, but, owing to the orthogonality of the two adjustments of the slide-screw tuner, this is accomplished easily and quickly.

CONCLUSIONS

The method presented here permits the measurement of the magnitude and phase of the reflection coefficient of coaxial connectors with or without bead supports. The magnitude of the reflection coefficient can be measured with a resolution of 0.0005 and an accuracy on the order of a few per cent. This compares favorably with the accuracy and resolution of a previous method¹ which is limited to the measurement of waveguide and coaxial connectors that do not have bead supports. However, the method described here is limited to the

¹ R. W. Beatty, "Measurements of reflections and losses of waveguide joints and connectors using microwave reflectometer techniques," IRE TRANS. ON INSTRUMENTATION, vol. I-9, pp. 219-226; September, 1960.

measurement of reflection coefficient, and is not adaptable to the measurement of connector losses. A practical advantage of this method is that a given test setup can be used to make measurements from a few hundred megacycles to the cutoff frequency of the slotted line.

This method has been applied to the design of a precision coaxial connector, and it has been found that connectors and bead supports can be designed and constructed with VSWR's smaller than 1.002 over the entire frequency range of the connector, *i.e.*, dc to just below the cutoff frequency. In the future it may be possible to do better, because no theoretical limitation has been reached, but only the practical limitations of holding mechanical tolerances and obtaining adequately smooth surface finishes.

APPENDIX

ANALYSIS OF MEASUREMENT TECHNIQUE

The measurement technique can be analyzed through the use of signal flow graphs as described by Hunton.² The analysis assumes that the connectors and the reference air line are lossless, and that the reflection coefficients of all components are less than 0.1. These conditions are met easily in any practical system.

The equivalent circuit for the complete system is shown in Fig. 4, and the corresponding signal-flow graph is shown in Fig. 5. (Although the method described here uses a slotted line, the signal-flow graph analysis applies equally well to other measuring instruments.) Shurmer³ has shown that "the properties of a lossless junction are uniquely defined by the complex value of reflection coefficient at a reference plane in the measuring line corresponding to matched conditions at the load, and that any such lossless system may therefore be represented by an equivalent system of a matched line with a reactance inserted at some particular plane." Therefore the susceptance B_m in the equivalent circuit of the slotted line simulates all the sources of error in the original slotted line that could cause it to read other than zero reflection coefficient when terminated in a matched load. This includes reflections from supporting beads, end of slot, and output connector, as well as an error in the characteristic impedance of the slotted section, and probe reflections interacting with a mismatched signal source. The equivalent circuit does not include the effect of variation in probe coupling, but this cancels out in the substitution method except for a small modulation effect. This modulation effect causes the amplitude of the sine-wave difference curve to vary by the same percentage as the probe coupling varies. Since the slotted line may easily

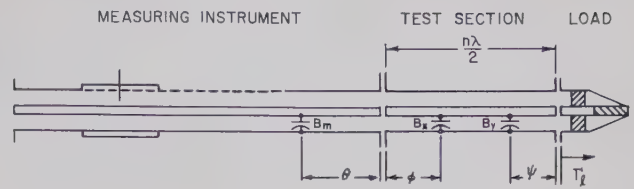


Fig. 4—Equivalent circuit for the analysis of the measurement technique. Shunt susceptances B_m , B_x , and B_y simulate the residual reflection of the slotted line and the reflections of the two unknown connectors.

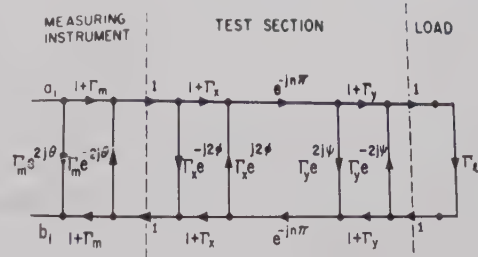


Fig. 5—Signal-flow graph corresponding to the equivalent circuit of Fig. 4.

be flattened to within 1 per cent over the section in use, the error from this source can be held to less than 1 per cent of the magnitude of the measured reflection coefficient.

The reflection coefficients of the unknown connectors are simulated with shunt susceptances located at particular positions along a one-half-wavelength section of constant-impedance transmission line. In the flow graph (Fig. 5), these three discontinuities have been transferred to the reference plane. All reflection coefficients are referred to the characteristic impedance of the precision air line, and the equivalent slotted line also has this characteristic impedance.

The reflection coefficient as measured by the equivalent slotted line must be determined for three conditions: 1) for the initial condition with the termination directly on the slotted line, 2) for the secondary condition with the connectors under test between the slotted line and termination, and 3) for the correct answer that would be obtained with a perfect slotted line and termination. By subtracting 1) from 2) and comparing this answer with 3), one can estimate the magnitude of the error.

The solution for the input reflection coefficient may be written by inspection, and all terms involving third- or higher-order products of Γ will be omitted under the assumption that no reflection-coefficient magnitude exceeds 0.1.

$$\begin{aligned} \Gamma = \frac{b_1}{a_1} &= \Gamma_m e^{2j\theta} + \Gamma_x e^{2j\phi} (1 + 2\Gamma_m) \\ &+ \Gamma_y e^{2j\psi} (1 + 2\Gamma_m + 2\Gamma_x) \\ &+ \Gamma_l (1 + 2\Gamma_m + 2\Gamma_x + 2\Gamma_y), \end{aligned} \quad (1)$$

² J. K. Hunton, "Analysis of microwave measurement techniques by means of signal flow graphs," IRE TRANS. ON MICROWAVE THEORY AND TECHNIQUES, vol. MTT-8, pp. 206-212; March, 1960.

³ H. V. Shurmer, "Transformation of the Smith chart through lossless junctions," Proc. IEE, vol. 105C, pp. 177-182; March, 1958.

where

$\Gamma_m e^{2j\theta}$ = reflection coefficient of measuring equipment referred to its output,

$\Gamma_x e^{-2j\phi}, \Gamma_y e^{2j\psi}$ = reflection coefficients of unknown connectors referred to ends of test section.

Γ_l = reflection coefficient of load referred to its input.

Γ_m, Γ_x , and Γ_y are the shunt susceptances in the equivalent circuit and have the form

$$\Gamma_m = \frac{-jB_m}{2 + jB_m}. \quad (2)$$

These susceptances are placed at electrical angles θ, ϕ , and ψ from the reference plane in the equivalent circuit.

The initial condition is obtained if Γ_x and Γ_y are made equal to 0 in (1). Denoting this by Γ' , we have

$$\Gamma' = \Gamma_m e^{2j\theta} + \Gamma_l (1 + 2\Gamma_m). \quad (3)$$

The difference between (1) and (3) is the apparent connector-reflection coefficient

$$\begin{aligned} \Gamma - \Gamma' &= \Gamma_x e^{-2j\phi} (1 + 2\Gamma_m) \\ &\quad + \Gamma_y e^{2j\psi} (1 + 2\Gamma_m + 2\Gamma_x) \\ &\quad + \Gamma_l (2\Gamma_x + 2\Gamma_y). \end{aligned} \quad (4)$$

The true reflection coefficient of both connectors can be obtained if Γ_m and Γ_l are made equal to zero in (1). Denoting this by Γ'' , we have

$$\Gamma'' = \Gamma_x e^{-2j\phi} + \Gamma_y e^{2j\psi} (1 + 2\Gamma_x). \quad (5)$$

Subtracting (5) from (4) gives the absolute error in measuring the reflection coefficient of the pair of connectors.

$$\begin{aligned} \Delta\Gamma &= \Gamma - \Gamma' - \Gamma'' \\ &= 2\Gamma_m \Gamma_x e^{-2j\phi} + 2\Gamma_m \Gamma_y e^{2j\psi} + 2\Gamma_l \Gamma_x + 2\Gamma_l \Gamma_y. \end{aligned} \quad (6)$$

This is a vector relationship, and it is very unlikely that all the vectors would add up in phase to yield the maximum possible error. However, the maximum value of the above expression is the sum of the magnitudes of the four individual vectors, and the minimum value is zero when the vectors happen to cancel. Therefore,

$$0 \leq |\Delta\Gamma| \leq 2(|\Gamma_m| + |\Gamma_l|)(|\Gamma_x| + |\Gamma_y|). \quad (7)$$

The error is a constant percentage of the sum of the reflection-coefficient magnitudes of the two connectors, and therefore reduces to zero with perfect connectors.

This is the maximum error in the measurement if no attempt is made to match the slotted line to the termination. If they are matched, then $\Gamma' = 0$ and from (3)

$$|\Gamma_m| \approx |\Gamma_l|. \quad (8)$$

Substituting (8) in (7),

$$0 \leq |\Delta\Gamma| \leq 4|\Gamma_l|(|\Gamma_x| + |\Gamma_y|) \quad (9)$$

or

$$0 \leq |\Delta\Gamma| \leq 4|\Gamma_m|(|\Gamma_x| + |\Gamma_y|). \quad (10)$$

If the tuner is part of the slotted line, then the reflection coefficient of the termination is the governing factor in the accuracy of the measurement, and (9) applies. If a tunable termination is used, then the residual error in the slotted line is the governing factor and (10) applies.

The relative advantage of each directional coupler described above depends on the physical arrangement and the desired electrical characteristics of the circuit in which it is to be incorporated. For instance, in an equiphase, symmetrical, parallel-feed antenna array, the hybrid-ring directional coupler has a definite advantage over the parallel-line and branch-line couplers because no phase-compensating element is necessary for the former. Also, the hybrid-ring coupler has broader bandwidth than does the branch-line coupler.

ANALYSIS OF THE HYBRID-RING DIRECTIONAL COUPLER

A general configuration of a hybrid-ring directional coupler is illustrated in Fig. 2. The characteristic admittances of the four arms are equal and normalized. The variable parameters are the two admittances Y_1 and Y_2 , which determine the degree of coupling of the output arms and the impedance matching condition for the input arm.

The analysis of this hybrid-ring coupler consists of the usual procedure of reducing the four-terminal network to a two-terminal network by taking advantage of the symmetry about the plane A-A. For example, when two in-phase waves of unit amplitude are applied to terminals 1 and 4, or to terminals 2 and 3, the current is zero at the plane A-A. As a result, the ring can be open-circuited at this plane and only one half of the circuit needs to be analyzed. This condition is called the even mode and all the parameters associated with this mode are denoted by the subscript e (Fig. 3). When two opposite-phase waves of unit amplitude are applied to terminals 1 and 4, or to terminals 2 and 3, the voltage is zero at the plane A-A. As a result, the ring can be short-circuited at this plane and, again, only one half of the circuit needs to be analyzed. This condition is called the odd mode and all parameters associated with this mode are identified by the subscript o (Fig. 4).

The equivalent circuits for these two modes are also shown in their respective figures. The incident and reflected waves are denoted as a and b , respectively.

Once the scattering matrices for the even and odd modes are known, the reflected waves in each arm can be determined. Then, by superimposing the waves of the two modes, we have the resultant reflected waves in each arm and a single incident wave in one arm.

To find the scattering matrix for each mode, we first derive the admittance matrix for each mode. From Fig. 3(d), we find that the admittance matrix for the even mode is

$$[Y]_e = j \begin{bmatrix} -Y_1 & Y_2 \\ Y_2 & Y_1 \end{bmatrix}. \quad (1)$$

From Figure 4(d), the admittance matrix for the odd mode is

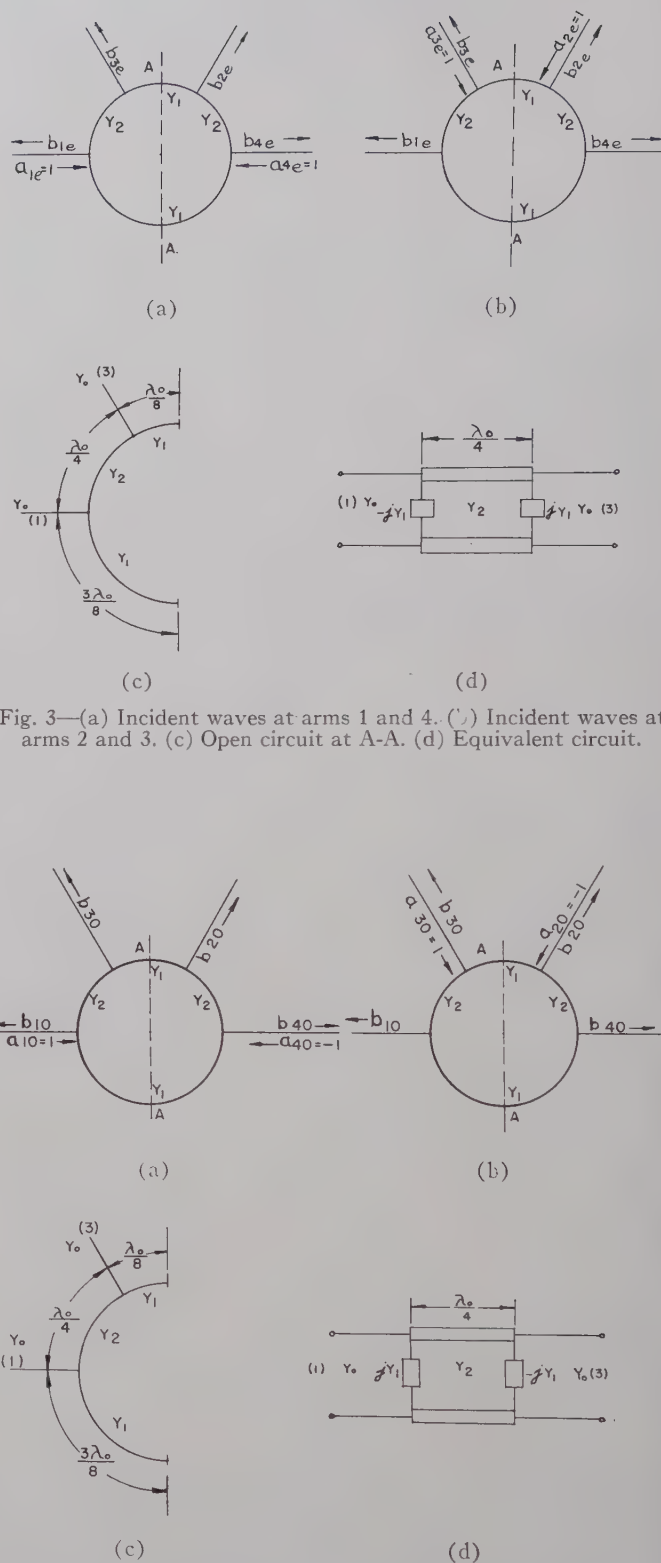


Fig. 3—(a) Incident waves at arms 1 and 4. (b) Incident waves at arms 2 and 3. (c) Open circuit at A-A. (d) Equivalent circuit.

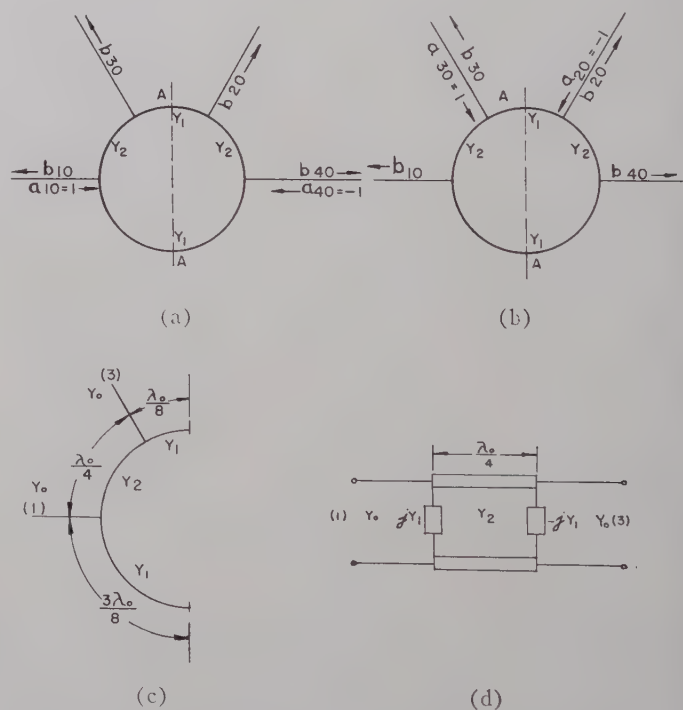


Fig. 4—Odd mode. (a) Incident waves at arms 1 and 4. (b) Incident waves at arms 2 and 3. (c) Short circuit at A-A. (d) Equivalent circuit.

$$[V]_o = j \begin{bmatrix} Y_1 & Y_2 \\ Y_2 & -Y_1 \end{bmatrix}. \quad (2)$$

The scattering matrix is related to the admittance matrix by

$$[S] = [I - V][I + V]^{-1}. \quad (3)$$

Carrying out the matrix operations, we have for the even-mode scattering matrix

$$[S]_e = \begin{bmatrix} \frac{1 - Y_1^2 - Y_2^2 + j2Y_1}{1 + Y_1^2 + Y_2^2} & \frac{-j2Y_2}{1 + Y_1^2 + Y_2^2} \\ \frac{-j2Y_2}{1 + Y_2^2 + Y_2^2} & \frac{1 - Y_1^2 - Y_2^2 - j2Y_1}{1 + Y_1^2 + Y_2^2} \end{bmatrix}, \quad (4)$$

and for the odd-mode scattering matrix

$$[S]_o = \begin{bmatrix} \frac{1 - Y_1^2 - Y_2^2 - j2Y_1}{1 + Y_1^2 + Y_2^2} & \frac{-j2Y_2}{1 + Y_1^2 + Y_2^2} \\ \frac{-j2Y_2}{1 + Y_1^2 + Y_2^2} & \frac{1 - Y_1^2 - Y_2^2 + j2Y_1}{1 + Y_1^2 + Y_2^2} \end{bmatrix}. \quad (5)$$

Recalling that the reflected waves are related to the incident wave by

$$[b] = [S][a], \quad (6)$$

we can now determine the reflected wave in each arm for each mode. Thus, for the first case in which the incident waves are at arms 1 and 4, the reflected waves for the even mode are

$$b_{1e} = b_{4e} = \frac{1 - Y_1^2 - Y_2^2 + j2Y_1}{1 + Y_1^2 + Y_2^2} \quad (7)$$

$$b_{2e} = b_{3e} = \frac{-j2Y_2}{1 + Y_1^2 + Y_2^2}, \quad (8)$$

and for the odd mode are

$$b_{1o} = -b_{4o} = \frac{1 - Y_1^2 - Y_2^2 - j2Y_1}{1 + Y_1^2 + Y_2^2} \quad (9)$$

$$b_{2o} = -b_{3o} = \frac{j2Y_2}{1 + Y_1^2 + Y_2^2}. \quad (10)$$

The resultant waves when the even and odd modes are superimposed are

$$a_1 = 2 \quad (11)$$

$$b_1 = 2 \left(\frac{1 - Y_1^2 - Y_2^2}{1 + Y_1^2 + Y_2^2} \right) \quad (12)$$

$$b_2 = 0 \quad (13)$$

$$b_3 = \frac{-j4Y_2}{1 + Y_1^2 + Y_2^2} \quad (14)$$

$$b_4 = \frac{j4Y_1}{1 + Y_1^2 + Y_2^2}. \quad (15)$$

Similarly, for the second case in which the incident waves are at arms 2 and 3, the reflected waves for the even mode are

$$b_{1e} = b_{4e} = \frac{-j2Y_2}{1 + Y_1^2 + Y_2^2} \quad (16)$$

$$b_{2e} = b_{3e} = \frac{1 - Y_1^2 - Y_2^2 - j2Y_1}{1 + Y_1^2 + Y_2^2}, \quad (17)$$

and for the odd mode are

$$b_{1o} = -b_{4o} = \frac{-2jY_2}{1 + Y_1^2 + Y_2^2} \quad (18)$$

$$b_{2o} = -b_{3o} = - \left(\frac{1 - Y_1^2 - Y_2^2 - j2Y_1}{1 + Y_1^2 + Y_2^2} \right). \quad (19)$$

The resultant waves when the even and odd modes are superimposed are

$$a_3 = 2 \quad (20)$$

$$b_1 = \frac{-j4Y_2}{1 + Y_1^2 + Y_2^2} \quad (21)$$

$$b_2 = \frac{-j4Y_1}{1 + Y_1^2 + Y_2^2} \quad (22)$$

$$b_3 = 2 \left(\frac{1 - Y_1^2 - Y_2^2}{1 + Y_1^2 + Y_2^2} \right). \quad (23)$$

The condition that the input arm in both cases be perfectly matched requires that b_1 in (12) and b_3 in (23) be zero, from which we get

$$Y_1^2 + Y_2^2 = 1. \quad (24)$$

The resultant waves for the two cases are summarized in Figs. 5(a) and 5(b). The output voltage ratio between arms 3 and 4 in Fig. 5(a) is

$$\frac{b_3}{b_4} = -\frac{Y_2}{Y_1}, \quad (25)$$

and the output voltage ratio between arms 1 and 2 in Fig. 5(b) is

$$\frac{b_1}{b_2} = \frac{Y_2}{Y_1}. \quad (26)$$

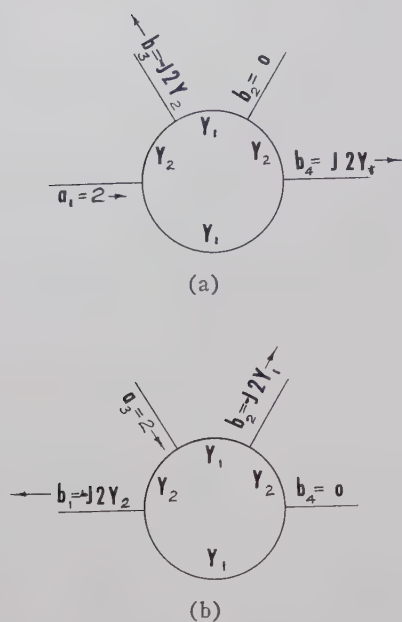


Fig. 5—Incident and reflected waves.

Eq. (25) states that for an input voltage at arm 1 the output voltages at arms 3 and 4 are 180° out of phase. Eq. (26) states that for an input voltage at arm 3, the output voltages at arms 1 and 2 are in-phase.

From the last three equations, one can design a matched power divider with any desired power ratio by using the proper admittances Y_1 and Y_2 . It can be observed that for equal power split, *i.e.*, $P_3/P_4=1$, Y_1 and Y_2 are equal to $1/\sqrt{2}$, which is recognized as the admittance for the well-known 3-db "rat race" ring.

Finally, the scattering matrix characterizing this directional coupler can be written as

$$[S] = \begin{bmatrix} 0 & 0 & -jY_2 & jY_1 \\ 0 & 0 & -jY_1 & -jY_2 \\ -jY_2 & -jY_1 & 0 & 0 \\ jY_1 & -jY_2 & 0 & 0 \end{bmatrix}. \quad (27)$$

The results obtained above are for a single frequency. To find the frequency dependence of this hybrid-ring coupler, it is necessary to use the equivalent circuits and derivations as given in the Appendix. The power emerging from each arm relative to the input power at arm 1 and the input VSWR as a function of frequency for a 3-db and a 10-db power split are plotted in Figs. 6(a) and 6(b), respectively. For comparison, the isolation and VSWR for a branch-line 3-db power split is also plotted on Fig. 6(a), from which we can see that the hybrid-ring coupler has broader bandwidth than the branch-line coupler. Due to the lack of available data on the parallel-line coupler, no comparison can be made with it at this time.

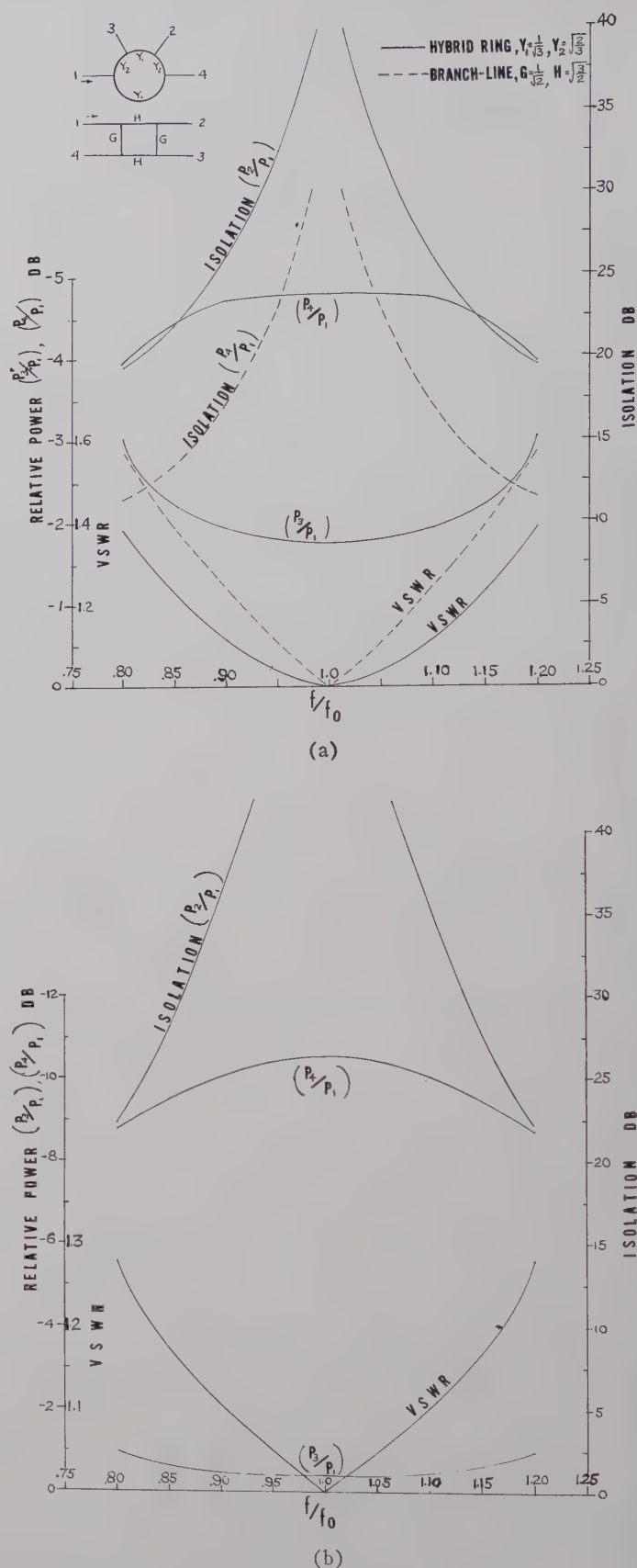


Fig. 6—(a) Relative power and VSWR for 3-db power split. (b) Relative power and VSWR for 10-db power split.

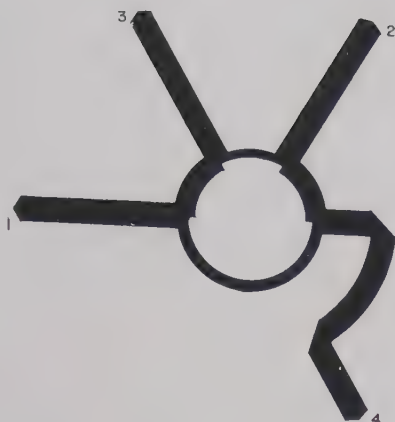


Fig. 7—2.5:1 Stripline power divider.

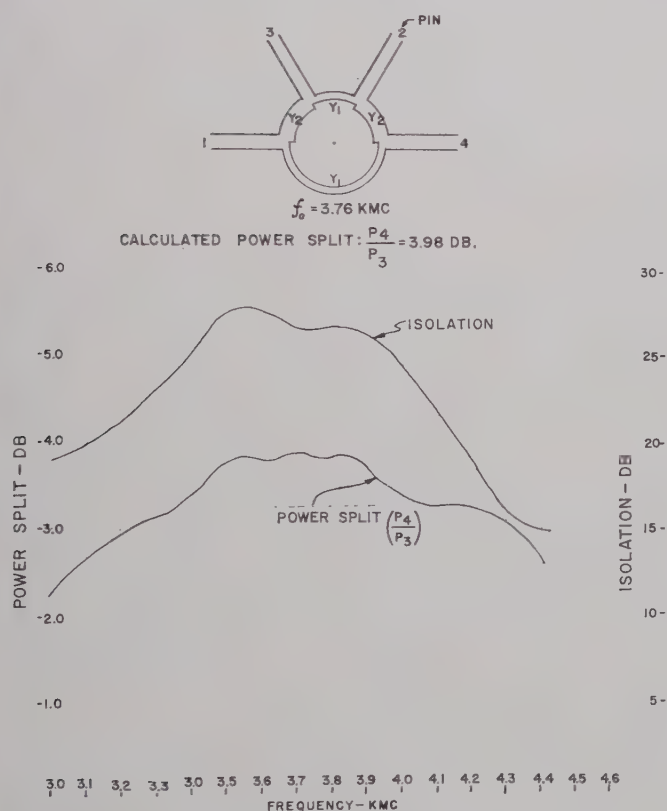


Fig. 8—Power split and isolation of hybrid-ring coupler.

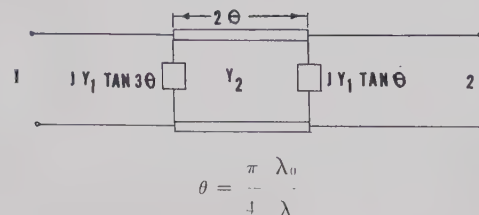


Fig. 9—Equivalent circuit for one-half of the ring circuit for the even mode.

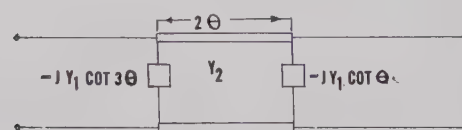


Fig. 10—Equivalent circuit for one-half of the ring circuit for the odd mode.

EXPERIMENTAL RESULTS

A stripline hybrid-ring directional coupler with a power split ratio of 3.98 db between the two output arms at the center frequency of 3.76 kMc was designed and tested. The configuration of this power divider is shown in Fig. 7. The measured power split and isolation are shown in Fig. 8. Close agreement is observed between measured and calculated values. The results obtained in this analysis are valid for any type of transmission line in which a T can be constructed. It might be worthwhile to point out another advantage of using the hybrid-ring coupler as a power divider in place of a Y -junction power divider. Generally, the power-split ratio of a power divider is controlled by varying some characteristic admittances, the allowable values of which are limited by constructional tolerances, in the circuit. For a Y junction, the power-split ratio is proportional to the admittance ratio between its output arms. For a hybrid-ring coupler, the power-split ratio is proportional to the square of the admittance ratio of the two variable admittances in the ring. Therefore, the maximum attainable power split in any transmission line is greater for the hybrid-ring coupler than for the Y -junction power divider.

APPENDIX

Admittance Matrix for the Even Mode

$$Y_{11e} = j(Y_1 \tan 3\theta - Y_2 \cot 2\theta) \quad (28)$$

$$Y_{22e} = j(Y_1 \tan \theta - Y_2 \cot 2\theta) \quad (29)$$

$$Y_{12e} = Y_{21e} = jY_2 \csc 2\theta. \quad (30)$$

Admittance Matrix for the Odd Mode

$$Y_{11o} = -j(Y_1 \cot 3\theta + Y_2 \cot 2\theta) \quad (31)$$

$$Y_{22o} = -j(Y_1 \cot \theta + Y_2 \cot 2\theta) \quad (32)$$

$$Y_{12o} = Y_{21o} = jY_2 \csc 2\theta \quad (33)$$

Scattering Matrix

$$[S] = [I - Y][I + Y]^{-1} = \begin{bmatrix} \frac{1 - Y_{11} + Y_{22} - Y_{11}Y_{22} + Y_{12}^2}{1 + Y_{11} + Y_{22} + Y_{11}Y_{22} - Y_{12}^2} & \frac{-2Y_{12}}{1 + Y_{11} + Y_{22} + Y_{11}Y_{22} - Y_{12}^2} \\ \frac{-2Y_{12}}{1 + Y_{11} + Y_{22} + Y_{11}Y_{22} - Y_{12}^2} & \frac{1 + Y_{11} - Y_{22} - Y_{11}Y_{22} + Y_{12}^2}{1 + Y_{11} + Y_{22} + Y_{11}Y_{22} - Y_{12}^2} \end{bmatrix} \quad (34)$$

1) *For the Even Mode:*

$$[S]_e = \begin{bmatrix} S_{11e} & S_{12e} \\ S_{21e} & S_{22e} \end{bmatrix}. \quad (35)$$

Substituting (28)–(30) into (34), we get

$$S_{11e} = \frac{1 - Y_2^2 + Y_1^2 \tan 3\theta \tan \theta - Y_1 Y_2 \cot 2\theta (\tan 3\theta + \tan \theta) + jY_1 (\tan \theta - \tan 3\theta)}{1 + Y_2^2 - Y_1^2 \tan 3\theta \tan \theta + Y_1 Y_2 \cot 2\theta (\tan 3\theta + \tan \theta) + j[Y_1 (\tan 3\theta + \tan \theta) - 2Y_2 \cot 2\theta]} \quad (36)$$

$$S_{12e} = S_{21e} = \frac{-j2Y_2 \csc 2\theta}{1 + Y_2^2 - Y_1^2 \tan 3\theta \tan \theta + Y_1 Y_2 \cot 2\theta (\tan 3\theta + \tan \theta) + j[Y_1 (\tan 3\theta + \tan \theta) - 2Y_2 \cot 2\theta]} \quad (37)$$

$$S_{22e} = \frac{1 - Y_2^2 + Y_1^2 \tan 3\theta \tan \theta - Y_1 Y_2 \cot 2\theta (\tan 3\theta + \tan \theta) + jY_1 (\tan 3\theta - \tan \theta)}{1 + Y_2^2 - Y_1^2 \tan 3\theta \tan \theta + Y_1 Y_2 \cot 2\theta (\tan 3\theta + \tan \theta) + j[Y_1 (\tan 3\theta + \tan \theta) - 2Y_2 \cot 2\theta]}. \quad (38)$$

2) *For the Odd Mode:*

$$[S]_o = \begin{bmatrix} S_{11o} & S_{12o} \\ S_{21o} & S_{22o} \end{bmatrix}. \quad (39)$$

Substituting (31)–(33) into (34), we get

$$S_{11o} = \frac{1 - Y_2^2 + Y_1^2 \cot 3\theta \cot \theta + Y_1 Y_2 \cot 2\theta (\cot 3\theta + \cot \theta) - jY_1 (\cot \theta - \cot 3\theta)}{1 + Y_2^2 - Y_1^2 \cot 3\theta \cot \theta - Y_1 Y_2 \cot 2\theta (\cot 3\theta + \cot \theta) - j[Y_1 (\cot 3\theta + \cot \theta) + 2Y_2 \cot 2\theta]} \quad (40)$$

$$S_{12o} = S_{21o} = \frac{-j2Y_2 \csc 2\theta}{1 + Y_2^2 - Y_1^2 \cot 3\theta \cot \theta - Y_1 Y_2 \cot 2\theta (\cot 3\theta + \cot \theta) - j[Y_1 (\cot 3\theta + \cot \theta) + 2Y_2 \cot 2\theta]} \quad (41)$$

$$S_{22o} = \frac{1 - Y_2^2 + Y_1^2 \cot 3\theta \cot \theta + Y_1 Y_2 \cot 2\theta (\cot 3\theta + \cot \theta) - jY_1 (\cot 3\theta - \cot \theta)}{1 + Y_2^2 - Y_1^2 \cot 3\theta \cot \theta - Y_1 Y_2 \cot 2\theta (\cot 3\theta + \cot \theta) - j[Y_1 (\cot 3\theta + \cot \theta) + 2Y_2 \cot 2\theta]}. \quad (42)$$

For two in-phase waves of unit amplitude incident on arms 1 and 4, the reflected waves for the even mode are

$$a_1 = 1, \quad a_4 = 1 \quad (43)$$

$$b_{1e} = b_{4e} = S_{11e} \quad (44)$$

$$b_{2e} = b_{3e} = S_{12e}. \quad (45)$$

For two opposite-phase waves of unit amplitude incident on arms 1 and 4, the reflected waves for the odd mode are

$$b_{1o} = -b_{4o} = S_{11o} \quad (46)$$

$$b_{3o} = -b_{2o} = S_{12o}. \quad (47)$$

Adding the even and odd modes together, we have the resultant incident and reflected waves

$$a_1 = 2 \quad (48)$$

$$b_1 = b_{1e} + b_{1o} = S_{11e} + S_{11o} \quad (49)$$

$$b_2 = b_{2e} + b_{2o} = S_{12e} - S_{12o} \quad (50)$$

$$b_3 = b_{3e} + b_{3o} = S_{12e} + S_{12o} \quad (51)$$

$$b_4 = b_{4e} + b_{4o} = S_{11e} - S_{11o}. \quad (52)$$

Similarly, for waves incident on arms 2 and 3, we have for the resultant incident and reflected waves

$$a_3 = 2 \quad (53)$$

$$b_1 = S_{12e} + S_{12o} \quad (54)$$

$$b_2 = S_{22e} - S_{22o} \quad (55)$$

$$b_3 = S_{22e} + S_{22o} \quad (56)$$

$$b_4 = S_{12e} - S_{12o}. \quad (57)$$

ACKNOWLEDGMENT

The author wishes to acknowledge Dr. J. Carpenter, F. Hennessey and A. B. Hadik-Barkóczy for their helpful suggestions concerning this paper.

A Coupled Strip-Line Configuration Using Printed-Circuit Construction that Allows Very Close Coupling*

WILLIAM J. GETSINGER†, MEMBER, IRE

Summary—A new strip-line configuration is presented, applicable to printed-circuit construction, that allows very close coupling to be achieved without resorting to very small coupling gaps and excessively critical dimensions. Graphs of even- and odd-mode fringing capacitances are given. These graphs can be used with simple formulas, which also are given, to determine the dimensions of the configuration that will give specified even- and odd-mode characteristic impedances or shunt capacitances.

The usefulness of the graphs and formulas was demonstrated by using them to design 3-db backward-couplers. The performance of the couplers in this new configuration was typical of similar couplers made in more conventional configurations, as expected. However, the devices shown have an advantage in that they can be manufactured by relatively inexpensive and rapid printed-circuit methods and, since the region between the conductors is solid dielectric, they are unusually rugged.

I. GENERAL

IN working with shielded strip-line, the need for closely coupled strips arises in designing 3-db couplers [1] and broad-band filters [2], [3]. The typical printed-circuit coupled strip-line configuration

consists of two slabs of dielectric sandwiched between parallel ground planes. One of the slabs has two parallel copper strips printed on it. Coupling is achieved by bringing adjacent edges of the two strips close enough to cause appreciable capacitance to exist between the strips. Very close coupling requires that the strips be brought very near each other. For the 3-db coupler, and even more for very broad-band parallel-coupled filters, the spacing between strips becomes too small to be made accurately using practical construction techniques because the allowable tolerance on the spacing decreases as the spacing decreases. Thus, there is a practical limit to the inter-strip capacitance that can be achieved with edge-coupled thin strips.

One solution to this problem has been to orient the coupled strips face-to-face and perpendicular to the ground planes. While this achieves large inter-strip capacitance, it is not always a desirable configuration, because it is difficult to build and it does not interconnect easily with more conventional strip-line circuits in which the strip is parallel to the ground planes. Also, current tends to concentrate at the thin edges of the strips in this construction, causing higher losses.

It is also possible to use thick bars for strips in order to achieve sufficient inter-strip capacitance, but this

* Received by the PGM-TT, June 2, 1961; revised manuscript received, July 7, 1961. This work was supported by the U. S. Army Signal Research and Development Laboratory, Fort Monmouth, N. J., as part of Contract DA 36-039 SC-74862, Sub-Task 3-26-01-701, DA Project 3-26-01-000.

† Electromagnetics Laboratory, Stanford Research Institute, Menlo Park, Calif.

possibility precludes the use of printed-circuit materials and techniques.

II. PROPOSED CONFIGURATION

A cross section of coupled strip-lines using the proposed construction is shown in Fig. 1. The two strips denoted by c are tied together at the ends of the microwave component in which they are used, while in the coupling region, strips c overlap the strip denoted by a . Thus, strips c form a single transmission line coupled to the transmission line formed by strip a . Large coupling between these two lines is achieved by using the parallel-plate capacitance caused by the overlapping. This configuration uses thin strips parallel to the ground planes, and thus is amenable to the use of printed-circuit techniques and materials. It connects easily with conventional strip-line circuits, and does not require critical tolerances. This construction will be denoted by the term *interleaving*.

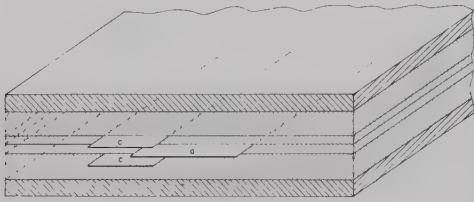


Fig. 1—Proposed strip-line configuration.

It is necessary to use a symmetrical construction with respect to the ground planes, requiring two outer center-strips for one line, in order to prevent radiation into a parallel-plate mode between the ground planes.

III. TECHNICAL DESCRIPTION

The characteristic impedance, Z_0 , of a lossless uniform transmission line operating in the TEM mode is related to its shunt capacitance by:

$$Z_0 \sqrt{\epsilon_r} = \frac{\eta}{(C/\epsilon)} \text{ ohms} \quad (1)$$

where

$\sqrt{\epsilon_r}$ is the relative dielectric constant of the medium in which the wave travels

η is the impedance of free space = 376.7 ohms per square

C/ϵ is the ratio of the static capacitance per unit length between conductors to the permittivity (in the same units) of the dielectric medium. This ratio is independent of the dielectric constant.

The even- and odd-mode impedances of coupled TEM lines [4], [5] can be found by substituting even- and odd-mode capacitances of the lines into (1).

A generalized schematic diagram of shielded coupled-strip transmission line is shown in Fig. 2. The circles represent the coupled conductors. The capacitance to

ground for a single conductor when both conductors are at the same potential is C_{oe} , the even-mode capacitance. The capacitance to ground when the two conductors are oppositely charged with respect to ground is C_{oo} , the odd-mode capacitance. It is assumed that the physical arrangement is such that the even-mode capacitances of the two conductors are the same, thus implying that the odd-mode capacitances are also the same. This paper relates these capacitances to the physical dimensions of the strips.

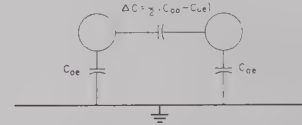


Fig. 2—Generalized schematic diagram.

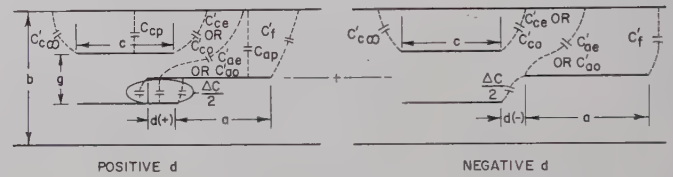


Fig. 3—Capacitances and dimension of proposed strip-line configuration.

The structure of Fig. 1 is composed of parallel planar surfaces. This makes it practical to consider the total capacitance of a given strip to be composed of parallel-plane capacitances plus appropriate fringing capacitances. (Fringing capacitances take into account the distortion of the field lines in the vicinity of the edges of the plane strips.) Fig. 3 relates the various capacitances to the geometry of the structure under consideration. Two diagrams are shown to clarify the definitions for strip a inserted in and withdrawn from strips c . All capacitances are defined on the basis of unit depth into the paper. The parallel-plane capacitances to one ground plane are given by:

$$\frac{C_{ap}}{\epsilon} = \frac{2a}{b} \quad (2)$$

$$\frac{C_{ep}}{\epsilon} = \frac{2c/b}{1 - g/b} \quad (3)$$

Capacitance ΔC , between the center strips, has been plotted as a function of g/b and d/g in Fig. 4. The fringing capacitances were found by conformal mapping techniques. The derivations are given in the Appendix. Graphs of the fringing capacitances as functions of g/b and d/g are given in Figs. 5–9. Notice that the parallel-plate and fringing capacitances are defined to apply from one side of the center line to the nearest ground plane, as shown in Fig. 3.

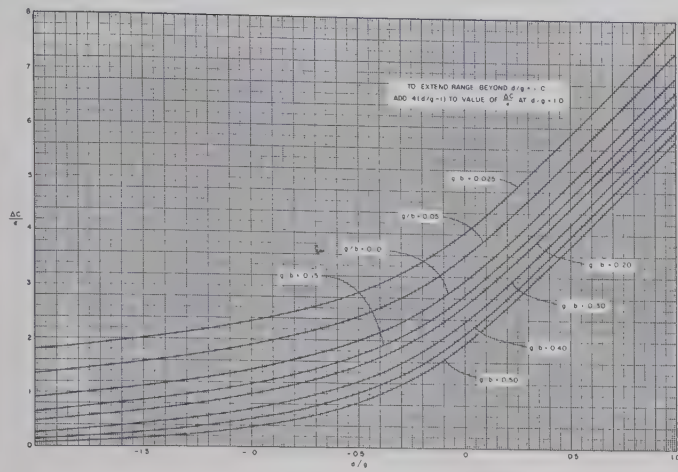


Fig. 4—Inter-strip capacitance.

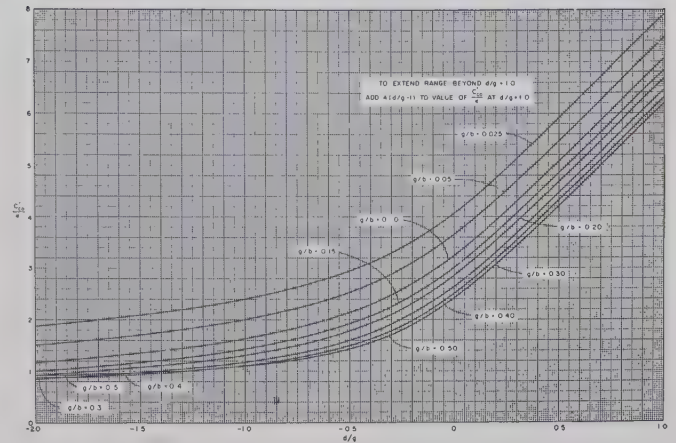
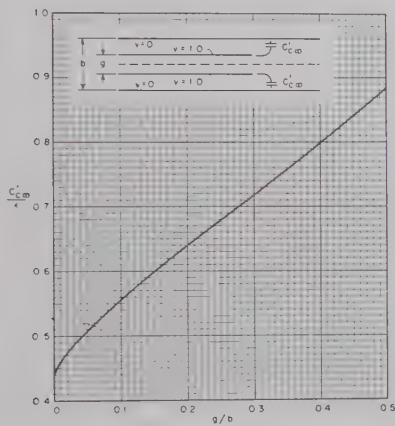
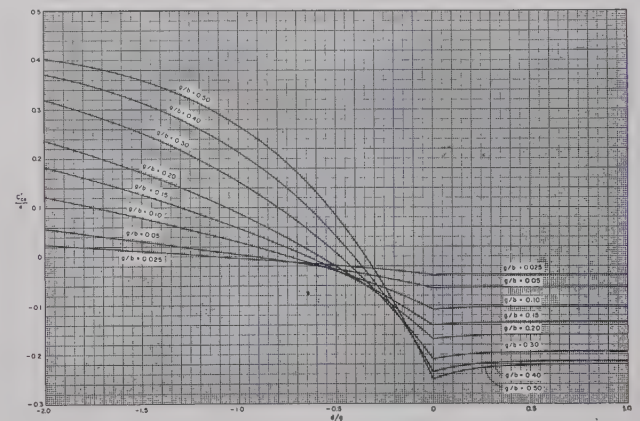
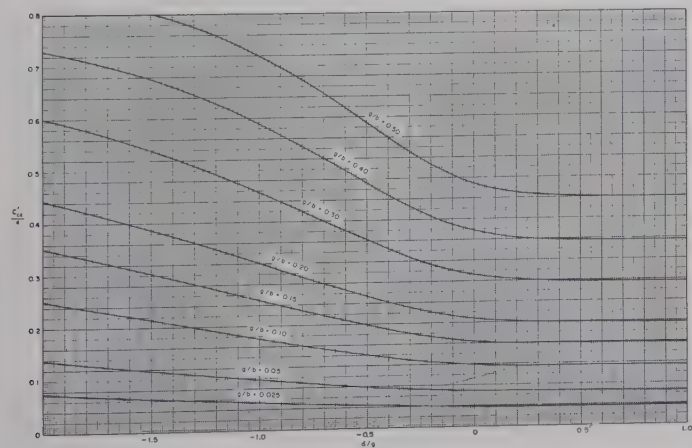
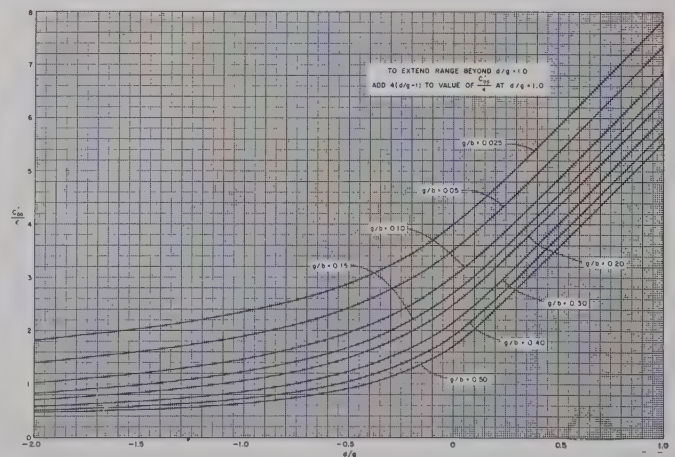
Fig. 7—Odd-mode fringing capacitance of strip c .

Fig. 5—Fringing capacitance of offset thin strip.

Fig. 8—Even-mode fringing capacitance of strip a .Fig. 6—Even-mode fringing capacitance of strip c .Fig. 9—Odd-mode fringing capacitance of strip a .

The total even-mode capacitance for either strip is given by the sum of all of the capacitances to ground associated with that strip when operating in the even mode:

$$C_{oe} = 2[C_{ae}' + C_f' + C_{ap}] = 2[C_{ce}' + C_{co}' + C_{cp}]. \quad (4)$$

Eq. (4) imposes the condition that the even-mode capacitances be the same for the two transmission lines. Similarly,

$$C_{oo} = 2[C_{ao}' + C_f' + C_{ap}] = 2[C_{co}' + C_{co}' + C_{cp}]. \quad (5)$$

When the strips are operating in the odd mode, they are oppositely charged, one positive and one negative, and thus a surface of zero potential exists somewhere between them. The odd-mode fringing capacitances include the capacitance (ΔC) to this wall of zero potential, as well as the capacitances to the actual ground plane.

When identical even-mode capacitances have been imposed on the two lines, it can be shown that the odd-mode capacitances are also the same. Subtraction of (4) from (5) gives

$$C_{oo} - C_{oe} = 2(C_{ao}' - C_{ae}') = 2(C_{co}' - C_{ce}'). \quad (6)$$

The total capacitance between the two lines is denoted ΔC and is given by

$$\Delta C = (1/2)(C_{oo} - C_{oe}). \quad (7)$$

This follows from consideration of the definitions of even- and odd-mode capacitances, as indicated on Fig. 2. The quantity $\Delta C/\epsilon$ is given as a function of d/g and g/b in Fig. 4. The capacitance C_f' is the same as C_{co}' at $g/b=0$, and its value is given by

$$\frac{C_f'}{\epsilon} = 0.441. \quad (8)$$

Through the use of the above relations and figures, it is possible to relate physical dimensions of the given configuration to even- and odd-mode capacitances or impedances.

IV. USE OF THE GRAPHS

Usually an engineer has already determined values of even- and odd-mode impedances, Z_{oe} and Z_{oo} , or even- and odd-mode capacitances, C_{oe} and C_{oo} , and wishes to determine the corresponding physical parameters. A simple procedure accomplishes this. Eq. (7) can be written

$$\Delta C/\epsilon = \frac{1}{2} \left(\frac{C_{oo}}{\epsilon} - \frac{C_{oe}}{\epsilon} \right). \quad (9)$$

Using (1) gives

$$\Delta C/\epsilon = \frac{\eta}{2\sqrt{\epsilon_r}} \left(\frac{1}{Z_{oo}} - \frac{1}{Z_{oe}} \right). \quad (10)$$

Values of b and g are selected, and then used with the value of $\Delta C/\epsilon$ found by (9) or (10) to determine d/g directly from the graph of Fig. 4. Next, having deter-

mined C_{oe}/ϵ from Z_{oe} and (1), it is possible to find C_{co}'/ϵ and C_{ce}'/ϵ from Figs. 5 and 6. These quantities are substituted in (11) to give c/b :

$$c/b = \frac{1 - g/b}{2} \left[\frac{1}{2} C_{oe}/\epsilon - C_{co}'/\epsilon - C_{ce}'/\epsilon \right]. \quad (11)$$

Finally, C_{ae}'/ϵ is found from Fig. 8 and substituted in (12) to give a/b .

$$a/b = \frac{1}{2} \left[\frac{1}{2} C_{oe}/\epsilon - C_{ae}'/\epsilon - 0.441 \right]. \quad (12)$$

Thus, all the physical dimensions are determined. These formulas are accurate for $a/b > 0.35$ and $(c/b)/(1 - g/b) > 0.35$. For narrower widths, simple corrections are possible which will be given in the next section.

Eqs. (11) and (12), used to determine c/b and a/b , were derived from (4) and use no odd-mode capacitances. Similar equations for determining a/b and c/b could have been derived using (5), and then no even-mode capacitances would have been involved. Both methods are equally valid. This paper includes graphs of both even- and odd-mode capacitances for completeness and for possible applications in which one mode may be of greater interest than another, although only the even-mode graphs, Figs. 6 and 8 will be used in the examples to follow.

In a specific device, the feeding lines connected to the coupled region may be constructed of single and dual strips in isolation from each other. The characteristic impedance of a single thin strip between parallel ground planes [6] is either the even- or odd-mode characteristic impedance of strip a when widely separated from strips c . Adding the fringing capacitances from the edges of a thin strip [see (8)] to the parallel plate capacitances from its surfaces [see (2)], and then substituting in (1) gives the following formula for the relative strip width a/b , in terms of the characteristic impedance Z_{os} , for an isolated single strip between parallel ground planes:

$$a/b = \frac{\eta}{4Z_{os}\sqrt{\epsilon_r}} - 0.441 \quad (13)$$

for $a/b > 0.35$.

Similarly, for thin dual strips between parallel ground planes, the fringing capacitances (Fig. 5) are added to the parallel plate capacitances (3) and substituted in (1) to yield

$$c/b = (1 - g/b) \left(\frac{\eta}{4Z_{od}\sqrt{\epsilon_r}} - C_{co}'/\epsilon \right) \quad (14)$$

for $(c/b)/(1 - g/b) > 0.35$, as the relation between relative strip width c/b , and the characteristic impedance, Z_{od} . Corrections for narrow strips will be given in the next section.

V. CONSIDERATIONS OF ACCURACY

If the strip widths a and c are allowed to become too small, then there is interaction of the fringing fields from the two edges, and the decomposition of total ca-

capacitance into parallel-plane capacitance and fringing capacitances (which are based on infinite strip widths), no longer is accurate. Cohn [1], [6] shows that for a single strip centered between parallel planes, the error in total capacitance from this cause is about 1.24 per cent for $w/(b-t)=0.35$, where w is the width of the strip, t is its thickness, and b is again the ground-plane spacing. If maximum error in total capacitance of approximately this magnitude is allowed, then it is necessary that $a/b > 0.35$ and $[(c/b)/(1-g/b)] > 0.35$.

Should these inequalities be too restricting, it is possible to make approximate corrections based on increasing the parallel-plate capacitance to compensate for the loss of fringing capacitance due to interaction of fringing fields. If an initial value, a_1/b is found to be less than 0.35, a new value, a_2/b can be used, where

$$a_2/b = (0.07 + a_1/b)/1.20 \quad (15)$$

provided $0.1 < a_2/b < 0.35$. A similar formula for correcting an initial value c_1/b , gives a new value, c_2/b as

$$c_2/b = [0.07(1 - g/b) + c_1/b]/1.20 \quad (16)$$

provided g/b is fairly small and $0.1 < (c_2/b)/(1-g/b) < 0.35$. These formulas are based on a linear approximation to the exact fringing capacitance of a single thin strip for a width to plate-spacing ratio between 0.1 and 0.35. As the relative strip width becomes narrower than 0.35, the fringing capacitance, defined as total capacitance less parallel plate capacitance, decreases from the value C_f' or C_{∞}' used in the derivations and graphs. The total capacitance is given by substituting into (1) the exact thin-strip formula for Z_o given in [6]. Eqs. (15) and (16) add sufficient parallel-plate capacitance to compensate for the loss of fringing capacitance. The loss of fringing is assumed to vary linearly below a relative width of 0.35, and it is also assumed that C_{∞}' decreases by the same amount as does C_f' . Although the formulas are analytically only approximate for coupled strips, they are sufficiently accurate for practical use because they do no more than give a small correction to a quantity that is reasonably close to the exact value. They can be used with both isolated and coupled strips.

The discontinuity in the slope of C_{ae}'/ϵ in Fig. 8 at $d/g=0$ is not a physical phenomenon, but is a mathematical result of considering dimension a to extend to the edge of strips c for positive d , while for negative d , dimension a extends to the edge of strip a , as shown in Fig. 3. The only practical effect of this situation is that the width of strip a is equal to dimension a when d is negative, but when d is positive the width of strip a is equal to the sum of dimensions a and d . This is shown clearly in Fig. 3.

In deriving the fringing capacitance, one of the assumptions made was that the strip was infinitely thin. Investigation of a graph given by Cohn [1], [6] shows that the fringing capacitance, C_f'/ϵ from a strip centered

between parallel ground planes increases by about 2 per cent for a 1 per cent increase in the ratio of strip thickness to plate spacing, for a very thin strip. Fringing capacitance is usually only part of the total capacitance involved in a strip-line circuit, so that for many situations, a strip no thicker than 1 or 2 per cent of the associated parallel-plate separation can be considered thin without serious error.

The derivations for the fringing capacitances are exact for infinitely thin strips with dimension a (see Fig. 3) extending infinitely far to the right while dimension c extends infinitely far to the left. The computed values from which the curves were plotted were accurate to three places after the decimal, although the curves themselves cannot be relied on to be closer than about ± 5 in the third significant figure, as plotted.

For insertion of the strip a between strips c beyond the maximum plotted, $d/g=1.0$, the even-mode values C_{ae}'/ϵ and C_{ce}'/ϵ do not change from their values at $d/g=1.0$, while $\Delta C/\epsilon$ and the odd-mode values C_{ao}'/ϵ and C_{co}'/ϵ , can be found simply by adding $4(d/g-1)$ to their values at $d/g=1$. For spacing between strips c greater than $g/b=0.5$, or for a separation $d/g < -2.0$, probably some different strip-line construction would be more suitable.

Finally, it should be noted that if these curves predict a value of d positive and approximately equal to or greater than c , the result is not valid. When strip a protrudes all the way between strips c in this manner, it merely means that too great a value of g/b was selected to realize the odd-mode capacitance. This restriction may be expressed mathematically by requiring that $d < c - (g/2)$. If this condition is not met for a desired set of capacitances, then it is necessary to make g/b smaller and determine new dimensions.

VI. APPLICATIONS

The graphs and procedures described above have been used to design strip-line 3-db couplers [1], [5].

A 3-db coupler was designed to have an input impedance of 50 ohms. Fig. 10 shows pertinent details of its construction. The dielectric material used, Rexolite #2200, has a published dielectric constant of 2.77. This material is commercially available with sheets of 0.001-inch copper bonded to the sides.

A center-frequency coupling value of -2.8 db, rather than -3.0 db, was chosen to allow for an expected decrease in coupling at frequencies away from the center frequency. Use of the formulas of [1] or [5] gave values of 125.15 ohms for Z_{oe} and 19.95 ohms for Z_{oo} . Substitution of these values in (1) gave $C_{oe}/\epsilon = 1.81$ and $C_{oo}/\epsilon = 11.34$. Using the laminate thicknesses shown on Fig. 10, it was found that $g/b = 0.0964$. Eq. (9) and Fig. 4 showed the required value of d/g to be 0.445. Then, use of the procedure described in the preceding section, including Eqs. (11) and (12), gave $a/b = 0.284$ and $c/b = 0.107$. (In the coupler constructed, a value of 0.097 was used for c/b because Fig. 5 had not been pre-

pared, and an approximate method was used to find C_{∞}/ϵ_r .) The coupler was made one-quarter wavelength long in the dielectric at the center frequency of 200 Mc.

Performance curves for this coupler are shown in Fig. 11. The behavior of the coupler is typical of 3-db backward couplers made in other configurations.

A second 3-db coupler was made on another project for parametric amplifier work. This coupler was designed to have a center frequency of 1000 Mc. In this design the strip widths were widened in accordance with (15) and (16) for correcting narrow strips. The dimensions are shown in Fig. 12. The bulk of input reflections were caused by reactance of the right-angle bends joining the feed lines to the coupling region. The purely capacitive tuning screws shown were much more effective in cancelling the reflections than were modifications of the structure of the bend or tabs on the feed lines at the bends. The greater effect of the bend reactance as frequency increases is shown in the performance curves for this coupler, Fig. 13. Fig. 14 is a photograph of the coupler.

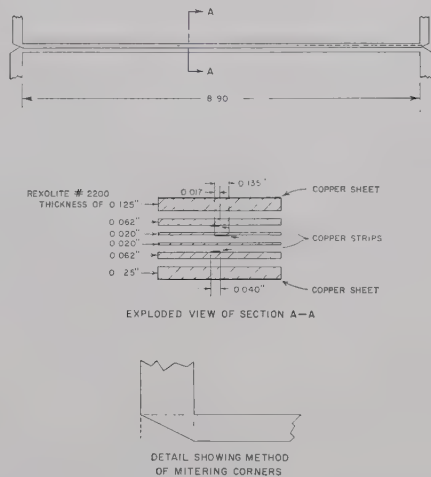


Fig. 10—Details of construction of 200-Mc 3-db backward coupler.

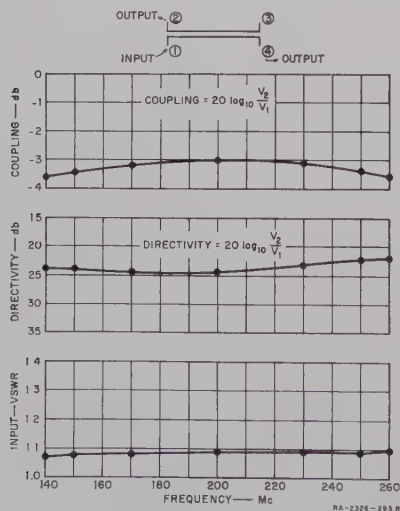


Fig. 11—Performance of 200-Mc 3-db backward coupler.

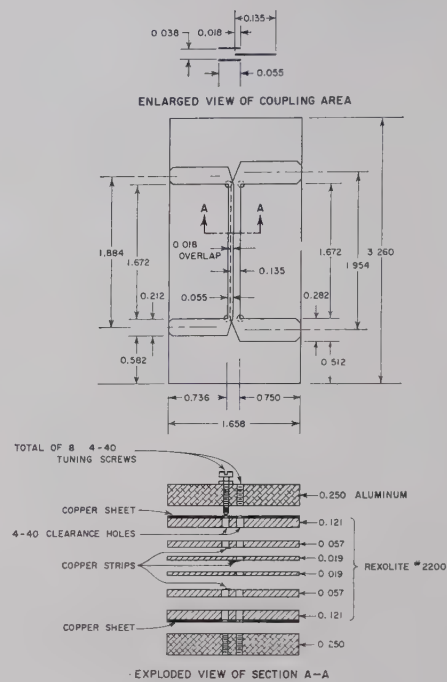


Fig. 12—Details of construction of 1000-Mc 3-db backward coupler.

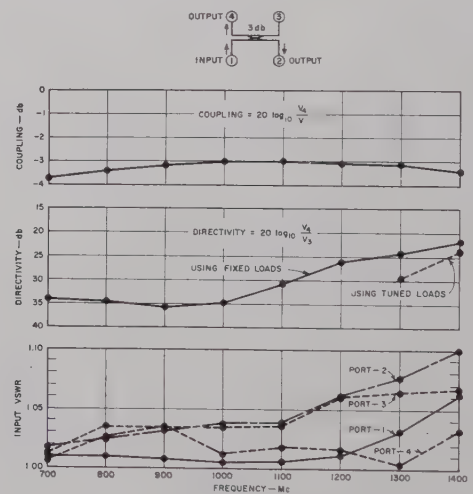


Fig. 13—Performance of 1000-Mc 3-db backward coupler.

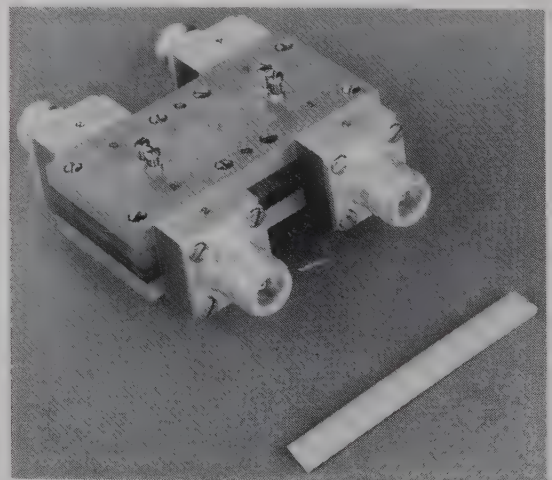


Fig. 14—1000-Mc 3-db backward coupler.

APPENDIX

DERIVATION OF FRINGING CAPACITANCES

A. Preliminary

It is desired to determine the static fringing capacitances shown on the structure of Fig. 3 by means of conformal mapping techniques [7], [8]. This can be done by subjecting the boundaries of the structure to transformations under which capacitance is invariant, and that lead to a new structure for which capacitance is known. Subtraction of parallel-plate capacitances of the original structure from the total capacitance then leaves the fringing capacitances. The analysis will be limited to structures in which strips c and a are so wide that interaction between fringing fields of the two edges of a single strip are negligible. As discussed in Section V, this requires that the approximate relations $a/b > 0.35$ and $[(c/b)/(1-g/b)] > 0.35$ be held. Under these conditions it is possible to let strip c extend infinitely far to the left, and strip a infinitely far to the right without disturbing the fringing fields appreciably in the region where the two strips interact. Also, the electric field can lie parallel to the horizontal center line where no conductor exists, but cannot cross it because of the symmetry of the structure, assuming the two conducting strips c are always at the same potential with respect to each other. Therefore a magnetic wall can be placed along the center line extending infinitely far to the left from the left edge of strip a . These modifications allow analysis of only half of the total symmetrical structure, as shown in Fig. 15(a). The mathematical model is shown in Fig. 15(b). Conductors are indicated by solid lines, and the magnetic wall is indicated by a dashed

line. The upper-case script letters of Fig. 15(b) denote pertinent points of the structure and will serve as references when transformations to different complex planes are made. The values chosen for the various points on the z plane will prove convenient under transformation.

The analysis consists essentially in transforming the contours of the structure on the z plane into a parallel-plate representation on the w plane, where capacitance can be computed directly. This procedure is complicated by having three conductors while only two are desired for a parallel-plate representation. This complication will be resolved by showing that there exists a surface of zero potential, which can be replaced by an electric wall, running between the conducting strips for the odd mode, and that this same surface can be treated as a magnetic wall for the even mode. Fig. 15(c) shows the wall running between points g , a saddle-point, and ∞ , following some curve whose exact shape is unknown. A subsequent transformation will rectify this curve, dividing the structure into two parts, each of which has only two conductors and can be further analyzed separately.

As a first step, the interior of the polygon $\alpha\beta\gamma\delta\alpha'$ will be mapped onto the upper half of a z_1 plane as shown in Fig. 16(a). The mapping is given by Kober [9] as

$$z = \frac{1-\alpha}{2} \ln(z_1 - 1) + \frac{1+\alpha}{2} \ln(z_1 + 1). \quad (17)$$

The points noted on the z plane are related to points on the real axis of the z_1 plane by

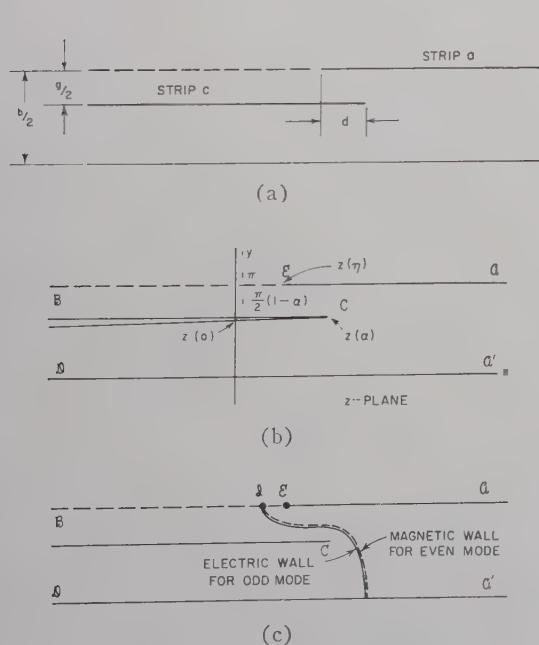


Fig. 15—Cross section of proposed configuration on z plane.

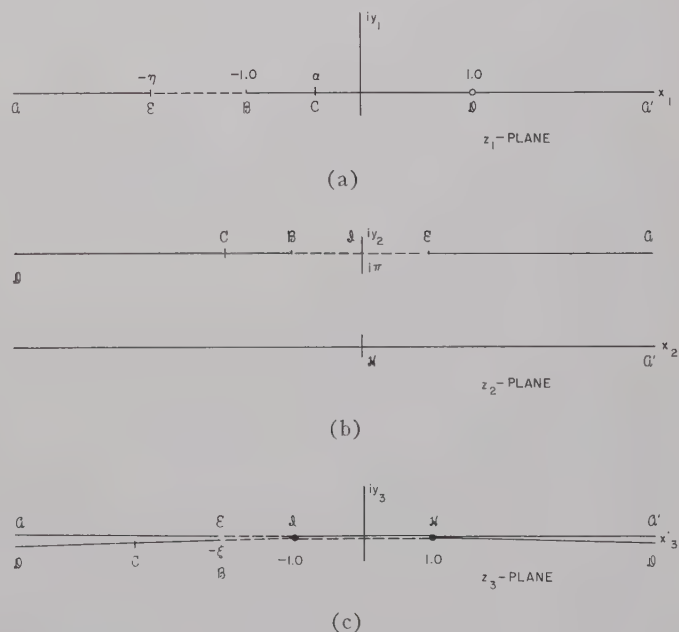


Fig. 16—Intermediate transformations from z plane.

$$\begin{aligned}
z(0) &= i \frac{\pi}{2} (1 - \alpha) \\
z(\alpha) &= \frac{1 - \alpha}{2} \ln(1 - \alpha) + \frac{1 + \alpha}{2} \ln(1 + \alpha) \\
&\quad + i \frac{\pi}{2} (1 - \alpha) \\
z(\eta) &= \frac{1 - \alpha}{2} \ln(1 + \eta) + \frac{1 + \alpha}{2} \ln(\eta - 1) + i\pi. \quad (18)
\end{aligned}$$

Notice that

$$\begin{aligned}
\eta &> 1.0 \\
-1.0 &< \alpha < 1.0. \quad (19)
\end{aligned}$$

The small circle at point \mathfrak{D} indicates an infinitely small gap at that point, such that the conductors on either side may be at different potentials. Point \mathfrak{D} is removed to $-\infty$ under the next transformation, which is to a z_2 plane. This transformation will place points \mathfrak{B} and \mathfrak{E} equidistant from the y_2 axis, as shown in Fig. 16(b). The transformation is

$$z_1 = 1 + \sqrt{2(\eta + 1)} e^{z_2}. \quad (20)$$

The source of this transformation, as with most transformations used in this chapter, is a combination of experience and the use of references [7]–[10]. However, although the derivations of the transformations may not be obvious, they may be checked at points of interest simply by substituting values of the independent variable and observing that the transformation gives the correct result for the dependent variable.

The structure on the z_2 plane will now be related to the given structure. The conductor between \mathfrak{A}' and \mathfrak{D} corresponds to the ground plane on the given structure. The conductor between \mathfrak{A} and \mathfrak{E} corresponds to strip a in the given structure, and the conductor between \mathfrak{B} and \mathfrak{D} corresponds to one of the strips c in the given structure. The z_2 plane structure is symmetrical about the y_2 axis. Under even-mode excitation both conducting strips a and c are at the same potential, and thus no electric field lines cross the y_2 axis. Therefore, a magnetic wall can be placed along the y_2 axis and left and right halves may be analyzed separately. Under odd-mode excitation the conducting strips a and c are oppositely charged with respect to the ground plane, and thus all electric field lines crossing the y_2 axis must cross normal to that axis to preserve symmetry. Therefore, an electric wall at zero potential may be placed along the y_2 axis and left or right half only need be analyzed. Notice that script letters \mathfrak{K} and \mathfrak{J} have been assigned to the end points of the line of symmetry. By means of the transformation

$$z_2 = \text{arc cosh } z_3 \quad (21)$$

the interior of the polygon $\mathfrak{A}\mathfrak{J}\mathfrak{K}\mathfrak{A}'$ goes into the upper

half of the z_3 plane, and the polygon $\mathfrak{J}\mathfrak{D}\mathfrak{K}$ goes into the lower half of the z_3 plane, as shown in Fig. 16(c). Only that portion of the x_3 axis between \mathfrak{J} and \mathfrak{K} is common to both upper and lower half-planes, and for this reason the x_3 axis is shown split beyond \mathfrak{K} and \mathfrak{J} . The solid line (conductor) between \mathfrak{K} and \mathfrak{J} is to be used for odd-mode analysis, while the dashed line (magnetic wall) is to be used for even-mode analysis.

On the z_3 plane \mathfrak{K} and \mathfrak{J} fall at $+1.0$ and -1.0 , as can be determined by substituting the known values of \mathfrak{K} and \mathfrak{J} on the z_2 plane into (21). In order to find $z_3(\mathfrak{B})$ it is necessary to work from the z_1 plane, where Kober [9] shows that $z_1(\mathfrak{B}) = -1.0$. Then, by successive substitution and manipulation of (20) and (21), it is found that

$$z_3(\mathfrak{B}) = -\frac{1}{2} \left[\frac{2}{\sqrt{2(\eta + 1)}} + \frac{\sqrt{2(\eta + 1)}}{2} \right] = -\xi \quad (22)$$

where $-\xi$ is the value of $z_3(\mathfrak{B})$ on the z_3 plane. Notice that

$$\xi > 1.0. \quad (23)$$

By the symmetry of the z_2 plane with respect to the imaginary axis and the nature of the transformation (21),

$$z_3(\mathfrak{E}) = z_3(\mathfrak{B}) = -\xi \quad (24)$$

although it should be noted that \mathfrak{E} and \mathfrak{B} are on opposite sides of a branch cut on the z_3 plane.

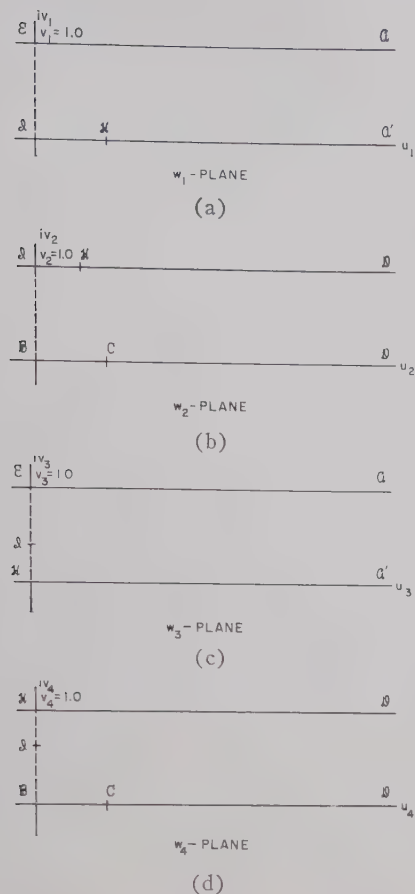
B. Odd-Mode Fringing Capacitance—Strip a

Now consider the odd mode, and investigate the fringing capacitance of strip a , which is associated with point \mathfrak{E} . The upper half of the z_3 plane is transformed to a parallel plate region on the w_1 plane by

$$z_3 = (\tfrac{1}{2}) [(\xi - 1) \cosh \pi w_1 - (\xi + 1)] \quad (25)$$

as shown on Fig. 17(a).

The total capacitance on the w_1 plane is parallel-plate capacitance. The amount of capacitance per unit permittivity between the w_1 -plane origin and some location $u_1 > 0$ is equal to u_1 , for unit depth into the paper, because there is unit spacing between the conducting planes. This is the odd-mode capacitance to one ground plane from strip a . The corresponding capacitance for strip a on the z plane is the fringing capacitance from the vicinity of \mathfrak{E} plus the parallel-plate capacitance, which will be defined as the amount of parallel-plate capacitance from strip a to ground, measured between $z(\alpha)$ (Edge \mathfrak{C}) and the mapping of u_1 mentioned above onto the z plane. Mathematically, the z -plane parallel-plate capacitance, relevant to some value u_1 on the w_1 plane, has the value $(1/\pi) \text{Re}[z(u_1) - z(\alpha)]$, as can be deduced from Fig. 15(b). Alternatively this defines the fringing capacitance in the odd

Fig. 17—Final configurations on w planes.

mode from strip a to one ground plane as the difference between the total capacitance to some value u_1 on the w_1 plane and the parallel-plate capacitance out to the mapping of u_1 on the z plane, as u_1 approaches infinity. This odd-mode fringing capacitance from strip a will be denoted by C_{ao}'/ϵ . From the above discussion,

$$C_{ao}'/\epsilon = \lim_{u_1 \rightarrow \infty} \left\{ u_1 - \operatorname{Re} \frac{1}{\pi} [z(u_1) - z(\alpha)] \right\}. \quad (26)$$

From a physical point of view, this definition of parallel-plane capacitance assumes that strips a and c always overlap. Mathematically, the definition of parallel-plane capacitance is wholly arbitrary, so that this physical defect in definition need not be ameliorated until the mathematical derivation is complete. When the proper substitutions have been made in (26), allowing the approach to the limit to take place, sufficient manipulation gives the final expression for C_{ao}'/ϵ as

$$C_{ao}'/\epsilon = \operatorname{Re} \frac{1}{\pi} \left[z(\alpha) - \ln \frac{(\eta + 3) - 2\sqrt{2(\eta + 1)}}{4} \right]. \quad (27)$$

C. Odd-Mode Fringing Capacitance—Strip c

Strip c is associated with points $\mathcal{B}\mathcal{C}\mathcal{D}$. Eq. (21) mapped the polygon $\mathcal{D}\mathcal{H}\mathcal{G}\mathcal{B}\mathcal{D}$ of the z_2 plane onto the lower half of the z_3 plane (Fig. 16). The lower half of

the z_3 plane is next mapped onto the w_2 plane by means of the transformation

$$z_3 = -\frac{1}{2}[(\xi + 1) + (\xi - 1) \cosh \pi \omega_2]. \quad (28)$$

Assuming unit depth into the paper, the total capacitance per unit permittivity as a function of u_2 is equal to u_2 . The parallel-plate capacitance to the adjacent ground plane of one of the strips c may be defined as

$$\frac{\operatorname{Re}[z(\alpha) - z(u_2)]}{(\pi/2)(1 - \alpha)},$$

from Fig. 15, in a manner similar to that defined for strip a . The difference between total capacitance and parallel-plate capacitance, relevant to some value of u_2 approaching infinity, is the odd-mode fringing capacitance of strip c , and will be denoted by C_{co}'/ϵ . Therefore, from the above discussion,

$$C_{co}'/\epsilon = \lim_{u_2 \rightarrow \infty} \left\{ u_2 - \operatorname{Re} \frac{[z(\alpha) - z(u_2)]}{(\pi/2)(1 - \alpha)} \right\}. \quad (29)$$

Again, substitution, passing to the limit, and manipulation yields the final result.

$$C_{co}'/\epsilon = \operatorname{Re} \frac{1}{\pi} \left[\frac{1 + \alpha}{1 - \alpha} \ln 2 + \ln \frac{8(\eta + 1)}{(\eta + 3) - 2\sqrt{2(\eta + 1)}} - \frac{2}{1 - \alpha} z(\alpha) \right]. \quad (30)$$

D. Even-Mode Fringing Capacitance—Strip a

In analyzing the even mode, the two strips, a and c are at the same potential, as previously discussed, and the plane $\mathcal{H}\mathcal{C}$ may be considered as a magnetic wall. For strip a , associated with point \mathcal{E} , the transformation from the upper half of the z_3 plane, Fig. 15(c) to a w_3 plane, Fig. 16(c), is

$$z_3 = (1/2)[(\xi + 1) \cosh \pi \omega_3 - (\xi - 1)]. \quad (31)$$

The definition and discussion of parallel-plate capacitance for strip a given in connection with odd-mode capacitance holds for this case also. The even-mode fringing capacitance is given by the difference between total capacitance and parallel-plate capacitance, so that by analogy with (26), the even-mode fringing capacitance for strip a is

$$C_{ae}'/\epsilon = \lim_{u_3 \rightarrow \infty} \left\{ u_3 - \operatorname{Re} (1/\pi) [z(u_3) - z(\alpha)] \right\}. \quad (32)$$

The substitutions and manipulations are much like those used to find C_{ao}'/ϵ . The result is

$$C_{ae}'/\epsilon = \operatorname{Re} \frac{1}{\pi} \left[z(\alpha) - \ln \frac{(\eta + 3) + 2\sqrt{2(\eta + 1)}}{4} \right]. \quad (33)$$

E. Even-Mode Fringing Capacitance—Strip c

The same reasoning and procedure may be used in finding the even-mode fringing capacitance from strip c as were used for the other three fringing capacitances

and, in fact, this was done in the original work on this problem. However, only three capacitances are required to describe a parallel coupled TEM structure, as in Fig. 2, and this indicates the possibility that if three fringing capacitances are known, the fourth may be related to them by a function which is independent of the geometry of the structure. This geometry-independent function, applicable to any parallel-coupled TEM structure that can be represented schematically by Fig. 2, is given by (6), which upon manipulation may be written as

$$C_{ce}'/\epsilon = C_{co}'/\epsilon - C_{ao}'/\epsilon + C_{ae}'/\epsilon = C_{co}'/\epsilon - \Delta C/\epsilon, \quad (34)$$

using (7) for the definition of $\Delta C/\epsilon$. Thus, the unknown fringing capacitance, C_{ce}'/ϵ , can be written as a linear combination of the other three fringing capacitances. Substitution of (27), (30), and (33) into (34) yields

$$C_{ce}'/\epsilon = \text{Re} \frac{1}{\pi} \left[\frac{1+\alpha}{1-\alpha} \ln 2 - \frac{2}{1-\alpha} z(\alpha) + \ln \frac{8(\eta+1)}{(\eta+3) + 2\sqrt{2(\eta+1)}} \right]. \quad (35)$$

This result agrees with that found for C_{ce}'/ϵ directly from the mapping.

F. Definition of Parallel-Plate Capacitance of Strip a

In mathematically determining the fringing capacitances for the centered center-strip, strip a , the equivalent parallel-plate capacitor on the z plane, Fig. 15, is extended to the right from $z(\alpha)$ for all cases. In considering the physics of the situation, it is apparent that a more realistic definition would have the parallel-plate capacitance for strip a computed from the edge of strip a , $z(\eta)$, except when strip a is shielded by strip c , and then the parallel-plate capacitance would be computed from the edge of the shielding strip c at $z(\alpha)$. In order for the plotted curves to agree with this physical definition, it was necessary to add a parallel-plate capacitance to computed values of C_{ao}'/ϵ and C_{ae}'/ϵ . This parallel-plate capacitance was added only when $z(\eta) > z(\alpha)$, and simply replaced that subtracted in the derivation. The value added to C_{ao}'/ϵ and C_{ae}'/ϵ was equal to $[z(\eta) - z(\alpha)]/\pi$. In terms of dimensions, this additional capacitance per unit permittivity can be expressed as $|2d/b|$ for $d < 0$. The plotted curves for strip a , Figs. 8 and 9, incorporate this term.

G. Derivation of C_{co}'/ϵ

The fringing capacitance C_{co}'/ϵ is that from the edge of a strip located between a parallel magnetic wall and a parallel electric wall, as indicated on the graph, Fig. 5. It can be specified mathematically as

$$C_{co}'/\epsilon = \lim_{d \rightarrow -\infty} C_{co}'/\epsilon \text{ or } C_{ce}'/\epsilon. \quad (36)$$

From Fig. 15 it can be seen that $z(\eta) \rightarrow \infty$ as $d \rightarrow -\infty$,

and on Fig. 16(a) this corresponds to $\eta \rightarrow \infty$. Thus, using (30),

$$C_{co}'/\epsilon = \lim_{\eta \rightarrow \infty} \text{Re} \frac{1}{\pi} \left[\frac{1+\alpha}{1-\alpha} \ln 2 + \ln \frac{8(\eta+1)}{(\eta+3) - 2\sqrt{2(\eta+1)}} - \frac{2}{1-\alpha} z(\alpha) \right] \quad (37)$$

or

$$C_{co}'/\epsilon = \frac{1}{\pi} \left[\frac{1+\alpha}{1-\alpha} \ln 2 + \ln 8 - \frac{2}{1-\alpha} \text{Re} z(\alpha) \right]. \quad (38)$$

The real part of $z(\alpha)$ is given in (18), and from Fig. 15, α is found to be related to g/b by

$$\alpha = 2g/b - 1. \quad (39)$$

Thus, C_{co}'/ϵ can be expressed in terms of g/b by

$$C_{co}'/\epsilon = \frac{1}{\pi} \left[2 \ln 2 - \ln(1 - g/b) - \frac{g/b}{1 - g/b} \ln g/b \right]. \quad (40)$$

This is plotted in Fig. 5. The fringing capacitance C_f'/ϵ is the value of C_{co}'/ϵ for $g/b=0$, and is

$$C_f'/\epsilon = \frac{2}{\pi} \ln 2 = 0.4413. \quad (41)$$

ACKNOWLEDGMENT

The author wishes to express his appreciation to Dr. G. L. Matthaei, who suggested the problem analyzed herein, for his encouragement and technical guidance during the course of this work.

BIBLIOGRAPHY

- [1] J. K. Shimizu and E. M. Jones, "Coupled-Transmission-Line directional couplers," IRE TRANS. ON MICROWAVE THEORY AND TECHNIQUES, vol. MTT-6, pp. 403-410; October, 1958.
- [2] S. B. Cohn, *et al.*, "Research on Design Criteria for Microwave Filters," Stanford Res. Inst., Menlo Park, Calif., Final Rept., SRI Project 1331, Contract No. DA 36-039 SC-64625; 1957.
- [3] G. L. Matthaei, "Design of wide-band (and narrow-band) band-pass microwave filters on the insertion loss basis," IRE TRANS. ON MICROWAVE THEORY AND TECHNIQUES, vol. MTT-8, pp. 580-593; November, 1960.
- [4] B. M. Oliver, "Directional electromagnetic couplers," PROC. IRE, vol. 42, pp. 1686-1692; November, 1954.
- [5] E. M. T. Jones and J. T. Bolljahn, "Coupled-Strip-Transmission-Line filters and directional couplers," IRE TRANS. ON MICROWAVE THEORY AND TECHNIQUES, vol. MTT-4, pp. 75-81; April, 1956.
- [6] S. B. Cohn, "Problems in strip transmission lines," IRE TRANS. ON MICROWAVE THEORY AND TECHNIQUES, vol. MTT-3, pp. 119-126; March, 1955.
- [7] W. R. Smythe, "Static and Dynamic Electricity," McGraw-Hill Book Co., Inc., New York, N. Y., ch. 4; 1939.
- [8] Ernst Weber, "Mapping of Fields" in "Electromagnetic Fields: Theory and Applications," John Wiley and Sons, Inc., New York, N. Y., vol. 1; 1950.
- [9] H. Kober, "Dictionary of Conformal Representations," Dover Publications, Inc., New York, N. Y., sec. 12.5, p. 155; 1952.
- [10] R. V. Churchill, "Introduction to Complex Variables and Applications," McGraw-Hill Book Co., Inc., New York, N. Y., Appendix II; 1948.
- [11] S. B. Cohn, "Shielded coupled-strip transmission line," IRE TRANS. ON MICROWAVE THEORY AND TECHNIQUES, vol. MTT-3, pp. 29-38; October, 1955.

The Measurement of Conductivity and Permittivity of Semiconductor Spheres by an Extension of the Cavity Perturbation Method*

K. S. CHAMPLIN†, MEMBER, IRE, AND R. R. KRONGARD†

Summary—A technique based on cavity perturbation theory is described with which one can determine the microwave conductivity and dielectric permittivity of a small sphere of completely arbitrary conductivity. These properties follow from the measured frequency shift and quality change occurring when the sample is inserted into a region of maximum electric field in a cavity resonator. The range of validity of the quasi-static internal field approximation is discussed, and curves are provided for extending the measuring technique beyond this range. The extended theory is valid for the entire conductivity range from zero to infinity. Measurements on several samples of known conductivity and permittivity in which the approximation is not satisfied are seen to agree with the theory. For highly conductive materials, the present method is closely related to the "eddy current loss" measuring technique discussed by others. The two methods are compared from the point of view of perturbation theory in order to determine their relative merits. Because the measuring technique employs a spherical sample, it may be applied profitably to materials with nonisotropic carrier mobilities and to semiconducting materials for which contact fabrication techniques are poorly known.

INTRODUCTION

C AVITY perturbation techniques have frequently been used to measure the complex magnetic and electric susceptibilities of many magnetic [1] and dielectric [2] materials. These measurements are performed by inserting a small appropriately shaped sample into a cavity resonator and determining the properties of the sample from the resultant change in quality and resonant frequency.

Such techniques have found very little use in research on materials with conductivities in the range of semiconductors. Several probable reasons are:

- 1) The assumption often made in perturbation calculations—that the fields are uniform throughout the sample—is usually not satisfied with semiconductors of practical size.
- 2) The conduction and displacement currents of semiconductors are often of the same order of magnitude at microwave frequencies. The simplifying assumptions which apply to either low-loss or high-loss materials are therefore not valid.
- 3) It is sometimes believed that the approximations inherent in perturbation methods preclude their use with materials of arbitrary conductivity.

* Received by the PGM-TT, March 13, 1961; revised manuscript received, July 11, 1961. Supported by the AF Office of Scientific Research of the Office of Aerospace Research, under Contract No. AF 49(638)-747, and by the Graduate School of the University of Minnesota, Minneapolis.

† Dept. of Electrical Engineering, Institute of Technology, University of Minnesota, Minneapolis, Minn.

The present paper treats the problem of determining the microwave conductivity and permittivity of a small sphere (~ 1 mm radius for x -band measurements, as shown in Fig. 1) of completely arbitrary conductivity. These properties follow from the measured frequency shift and quality change occurring when the sample is inserted into a region of maximum electric field in a cavity resonator. The method is quite general and requires no *a priori* knowledge concerning the conductivity range of the sample. For materials of arbitrary conductivity, both the frequency shift and quality change are required to determine uniquely either the conductivity or the permittivity. Furthermore, the uniform internal field approximation often made in perturbation calculations is found to limit measurement to materials of low conductivity. A computer solution of the field equations removes this restriction, thus extending the measuring technique to high conductivity materials.

The measuring technique should apply to the systematic study of new semiconducting materials such as the organic semiconductors. For these materials, many of which have extremely nonisotropic carrier mobilities,

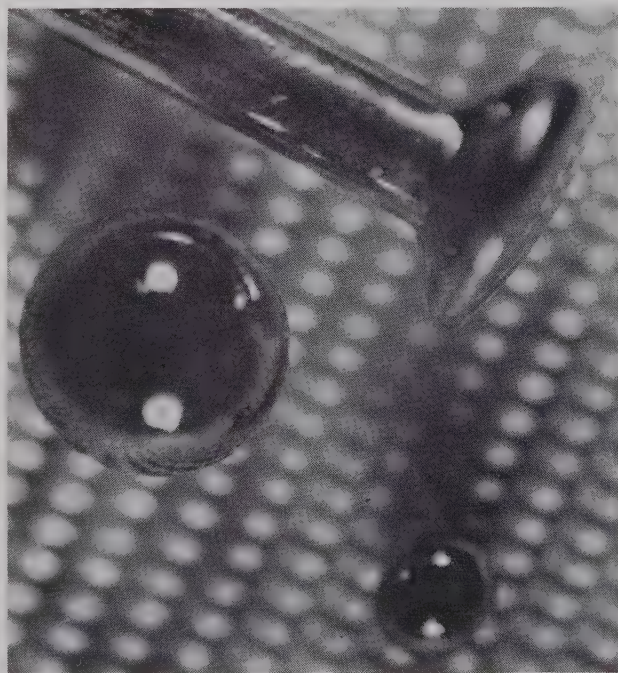


Fig. 1—Spherical samples of Si and Ge with radii of 1.0 mm and 0.4 mm, respectively. A common pin is included for size comparison.

the techniques of fabricating good "ohmic" contacts are totally unknown. In addition to the obvious advantage of eliminating contacts, the microwave technique has the further advantage of permitting measurement along various crystallographic directions by merely rotating the specimen.

I. THEORY

A. The Perturbation Formula

Consider a single oscillatory mode of a cavity resonator. If a perturbing specimen, small compared with the spatial variation of the unperturbed fields, is introduced into the cavity, the complex natural decay frequency changes by an amount [3]–[8]¹

$$\frac{\delta\hat{\omega}}{\hat{\omega}} = - \frac{\hat{\mathbf{P}} \cdot \hat{\mathbf{E}}_0^* + \hat{\mathbf{M}} \cdot \hat{\mathbf{H}}_0^*}{4W}, \quad (1)$$

where a complex quantity is denoted by a circumflex above it. In (1), $\hat{\mathbf{E}}_0$ and $\hat{\mathbf{H}}_0$ are the unperturbed fields at the location of the specimen, $\hat{\mathbf{P}}$ and $\hat{\mathbf{M}}$ are the specimen's total induced electric and magnetic moments observed externally, and W is the energy stored in the cavity. Although (1) applies to the transient case, measurements are generally obtained from the sinusoidal steady state. For the high- Q values of interest, these viewpoints are related by

$$\hat{\omega} = \omega_0 + j(\omega_0/2Q), \quad (2)$$

in which ω_0 is the resonant frequency for forced oscillations.

Placing the sample at an electric field maximum results in $\hat{\mathbf{H}}_0 = 0$, while the stored energy follows from the relation (mks units)

$$W = (1/2)\epsilon_0 \int_{\text{cavity}} |\hat{\mathbf{E}}|^2 dv \quad (3)$$

where $\hat{\mathbf{E}}$ is the unperturbed vector field distribution for the given mode. There remains only to determine $\hat{\mathbf{P}}$.

Casimir has solved for the magnetic moment of a ferromagnetic sphere in an initially uniform high-frequency magnetic field [9]. Because of the dual nature of Maxwell's equations, his solution applies also to the electric moment of a semiconducting sphere in a high-frequency electric field. The result, for a sphere of radius R and complex relative permittivity $\hat{\epsilon}_r$ is (see Appendix)

$$\hat{\mathbf{P}} = 3\epsilon_0 \left\{ \frac{\hat{\epsilon}_r \hat{v}(\hat{\gamma}R) - 1}{\hat{\epsilon}_r \hat{v}(\hat{\gamma}R) + 2} \right\} \left(\frac{4}{3} \pi R^3 \right) \hat{\mathbf{E}}_0, \quad (4)$$

¹ The integral form of the perturbation formula is derived in references [3]–[7]. For small samples, (1) and the more general integral form are equivalent.

in which $\hat{\gamma}$ is the propagation constant for plane waves in the material, and $\hat{v}(\hat{\gamma}R)$ is given by

$$\hat{v}(\hat{\gamma}R) = -2 \left\{ \frac{(\hat{\gamma}R) \cosh(\hat{\gamma}R) - \sinh(\hat{\gamma}R)}{(\hat{\gamma}R) \cosh(\hat{\gamma}R) - \{1 + (\hat{\gamma}R)^2\} \sinh(\hat{\gamma}R)} \right\}. \quad (5)$$

The imaginary part of the complex permittivity $\hat{\epsilon}_r$ results from both dielectric and conductive losses. For semiconductors in which conductive losses predominate,

$$\hat{\epsilon}_r = \epsilon_r - j\sigma_r \quad (6)$$

is a convenient convention, where the *relative conductivity* σ_r is equal to $\sigma/\omega\epsilon_0$ if dielectric losses can be neglected. The utility of this notation results from σ_r then being simply proportional to the conductivity in mks units, e.g., $\sigma_r = (0.53)\sigma$ at 9.6 kMc.

Because of the form of (4), we define the *effective* complex permittivity of the sphere by

$$\begin{aligned} \hat{\epsilon}_{r(\text{eff})} &= \hat{\epsilon}_r \hat{v}(\hat{\gamma}R) \\ &= \epsilon_{r(\text{eff})} - j\sigma_{r(\text{eff})}. \end{aligned} \quad (7)$$

Methods for converting from effective to actual values will be given in Section I-D. Combining (1), (3), (4) and (7) leads to

$$\frac{\delta\hat{\omega}}{\hat{\omega}} = - (3/2)(1/C_c)(v_s/v_c) \left[\frac{\hat{\epsilon}_{r(\text{eff})} - 1}{\hat{\epsilon}_{r(\text{eff})} + 2} \right], \quad (8)$$

where v_s and v_c are the volume of the sample and of the cavity, respectively, and C_c is the cavity constant,

$$C_c = \frac{1}{v_c} \int_{\text{cavity}} \left| \frac{\mathbf{E}}{\mathbf{E}_{\text{max}}} \right|^2 dv, \quad (9)$$

a quantity readily evaluated for a given mode; e.g., $C_c = \frac{1}{4}$ for a rectangular cavity oscillating in the TE_{10n} mode.

B. Inversion of the Perturbation Formula

Assuming that the Q of the perturbed resonator is fairly high, (8) may be written

$$\begin{aligned} \left\{ 1 + \frac{1}{K} \frac{\delta\omega_0}{\omega_0} \right\} + j \left\{ \frac{1}{K} \delta(1/2Q) \right\} \\ = \frac{3}{\{\epsilon_{r(\text{eff})} + 2\} - j\{\sigma_{r(\text{eff})}\}}, \end{aligned} \quad (10)$$

where

$$K = (3/2)(1/C_c)(v_s/v_c). \quad (11)$$

Eq. (10) is of the form of the complex transformation

$$\hat{Z} = 3/\hat{w}^*, \quad (12)$$

where $\hat{Z} = X + jY$ relates to the experimental parameters and $\hat{w} = u + jv$ to the physical properties of the

sphere. Separating (10) into real and imaginary parts yields

$$\left\{1 + \frac{1}{K} \frac{\delta\omega_0}{\omega_0}\right\} = \frac{3\{\epsilon_r(\text{eff}) + 2\}}{\{\epsilon_r(\text{eff}) + 2\}^2 + \{\sigma_r(\text{eff})\}^2}, \quad (13)$$

$$\left\{\frac{1}{K} \delta(1/2Q)\right\} = \frac{3\{\sigma_r(\text{eff})\}}{\{\epsilon_r(\text{eff}) + 2\}^2 + \{\sigma_r(\text{eff})\}^2}. \quad (14)$$

The inverse transformation is, of course, of the same form. Thus

$$\{\epsilon_r(\text{eff}) + 2\} = \frac{3\left\{1 + \frac{1}{K} \frac{\delta\omega_0}{\omega_0}\right\}}{\left\{1 + \frac{1}{K} \frac{\delta\omega_0}{\omega_0}\right\}^2 + \left\{\frac{1}{K} \delta(1/2Q)\right\}^2}, \quad (15)$$

$$\{\sigma_r(\text{eff})\} = \frac{3\left\{\frac{1}{K} \delta(1/2Q)\right\}}{\left\{1 + \frac{1}{K} \frac{\delta\omega_0}{\omega_0}\right\}^2 + \left\{\frac{1}{K} \delta(1/2Q)\right\}^2}. \quad (16)$$

Eqs. (15) and (16) separately yield $\epsilon_r(\text{eff})$ and $\sigma_r(\text{eff})$ from the measured changes in ω_0 and Q .

Fig. 2 shows the relative frequency shift and quality

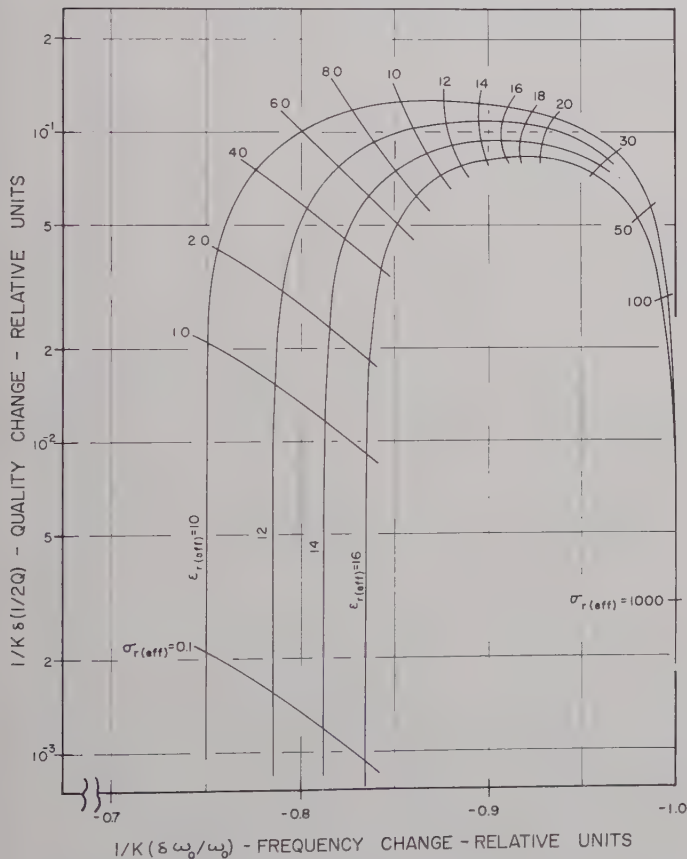


Fig. 2—Relative frequency shift and quality change as function of effective relative permittivity and conductivity of small semiconductor sphere. Sphere is placed at location of maximum electric field.

change for several values of $\epsilon_r(\text{eff})$ and $\sigma_r(\text{eff})$. For small $\sigma_r(\text{eff})$, the frequency change depends only on $\epsilon_r(\text{eff})$, and $\delta(1/Q)$ varies directly as $\sigma_r(\text{eff})$. Spencer, *et al.*, have measured the complex permittivity of small ferrite spheres with effective conductivities in this range [1]. At the other end of the $\sigma_r(\text{eff})$ scale, $\delta\omega_0/\omega_0$ approaches a constant independent of $\epsilon_r(\text{eff})$, while an inverse relationship exists between $\delta(1/Q)$ and $\sigma_r(\text{eff})$. One sees that in general, *both* experimental parameters are required to determine *either* $\epsilon_r(\text{eff})$ or $\sigma_r(\text{eff})$.

C. The Quasi-Static Field Approximation

Frequently, as in [1], one assumes that $|\hat{\gamma}R|$ is small compared with unity. The field distribution then follows from the static solution by merely extending ϵ_r to complex values. For a semiconducting sphere in an initially uniform time-varying field, the quasi-static field within the sphere is again uniform; and the sphere acquires an electric moment given by (4) with $\hat{v}(\hat{\gamma}R) = 1$. Thus, for the quasi-static case,

$$\epsilon_r(\text{eff}) = \epsilon_r,$$

$$\sigma_r(\text{eff}) = \sigma_r. \quad (17)$$

The terms neglected in (4) by this approximation are those in $(\hat{\gamma}R)^2$ and higher orders.

The range of validity of the quasi-static approximation at 9.6 kMc can be determined from Fig. 3. If one limits $|\hat{\gamma}R|$ to values less than, say, $\frac{1}{2}$, a germanium sphere of $\frac{1}{2}$ -mm radius restricts measurement to resistivities greater than about 10 ohm-cm ($\sigma_r \lesssim 20$). Reducing the radius extends the range of validity. One can see, however, that practical considerations will prevent utilizing the quasi-static approximation with very low resistivity materials. For radii larger than about $\frac{3}{4}$ mm, the approximation is never valid regardless of the resistivity because of the large dielectric constant.

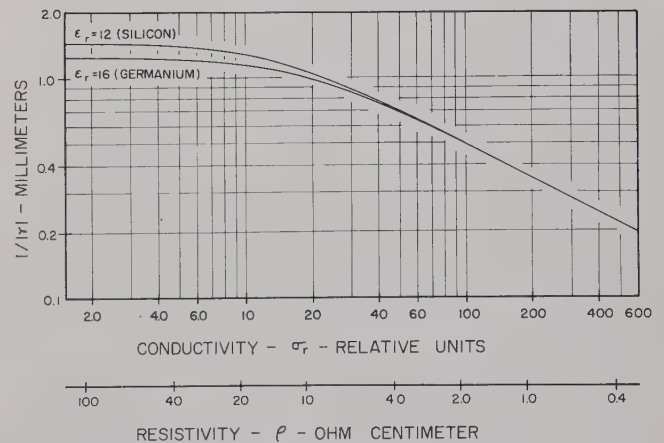


Fig. 3—Magnitude of inverse propagation constant as a function of conductivity for silicon and germanium. $f = 9.6$ kMc. For convenience, resistivity scale is also shown.

D. The Exact Solution—Conversion from Effective to Actual Values

For materials with magnetic permeabilities equal to unity, one can write

$$(\gamma R) = j\omega(\mu_0\epsilon_0)^{1/2}(\epsilon_r R^2)^{1/2}. \quad (18)$$

Since, at a given frequency, (γR) is a function of the single complex variable $(\epsilon_r R^2)$, (5) leads to the following complex relationship between $(\epsilon_r R^2)$ and $(\epsilon_{r(\text{eff})} R^2)$:

$$\{\epsilon_{r(\text{eff})} R^2\} = -2\{\epsilon_r R^2\} \left[\frac{(\gamma R) \cosh(\gamma R) - \sinh(\gamma R)}{(\gamma R) \cosh(\gamma R) - \{1 + (\gamma R)^2\} \sinh(\gamma R)} \right]. \quad (19)$$

Eq. (19) has been evaluated for a frequency of 9.6 kMc with a high-speed digital computer. The results of these computations are shown in Figs. 4–6.

Figs. 4 and 5 show $a^2\epsilon_{r(\text{eff})}$ and $a^2\sigma_{r(\text{eff})}$ as functions of $a^2\epsilon_r$ and $a^2\sigma_r$, where a is the sphere radius in millimeters. At certain values, a type of dimensional resonance results in $\epsilon_{r(\text{eff})}$ changing sign. The positive range of $\epsilon_{r(\text{eff})}$ is shown in Fig. 4 and the negative range in Fig. 5. One sees from Fig. 5 that the results become less dependent on ϵ_r as σ_r increases. For $\epsilon_r \ll \sigma_r$, ($\rho \lesssim 1$ ohm cm for Ge and Si) a unique relationship exists between $a^2\sigma_{r(\text{eff})}$ and $a^2\sigma_r$, which is independent of ϵ_r . This relationship is shown in Fig. 6.

Although the curves of Figs. 4–6 were derived for $f=9.6$ kMc and $\mu_r=1$, one can easily extend their use to other frequencies and (real) permeabilities by introducing the "corrected" radius a' defined by

$$a' = \mu_r^{1/2} \frac{f(\text{kMc})}{9.6} a. \quad (20)$$

The plots in Figs. 4–6 are useful for estimating the accuracy of the quasi-static approximation as well as for converting from effective to actual values. As an example of the former, consider the solid curve $a^2\epsilon_r=4$ in Fig. 4 which applies to the $\frac{1}{2}$ -mm germanium sphere discussed in the previous section. At low conductivities, $\sigma_{r(\text{eff})}/\sigma_r=1.03$. As conductivity increases, the ratio decreases but is still about 0.925 for $a^2\sigma_r=80$ (Fig. 5). One concludes that with a $\frac{1}{2}$ -mm germanium sphere, the quasi-static approximation introduces less than 8 per cent error in the measured conductivity for $\sigma_r < 320$ ($\rho \lesssim 0.6$ ohm-cm). Thus, as far as conductivity measurements are concerned, the quasi-static approximation is much less restrictive than one might assume from Fig. 3. For $\sigma_r > 320$, it becomes necessary to correct the effective conductivity. In this range, however, $\epsilon_r \ll \sigma_r$ so that Fig. 6 applies.

When the conductivity is large enough that $\epsilon_r \ll \sigma_r$ and $500 < a^2\sigma_r$ are simultaneously satisfied, the asymptotic approximation to the curve in Fig. 6 yields

$$a^2\sigma_{r(\text{eff})} = -a^2\epsilon_{r(\text{eff})} = \{5\sqrt{2}\} \{a^2\sigma_r\}^{1/2}, \quad (21)$$

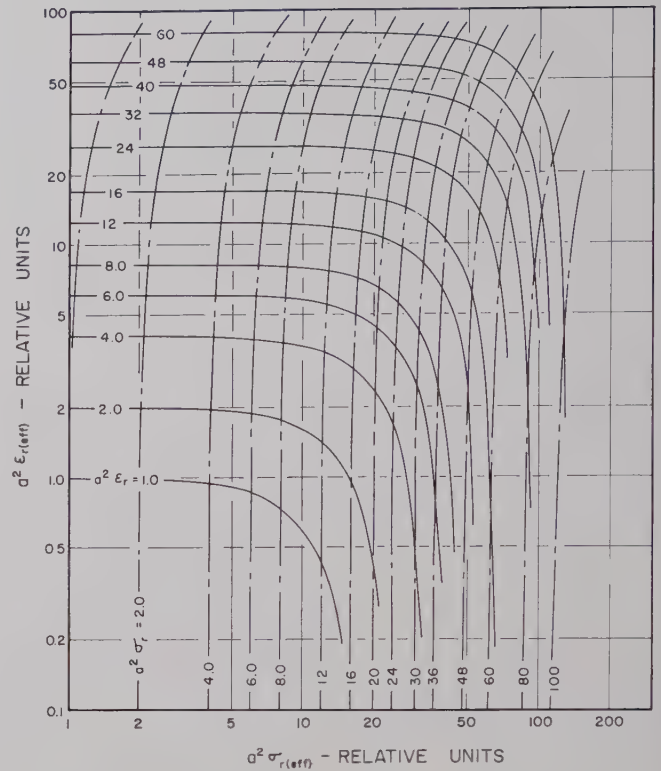


Fig. 4—Relationship between effective and actual values of relative permittivity and conductivity for sphere of radius a (millimeters) $f=9.6$ kMc, $\mu_r=1$, $\epsilon_r(\text{eff}) > 0$.

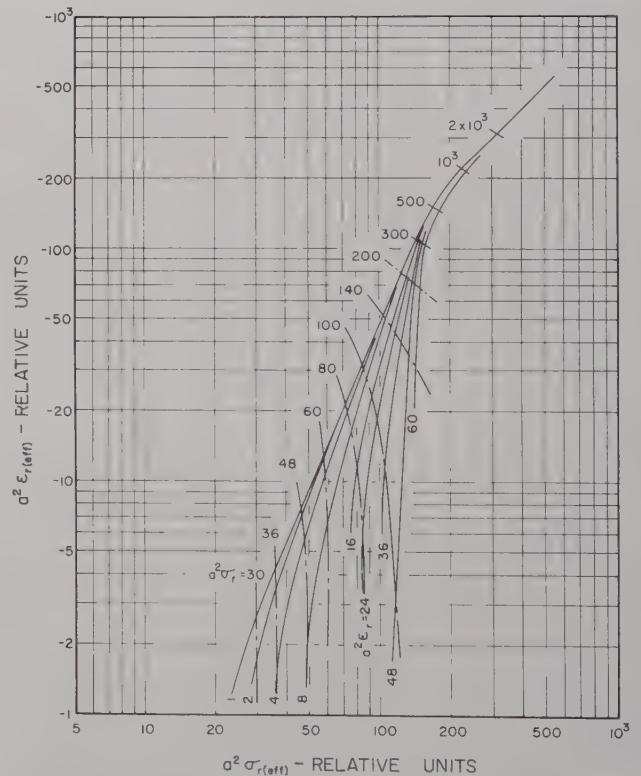


Fig. 5—Relationship between effective and actual values of relative permittivity and conductivity for sphere of radius a (millimeters). $f=9.6$ kMc, $\mu_r=1$, $\epsilon_r(\text{eff}) < 0$.

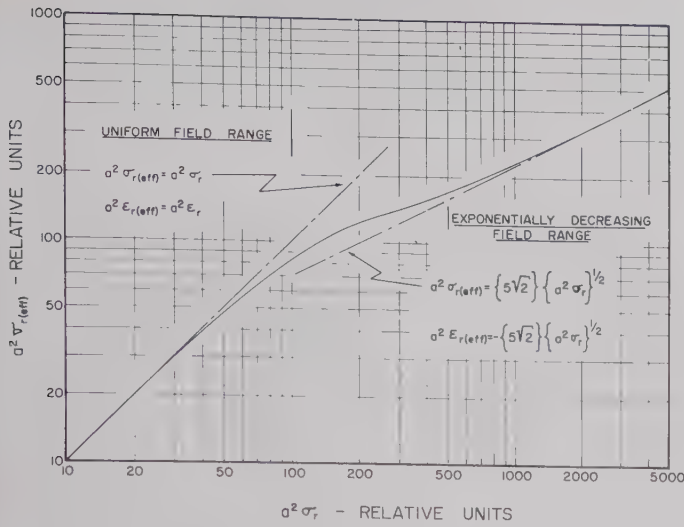


Fig. 6—Relationship between effective and actual relative conductivity for sphere of radius a (millimeters). $\epsilon_r \ll \sigma_r$, $f = 9.6$ kMc, $\mu_r = 1$.

while (13) and (14) become

$$\left\{ \frac{1}{K} \delta(1/2Q) \right\} = - \left\{ 1 + \frac{1}{K} \frac{\delta\omega_0}{\omega_0} \right\} = \left(\frac{3}{2} \right) \frac{1}{\sigma_r(\text{eff})}. \quad (22)$$

Combining, one has

$$\sigma_r = (0.045) \frac{a^2}{\left\{ \frac{1}{K} \delta(1/2Q) \right\}^2}. \quad (23)$$

Thus, for very high-conductivity materials, σ_r can be determined analytically from measurements of quality change alone.

E. The "Eddy Current Loss" Method

The conductivity of highly-conductive spheres can also be measured by the "eddy current loss" method. With this method, one determines the conductivity from the change in Q which results from inserting the sample into a region of maximum magnetic field in a cavity resonator.

The eddy current loss method was first discussed by Linhart, *et al.*, who analytically determined the conductivity of a sphere that was large compared with the skin depth [10]. The size restriction was later removed by Kohane and Servitz with a graphical evaluation procedure [11]. Both papers contain the tacit assumption which led to Fig. 6; *i.e.*, $\epsilon_r \ll \sigma_r$ ($\rho \gtrsim 1$ ohm-cm for Si and Ge). Further, the method of Linhart, *et al.*, applies to the region $500 < a^2 \sigma_r$, for which the asymptotic approximation in Fig. 6 and (23) are justified.

For comparison with the "standard" method, it is informative to discuss the eddy current loss method from the standpoint of perturbation theory. According

to Casimir [9], a sphere of relative permeability $\hat{\mu}_r$ in a high-frequency magnetic field acquires a magnetic moment

$$\hat{M} = 3\mu_0 \left[\frac{\hat{\mu}_r \hat{v}(\hat{\gamma}R) - 1}{\hat{\mu}_r \hat{v}(\hat{\gamma}R) + 2} \right] \left\{ \frac{4}{3} \pi R^3 \right\} \hat{H}_0, \quad (24)$$

in complete analogy with (4). Again, $\hat{v}(\hat{\gamma}R)$ is defined by (5). Since electric and magnetic fields enter (1) in exactly the same way, the work in Sections I-A and I-B can be extended to the present case by merely redefining the cavity constant in terms of magnetic fields and replacing $\hat{\epsilon}_r(\text{eff})$ with $\{\hat{\mu}_r \hat{v}(\hat{\gamma}R)\}$. For nonmagnetic materials ($\hat{\mu}_r \cong 1$), as considered in references [10] and [11], one then has the following:

- 1) The real part of $\hat{v}(\hat{\gamma}R)$ replaces $\epsilon_r(\text{eff})$,
- 2) The imaginary part of $\hat{v}(\hat{\gamma}R)$ replaces $-\sigma_r(\text{eff})$.

Performing these substitutions in (14) and evaluating for $\epsilon_r \ll \sigma_r$ leads to the transcendental equation which has been plotted by Kohane and Servitz [11].

For large $|\hat{\gamma}R|$, $\hat{v}(\hat{\gamma}R)$ approaches $2/(\hat{\gamma}R)$. The transcendental expression then becomes

$$\left\{ \frac{1}{K} \delta(1/2Q) \right\}_e = \frac{3}{2\sqrt{2}} \frac{1}{\omega(\mu_0\epsilon_0)^{1/2}R} \frac{1}{\sigma_r^{1/2}}, \quad (25)$$

in agreement with Linhart, *et al.* [10]. For the same approximation, the standard method leads to [see (23)]

$$\left\{ \frac{1}{K} \delta(1/2Q) \right\}_s = \frac{3}{2\sqrt{2}} \omega(\mu_0\epsilon_0)^{1/2}R \frac{1}{\sigma_r^{1/2}}. \quad (26)$$

Thus, at 9.6 kMc the observed quality change by the two methods has the ratio

$$\frac{\left\{ \frac{1}{K} \delta(1/2Q) \right\}_e}{\left\{ \frac{1}{K} \delta(1/2Q) \right\}_s} = \left(\frac{5}{a} \right)^2, \quad (27)$$

where a is the sphere radius in millimeters.

The following comparisons can now be made:

1) The standard method has several advantages over the eddy current loss method if the conductivity is not too large. The standard method is useful over a very wide conductivity range; it may be used with materials with $\mu_r \neq 1$; and unlike the eddy current loss method, it gives a single valued result.

2) On the other hand, the eddy current loss method is probably preferable for conductivity measurements in the range $500 < a^2 \sigma_r$, because there is a larger quality change for a given σ_r than with the standard method if the radius is less than 5 mm (as the original assumptions require). The eddy current loss method should thus yield greater accuracy in this conductivity range.

TABLE I
TYPICAL MEASUREMENTS

	ρ_{dc} Ω cm	a mm	δP db	δf mcs	$a^2\epsilon_r(\text{eff})$	$a^2\sigma_r(\text{eff})$	$a^2\epsilon_r$	$a^2\sigma_r$	ϵ_r	ρ Ω cm
Sample 1 n-type Si	250	0.945	1.94	10.39	11.12	0.743	10.4	0.683	11.6	248
Sample 2 p-type Si	135	1.026	4.03	13.30	12.91	1.58	12.3	1.47	11.6	136
Sample 3 n-type Ge	37	1.55	9.13	20.49	22.12	8.32	21.12	6.90	15.9	36.3
Sample 4 n-type Ge	10	0.982	9.81	13.96	13.47	21.78	15.0 ± 1	19.8	15.6 ± 1	9.8
Sample 5 n-type Si	3	1.033	7.27	17.39	-1.43	67.22	15 ± 5	65.0	15 ± 5	3.1

II. EXPERIMENTAL RESULTS

Measurements of microwave conductivity and permittivity have been performed on a number of single-crystal germanium and silicon specimens. An under-coupled, rectangular transmission cavity, oscillating in the TE_{103} mode, was used in these studies. The sample was placed on a slight indentation in the center of a thin mylar film stretching horizontally across the middle of the cavity. The film supported the sample at the cavity's geometric center, yet left the empty cavity field relatively undisturbed. Opening and closing the cavity during measurement was avoided by inserting the sample through a small hole at a region of minimum wall current. The empty cavity had a resonant frequency of 9.482 kMc, a loaded Q of 7650, and a volume of 15.18 cm³ [3].

The response curve of the cavity was displayed on an oscilloscope by frequency modulating the klystron source. A marker pulse indicating the absorption frequency of a cavity wavemeter was superimposed on this resonance curve and used for measuring frequency differences. The change in quality caused by the sample was determined from the change in transmitted power as measured with a precision attenuator by using the following relation [12]:

$$\delta(1/2Q) = \frac{1}{2Q_0} \left[\left(\frac{P_1}{P_0} \right)^{1/2} - 1 \right], \quad (28)$$

where Q_0 is the loaded Q of the empty cavity.

Typical results are shown in Table I. Even for the samples with large resistivity, the quasi-static approximation is not justified in these measurements since $|\hat{\gamma}R|$ is of the order of unity (see Fig. 3). The approximation gets worse as resistivity decreases. Indeed, for sample 5, the effective permittivity is actually negative. Although permittivity measurements are rather inaccurate in this range, the corrected value is of the right order of magnitude. The agreement between values of resistivity measured by dc and by microwave means is seen to be excellent.

III. CONCLUSIONS

The preceding discussion has developed the relationships between the electrical properties of a small sphere of completely arbitrary conductivity and the frequency shift and quality change resulting from its insertion into a cavity resonator. For experiments in which the quasi-static field approximation is justified, the inversion formulas (15) and (16) yield the conductivity and permittivity of the sphere in terms of the experimental parameters. For the general case, however, (15) and (16) yield only "effective" values which are then converted to the "actual" conductivity and permittivity with the aid of Figs. 4-6. Measurements on materials not satisfying the quasi-static approximation show good agreement with the theory.

The above method may possibly be applicable to the observation of such semiconductor phenomena as the photoconductive effect, the magnetoresistive effect, and the "hot" electron effect, as well as to the simpler measurement of static conductivity. Since "ohmic" contacts are not used, these measurements can be made on materials for which contact fabrication techniques are not well understood. Furthermore, the spherical geometry should allow one to perform separate electrical measurements along the various crystal axes of non-isotropic solids by merely rotating a single specimen.

APPENDIX

THE ELECTRIC MOMENT OF A SEMICONDUCTING SPHERE IN A TIME-VARYING ELECTRIC FIELD

Consider a sphere of radius R in a time-varying electric field. Assume that the sphere is sufficiently small so that the external field in its neighborhood is quasi-static, reducing to a uniform field in the Z direction \hat{E}_{z0} at large distances. Since the magnitudes of the constitutive parameters are to be unrestricted, no such assumption will apply to the internal field. This problem, whose magnetic analogue has been discussed by Casimir [9], is thus a step beyond the quasi-static treatment.

In view of the solenoidal character of the complex dis-

placement vector, it can be derived from a vector potential $\hat{\mathbf{A}}$ whose divergence is zero. Thus

$$\left. \begin{aligned} \epsilon(r)\hat{\mathbf{E}} &= \nabla \times \hat{\mathbf{A}} \\ \nabla \cdot \hat{\mathbf{A}} &= 0 \end{aligned} \right\} \quad (29)$$

and

$$\epsilon(r) = \begin{cases} \epsilon_0 & \text{for } R < r \\ \epsilon_0\epsilon_r & \text{for } r < R. \end{cases} \quad (30)$$

The vector potential satisfies

$$\nabla^2 \hat{\mathbf{A}} = 0 \quad \text{for } R < r \quad (31)$$

$$\nabla^2 \hat{\mathbf{A}} - \hat{\gamma}^2 \hat{\mathbf{A}} = 0 \quad \text{for } r < R \quad (32)$$

with

$$\hat{\gamma} = j\omega\{\mu_0\epsilon_0\epsilon_r\}^{1/2},$$

and the boundary conditions that $\hat{\mathbf{A}}$ and the tangential component of $\hat{\mathbf{E}}$ are continuous at the surface of the sphere.

Just as in the quasi-static treatment, the external field is the superposition of the uniform field \hat{E}_{z0} and that of a dipole in the z direction with moment \hat{P}_z .

$$\left. \begin{aligned} A_x &= - (1/2)\epsilon_0\hat{E}_{z0}y - \hat{P}_z \frac{y}{4\pi r^3} \\ \hat{A}_y &= + (1/2)\epsilon_0\hat{E}_{z0}x + \hat{P}_z \frac{x}{4\pi r^3} \end{aligned} \right\} \quad (33)$$

Inside the sphere, we put formally

$$\left. \begin{aligned} \hat{A}_x &= -\hat{f}(\hat{\gamma}r)y, \\ \hat{A}_y &= +\hat{f}(\hat{\gamma}r)x. \end{aligned} \right\} \quad (34)$$

Substituting (34) into (32) leads to

$$\hat{f}'' + \frac{4}{(\hat{\gamma}r)}\hat{f}' - \hat{f} = 0 \quad (35)$$

which has the solution

$$\begin{aligned} \hat{f}(\hat{\gamma}r) &= a \left\{ \frac{(\hat{\gamma}r) \cosh(\hat{\gamma}r) - \sinh(\hat{\gamma}r)}{(\hat{\gamma}r)^3} \right\}, \\ &= a\hat{\mu}(\hat{\gamma}r) \end{aligned} \quad (36)$$

where a is a constant to be determined from boundary conditions.

From the continuity of $\hat{\mathbf{A}}$ at the surface one has

$$a\hat{\mu}(\hat{\gamma}R) - \frac{\hat{P}_z}{4\pi R^3} = (1/2)\epsilon_0\hat{E}_{z0}, \quad (37)$$

and from the continuity of the tangential component of $\hat{\mathbf{E}}$,

$$\frac{a}{\epsilon_r} \{ 2\hat{\mu}(\hat{\gamma}R) + (\hat{\gamma}R)\hat{\mu}'(\hat{\gamma}R) \} + \frac{\hat{P}_z}{4\pi R^3} = \epsilon_0\hat{E}_{z0}. \quad (38)$$

Solving (37) and (38) for \hat{P}_z yields the desired result,

$$\hat{P}_z = 3\epsilon_0 \left\{ \frac{\epsilon_r\hat{\mu}(\hat{\gamma}R) - 1}{\epsilon_r\hat{\mu}(\hat{\gamma}R) + 2} \right\} \left(\frac{4}{3} \pi R^3 \right) \hat{E}_{z0}, \quad (39)$$

where

$$\hat{\mu}(\hat{\gamma}R) = \frac{2\hat{\mu}(\hat{\gamma}R)}{2\hat{\mu}(\hat{\gamma}R) + (\hat{\gamma}R)\hat{\mu}'(\hat{\gamma}R)} \quad (40)$$

$$\hat{\mu}(\hat{\gamma}R) = -2 \left\{ \frac{(\hat{\gamma}R) \cosh(\hat{\gamma}R) - \sinh(\hat{\gamma}R)}{(\hat{\gamma}R) \cosh(\hat{\gamma}R) - \{1 + (\hat{\gamma}R)^2\} \sinh(\hat{\gamma}R)} \right\}. \quad (41)$$

ACKNOWLEDGMENT

The authors would like to thank J. E. Holte for his helpful assistance in programming the Univac 1103 digital computer and to D. Long of the Minneapolis Honeywell Research Center, Minneapolis, Minn., for supplying the bulk semiconductor samples upon which the measurements were made.

REFERENCES

- [1] See, e.g., E. G. Spencer, R. C. LeCraw, and F. Reggia, "Measurement of microwave dielectric constants and tensor permeabilities of ferrite spheres," *Proc. IRE*, vol. 44, pp. 790-800; June, 1956.
- [2] G. Birnbaum and J. Franeau, "Measurement of the dielectric constant and loss of solids and liquids by a cavity perturbation method," *J. Appl. Phys.*, vol. 20, pp. 817-818; August, 1949.
- [3] J. Muller, "Untersuchung über Elektromagnetische Hohlraume," *Z. Hochfrequenztech. Elektroak.*, vol. 54, pp. 157-161; 1939.
- [4] H. A. Bethe and J. Schwinger, Cornell University, Ithaca, N. Y., NDRC Rept. D1-117; 1943.
- [5] J. C. Slater, "Microwave electronics," *Rev. Mod. Phys.*, vol. 18, pp. 441-512; October, 1946.
- [6] H. B. G. Casimir, "On the theory of electromagnetic waves in resonant cavities," *Philips Research Repts.*, vol. 6, pp. 162-182; June, 1951.
- [7] R. A. Waldron, "Perturbation theory of resonant cavities," *Proc. IEE*, vol. 107C, pp. 272-274; September, 1960.
- [8] C. H. Papas, "Thermodynamic consideration of electromagnetic cavity resonators," *J. Appl. Phys.*, vol. 25, pp. 1552-1553; December, 1954.
- [9] H. B. G. Casimir, "On the theory of eddy currents in ferromagnetic materials," *Philips Research Repts.*, vol. 2, pp. 42-54; February, 1947.
- See also N. Bloembergen, "On the magnetic resonance absorption in conductors," *J. Appl. Phys.*, vol. 23, pp. 1383-1389; December, 1952.
- See also J. O. Artman, "Effects of size on the microwave properties of ferrite rods, discs and spheres," *J. Appl. Phys.*, vol. 20, pp. 92-98; January, 1957.
- [10] J. G. Linhart, I. M. Templeton and R. Dunsmuir, "A microwave resonant cavity method for measuring the resistivity of semiconducting materials," *Brit. J. Appl. Phys.*, vol. 7, pp. 36-37; January, 1956.
- [11] T. Kohane and M. H. Sirvetz, "The measurement of microwave resistivity by eddy current loss in small spheres," *Rev. Sci. Instr.*, vol. 30, pp. 1059-1060; September, 1959.
- See also T. Kohane, "The measurement of microwave resistivity by eddy current loss in small spheres," *IRE TRANS. ON INSTRUMENTATION*, vol. 1-9, pp. 184-186; September, 1960.
- [12] C. J. Montgomery, R. H. Dicke and E. M. Purcell, Eds., "Principles of Microwave Circuits," M.I.T. Rad. Lab. Ser., McGraw-Hill Book Co., Inc., New York, N. Y., 288 pp.; 1948.

The Dominant Cutoff Wavelength of a Lunar Line*

A. Y. HU†, MEMBER, IRE, AND A. ISHIMARU‡, MEMBER, IRE

Summary—A method is presented for calculating the lowest cutoff wavelength of a new microwave transmission line, the "lunar line," which is formed by two eccentric circular metal tubes connected with a metal bar or tangential to each other. The lunar-shaped cross section is approximated by introducing a series of steps in the outer guide wall and by dividing the cross section into m fan-shape regions. Thus, the problem is reduced to one of a multiple-step waveguide and can be solved by introducing the angular parameter α_i for the individual regions. The radial boundary conditions require a combination of Bessel functions of noninteger order for each region. The common boundaries between regions give m integral equations that represent the total power in one region transferred into the next region. The integral equations are solved approximately by solving only the first terms of an infinite series expansion of the tangential electric field at the common boundary. The solution of the m -stepped waveguide results in a system of $2m$ equations containing $2m$ unknowns: the cutoff wave number β_c , the order of the Bessel function p_i , and the angular parameter α_i . A successive approximation method is applied to obtain the cutoff wavelength. The calculated value is in close agreement with experimental results.

I. INTRODUCTION

IN 1959 a new microwave transmission line, the "lunar line," was developed at The Boeing Airplane Company. The lunar line is an eccentric version of Schelkunoff's coaxial cylinders with a radial baffle¹ and is formed by two eccentric circular metal tubes which are either connected with a metal bar or are tangential to each other (Figs. 1 and 2). The cutoff frequency of the lunar line is lower than that of circular or coaxial waveguides with the same outside diameter, propagating TE₁₁ mode. Its low impedance and wide bandwidth characteristics may make it useful as a transmission line, a filter, a cavity, or a feeder for an array of slot antennas.

Conventional methods of determining the cutoff wavelength cannot be applied to lunar line because of its complicated cross section. In 1958 Iashkin²⁻⁴ proposed a new method for determining the dominant cutoff frequencies of waveguides with triangular and

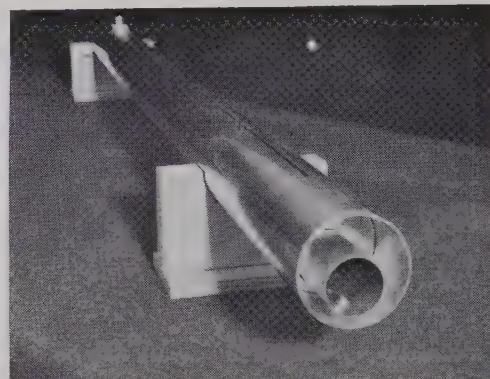
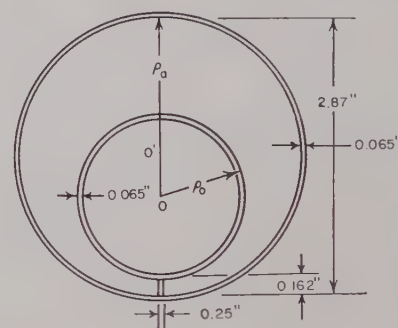


Fig. 1—Photograph of a lunar line.



$\rho_a = 1.8955$ inches

$\rho_0 = 0.8125$ inches

Fig. 2—Cross section of a lunar line.

trapezoidal cross sections. He approximated the cross section with a series of steps and introduced new angular parameters α_i which reduced the problem to a simple system of equations. However, because his solution is restricted to a waveguide which can be approximated by multisteped rectangular regions, it cannot be applied directly to the lunar line which has circular boundaries.

In this paper, Iashkin's method is extended to waveguides with circular boundaries. A system of equations involving the cutoff wave number β_c , the order of the Bessel function p_i , and the angular parameter α_i , is obtained and solved approximately. The numerically calculated cutoff wavelength of the lunar line is in close agreement with experimental results.

II. STATEMENT OF THE PROBLEM

Consider the lunar line with the cross section shown in Fig. 2. It is assumed that only the dominant TE mode is propagating, and that the guide wall is perfectly conducting. The z component of the magnetic field, H_z , perpendicular to the cross section of the lunar line,

* Received by the PGMTT, May 8, 1961; revised manuscript received, July 26, 1961. The work was performed under Contract No. AF 19(604)-6189 with the AF Cambridge Res. Center, Bedford, Mass., Rept. No 1, February, 1961.

† Boeing Airplane Co., Transport Div., Renton, Wash.

‡ Dept. of Elec. Engrg., Univ. of Washington, Seattle, Wash.

¹ S. A. Schelkunoff, "Electromagnetic Waves," D. Van Nostrand Co., Inc., New York, N. Y., p. 392; 1943.

² A. I. Iashkin, "A method of approximate calculation for waveguides of triangular and trapezoidal cross-section," *Radiotekhnika, USSR*, vol. 3, pp. 1-9; 1958.

³ A. I. Iashkin, "A method of approximate calculation of waveguides with complicated cross-sectional form," *Radiotekh. i elektron., USSR*, vol. 3, pp. 831-833; 1958.

⁴ A. I. Iashkin, "The calculation of the fundamental critical wavelength for a rectangular waveguide with longitudinal rectangular channels and ridges," *Radiotekhnika, USSR*, vol. 13, pp. 8-14; 1958.

satisfies the two-dimensional wave equation

$$(\nabla_t^2 + \beta_c^2)H_z = 0; \quad \frac{\partial H_z}{\partial n} = 0 \text{ on the boundary,} \quad (1)$$

where ∇_t is the gradient operator transverse to the z axis, β_c is the cutoff wave number, and the cutoff wavelength is given by $\lambda_c = (2\pi/\beta_c)$.

III. APPROXIMATION BY MULTISTEPED REGIONS

With conventional methods, it is not possible to obtain an exact solution for (1) when it pertains to the lunar shaped region shown in Fig. 2. An approximate solution can be obtained by deforming the outer boundary of the cross section into a series of steps (Fig. 3). If the deformations are not large and have alternate signs, their effect will be negligible, and the cutoff wavelength of the original lunar line will be approximately the same as that of a waveguide with a multisteped cross section. Thus, the problem is reduced to one of finding the cutoff wavelength of the multisteped waveguide. The precision of the calculated cutoff wavelength depends on the number of steps in the cross section.

IV. SOLUTION BY MEANS OF THE PARAMETERS α_i

The lunar line shown in Fig. 3 is deformed by eighteen fan-shape regions. Because of their symmetry about $\phi = \pi$, only nine of the eighteen regions must be considered. For a cylindrical coordinate system, the i th region is defined by

$$\phi_{i-1} \leq \phi \leq \phi_i, \\ \rho_0 \leq \rho \leq \rho_i,$$

where

$$i = 1, 2, \dots, 9.$$

The solution of (1) for each region is⁵

$$H_{z_i} = \sum_{n=1}^{\infty} C_{in} Z_{p_{in}}(\beta_c \rho) \cos p_{in}(\phi - \alpha_{in}), \quad (2)$$

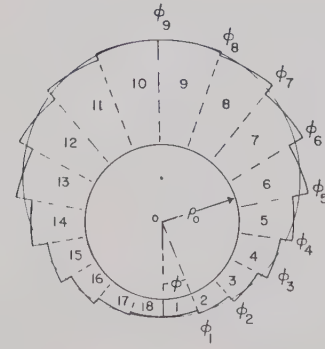
where p is the order of the Bessel function and C is the coefficient of the series solution. The function Z_p represents the following combination of Bessel functions:

$$Z_{p_{in}}(\beta_c \rho) = J_{p_{in}}'(\beta_c \rho_0) N_{p_{in}}(\beta_c \rho) - N_{p_{in}}'(\beta_c \rho_0) J_{p_{in}}(\beta_c \rho). \quad (3)$$

Application of the boundary condition yields

$$\left. \frac{\partial H_{z_i}}{\partial \rho} \right|_{\rho=\rho_i} = 0, \quad \text{or} \quad Z_{p_{in}}'(\beta_c \rho_i) = 0 \quad (4)$$

⁵ N. Marcuvitz, "Waveguide Handbook," McGraw-Hill Book Co., Inc., New York, N. Y., pp. 66-80; 1951.



$\rho_0 = 0.8125$ inches	
ρ_i = length from center o to outside of i th fan-shape region	
$\rho_1 = 0.98$ inches	$\phi_1 = 20^\circ$
$\rho_2 = 1.04$ inches	$\phi_2 = 40^\circ$
$\rho_3 = 1.12$ inches	$\phi_3 = 60^\circ$
$\rho_4 = 1.23$ inches	$\phi_4 = 80^\circ$
$\rho_5 = 1.36$ inches	$\phi_5 = 100^\circ$
$\rho_6 = 1.53$ inches	$\phi_6 = 120^\circ$
$\rho_7 = 1.68$ inches	$\phi_7 = 140^\circ$
$\rho_8 = 1.81$ inches	$\phi_8 = 160^\circ$
$\rho_9 = 1.86$ inches	$\phi_9 = 180^\circ$

Fig. 3—Cross section of an 18-stepped form of a lunar line.

and

$$\left. \frac{\partial H_{z_1}}{\partial \phi} \right|_{\phi=0} = 0, \quad \text{so} \quad \alpha_{in} = 0. \quad (5)$$

The fields must be continuous across the common boundary between the i and the $i+1$ regions ($\rho_0 \leq \rho \leq \rho_i$, $\phi = \phi_i$); thus

$$\sum_{n=1}^{\infty} C_{in} Z_{p_{in}}(\beta_c \rho) \cos p_{in}(\phi_i - \alpha_{in}) \\ = \sum_{n=1}^{\infty} C_{(i+1)n} Z_{p_{(i+1)n}}(\beta_c \rho) \cos p_{(i+1)n}[\phi_i - \alpha_{(i+1)n}] \quad (6)$$

and

$$\sum_{n=1}^{\infty} C_{in} \frac{1}{\rho} p_{in} Z_{p_{in}}(\beta_c \rho) \sin p_{in}(\phi_i - \alpha_{in}) \\ = \sum_{n=1}^{\infty} C_{(i+1)n} \frac{1}{\rho} p_{(i+1)n} Z_{p_{(i+1)n}}(\beta_c \rho) \sin p_{(i+1)n}[\phi_i - \alpha_{(i+1)n}] \\ = \Phi_i(\rho). \quad (7)$$

The unknown function $\Phi_i(\rho)$ is the radial electric field of the i th region. Expressed in a series form, $\Phi_i(\rho)$ is

$$\Phi_i(\rho) = \sum_{n=1}^{\infty} D_{in} \frac{Z_{p_{in}}(\beta_c \rho)}{\rho}. \quad (8)$$

The first approximation may be obtained by taking the first term of the expansion

$$\Phi_i(\rho) = D_{i1} \frac{Z_{p_{i1}}(\beta_c \rho)}{\rho}. \quad (9)$$

The function $Z_{p_{in}}$ has the following properties:⁶

$$\int_{\rho_0}^{\rho_i} Z_{p_{in}}(\beta_c \rho) Z_{p_{iv}}(\beta_c \rho) \frac{d\rho}{\rho} = 0, \quad \text{for } n \neq v, \quad (10)$$

$$\int_{\rho_0}^{\rho_i} Z_{p_{in}}^2(\beta_c \rho) \frac{d\rho}{\rho} = \frac{1}{2p_{in}} [I_{p_{in}}(\rho_i) - I_{p_{in}}(\rho_0)],$$

for $n = v$. (11)

The functions $Z_{p_{in}}$ are orthogonal in i th region. This orthogonality property can be used to determine C_{in} and $C_{(i+1)n}$ from (7) in terms of the integral involving the $\Phi(\rho)$ function. Thus

$$C_{in} = \frac{2 \int_{\rho_0}^{\rho_i} \Phi_i(\xi) Z_{p_{in}}(\beta_c \xi) d\xi}{\sin p_{in}(\phi - \alpha_{in}) [I_{p_{in}}(\rho_i) - I_{p_{in}}(\rho_0)]}, \quad (12)$$

$$C_{(i+1)n} = \frac{2 \int_{\rho_0}^{\rho_{i+1}} \Phi_{i+1}(\xi) Z_{p_{(i+1)n}}(\beta_c \xi) d\xi}{\{\sin p_{(i+1)n}[\phi - \alpha_{(i+1)n}]\} \{I_{p_{(i+1)n}}[\rho_{(i+1)}] - I_{p_{(i+1)n}}(\rho_0)\}}. \quad (13)$$

Substituting C_{in} and $C_{(i+1)n}$ into (6) and simplifying yields the following integral equation:

$$\begin{aligned} \sum_{n=1}^{\infty} \frac{\cot p_{in}(\phi - \alpha_{in}) \int_{\rho_0}^{\rho_i} \Phi_i(\xi) Z_{p_{in}}(\beta_c \xi) Z_{p_{in}}(\beta_c \rho) d\xi}{I_{p_{in}}(\rho_i) - I_{p_{in}}(\rho_0)} \\ = \sum_{n=1}^{\infty} \frac{\cot p_{(i+1)n}[\phi - \alpha_{(i+1)n}] \int_{\rho_0}^{\rho_{i+1}} \Phi_{i+1}(\xi) Z_{p_{(i+1)n}}(\beta_c \xi) Z_{p_{(i+1)n}}(\beta_c \rho) d\xi}{I_{p_{(i+1)n}}(\rho_{i+1}) - I_{p_{(i+1)n}}(\rho_0)}. \end{aligned} \quad (14)$$

The limits of the right side of the integral in (14) are $\rho_0 \rightarrow \rho_{i+1}$, but at $\phi = \phi_i$ and at $\rho_i \leq \rho \leq \rho_{i+1}$, the function $\Phi(\xi) = \partial H_z / \partial n = 0$. Therefore the limits change to $\rho_0 \rightarrow \rho_i$.

Eq. (14) is an integral equation for the unknown function $\Phi(\xi)$ and insures the continuity of the z component of the magnetic field at the boundary. Therefore, the unknown functions $\Phi_i(\xi)$ and $\Phi_{i+1}(\xi)$ are equal at the common boundary, and the function $\Phi_i(\xi)$ is used for a small region.

The equation which determines the cutoff wave number can be obtained by multiplying both sides of (14) by $\Phi_i(\rho)$ and by integrating over the boundary ρ_0 to ρ_i . Since $\Phi_i(\rho)$ is the tangential electric field and both sides of (14) are the z component of the magnetic field, this procedure insures that the total power of the i th region will be transferred into $(i+1)$ th region, that is

$$\int_{\rho_0}^{\rho_i} \Phi_i(\rho) H_{z_i}(\rho) d\rho = \int_{\rho_0}^{\rho_i} \Phi_i(\rho) H_{z_{(i+1)}}(\rho) d\rho. \quad (15)$$

⁶ G. N. Watson, "A Treatise on the Theory of Bessel Functions," Cambridge University Press, Cambridge, Eng., p. 135; 1958.

Substituting (9) and (14) into (15) and integrating gives

$$\begin{aligned} \frac{\cot p_{i1}(\phi_i - \alpha_{i1})}{(2p_{i1})^2} [I_{p_{i1}}(\rho_i) - I_{p_{i1}}(\rho_0)] \\ = \sum_{n=1}^{\infty} \frac{\cot p_{(i+1)n}[\phi_i - \alpha_{(i+1)n}]}{[I_{p_{(i+1)n}}(\rho_{i+1}) - I_{p_{(i+1)n}}(\rho_0)]} \\ \cdot \left\{ \left[\frac{\beta_c \rho_i Z_{p_{i1}}(\beta_c \rho_i) Z'_{p_{(i+1)n}}(\beta_c \rho_i)}{(p_{i1})^2 - p_{(i+1)n}^2} \right]^2 \right\}. \end{aligned} \quad (16)$$

Between region 9 and 10, (16) is reduced to

$$\frac{\cot p_{91}(\phi_9 - \alpha_{91})}{(2p_{91})^2} [I_{p_{91}}(\rho_9) - I_{p_{91}}(\rho_0)] = 0, \quad (17)$$

since

$$\rho_9 = \rho_{10}, \quad \text{and} \quad Z'_{p_{10n}}(\beta_c \rho_9) = Z'_{p_{10n}}(\beta_c \rho_{10}) = 0.$$

Substituting $\phi_9 = \pi$ into (17) gives

$$p_{91}(\pi - \alpha_{91}) = \frac{\pi}{2}, \quad \text{or} \quad \alpha_{91} = \pi - \frac{\pi}{2p_{91}}. \quad (18)$$

At the boundary $\phi = \pi$, the field $E \propto \partial H_z / \rho \partial \phi$ is symmetric and the field H_z is zero. Thus, for the region represented in Fig. 3, a system of equations is obtained which consists of nine equations of type (4), eight equations of type (16), and one equation of type (18). Generally it is not possible to solve these equations because an infinite number of α_{in} and p_{in} must be determined. However, it is shown in Section V that (4) ad-

mits only one positive real root p_{i1} , and the rest of the roots are complex. The parameters p_{i1} and α_{i1} represent the dominant TE₁₁ propagating mode. Therefore, an approximate solution is obtained by neglecting all of the nonpropagating modes. This approximation reduces the series in (16) to one term. Thus, eighteen equations of type (4), (16) and (18) contain eighteen unknown quantities β_c , $\alpha_2, \dots, \alpha_9$, (drop the subscript one of α_{i1}) and p_{11}, \dots, p_{91} .

To solve for β_c , assume an appropriate value of β_c and substitute this value into (4), (16) and (18) for calculating α_9 . Two α_9 parameters are obtained for each β_c value. When the assumed value of β_c increases, the value of α_9 from (16) decreases and the value of α_9 from (18) increases. Therefore, the true value of β_c can be determined graphically from the point where the value of these two α_9 are equal.

V. SAMPLE CALCULATION OF THE CUTOFF WAVELENGTH OF A LUNAR LINE

In order to choose some appropriate value of β_c , a simplified case is first considered. Then the value of β_c is varied near the chosen value to obtain the true β_c .

In the deformation from the lunar-line cross section, to a one-stepped, fan-shape region, the approximate cutoff wave number may be chosen as

$$\beta_c = \frac{2\pi}{2(\rho_{\text{average}} \times 190^\circ)} = 0.70. \quad (19)$$

The fan-shape is stretched to form a rectangular waveguide, and the dimension a is $\rho_{\text{average}} \times 190^\circ$; therefore, the cutoff wavelength is $2a$.

Substituting $\beta_c = 0.70$, into nine equations of type (4) and using the Bessel Function recurrence relations, gives

$$\begin{aligned} Z_{p_{i1}}'(\beta_c \rho_i) = \frac{1}{4} \{ & [J_{p_{i1}-1}(\beta_c \rho_0) - J_{p_{i1}+1}(\beta_c \rho_0)] \\ & \cdot [N_{p_{i1}-1}(\beta_c \rho_i) - N_{p_{i1}+1}(\beta_c \rho_i)] \\ & - [N_{p_{i1}-1}(\beta_c \rho_0) - N_{p_{i1}+1}(\beta_c \rho_0)] \\ & [J_{p_{i1}-1}(\beta_c \rho_i) - J_{p_{i1}+1}(\beta_c \rho_i)] \}. \quad (20) \end{aligned}$$

The $Z_{p_{i1}}'(\beta_c \rho_i)$ functions are symmetrical with respect to the $p_i = 0$; therefore, the equation $Z_{p_{i1}}'(\beta_c \rho_i) = 0$ has one positive root, and must have an equal negative root. Since H_z is symmetric with respect to the $p_i = 0$, only the positive root p_{i1} needs to be considered.

The values $\beta_c \rho_0$ and $\beta_c \rho_i$ are too small to be considered with the ordinary approximate formula for the large argument Bessel Functions. However, because the series form of these Bessel Functions converges rather rapidly, the finite terms are used for approximate computations to obtain the roots p_i and the parameters α_i of each β_c value.

The graphical method is used to plot the function $Z_{p_{i1}}'(\beta_c \rho_i)$ against p_i (Fig. 4 shows 4 $Z_{p_{i1}}'(\beta_c \rho_{i1})$ vs the p_{i1} curve) and the root, p_{11} , of (4) is 0.625. Similarly the roots $p_{21} \dots p_{91}$ can be obtained. They are

$$\begin{aligned} p_{11} &= 0.625 & p_{61} &= 0.803 \\ p_{21} &= 0.648 & p_{71} &= 0.849 \\ p_{31} &= 0.673 & p_{81} &= 0.886 \\ p_{41} &= 0.708 & p_{91} &= 0.899. \\ p_{51} &= 0.7501 & & \end{aligned} \quad (21)$$

The curve in Fig. 4 shows only one positive real root. It is difficult to find complex roots of the equation $Z_{p_{i1}}'(\beta_c \rho_i) = 0$ for a small argument. However, the high modes of the field, H_z , are assumed to attenuate very quickly. Substituting β_c , $\alpha_1 = 0$ and nine p_{i1} roots into eight equations of type (16), α_2 through α_9 are obtained: α_9 is 1.1832. If p_{91} is substituted into (18), the result, $\alpha_9 = 1.3943$, is different from that obtained by computing equations of type (16). Therefore, the value $\beta_c = 0.70$ does not satisfy this system of eighteen equations. However, if it is assumed that $\beta_c = 0.64$ and $\beta_c = 0.67$, and α parameters are computed using the same procedure as that used to compute $\beta_c = 0.70$, the data listed in Table I result.

When $\beta_c = 0.67$, the α_9 computed from equations of type (16) and that computed from (18) are close, therefore $\beta_c = 0.67$ satisfies the system of eighteen equations. However, other lower values of β_c have been computed in which the two α_9 parameters are different. Therefore,

TABLE I
COMPUTING α_1 PARAMETER

i	$\beta_c = 0.64$			$\beta_c = 0.67$			$\beta_c = 0.70$		
	$\beta_c \rho_i$	\hat{p}_{i1}	α_i	$\beta_c \rho_i$	\hat{p}_{i1}	α_i	$\beta_c \rho_i$	p_{i1}	α_i
0	0.52			0.544375			0.56875		
1	0.6272	0.571	0	0.6566	0.599	0	0.686	0.625	0
2	0.6656	0.592	0.1365	0.6968	0.621	0.1087	0.728	0.648	0.1225
3	0.7168	0.617	0.2673	0.7504	0.642	0.1735	0.784	0.673	0.2234
4	0.7872	0.649	0.4371	0.8241	0.677	0.4787	0.861	0.708	0.4394
5	0.8704	0.687	0.6591	0.9112	0.718	0.7534	0.952	0.7501	0.6874
6	0.9792	0.735	0.9180	1.0251	0.771	1.0161	1.071	0.803	0.9342
7	1.0752	0.777	1.1512	1.1256	0.814	1.1657	1.176	0.849	1.1096
8	1.1584	0.813	1.3611	1.2127	0.851	1.2935	1.267	0.886	1.1872
9*	1.1904	0.829	1.5744	1.2462	0.863	1.3363	1.302	0.899	1.1832
9†			1.2468			1.32144			1.3943

* α_9 computing from type (16) equations.

† α_9 computing from (18).

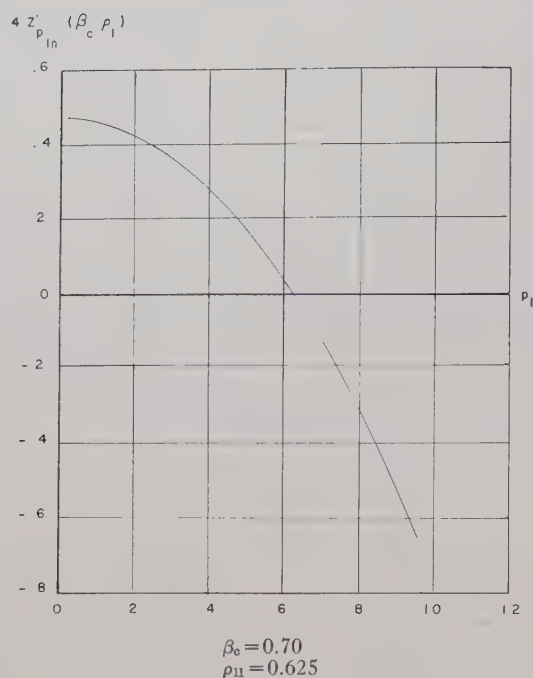


Fig. 4— $4Z'_{p_{ln}}(\beta_c, p_1)$ vs p_1 curve

$\beta_c = 0.67$ is the dominant cutoff approximate wave number of the experimental lunar line. The calculated value is in close agreement with experimental results.

VI. EXPERIMENTAL RESULTS

The lunar line used in the experiment was formed by two eccentric circular metal tubes, connected with a metal bar (Fig. 1). The waveguide wavelength of the lunar line was measured by the slotted section, audio-modulated signal source method. A crystal detector from an HP Model 805B slotted line was used to measure the free space wavelength λ . The crystal detector from the lunar line was used to measure the waveguide

wavelength λ_g . The distance between two adjacent minimum positions indicated on the VSWR meter is equal to half a wavelength. The mean value $\lambda_g/2$ was taken as the average of four such readings. The ends of the lunar line were terminated in adjustable short circuits. Care was taken in adjusting the position of these short circuits to obtain a resonant standing wave distribution within the lunar line cavity at the measuring frequency.

The experimental result of an average cutoff wavelength of the lunar line is 9.577 inches, the cutoff wave number β_c is 0.6561.

Using the same method, the waveguide wavelengths of circular and of coaxial waveguides were measured for comparison.

For a circular waveguide of radius, $a = 1.435$ inches, a waveguide wavelength $\lambda_g = 8.52$ inches was measured at a frequency of 2800 Mc. The experimental cutoff wavelength λ_c is 4.84 inches. For a coaxial waveguide, whose outer conductor radius a is 1.435 inches and whose inner conductor radius b is 0.8125 inch, a waveguide wavelength of $\lambda_g = 8.56$ inches was measured at a frequency of 2200 Mc. The experimental cutoff wavelength λ_c is 6.8 inches. The experimental results are in close agreement with the calculated value of cutoff wavelengths for circular and coaxial waveguides. The dominant cutoff wavelength of a lunar line is lower than that of circular and coaxial waveguides having the same outside diameter.

ACKNOWLEDGMENT

The authors wish to express their appreciation to C. D. Lunden and D. E. Isbell for their suggestions and to acknowledge the help of the various members of the Research Unit and of the 704 Computing Unit, Transport Division, Boeing Airplane Company.

The Negative-Conductance Slot Amplifier*

M. E. PEDINOFF†

Summary—It has been suggested that the incorporation of active solid-state devices into the elements of an antenna may lead to the simplification of the over-all microwave system and at the same time to a reduction in size, power and weight requirements. This paper will discuss several approaches to a study of the microwave properties of a slotted antenna element shunted by a tunnel diode biased into its negative-conductance region. The first approach involves calculation of the lumped parameter equivalent circuit of the slot amplifier system at resonance and can be extended to determination of the gain bandwidth and noise performance of the device, whereas the second approach is concerned with the admittance of the slot and the diode as a function of frequency over a wide frequency range. The latter method of analysis successfully predicts the conditions of oscillation and amplification at fundamental as well as higher frequency resonances and leads to a method for stabilization of the system. Preliminary experimental results indicate a transmission gain of 21.5 db at 2.7 kMc with a Hughes Number PC-3 GaAs tunnel diode in the slot amplifier.

I. INTRODUCTION

DURING the past few years, amplification techniques and devices available to the systems designer have been improved steadily to the point where the concept of low noise amplification within the elements of an antenna could be translated into a workable system. Several systems^{1,2} reported in the literature have demonstrated the feasibility of obtaining parametric amplification and conversion gain by the use of solid-state diodes integrated into the antenna configuration; thus amplification occurs in the region of reception, and transmission losses which degrade system performance are eliminated. These devices have been used with log periodic arrays and cylindrical wire antennas. This paper describes the application of an amplification technique which uses the negative conductance of a tunnel diode in a linear magnetic radiator, namely the waveguide endplate slot antenna.^{3,4} An interesting property of the endplate slot is that when it is operated at resonance, it can be used with slight adjustment to couple all of the energy in the incident wave out into space, or it can provide unity

coupling to another waveguide. Thus, by placing a negative conductance element within the slot, one can obtain transmission gain through the slot for the case of electromagnetic radiation coupled to the waveguide from space or from another waveguide. Due to the bilateral nature of the slot-diode system, one obtains gain for waves incident on the slot from either direction; but in addition, the presence of the diode within the otherwise matched slot produces a mismatch and an attendant reflection coefficient greater than unity in the direction of incidence. In many applications such as a waveguide line amplifier, the large reflected component of the wave can again reflect from regions of impedance mismatch and give rise to feedback oscillations unless proper isolation is used; but for the antenna receiving application, the wave reflected from the slot is radiated into space, thus eliminating one source of instability. This ultimately results in a reduction of the available gain by approximately 3 db, but saves considerable weight and space by the elimination of the need for a circulator and at least one isolator.

II. THEORY

Waveguide Endplate Slot

Tunnel Diode in an Endplate Slot: Consider the antenna system formed by placing a tunnel diode at the center of a horizontal centered slot cut in an infinite endplate which terminates a waveguide supporting the TE₁₀ mode, as shown in Fig. 1. Severson³ has shown that transverse broadwall slots present a series impedance to the dominant mode in the guide and can be represented by an equivalent circuit consisting of a lumped inductance, a lumped capacitance and a radiation resistance all in parallel at the frequency of resonance of the slot. Watson⁴ has shown that if the waveguide is terminated by a thin perfect conductor and the series slot is moved from the broad wall to the center of the endplate, then the slot retains its parallel, resonant, equivalent circuit and the slot impedance is now the terminating impedance for the waveguide. Thus the slot presents a parallel impedance to the dominant mode in the guide. This is illustrated in Fig. 2(a)–2(d). In this analysis we are concerned with the impedance which the slot and waveguide system presents to the terminals of the tunnel diode at the center of the slot. In other words, it is important to deduce the relationship between the wave impedance of the slot as seen from the input end⁵ of the waveguide and the driving point impedance of

* Received by the PGM-TT, June 8, 1961; revised manuscript received, July 31, 1961. The research reported in this paper has been sponsored by the Electronic Res. Directorate of the AF Cambridge Res. Ctr., Air Res. and Dev. Command, Bedford, Mass., under Contract No. AF 19(604)-8386.

† Hughes Aircraft Co., Malibu, Calif.

¹ A. D. Frost, "Parametric amplifier antenna," *PROC. IRE*, vol. 48, pp. 1163–1164; June, 1960.

² C. H. Boehner, J. R. Copeland, and W. J. Robertson, "Antennaversers and Antennafiers—Unified Antenna and Receiver Circuitry Design," *Abstracts of 10th Annual Symp. on USAF Antenna Research and Development Program*, University of Illinois, Urbana, sponsored by Wright Air Dev. Div., Wright AFB, Dayton, Ohio, October 3–7, 1960.

³ A. F. Stevenson, "Theory of slots in rectangular waveguides," *J. Appl. Phys.*, vol. 19, pp. 25–38; January, 1948.

⁴ W. H. Watson, "The Physical Principles of Waveguide Transmission and Antenna Systems, Clarendon Press, Oxford, Eng., p. 89; 1947.

⁵ In the equivalent circuits presented here which refer to a waveguide input it is assumed that the input terminals are an integral number of half wavelengths from the endplate, or that the lumped equivalent circuit refers to the plane of the slot.

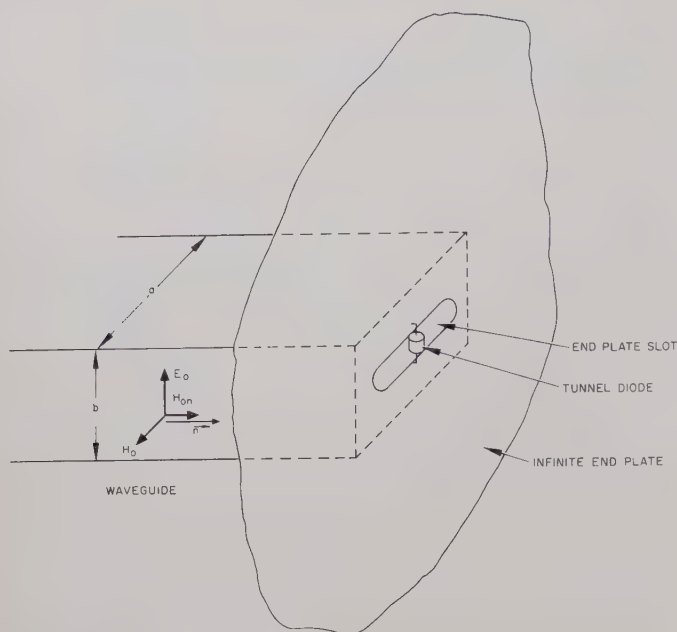


Fig. 1—Endplate slot containing a tunnel diode.

the slot as seen from a pair of terminals placed near the centers of the long walls of the slot [see Fig. 2(c) and (d)]. Thus the endplate slot acts simultaneously as a resonant circuit and as an impedance transformer. This impedance transformation ratio will be derived in a later section.

The microwave equivalent circuit of the tunnel diode has been described in the literature by several authors^{6,7} and is shown in Fig. 3 where the negative conductance is determined by the dc current-voltage characteristics of the diode shown in Fig. 4. By placing the tunnel diode across the slot (terminals ZZ'), one obtains the equivalent circuit shown in Fig. 5. If the waveguide is terminated by a constant current generator with an internal impedance equal to Z_0 , the characteristic impedance of the waveguide for the dominant mode, the equivalent circuit of the system referred to the center of the slot is given by Fig. 6 for the frequency of resonance of the slot. At frequencies far removed from resonance this equivalent circuit is not valid. This, then, is the circuit describing the transmission amplifier, and it is easily converted to the receiving amplifier by transposing the constant current generator to the position of r_s . Thus, a wave incident on the slot from the right will induce a current in the system across terminals ZZ' , and the magnitude of this current will be determined in part by absorption cross section of the slot. Fig. 7 demonstrates the lumped parameter equivalent circuit for the receiving amplifier and the feasibility of increasing the source and load currents by means of the negative con-

⁶ H. S. Sommers, Jr., "Tunnel diodes as high frequency devices," *Proc. IRE*, vol. 47, pp. 1201-1206; July, 1959.

⁷ B. Sklar, "Tunnel diode, its action and properties," *Electronics*, vol. 32, pp. 54-57; November, 1959.

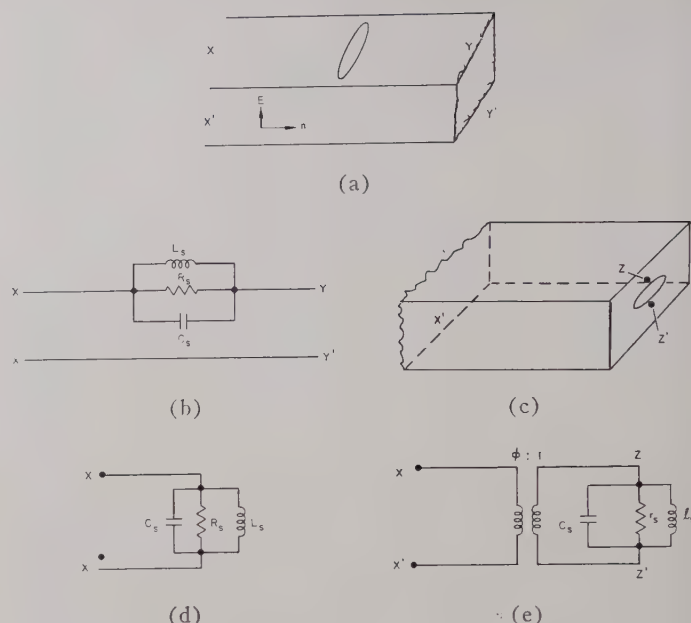


Fig. 2—Geometrical representation and circuit equivalents of slots. (a) Series slot in broad wall of a waveguide. (b) Equivalent circuit of series slot in broad wall. (c) Shunt slot in endplate of a waveguide. (d) Equivalent circuit of shunt slot in endplate of a waveguide. (e) Equivalent circuit of endplate slot showing impedance transformation property of slot at resonance.

ductance which is transformed by the reactive network to terminals ZZ' .

The preceding qualitative lumped parameter equivalent circuit analysis has been presented in order to provide the reader with some physical insight into the amplification behavior of this device and is based largely on heuristic arguments. The equivalent circuit for the slot is valid only near resonance, and the presence of an obstruction in the center of the slot such as a tunnel diode provides a sufficient lumped reactance to alter the coupling of the slot to the waveguide. This results in a shift in slot resonant frequency and an alteration of the elements of the equivalent network. If the dimensions of the diode become appreciable with respect to slot wavelength the fields will be distorted and the equivalent circuit parameters will be altered.

In view of the fact that the circuit is valid only over a narrow frequency range and must be changed for each higher order resonance of the device, it is of limited usefulness for determining stability conditions over a wide range of frequency. However, the lumped parameter equivalent circuit can be used to estimate the gain bandwidth product of the system.

Properties of the Resonant Endplate Slot Terminating a Waveguide: Stevenson⁸ has shown that for the case of a slot in one wall of an infinite (terminated) waveguide the voltage amplitude P at the center of the slot near resonance is related to the amplitude A of an incident TE_{10} wave by the formula

$$P/A = \zeta/Ka, \quad (1)$$

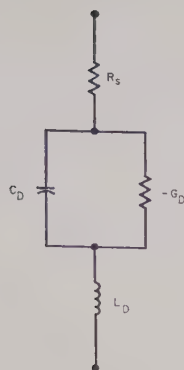


Fig. 3—Equivalent circuit of tunnel diode biased into the negative-conductance region.

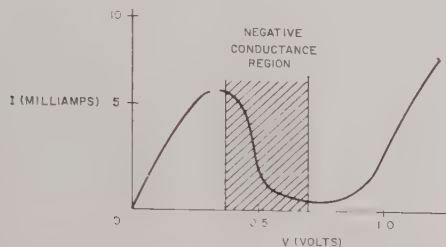


Fig. 4—Typical current vs voltage characteristic of a tunnel diode.

where ζ and K are complex dimensionless quantities defined in (2) and (3) and a is the broadwall dimension of the waveguide.

$$\zeta = \int_{-\lambda/4}^{\lambda/4} f(\xi) \cos k\xi d\xi, \quad (2)$$

where $f(\xi)/a$ denotes the component of H along the slot at the point ξ in an $H_{01}(\text{TE}_{10})$ wave of unit amplitude traveling in the positive Z direction.

$\text{Re}(K)$

$$= -73/60\pi - (\gamma/2) |\zeta|^2 \text{ (endplate slot only)} \quad (3a)$$

$\text{Re}(K)$

$$= -\gamma |\zeta|^2 \text{ (guide to guide endplate coupling slot)}, \quad (3b)$$

where $\gamma = 1/\pi^2 k U a b$, $k = 2\pi/\lambda$, $U = k_g = 2\pi/\lambda_g$, and b is the height of the guide.

The amplitudes of the reflected and transmitted waves in the guide generated by the voltage induced in the slot are given by

$$B/P = \zeta/\pi^2 k U b$$

$$C/P = \zeta^*/\pi^2 k U b \text{ (for guide to guide case only)}, \quad (4)$$

where the star denotes the complex conjugate.

Applying these equations to the case of the waveguide terminated by an endplate slot one finds that the wave reflected from the endplate consists of two components. One component is due to the endplate in the absence of the slot and the other due to the presence of the

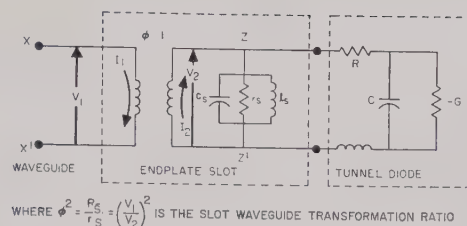


Fig. 5—Equivalent circuit of tunnel diode slot configuration referred to waveguide input terminals.

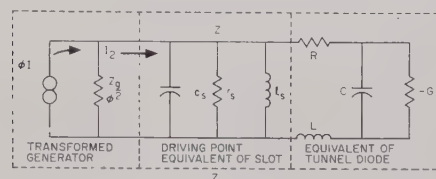


Fig. 6—Equivalent circuit of tunnel diode slot transmission amplifier including matched generator at waveguide input.

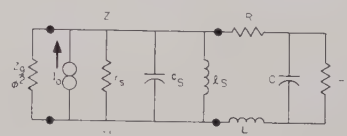


Fig. 7—Equivalent circuit of tunnel diode receiving amplifier.

slot. Thus, if the amplitude of the incident wave is A and the reflection coefficient of the plate is -1 , one obtains for the reflected component from (1) and (3)

$$B' = -A + B = -A \left(1 - \frac{\gamma \zeta^2}{K}\right) \quad (5a)$$

or

$$\Gamma = \frac{B'}{A} = -1 + \frac{\gamma \zeta^2}{K}, \quad (5b)$$

where Γ is the reflection coefficient of the system referred to the plane of the slot.

The impedance of the endplate slot normalized to the waveguide is then defined by

$$Z_n = \frac{1 + \Gamma}{1 - \Gamma} = \frac{\gamma \zeta^2}{2K - \gamma \zeta^2} = \frac{-30\pi \gamma \zeta^2}{73}. \quad (6)$$

Consider now an endplate containing a slot of length $2L$ and width 2ϵ with its center displaced by x_0 from the narrow wall of the guide and oriented at an angle θ relative to the broadwall (see Fig. 8). Letting the X axis be parallel to the broadwall, one obtains from Stevenson's solution for the fields in the guide the magnetic component H_x

$$H_x = \left(j \frac{\pi}{a} U_{01}\right) \sin \frac{\pi x}{a}. \quad (7)$$

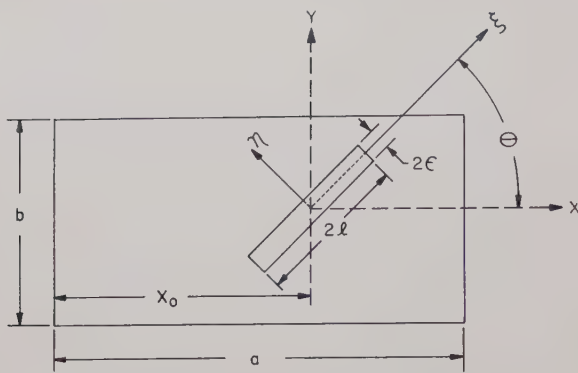


Fig. 8—Endplate slot position and orientation.

The component of H along the slot then has the form

$$\begin{aligned} \frac{f(\xi)}{a} &= 2H_{xi} = 2H_x \cos(\theta) \\ &= \left(j \frac{2\pi}{a} U_{01} \right) \sin \left(\frac{\pi(x_0 + \xi \cos \theta)}{a} \right) \cos \theta, \quad (8) \end{aligned}$$

where the factor 2 in front of H_{xi} is to account for the incident and reflected fields at the endplate. Combining (8) and (2), one obtains

$$\zeta = -j4\pi \frac{U_{01}}{k} \cos \theta \left[\frac{\sin \left(\frac{\pi x_0}{a} \right) \cos \left(\frac{\pi}{4} \frac{\lambda}{a} \cos \theta \right)}{1 - \left(\frac{\lambda}{2a} \right)^2 \cos^2 \theta} \right]. \quad (9)$$

For the centered horizontal endplate slot the parameters X_0 and θ have the values $x_0 = a/2$, $\theta = 0$, and the function ζ is given by

$$\zeta = -j4\pi \frac{U_{01}}{k} \frac{\cos \frac{\pi \lambda}{4a}}{1 - \left(\frac{\lambda}{2a} \right)^2} = -j4\pi \frac{\cos \left[\frac{\pi}{2} \sin i \right]}{\cos i}, \quad (10)$$

where $\sin i = \lambda/2a$ and $\cos i = \lambda/\lambda_g = U_{01}/k$.

In general, the endplate function $|\zeta|^2$ has the form

$$|\zeta|^2 = \frac{16\pi^2 \cos^2 i \cos^2 \theta \sin^2 \frac{\pi x_0}{a} \cos^2 \left(\frac{\pi}{2} \sin i \cos \theta \right)}{[1 - \sin^2 i \cos^2 \theta]^2}. \quad (11)$$

The normalized impedance of the centered horizontal endplate slot thus becomes

$$\begin{aligned} Z &= \frac{30\pi}{73} \times \frac{1}{\pi^2 k U a b} \times \frac{16\pi^2 \cos^2 i \cos^2 \left(\frac{\pi}{2} \sin i \right)}{\cos^4 i} \\ &= 2.09 \frac{a}{b} \frac{\sin^2 i}{\cos^3 i} \cos^2 \left(\frac{\pi}{2} \sin i \right). \quad (12) \end{aligned}$$

The preceding analysis can be extended to the more general case of a displaced rotated endplate slot by the use of (9) and (6). (While this analysis is not new it ap-

pears in the literature in sufficiently ambiguous form as to require restatement here.)

Thus it is apparent that the slot presents an impedance to the reference plane of the waveguide given by

$$Z_{in} = Z_n Z_g = \left(\frac{\gamma \zeta^2}{2K - \gamma \zeta^2} \right) Z_g, \quad (13)$$

where Z_g is the characteristic impedance of the guide for the dominant mode of propagation, and Z_{in} is the waveguide input impedance.

Hence the slot behaves as an impedance transformer which transforms the driving point impedance of the resonant slot radiating into a half space ($2R_s$) into the input impedance given by (13) above. This impedance transformation ratio ϕ^2 is defined as the quotient of the input impedance Z_{in} and the slot impedance $2R_s$.

$$\phi^2 = \frac{Z_{in}}{2R_s} = \left(\frac{\gamma \zeta^2}{2K - \gamma \zeta^2} \right) \frac{Z_g}{2R_s}, \quad (14)$$

where

$$R_s = \frac{(120\pi)^2}{4 \times 73} \quad (15)$$

for a halfwave resonant slot.⁸

An equivalent circuit representation of this transformer is given in Figs. 8 and 9. If the waveguide is terminated in a matched load, the impedance presented to the driving point of the slot due to this load is given by

$$Z = \frac{Z_g}{\phi^2} = \left(\frac{2K - \gamma \zeta^2}{\gamma \zeta^2} \right) 2R_s. \quad (16)$$

Since this impedance is in parallel with the slot radiation resistance $2R_s$, the total driving point admittance of the resonant endplate slot coupled to a matched waveguide is found to be

$$Y_s = \frac{1}{2R_s} \left(1 + \frac{\gamma \zeta^2}{2K - \gamma \zeta^2} \right). \quad (17)$$

By applying conservation of power⁹ to the guide-to-guide mutual endplate slot, *i.e.*, the resonant transverse iris, the driving point impedance of the slot radiating in one direction is found to be equal to

$$Z_{slot} = \frac{2(377)}{\gamma(\zeta)^2} = 2\eta/\gamma(\zeta)^2. \quad (18)$$

⁸ Putnam in the book noted below has shown that experimental values for the driving point impedance of resonant slots are centered about 350 ohms, and that the spacing of the centered driving points has a pronounced influence on this impedance.

J. L. Putnam, "Input impedances of centre-fed slot aeriels near half wave resonance," *J. IEE (London)*, vol. 95, pt. 3A, p. 290; 1948.

⁹ By assuming a wave of unit amplitude incident on the slot, one can compute the power incident on the slot, the power reflected from the slot, and the power transmitted through the slot, as well as the voltage induced at the center of the slot. Then equating the transmitted power in terms of the slot voltage and impedance to the net power in the dominant mode we may obtain (18).

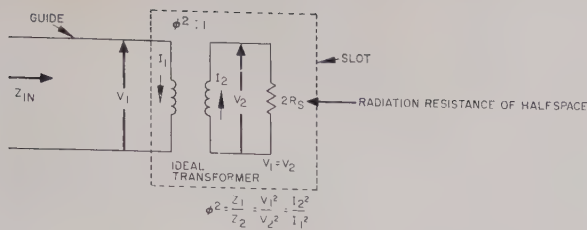


Fig. 9—Equivalent transformer—endplate slot.

If the resonant slot feeds a matched guide, all of the energy incident on the slot is transmitted and the input impedance is equal to Z_0 . Therefore, a transformation ratio¹⁰ $(\phi')^2$ can be defined by

$$(\phi')^2 = \frac{Z_0}{2\eta/\gamma(\zeta)^2} = \left(\frac{\gamma(\zeta)^2}{2\eta} \right) Z_0. \quad (19)$$

(see Fig. 10). Thus the matched load Z_0 transforms into the slot as $Z_0/(\phi')^2$. Adding this transformed impedance to that of the diode Z_D one gets

$$Z = \left(\frac{1}{Z_D} + \frac{(\phi')^2}{Z_0} \right)^{-1}. \quad (20)$$

Transforming back to the input yields the input impedance Z_{in} or admittance Y_{in} ;

$$Z_{in} = (\phi')^2 \left[\frac{1}{Z_D} + \frac{(\phi')^2}{Z_0} \right]^{-1} \\ Y_{in} = \frac{Y_D}{(\phi')^2} + Y_0 = Y_0 \left(\frac{2\eta Y_D}{\gamma(\zeta)^2} + 1 \right). \quad (21)$$

Eq. (21) is an approximation relating the measured waveguide input admittance to the admittance of the diode in the waveguide slot. It is understood here that the transformation ratio $(\phi')^2:1$ relates the driving point impedance of the unobstructed guide-to-guide coupling slot to the input impedance of the waveguide. Any change in boundary conditions at the slot such as the presence of the diode or a change in guide height will alter this transformation ratio. However, if the circuit is analyzed from the viewpoint that the tunnel diode located at the center of the slot "sees" a constant current generator of internal impedance $Z_0/(\phi'')^2$ on the left and a load of impedance equal to $Z_0/(\phi'')^2$ on the right, where $(\phi'')^2$ is the true impedance transformation ratio, then the circuit shown in Fig. 11 will adequately represent the system, provided ϕ' is replaced by ϕ'' . Two problems preclude a meaningful analysis of the equivalent circuit of the slot tunnel diode guide-to-guide coupler. The first of these is based on the fact that at resonance it is difficult to compute the exact transformation ratio $(\phi'')^2$, and the second arises because it is difficult to determine the transformation ratio at fre-

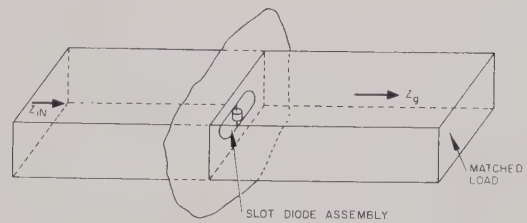


Fig. 10—Sketch of endplate slot—diode assembly acting as a guide-to-guide coupler.

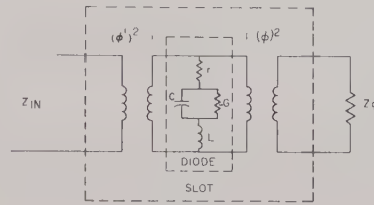


Fig. 11—Equivalent circuit of endplate slot diode guide-to-guide coupler.

quencies removed from the fundamental slot resonance.

As a consequence of the above analysis, the conclusion was drawn that ordinary waveguide measurements made on endplate slots and guide-to-guide coupling slots containing negative resistance diodes would yield information which could not be readily correlated with theory at frequencies off resonance. Moreover, at resonance the theory could be evaluated only by means of a parameter ϕ'' which in turn was not simply deducible from experiment because of the peculiarities of negative impedances. However, the form of the equivalent circuit obtained should be amenable to gain and noise analyses. In the next section a method of analysis is presented which qualitatively predicts the behavior of diode slot systems and is applicable to waveguide slot systems as well as slots in infinite conducting planes.

Admittance Analysis

Admittance Analysis of Tunnel Diode Slot Systems: An evaluation of (15) and (18), which describes the driving point impedance of an endplate slot and a guide-to-guide coupling slot, respectively, shows that the driving point radiation resistances of the slot radiating into space and into a matched waveguide differ by approximately 30 per cent for the case where $\lambda = 1.4a$ and $a = 2b$ (typical values for these waveguide parameters). Therefore, one can expect that the admittance properties of both slot geometries will show similar behavior as a function of frequency with the exception that the conductance of the guide-to-guide coupling slot will exceed that of the endplate slot by 30 per cent. Apparently here the role of the environment of the slot is to determine the degree of coupling of the slot field to the boundaries and has little effect on the resonant frequency of the slot. However, in the case of an endplate slot backed by a resonant cavity, Putman⁸ has shown that the presence of the cavity gives rise to a doubling of the resistive component of the impedance for all

¹⁰ Use of (6), (10) and (15) in (14) indicates that ϕ' in (19) is identical to (ϕ) in (14). This implies that the field configurations on either side of the slot are independent of each other.

cavity dimensions, and a marked dependence of the reactance at all frequencies on cavity dimensions. This is attributed to the natural reactance of the cavity in shunt with that of the slot.

In the light of this information, it was concluded that the driving point behavior of a resonant slot radiating endwise into two matched waveguides would be quite similar to that of a resonant slot cut in an infinite conducting plane and radiating into space. Hence an admittance analysis of the free space slot diode systems should predict qualitatively the behavior of the waveguide endplate diode slot and the guide-to-guide slot diode coupler systems as a function of frequency.

Calculation of the Driving Point Admittance of a Resonant Slot Cut in an Infinite Conducting Plane: By using an application of Babinet's principle¹¹ it can be shown that the radiation (driving point) impedance of a strip dipole and its slot complement are reciprocally related by the expression

$$Z_s = \frac{(Z_0)^2}{4Z_w}, \quad (22)$$

where $Z_0 = 120 \pi$, Z_s is the impedance of the slot, and Z_w is the impedance of a strip dipole of the same shape and size as the slot. This relationship is not restricted to resonance conditions; hence, if the impedance of the strip dipole is known as a function of frequency, then one can calculate the corresponding complementary slot impedance as a function of frequency. The slot admittance can be calculated from (22) by inserting the equation

$$Y_s = \frac{4}{(Z_0)^2} Z_w, \quad (23)$$

where Y_s is the driving-point admittance of the slot.

One point to be considered here is that the usual tabulations of impedance data presented by King¹² and others have been obtained from calculations based on wire antennas of circular cross section, whereas the complement of a slotted antenna is a flat strip. Hallen¹³ has shown that if the flat strip antenna has a width equal to W then it is equivalent in cross section to a wire of radius

$$a = \frac{W}{4}. \quad (24)$$

Since impedance data is usually tabulated for various values of the ratio of antenna length to diameter ($2h/2a$), this aspect parameter for the slot complement

can be written as

$$\frac{h}{a} = \frac{4h}{W}, \quad (25)$$

where $2h$ is the slot length and W is the slot width. The thickness-length parameter is sometimes described by the function

$$\Omega = 2 \ln \frac{2h}{a}. \quad (26)$$

The equivalent dimension parameter h/a or Ω for the slot is thus calculated from (24) or (25) and is used to select the appropriate tabulated wire dipole impedance data from King.¹² This impedance data is then converted by means of (23) into slot admittance data.

The device used in this experiment contained a slot of length 2.25 in and of width 0.030 in. Thus, from (25) and (26), the thickness-to-length parameters were found to be $h/a = 150$ and $\Omega = 2 \ln (2h/a) = 11.4$. Returning to the dipole data given by King, it was concluded that the resistance and reactance of a wire dipole of thickness-to-length ratio (h/a) equal to 122.4 was sufficiently accurate for use in evaluation of the slot admittance near the first resonance. Taking the real and imaginary parts of (23), the slot conductance and susceptance were computed from the relations

$$G_s = \frac{R_w}{35,476}$$

$$B_s = \frac{X_w}{35,476}, \quad (27)$$

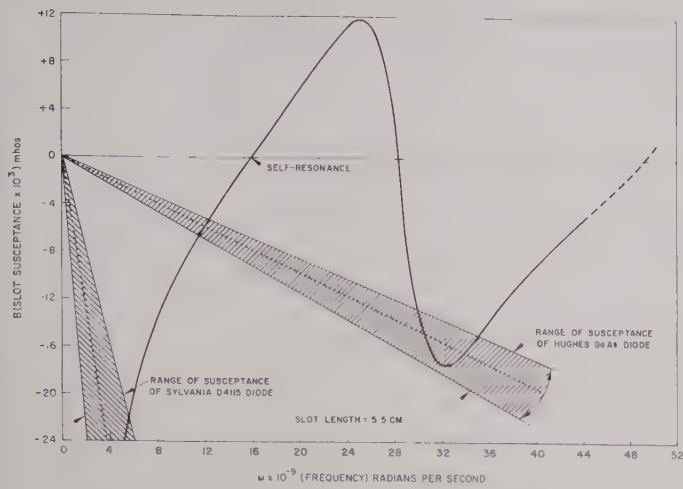
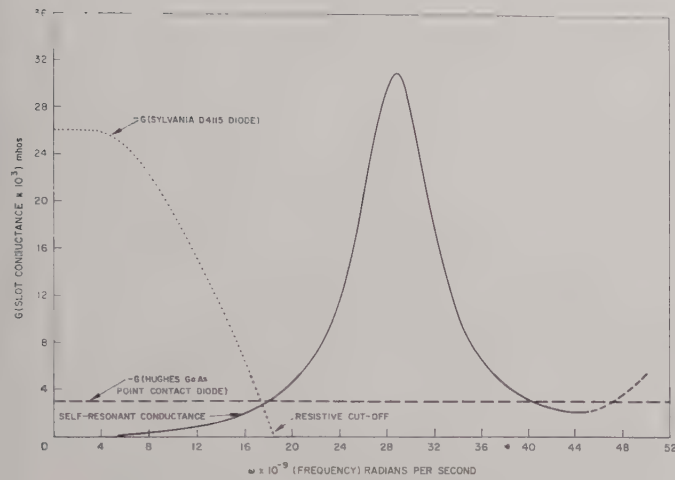
where R_w and X_w are the real and imaginary parts of the dipole impedance, and G_s and B_s are the conductance and susceptance of the slot, respectively. The admittance data thus obtained is shown as a function of frequency in Figs. 12 and 13. Comparison of these graphs of the calculated slot conductance and slot susceptance as a function of frequency with measured values of slot resistance and reactance as a function of frequency obtained by Putman indicates that the theoretical and experimental curves have the same general form but differ slightly in scale factor. For example, the calculated conductance of the slot at resonance ($\lambda/2$) is 2×10^{-3} mho and is somewhat smaller than a value of 2.8×10^{-3} mho measured at lower frequencies by Putman. This discrepancy between theoretical and empirical values of resonant slot admittance has been discussed by Bailey¹⁴ who concludes that these values may differ by 20 per cent barring experimental inaccuracies and driving-point effects. The purpose of this comparison has been to show that the driving-point admittance as a function of frequency of a slot cut in an infinite conducting plane can be qualitatively predicted by

¹¹ H. G. Booker, "Slot aeriels and their relation to complementary wire aeriels (Babinet's principle)," *J. IEE (London)*, vol. 93, Part 3A, p. 620; 1946.

¹² R. W. P. King, "The Theory of Linear Antennas," Harvard University Press, Cambridge, Mass., p. 173; 1956.

¹³ E. Hallen, "Theoretical investigations into the transmitting and receiving qualities of antennae," *Nova Acta Regiae Soc. Sci. Upsaliensis*, ser 4, vol. 11, pt. 1, p. 1; 1938.

¹⁴ C. E. G. Bailey, "Slot feeders and slot aeriels," *J. IEE (London)*, vol. 93, pt. 3A, p. 615; 1946.

Fig. 12—Slot susceptance as a function of ω .Fig. 13—Slot conductance as a function of ω .

means of the preceding computational steps. Moreover, the results of the calculation should be sufficiently accurate to enable prediction of the shifted resonance frequencies and the net driving-point conductances which will result when a microwave tunnel diode is placed across the center of the slot.

Conductance Transformation of a Tunnel Diode: If a semiconductor diode, such as a tunnel diode, is now placed at the feed terminals of the slot, the frequencies of resonance and the total conductance of the system at these resonance frequencies can be determined by superimposing the diode conductance and susceptance on the graphs of slot conductance and susceptance with the signs reversed. The resonance frequencies would, therefore, occur whenever the diode susceptance and the slot susceptance intersected.

In order to plot the diode susceptance and conductance in conformity with the foregoing scheme, one must first transform the equivalent circuit of the diode. By neglecting the series inductance of the tunnel diode equivalent circuit one obtains a three-element circuit which can be conveniently reduced to two elements (see Figs. 14 and 15). Since the impedances of both circuits

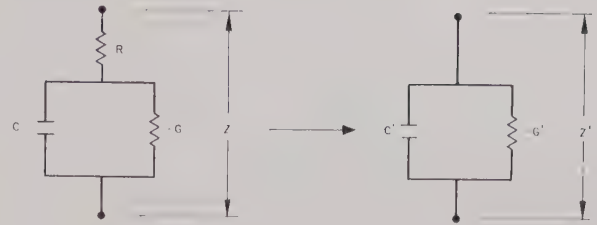


Fig. 14—Tunnel diode simplified equivalent circuits.

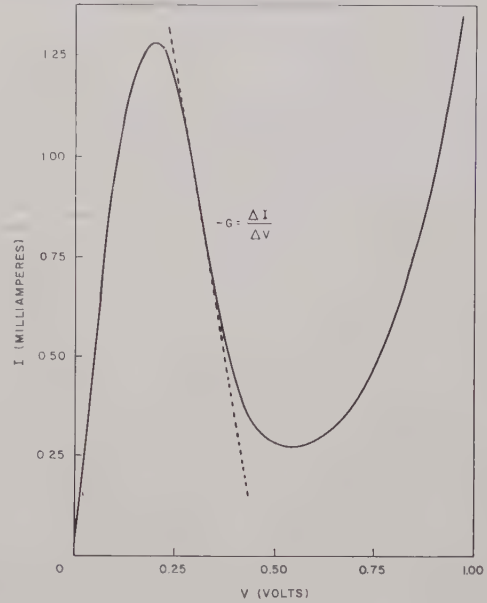


Fig. 15—I-V characteristic of Hughes PC-3 GaAs tunnel diode.

are equal, one can write

$$Z' = \frac{1}{j\omega C' - G'} = Z = R + \frac{1}{j\omega C - G} \quad (28)$$

The resistive cutoff frequency $\omega = \omega(\max)$, occurs when $\text{Real } Z(\omega) = 0$. Solving for $\omega \max$ yields

$$f_{\max} = \frac{G}{2\pi C} \sqrt{\frac{1}{GR} - 1}, \quad (29)$$

where for later use we define

$$\alpha = f/f_{\max} = \omega/\omega_{\max}. \quad (30)$$

By equating the real and imaginary parts of (28) one obtains

$$C' = \frac{C}{(1 - RG)^2 + \omega^2 R^2 C^2} \quad (31)$$

$$-G' = \frac{-G + RG^2 + \omega^2 C^2 R}{(1 - RG)^2 + \omega^2 R^2 C^2}. \quad (32)$$

Using (29) and (30) to eliminate the capacitance C from the denominator of (31) for C' and from the numerator and denominator of (32) for $-G'$ yields

$$\frac{1}{G'} = \frac{1}{G(1 - \alpha^2)} - R, \quad (33)$$

and

$$C' = \frac{C}{(1 - RG)(1 - RG + \alpha^2 RG)} \quad (34)$$

For frequencies far below cutoff $a \ll 1$ and

$$\frac{1}{G'} \approx \frac{1}{G} - R \quad (35)$$

$$C' \approx \frac{C}{(1 - RG)^2} \quad (36)$$

A typical calculation performed on the Sylvania D4115 B Tunnel Diode indicates that at low frequencies the negative resistance and the capacitance of the diode are given approximately by

$$\begin{aligned} \frac{1}{G'} &\approx 36.4\Omega \quad \text{or} \quad G' \approx 2.74 \times 10^{-2} \text{ mhos} \\ C' &\approx 7 \text{ pf} \quad \text{for} \quad \omega < 19 \times 10^9 \approx \omega_{\text{max}} \end{aligned} \quad (37)$$

Plots of diode conductance G' and susceptance $-\omega C'$ are shown in Figs. 12 and 13 superimposed on the calculated values of slot conductance G and susceptance B . In addition, the estimated conductance and susceptance of the Hughes point contact Gallium Arsenide (PC-23) tunnel diode are shown on the same figures for comparison.

It is apparent from a study of Figs. 12 and 13 that at resonance the Sylvania tunnel diode cannot provide stable amplification because the negative conductance of the diode greatly exceeds the slot conductance, and will, therefore, give rise to large amplitude oscillations. Similarly in the case of the Hughes diode (PC-23) at resonance the negative conductance slightly exceeds the positive conductance and gives rise to oscillations.

Admittance Transformation Within the Slot: In order to stabilize the diode-slot system, some technique must be used to effect a transformation of the slot conductance and/or susceptance presented to the diode so that either the resulting conductance at resonance is positive or the resonant frequencies of the system are shifted into regions where the net conductances are non-negative. Several techniques are available which will cause the admittance presented to the diode to change. The first of these is the impedance or admittance transformation obtained when a dipole is fed asymmetrically. It can be shown that if the voltage distribution of an infinitesimally thin resonant slot antenna is independent of feed position, then the driving point resistance at resonance as a function of feed position is given by

$$R(d) = R_s \left[\sin \frac{\pi}{2} \frac{d}{l} \right]^2, \quad (38)$$

where $R_s \cong 480\Omega$ is the radiation resistance of the half-wavelength slot when center fed at resonance, d is the position of the feed from one end of the slot, and $2l$ is the slot length. Inversion of (38) yields the resonant

conductance of the slot as a function of feed position

$$G_s(d) = \frac{1}{R_s \left[\sin \frac{\pi}{2} \frac{d}{l} \right]^2} \quad (39)$$

It is apparent that the conductance presented to the diode at slot resonance can vary from approximately 2×10^{-3} mho with the diode at the center of the slot to ∞ mho with the diode at the end of the slot (for a thick slot the conductance at the end of the slot is finite).

According to King¹⁵ the input impedance of an asymmetrical-fed antenna is equal to the sum of the impedances of two antennas of different and quite arbitrary lengths. This conclusion is based on the evidence that the current distribution in each part of the antenna is largely independent of the other part. The antenna impedances under consideration here are half impedances calculated on the basis of center fed antennas of half lengths equal to the lengths of the asymmetrical elements. These half impedances are directly obtained from the impedance data computed for center fed elements by merely dividing the resistance and reactance by two. In fact the same impedance plot suffices to describe the impedance of these elements of dissimilar length provided the frequency scale on the abscissa of the data is adjusted to account for the different lengths. Thus, for an antenna fed near one end, one adds half of the impedance of a vanishingly small antenna to half the impedance of an antenna of almost twice the length of the total antenna. Further analysis of this system indicates that below resonance the effect of shifting the feed to one end is to increase the driving point impedance of the wire antenna. In a similar manner one finds that the admittance of a slot fed near one end is a large quantity near resonance for the slot. Moreover, this method of analysis of asymmetrical feeding of slots indicates that the net susceptance of the slot does not remain constant as one moves the driving point of the slot.

The conclusion drawn from the analysis of impedance transformation due to a shift in the driving point of the endplate slot is that for a given driving point (diode) location it is possible, using King's technique, to compute the driving point conductance and susceptance presented to the diode. However, if one requires the complete admittance behavior as a function of frequency for all slot positions, the data manipulation would require computer processing and plotting. In addition, the results would not possess a high degree of accuracy for determining system resonance frequencies because of the absence of susceptance data describing the local field perturbation due to the diode package within the slot.

A second technique for altering the slot admittance involves the use of a lumped admittance element placed within the slot. For example, by placing a rod through a hole cut in one wall of the slot, one can produce an obstacle within the slot whose behavior will be analo-

¹⁵ King, *op. cit.*, p. 406.

gous to that of an obstacle in a waveguide. It has been experimentally determined that a slot which is resonant at 4 kMc can be suitably loaded by an obstacle so that it resonates at a frequency below 3 kMc. By applying Babinet's principle to cylindrical antennas it is observed that lengthening a half-wave dipole makes it more inductive, whereas lengthening a half-wavelength slot makes it more capacitive and shortening it makes it more inductive. Therefore, a slot cut to resonate at a given frequency will be inductive below resonance. Introducing an obstacle which incompletely fills the slot and provides the required amount of capacitance will restore the condition of resonance. It is thus apparent that by reducing the length of the slot one can shift the slot resonances to higher frequencies; then by placing a variable shunt capacitance at the center of the slot one can tune the slot in order to bring the fundamental resonance of the slot back to its original frequency. As a result of this manipulation the fundamental resonance will be unchanged, but all higher frequency resonances will be shifted to new frequencies, some higher and some lower than before. Furthermore, the resonant conductance of the slot will be reduced by this adjustment.

Returning to Figs. 12 and 13, it is seen that the presence of a lumped capacitance due to the diode or another obstacle at the center of the slot will shift the first resonance of the system to a lower frequency than one would obtain in the absence of capacitive loading. Therefore, if amplification is required at a given frequency, the slot must be designed so that the first resonance, after loading, falls at this frequency and all other resonances occur at frequencies where the net conductances of the system are positive. In order to avoid a detailed cut and try procedure, it is possible to provide the slot with a variable capacitance at the center to facilitate tuning to resonance. Another useful variable parameter is the tunnel diode bias voltage. By carefully controlling this voltage, the diode conductance can be varied from its maximum negative value through zero to a positive value. Thus by manipulating a variable capacitance and the diode bias voltage, it is possible to tune an appropriately selected diode slot system into the condition of oscillation or of stable amplification.

III. EXPERIMENTAL PROGRAM

Slot Amplifier

The theoretical analysis presented earlier in this paper yielded insight into the behavior of tunnel diode slot amplifiers located in infinite conducting plates, but no concise theoretical development was obtained which would predict the behavior of the waveguide slot-diode amplifier system over a wide range of frequency. On the basis of experimental results presented by Watson¹⁶ it was observed that the normalized admittance of slots cut in waveguide was quite similar to that of slots in an infinite conducting plane with the exception of a scale factor over a wide range of frequency. Hence it was concluded that the stability analysis of the "free space"

slot-diode system also applied approximately to the waveguide endplate slot-diode and guide-to-guide slot-diode coupler systems. Therefore, the experiment which was chosen to test the theoretical hypotheses expounded earlier included the guide-to-guide endplate mutual coupling slot. This resulted in the simplest experimental configuration in which the slot would still manifest many of the properties of an antenna and at the same time eliminated the need for an anechoic room.

The experimental apparatus consisted of an S-band signal generator coupled into a slotted line through a directional coupler and a 20-db waveguide attenuator; and an S-band spectrum analyzer connected by means of a 40-db strip-line isolator and a variable waveguide attenuator to the opposite end of the slotted line (see Fig. 16). In practice, the endplate slot containing the tunnel diode was inserted between the slotted line and the variable attenuator and the apparatus was adjusted to produce stable amplification. The slotted plate was then removed from the apparatus and the attenuator setting was changed to bring the transmitted signal back up to its previous value. The difference in these attenuator settings thus yielded the insertion gain of the system. In essence this method of measurement compares the transmissivity of the slot amplifier with that of a passive resonant slot, since the resonant slot will present a normalized conductance of unity to the incident wave in the guide.

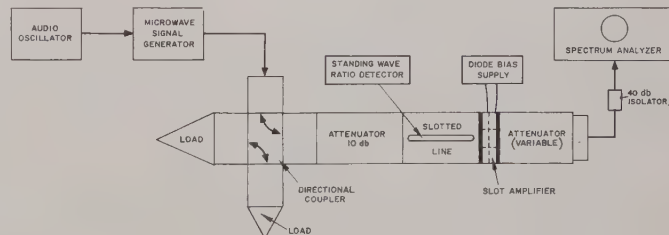


Fig. 16—Tunnel diode slot amplifier setup.

The endplate apparatus shown in Fig. 17 was originally designed to resonate unloaded at 2.7 kMc. However, the loading of the diode depressed the resonant frequency below the range of measurement of the apparatus. In the experiment performed in the laboratory, a second slotted endplate (designed to resonate above 4 kMc unloaded) with a movable obstacle in the slot was placed adjacent to and in contact with the semi-bifurcated endplate containing the tunnel diode. By varying the position of the obstacle as well as the diode bias, a condition of resonance was encountered at which the slot exhibited transmission gains of 8, 16 and 21 db in the neighborhood of 2.7 kMc with different diodes, and a 3 db bandwidth of 21 Mc was observed for the amplifier with a center frequency gain of 16 db. The frequency response plot is shown in Fig. 18. It was assumed at that time that the inductance furnished by the second endplate was sufficient to shift the first resonance into a frequency region where the slot conductance exceeded the diode negative conductance. However, the auxiliary slot shortened the original slot containing the

¹⁶ Watson, *op. cit.*, pp. 82-85.

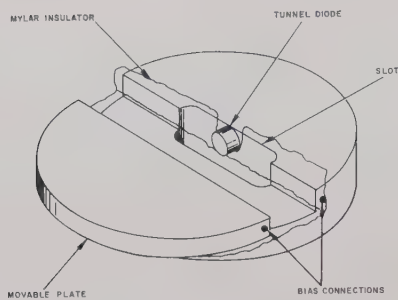


Fig. 17—Solid-state antenna configuration.

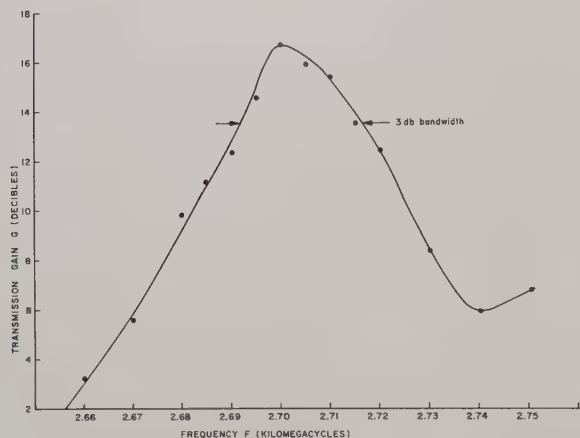


Fig. 18—Transmission gain as a function of frequency for the tunnel diode slot amplifier.

diode thus elevating its resonant frequency and influencing the positions of all system resonances in some manner as well as the conductance of the system as a function of frequency. It is obvious from the amplifying behavior of the system that this technique does not shift any higher resonances into negatively conducting regions; otherwise the power gain of the system at the first resonance would be negligible.

Slot Oscillator

During the course of the experimentation on active slot elements, it was observed that when a diode (Sylvania D4115 B) was located off center and suitably biased, the slot system would radiate a -38 dbm microwave signal in the neighborhood of 3 kMc. This frequency was dependent on slot position as well as bias voltage, but the amplitude was essentially independent of these conditions over a wide range of frequency. When a low level signal (-60 dbm) from the microwave signal generator was fed into the system it was observed that if the two signals were a fraction of a megacycle apart the oscillator would lock onto the incoming signal. This behavior was amplitude dependent, since very weak signals would not "pull" the oscillator, and very strong ones would give rise to harmonic generation and mixing.

IV. CONCLUSIONS

It is beyond the scope of this paper to analyze in detail the complete frequency dependence of system admittance because of a lack of adequate data describing the electrical parameters of the experimental tunnel diodes used in the experiment and because of the limited accuracy of the values of slot admittances which are based on theoretical wire dipole impedance calculations. However, the analysis and the results presented thus far indicate that if the conductance and susceptance of a tunnel diode are known over a wide frequency range it is possible to design a slot environment which will insure stable system behavior. Also, the variability of the diode admittance as a function of bias voltage provides a method for adjustment of the system. The equivalent circuits are presented in a form suitable for gain bandwidth and noise analyses, but no attempt has been made here to optimize the performance of the device.

The experimental work conducted on the project to date has been conducted entirely within a waveguide system. On the basis of the observed behavior it is expected that similar results will be obtained when the active slot elements are tested as antenna elements which couple to "space." It is anticipated that in the amplifier case a multiple element active array will require isolation devices between elements to prevent feedback oscillation from occurring.

The results presented indicate that the "solid-state antenna" concept may play a significant role in future radar systems. The diode slot amplifier can be used in an amplifying array in which the phase shift of each element is controlled by the diode bias voltage or by means of a varactor diode shunting the tunnel diode. On the other hand, the behavior of the slot-oscillator indicates the possibility of using an array of tunnel diode slot oscillators backed by a common cavity as a short range solid state transmitting antenna. These slot devices are compact and require a minimum of waveguide circuitry and in some instances can be used to convert directly from a microwave frequency to a low radio frequency by using the tunnel diode as an autodyne down converter. By backing the slot amplifier with a suitable resonant cavity, it may be used in conjunction with a circulator to form a reflection amplifier, and by cascading slot amplifiers and isolators it should be possible to produce a slotted traveling-wave amplifier.

ACKNOWLEDGMENT

The author wishes to acknowledge Dr. W. H. Kummer for his encouragement and interest in this work, and Dr. A. T. Villeneuve for many rewarding hours spent in discussion of the properties of slotted antennas. To Dr. L. L. Bailin and many colleagues at Hughes Aircraft Company the author wishes to express his gratitude for their unstinting support.

Correspondence

Measurement of the Conversion Conductances of Esaki Mixer Diodes*

In order to compare the theoretically predicted and the experimentally observed behavior of frequency converters using Esaki diodes, it is necessary to evaluate various mixer parameters, in particular, the conductance elements of the conversion matrix. As is well known, these conductance elements are certain Fourier coefficients of the periodic series representing the incremental time-varying diode conductance.¹ This conductance is produced by the large local oscillator (LO) voltage acting on the nonlinear diode. Although one can determine these element values using a numerical Fourier analysis, this approach is both time-consuming and laborious.² As an alternative, we suggest an experimental technique originally proposed by Dicke over ten years ago for use with conventional (positive-conductance) crystal mixer diodes.¹ Since this method is quite easy to apply in that it only involves several low-frequency bridge measurements and one standing-wave measurement, and since, apparently, it is not well known, we shall risk repetition by describing a simplified version of it which we have modified to apply to Esaki diodes.

To simplify the problem we assume that in the voltage and frequency range in which it is to be operated as a mixer, the Esaki diode can be represented adequately as a nonlinear conductance in parallel with a voltage independent junction capacitance. We also postulate that the LO voltage is sinusoidal and that all but three signal voltages generated in the mixing process can be considered terminated in short circuits. These three correspond to the input (RF) frequency ω_1 , the output (IF) frequency ω_2 , and the image frequency ω_3 . Without loss of generality, we assume down conversion with the RF frequency above the LO frequency ω_0 . That is, $\omega_2 = \omega_1 - \omega_0$, and $\omega_3 = 2\omega_0 - \omega_1$. In this case the small-signal equivalent circuit of the mixer is that shown in Fig. 1.^{1,2} The conductances g_0, g_1, g_2 are the first three Fourier coefficients of the

time-varying conductance that we wish to evaluate. The capacitance C represents the diode junction capacitance.

Dicke's method can only be applied if the diode presents a positive conductance to the LO. This condition can be fulfilled by loading the diode with a stabilizing conductance G_s which is slightly larger in magnitude than the most negative value of the diode conductance.³ This conductance should be connected directly across the diode terminals, if possible. It also can be placed within a multiple of a half-wavelength from it (measured at the LO frequency) provided the diode does not oscillate. For computational purposes, it can be incorporated in the equivalent circuit as a shunt element across each of the three signal ports.

To evaluate the three mixer conductances, Dicke proposed that one measure the mixture admittance at the IF port using a bridge whose test frequency ω_2 is very small compared to the LO frequency. This insures that for all practical purposes the generated RF and image frequencies can be assumed equal to the LO frequency ω_0 . For example, if the bridge frequency were 1 kc and the LO frequency were 500 Mc, the image, RF, and LO frequencies would be within 4×10^{-4} per cent of each other. Thus, if only the LO and the low-frequency bridge are applied to the stabilized diode, the resulting RF and image signals "see" the same circuit termination at their respective ports. Furthermore, this termination is just equal to the admittance presented to the diode by the LO source, since the RF, image, and LO frequencies are nearly equal. Let this admittance be denoted by y_s :

$$y_s = g_s + jb_s.$$

For convenience we include the susceptance of the diode capacitance at the RF-image-LO ports as part of b_s ; that is, b_s contains the component $\omega_1 C \approx \omega_3 C \approx \omega_0 C$ in addition to any external susceptance presented by the LO circuit.

Under the above measurement conditions, the output admittance Y_{out} presented to the bridge at the IF port is given by

$$Y_{out} = g_0' - \frac{2g_1^2(g_0' + g_s - g_2)}{(g_0' + g_s)^2 - g_2^2 + b_s^2} + j\omega_2 C, \quad (1)$$

where $g_0' = g_0 + G_s$. By measuring the conductive part of Y_{out} for three independent LO admittances g_s, b_s , one obtains three equations which can be solved for the unknowns g_0' (hence g_0), g_1^2 , and g_2 . The junction capacitance C can be obtained from the imaginary part of Y_{out} for any of the three independent terminations. In the Dicke method the three independent RF-image port terminations are determined by a

simple standing-wave measurement in the LO circuit. To show how this is accomplished, we must first describe the test procedure in some detail.

The LO source driving the stabilized diode is connected to the latter through a matched transmission line or waveguide and a tuner as indicated in Fig. 2(a). The tuner

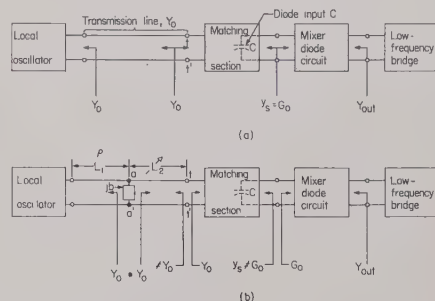


Fig. 2—The Dicke measurement circuit. (a) Matched conditions. (b) Mismatched conditions.

is assumed to be lossless, or nearly so. The diode input capacitance C is considered part of the tuner. The diode bias voltage is set to the desired operating point, and the LO output is adjusted to some prescribed amplitude as registered, for example, by the change in diode bias current. The tuner is then adjusted for a match in the LO line.⁴ Since this adjustment may affect the LO excitation at the diode, it may be necessary to readjust the LO to restore the bias current to its previous value.

It can be shown^{1,2} that the average (large-signal) conductance G_0 presented by the diode to the tuner is given by

$$G_0 = g_0' - g_2. \quad (2)$$

Since the tuner is lossless, under matched conditions the LO admittance presented to the diode at the tuner output terminals is real and obviously equal to G_0 . That is,

$$y_s = g_s + jb_s = G_0 = g_0' - g_2. \quad (3)$$

Next an arbitrary susceptance jb , such as produced by a stub, is applied across the LO line section at, say, the plane $a-a'$ indicated in Fig. 2(b). The LO output is readjusted, if necessary, to restore the previous bias current. This insures that the LO excitation at the diode terminals remains constant. Thus the admittance at the tuner input terminals $t-t'$ and at the susceptance plane "looking" toward the diode is the same as in the matched condition, namely Y_0 , the line admittance. In other words, the VSWR in the line section L_2 is still unity. However, this is not the case for the VSWR in the line section L_1 between the LO source and the susceptance plane. We shall denote this VSWR by ρ . Clearly, the admittance y_s "looking" back to the LO from the

Fig. 1—Equivalent circuit of an Esaki mixer.

* Received by the PGM-TT, July 17, 1961.
¹ H. Torrey and C. Whitmer, "Crystal Rectifiers," McGraw-Hill Book Co., Inc., New York, N. Y., 1948.
² R. A. Fucel, "Theory of the Esaki Diode Frequency Converter," *Solid State Electronics*, vol. 3, November 1961.

³ In practice, to insure stability, G_s may also have to satisfy other inequalities determined by the (neglected) series resistance and inductance. For further details see, for example:

U. S. Davidsohn, Y. C. Hwang, and G. B. Ober, "Designing with tunnel diodes," *Electronic Design*, vol. 8, pt. 2, pp. 66-71; February 17, 1960.

⁴ Measurement of the equivalent circuit parameters of tunnel diodes, "General Radio Experimenter," vol. 34, pp. 3-8, July-August, 1960.

⁴ It is permissible in this case to speak of a match because the diode has been rendered passive by the stabilizing conductance.

diode terminals is no longer equal to G_0 , the value established in the previous step.

Suppose now that with the susceptance in place the line section L_2 is varied in length, say, by a line stretcher. Since this section sees a match at its output terminals $t-t'$ (the tuner is unaltered), it follows that the admittance presented to the LO does not change in this operation; that is, the LO excitation at the diode terminals is independent of L_2 . On the other hand, the admittance looking back from the diode terminals does vary with L_2 and, in fact, traces the circle shown in Fig. 3, as is well known from transmission line theory.⁵

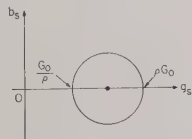


Fig. 3—Locus of the admittance y_s .

Using the equation for this circle one may eliminate the term b_s^2 in (1). The real part G_{out} of the resulting expression takes the form

$$G_{out} = g_0' - \frac{2g_1^2(g_0' + g_s - g_2)}{(g_0'^2 - g_2^2 - G_0^2) + g_s[2g_0' + G_0(1 + \rho^{-1})]} \quad (4)$$

This expression applies to any setting of the line stretcher. Since G_{out} is an increasing function of g_s , it follows that as the line stretcher is varied, the highest and lowest values of G_{out} measured by the bridge, which we denote by g_h and g_l , correspond to the highest and lowest values of g_s , namely, ρG_0 and G_0/ρ , respectively. It also is evident that G_{out} measured in the previous matched condition, which we denote by g_m , corresponds to $g_s = G_0$, $\rho = 1$.

Applying these three sets of conditions to (4) and using the identity for G_0 given by (2), we obtain three simultaneous equations which we can then solve for the mixer conductances. We obtain

$$g_0 = g_0' - G_s \quad (a)$$

$$g_1^2 = g_0'(g_0' - g_m) \quad (b)$$

$$g_2 = \frac{1 - k(\rho + 1)}{1 + k(\rho - 1)} g_0' \quad (c) \quad (5)$$

where

$$k = \frac{g_m - g_l}{g_h - g_m} \quad \text{and} \quad g_0' = g_h + \frac{g_h - g_l}{\rho k - 1}$$

It is unnecessary to resolve the algebraic sign of g_1 , since only $|g_1|$ or g_1^2 appear in equations pertaining to mixers.^{2,6} Thus the desired mixer conductances can be calculated using four easily measured quantities.

Several precautions should be observed using Dicke's method. For example, an attenuator should be inserted between the LO and the standing-wave indicator to isolate

the line from any admittance fluctuations of the LO. The attenuator can also be used to vary the oscillator output. It might be mentioned at this point that the tuner need not be connected directly to the diode terminals but can be any multiple of a half wavelength away from the diode reference plane. The audio bridge signal amplitude should be no greater than about 5 mv $p-p$ to insure linear operation at the IF terminals.

A schematic diagram of a possible mixer test jig is shown in Fig. 4. The blocking capacitor C_b isolates the bias supply from the LO circuit. A path for direct current must exist in the bridge circuit, however.

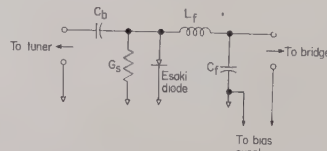


Fig. 4—A possible mixer test circuit for the Dicke method.

The choke L_f and capacitor C_f decouple the bridge from the LO circuit. The reactance of L_f and the susceptance of C_f should be large at the LO frequency but small at the bridge frequency. If C_f is too large, one must reduce the measured output capacitance by the value of C_f to obtain the true diode capacitance C .

In closing it should be mentioned that if the diode series impedance is not negligible or if the diode capacitance is voltage dependent, the more general but less convenient form of Dicke's method must be employed.¹

R. A. PUCEL
Research Division
Raytheon Company
Waltham, Mass.

A Versatile Phase Measurement Method for Transmission-Line Networks*

Current phase-measurement methods¹ for transmission-line circuits fall into two general categories. The first is the comparison method, where the path under measurement is compared with another calibrated, variable one. The phase shift through the variable path is adjusted to equal that of the unknown path, and this condition is shown by a null detector. Null indication by both phase and amplitude adjustment is usually required; however, null indication by phase adjustment alone² can be effected. The

second category of phase measurements includes those measurements which provide voltage or meter output indication of phase angle. This category includes direct high frequency phase-detector circuits of limited frequency range or frequency-conversion methods where analog or digital circuits measure phase at a converted lower frequency.

The new method to be described here is an extension of the second category, which is the meter or voltage indication of phase. It is capable of direct measurement over a broad frequency range. Fig. 1 shows the arrangement of the phase meter equipment. The RF signal source for the phase measurement is amplitude modulated (sine wave or square wave). This modulation signal is carried as a sync to the synchronous detector. The RF signal is split, with one path going directly to one end of the slotted line as a reference phase signal and the other path going through the network under measurement. The output of the latter network feeds the other end of the slotted line as the unknown phase signal.

Fig. 2 develops the relations between the two RF field vectors, the individual square detector probe outputs, and the differential output of the two probes constituting the phase detector. The independent variable is the relative phase angle θ of the two RF signals for a fixed position X in the slotted line or the converse, variable position with fixed phase angle.

The vector diagram shows the resultant field vector E_r vs the RF phase angle θ . With a square law detector, the cosine law of triangles shows the output to be a constant term $(E_1^2 + E_2^2)$ plus one varying with the cosine of phase angle θ . This relation is plotted for equal and unequal reference and unknown vectors E_1 and E_2 .

The differential output $(V_a - V_b)$ of a pair of spaced probes is proportional to the sine of the phase angle. This allows the use of calibrated scales on the meter. The positive and negative output is provided by using a modulated RF test signal and a synchronous detector at the output of the amplifier. The meter and voltage output is calibrated by moving the phase detector successively to positions for the maximum positive and negative outputs. The amplifier gain and a balance control are adjusted so that these two outputs are fixed meter currents labelled $+90^\circ$ and -90° . After calibration, the phase detector is positioned at the exact center of the slotted line to read the absolute phase difference of the two input signals referred to slotted line input terminals. The meter indication covers a 180° sector; to determine which of the two possible sectors the phase lies in, the phase detector is moved toward the unknown input. If meter motion is positive, the meter indication is correct. If a negative motion is obtained, the phase lies in the 90° to 270° sector and the actual angle is 180° minus the angle indicated on the meter.

High resolution is obtained by operating the phase meter near a zero and increasing the gain by definite amounts corresponding to meter scales; typical ranges are $\pm 90^\circ$, $\pm 20^\circ$, $\pm 6^\circ$, $\pm 2^\circ$, etc. In this mode of operation the distance of the phase detector from the center of the line is converted to a phase

⁵ W. C. Johnson, "Transmission Lines and Networks," McGraw-Hill Book Co., Inc., New York, N. Y., 1950.

⁶ C. S. Kim and J. E. Sparks, "Tunnel Diode Converters," *Proc. Natl. Electronics Conf.*, vol. 16, pp. 791-800; 1960.

* Received by the PGM-TT, June 6, 1961.

¹ F. E. Terman and J. M. Pettit, "Electronic Measurements," McGraw-Hill Book Co., Inc., New York, N. Y., p. 267; 1952.

² S. D. Robertson, "A method of measuring phase at microwave frequencies," *Bell Sys. Tech. J.*, vol. 28, pp. 59-103; 1949.

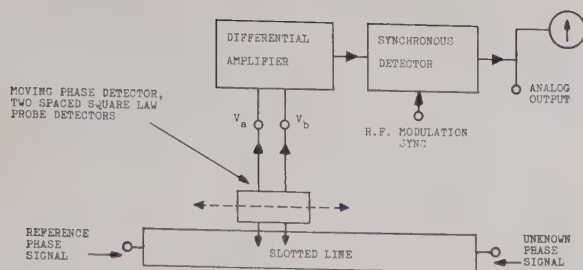


Fig. 1—Direct-reading microwave phase meter (using double square-law probe phase detector on slotted line).

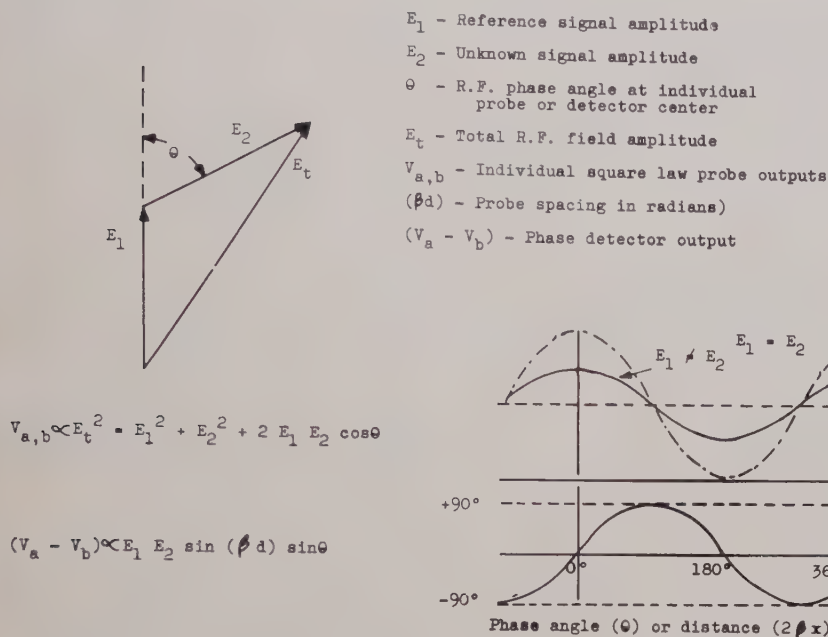


Fig. 2—Individual probe and phase detector output relations.

angle ($2\beta x$) and this angle is added to the meter indication.

The spacing of the two probes determines only the sensitivity of the phase detector. For broad frequency use, the spacing can be a quarter wavelength at the center frequency.

Phase measurement accuracy in transmission systems is frequently limited by reflections. The moving-probe type of phase detector provides inherently low reflection measurement apparatus. Equality of reference and unknown signal amplitudes is not required for operation; however, it is desirable in order that errors due to reflections of the strong signal in the weak signal channel may be kept to a minimum value.

This phase meter method has been used from 300 Mc through X band with 10:1 frequency range for a fixed spacing of the two probes.

For power levels of 1 to 10 mw for the reference and unknown signals, a sensitivity of 0.1° has been obtained with 1-kc modulation.

PETER LACY
Wiltron Company
Palo Alto, Calif.

A VHF High-Power Y-Circulator*

A number of articles [1] on the theory, design and application of three-port circulators may be found in the literature. Specific devices of this kind are commercially available for low signal power levels. In this letter a high-power version of a three-port or Y-circulator is presented. The characteristics measured at high power are compared with measurements performed at low power.

A strip-line structure was chosen for the junction configuration. To obtain a required $\pm 2\frac{1}{2}$ per cent bandwidth at the center frequency of 220 Mc, with a constant applied magnetic field, the junction geometry of the center conductor was chosen in the form of a clover leaf. A MnMg aluminate ferrite (such as Trans-Tech 414)¹ with a low saturation magnetization was selected to obtain the desired performance at these low frequencies. The rather unfavorable temperature characteristics of this material, however, necessitated forced cooling. The ferrite disks above

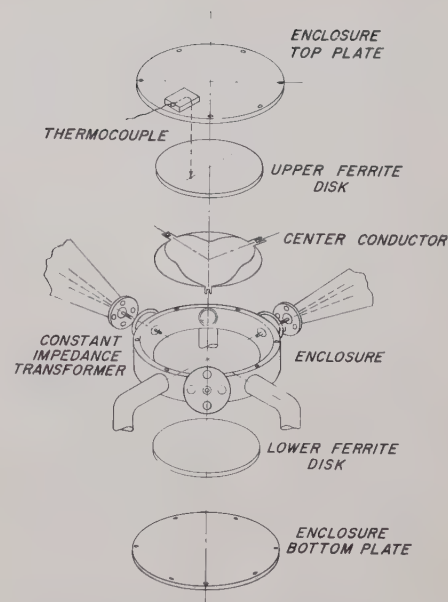


Fig. 1—Exploded view of the Y-circulator element.

and below the strip-line junction are placed in a pillbox enclosure. The space between the edge of the circulator ferrite disks and the inner wall of the circular enclosure is filled with a coolant of low loss, high dielectric strength fluid such as Freon 113 (Trichlorotrifluoroethane).²

In the high power environment, care has to be taken to avoid discontinuities in dielectrics to prevent electrical breakdown. On the design being presented, electrical breakdown was observed with dc above 15 kv. The attenuation introduced by the dielectric loss of the coolant is insignificant in the 200-Mc region.

The circulator element was designed with the following geometric parameters. A ferrite disk of 5-in diameter is used. The enclosure diameter was chosen to be 7 in. Fluid inlets and outlets are distributed around the periphery of the circular enclosure and located in the three electrically-neutral regions (60° off each port). A thermocouple consisting of a Chromel-Alumel wire pair is attached to the top ferrite disk so as not to interfere with the circulating coolant. Two holes are situated at the top and bottom ground plate to facilitate the escape of air during the filling process. Fig. 1 shows an exploded view of the circulator element.

To enable the investigation of the circulator over an appreciable bandwidth a broadband transformer design was selected for the three ports. For a limited frequency band of operation, a compensated transformer of reduced length is desirable to reduce the overall size and weight of the circulator.

A coolant such as Freon 113 was selected primarily for electrical reasons. The ferrite disk temperature has to be kept at approximately 24°C at a maximum of 2 kw average transmitted RF power. The dissipated power is then of the order of 200 w. The cooling volume of the circulator is in the order of 120

* Received by the PGMTT, July 25, 1961; revised manuscript received, August 31, 1961.

¹ TT414 is a product of Trans-Tech., Inc., Gaithersburg, Md.

² Freon 113 is a product of the Du Pont Co., Wilmington, Del.

cm³. This volume is replaced two to three times per second. A by-pass valve has been included to control the flow rate of the liquid through the circulator. The cooling system operates in a closed loop.

MEASUREMENTS

Electrical characteristics of the device were obtained at both low and high signal power levels. The low power measurements provided a reference for the performance evaluation of the component when subjected to high transmitted power. During the developmental work an interesting phenomenon was observed. Isolations in the order of 50 db or more could be obtained in discrete ferrite temperature regions. The insertion loss however remained unaffected by large changes of ferrite temperature. This temperature effect can easily be observed on TT414 ferrite as the temperature for optimum circulator performance lies in the room temperature region. These observations suggest that materials with high Curie temperature could be used in low-frequency circulators providing the device is operated at a temperature other than room ambient. Experiments performed at room temperature on VHF circulators containing high M_s (magnetization saturation) materials were unsuccessful. Similar measurements under various temperature conditions were performed with the circulator presented here. The obtained isolation and loss at low power levels for varying ferrite temperatures is illustrated together with the characteristics obtained at high power levels (Fig. 4). The magnetic field has been adjusted at each temperature point for maximum isolation. A ferrite temperature for optimum circulator performance was established in the vicinity of 24°C.

Fig. 2 illustrates the isolation and loss characteristics of the circulator for variable magnetic fields at different ferrite temperatures. The isolation characteristic for a constant applied magnetic field is also included for a ferrite temperature of 24°C. Fig. 3 shows the applied magnetic field for maximum isolation as a function of ferrite temperature. The ferrite disk temperature was controlled by means of the circulating fluid surrounding the ferrite disks. The measurements were performed after the device reached thermal equilibrium.

The VSWR of the circulator was measured at low power levels in the frequency region of 215 to 225 Mc and was in the order of 1.08:1 maximum.

HIGH POWER MEASUREMENTS

The circulator was used as a duplexer substitute in a radar front end. A matched dummy load simulated the antenna. The isolation between the transmitter and the receiver terminals was measured as a function of the ferrite temperature, or indirectly as a function of the transmitted power. The results obtained are compared with the isolation-ferrite temperature measurements at low power levels. In most cases the high power measurements were made at thermal equilibrium of the ferrite disks. Some instantaneous temperature-isolation checks were made to verify the measured slope of the isolation-temperature function obtained at high transmitted power.

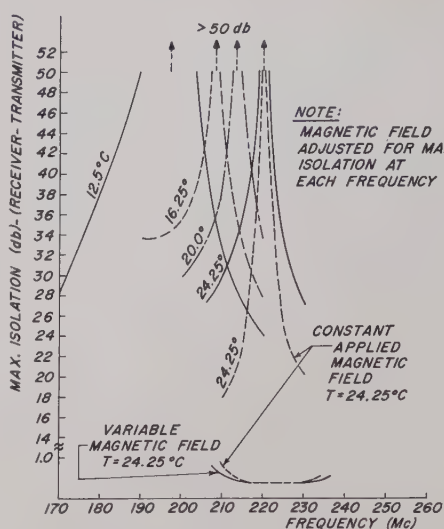


Fig. 2—Maximum isolation vs frequency for varying ferrite temperature.

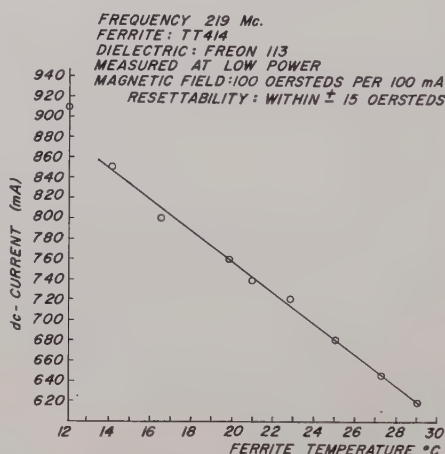


Fig. 3—Applied magnetic field for maximum isolation as a function of temperatures varying from 12°C to 29°C.

The measured ferrite temperature does not reflect the true temperature existing in the active region of the ferrite disks, as the heat distribution can be assumed to be non-uniform. The refrigerated coolant circulating through the circulator element causes additional thermal disturbances. The relation between the measured and the true ferrite temperature is given in Fig. 4. This relation was obtained by comparison of the low and high power characteristics. The existing temperature gradient can be evaluated from these measurements.

Fig. 4 also shows the isolation obtained as a function of the measured ferrite temperature at low and high magnitudes of transmitted power.

The low and high power measurements can be compared to evaluate the high power performance of the device. The temperature difference between points of equal isolation obtained at low and high power furnished a means of comparison. The width between points of equal isolation differs in the order of 0.2°C, which can be considered well within the accuracy of the measurement.

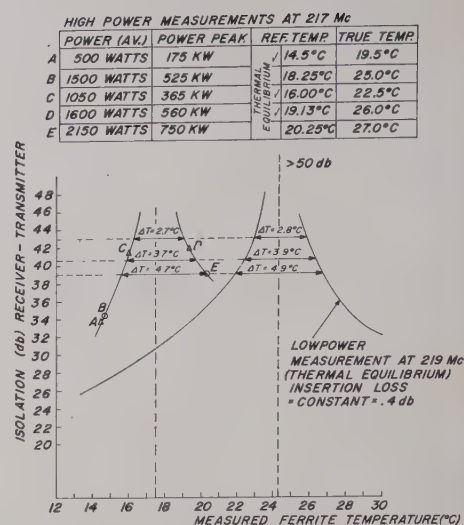


Fig. 4—Comparison of the isolation-temperature characteristics obtained at low and high transmitted power levels.

The comparison shows that the relative isolation-temperature characteristics do not differ appreciably; therefore the performance of the device can be considered independent of the magnitude of the transmitted power for the range of power levels used in these experiments.

Peak power of 1 Mw was applied over a short period of time. No electrical breakdown or deterioration of the circulator characteristics was observed.

CONCLUSION

An insertion loss of 0.3 to 0.5 db and an isolation of 50 db or more can be obtained at the center frequency for which the circulator was designed. The necessary magnetic field is not excessive at low frequencies, the dc control power being of the order of 10 to 20 w. No significant changes in electrical characteristics were observed when the device was subjected to transmitted RF power in excess of 2 kw with a peak power in the order of 1 Mw.

In conclusion a summary of performance data obtained with the above high-power Y-circulator structure is presented.

TABLE I

Frequency (Mc)	Variable magnetic field		Constant field		VSWR
	Isolation (db)	Loss (db)	Isolation (db)	Loss (db)	
225	32	0.4	24	0.45	1.08
219	>50	0.4	>50	0.40	
215	36	0.4	24	0.55	

G. V. BUEHLER
A. F. EIKENBERG
Research Division
Electronic Communications, Inc.
Timonium, Md.

BIBLIOGRAPHY

- [1] U. Milano, J. H. Saunders and L. Davis, "A Y-junction stripline circulator," IRE TRANS. ON MICROWAVE THEORY AND TECHNIQUES, vol. MTT-8, pp. 346-351; May, 1960.
- [2] G. V. Buehler and A. F. Eikenberg, "Broadband Ferrite Components," Electronic Communications, Inc., Timonium, Md., Final Dev. Rept., Sec. 3, Bureau of Ships Contract N0bsr-77602; July, 1961.

N-Terminal Power Divider*

Recently Wilkinson¹ has described an N -way hybrid power divider which decouples the outputs. This device can be arrived at by observing that its scattering matrix is

$$S = \frac{j}{\sqrt{n}} \begin{bmatrix} 0 & 1 & 1 & 1 & \dots & 1 \\ 1 & \vdots & \vdots & \vdots & \vdots & \vdots \\ 1 & \vdots & \vdots & \vdots & \vdots & \vdots \\ 1 & \vdots & \vdots & \vdots & \vdots & \vdots \\ 1 & \vdots & \vdots & \vdots & \vdots & \vdots \\ \vdots & \vdots & \vdots & \vdots & \vdots & \vdots \\ \vdots & \vdots & \vdots & \vdots & \vdots & \vdots \\ \vdots & \vdots & \vdots & \vdots & \vdots & \vdots \\ \vdots & \vdots & \vdots & \vdots & \vdots & \vdots \end{bmatrix}$$

Then

$$S^2 = \frac{1}{n} \begin{bmatrix} n & 0 & 0 & 0 & \dots & 0 \\ 0 & 1 & 1 & 1 & \dots & 1 \\ 0 & 1 & 1 & 1 & \dots & 1 \\ 0 & 1 & 1 & 1 & \dots & 1 \\ 0 & 1 & 1 & 1 & \dots & 1 \\ \vdots & \vdots & \vdots & \vdots & \vdots & \vdots \\ \vdots & \vdots & \vdots & \vdots & \vdots & \vdots \\ \vdots & \vdots & \vdots & \vdots & \vdots & \vdots \\ \vdots & \vdots & \vdots & \vdots & \vdots & \vdots \end{bmatrix}$$

and

$$S^3 = \frac{-j}{n\sqrt{n}} \begin{bmatrix} 0 & n & n & n & \dots & n \\ n & 0 & 0 & 0 & \dots & 0 \\ n & 0 & 0 & 0 & \dots & 0 \\ n & 0 & 0 & 0 & \dots & 0 \\ n & 0 & 0 & 0 & \dots & 0 \\ \vdots & \vdots & \vdots & \vdots & \vdots & \vdots \\ \vdots & \vdots & \vdots & \vdots & \vdots & \vdots \\ \vdots & \vdots & \vdots & \vdots & \vdots & \vdots \\ \vdots & \vdots & \vdots & \vdots & \vdots & \vdots \end{bmatrix} = -S.$$

Then

$$\begin{aligned} y &= (1 - S)(1 + S)^{-1} \\ &= (1 - S)^2(1 - S^2)^{-1} \\ &= (1 - 2S + S^2)S(S - S^3)^{-1} = -S \\ &= -S^2S^{-1} = (S - S^2 + S^3)S^{-1} \\ &= 1 - S + S^2 \end{aligned}$$

(See below²)

$$Y = \begin{bmatrix} 0 & \frac{-j}{\sqrt{n}} & \frac{-j}{\sqrt{n}} & \frac{-j}{\sqrt{n}} & \dots & \frac{-j}{\sqrt{n}} \\ \frac{-j}{\sqrt{n}} & \frac{n-1}{n} & \frac{-1}{n} & \frac{-1}{n} & \dots & \frac{-1}{n} \\ \frac{-j}{\sqrt{n}} & \frac{-1}{n} & \frac{n-1}{n} & \frac{-1}{n} & \dots & \frac{-1}{n} \\ \frac{-j}{\sqrt{n}} & \frac{-1}{n} & \frac{-1}{n} & \frac{n-1}{n} & \dots & \frac{-1}{n} \\ \vdots & \vdots & \vdots & \vdots & \vdots & \vdots \\ \vdots & \vdots & \vdots & \vdots & \vdots & \vdots \end{bmatrix}$$

This represents $n(3\lambda/4)$ transmission lines of characteristic admittance $\sqrt{(n/n)}Y_0$, each terminated in a pure conductance of value $(n-1)/n$ and coupled to the output of every other line by transfer admittance (conductance) of $1/n$ in units of Y_0 , when all outputs except the one considered are short circuited.

* Received by the PGMTT, July 20, 1961.

¹ E. J. Wilkinson, "An N -way hybrid power divider," IRE TRANS. ON MICROWAVE THEORY AND TECHNIQUES, vol. MTT-8, pp. 116-118; January, 1960.

² $Y = -S$ does not lead to a realizable microwave network.

It is not hard to see that the termination shown in Fig. 1 satisfies this requirement. Moving the reference of S by $\lambda/2$, lines in Y become $\lambda/4$ lines and the final network is (Fig. 2).

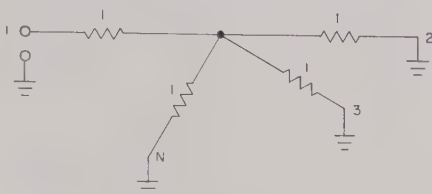


Fig. 1.

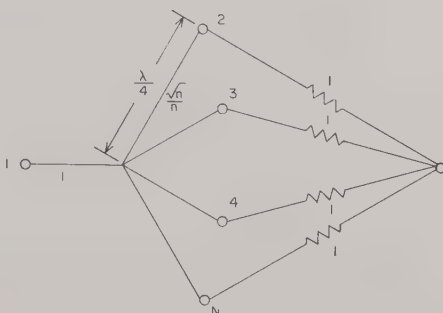


Fig. 2.

R. W. PETERSON
Control Data Corp.
Minneapolis, Minn.

10-DB X_L Cross Guide Coupler*

Two interesting points were noted while working with half-height cross guide couplers. The first was that if the same size coupling holes were used as in the full size waveguide, coupling was increased approximately 3 db. The second, and more important, was that the value of coupling was much more constant over a given frequency band, with essentially no change in directivity.

With this information, a standard 15 ± 1 db coupler in WR 112 waveguide was taken, and step transitions of various heights were designed to insert into the coupling area. By inserting steps to reduce the waveguide to a half-height size, the 3-db increase in coupling was noted and the coupling flattened out to 12 ± 0.5 db over the desired 7.5 to 8.5 kMc frequency range. By using only one step, coupling was increased to 13 ± 0.5 over the same frequency band.

The need of a 10-db cross guide coupler resulted in Fig. 1.

Coupling, previous to inserting the steps, was 13.8 db to 15.8 db over the 7.5- to 8.5-kMc range with greater than 20-db directivity. After inserting the steps, coupling

varied from 9.9 db to 10.2 db over the same frequency range with greater than 20-db directivity. A maximum VSWR of 1.13 was obtained in the secondary arm.

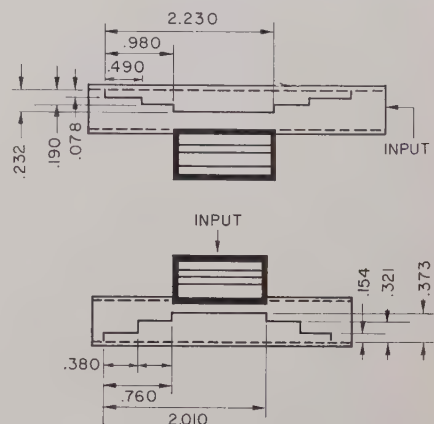
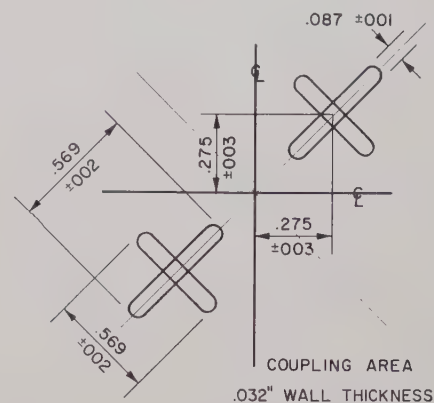


Fig. 1.

Electrically, a good coupler is needed to start with since a change in VSWR due to the step causes a decrease in directivity. Also a smaller step in the primary arm is desirable both for input VSWR and higher power requirements. Mechanically the steps should be brazed in place since a loose step causes large variations in coupling.

Cross guide couplers with greater coupling have been built at the expense of directivity which drops down to 15 db or lower.

RICHARD Z. GERLACK
Heavy Military Electronics Dept.
General Electric Company
Syracuse, N. Y.

Design Note on an L-Band Strip-Line Circulator*

The technique of using magnetized yttrium-iron-garnet slabs in dielectrically-loaded strip transmission line as the non-reciprocal elements in a UHF and low-

* Received by the PGMTT, May 10, 1961.

* Received by the PGMTT, July 7, 1961.

microwave frequency, 4-port circulator has been demonstrated most effectively by Arams, *et al.*¹ This communication reports the results of an independent and concurrent development program at our laboratory which led to a similar L-band circulator using a somewhat different configuration.

A block diagram of our circulator is given in Fig. 1. It employs a gyrator which provides 180° of differential phase shift and two simple 90° hybrids of the quarter-wave, coupled stripline type. Such hybrids covering an octave bandwidth are readily obtainable.

The circulator described by Arams, *et al.*, used two 90° differential phase shift sections which required the development of a wide-band coaxial magic tee. Their arrangement permitted use of shorter yttrium-iron-garnet slabs than in the case of a gyrator and formed a convenient package in the UHF range. Comparable losses are obtainable with either arrangement, since only one-half of the energy incident on a circulator using a gyrator is attenuated in the longer slabs.

A cross section of the low-loss gyrator is shown in Fig. 2. Best results were obtained using yttrium-iron-garnet slabs (6.0" × 0.396" × 0.250") with low saturation magnetization ($4\pi M_s = 600$ gauss) and narrow linewidth ($\Delta H = 50$ oersteds). The garnet was biased

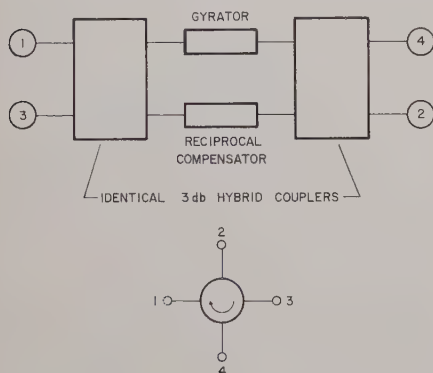


Fig. 1—Block diagram of circulator with circulator symbol.

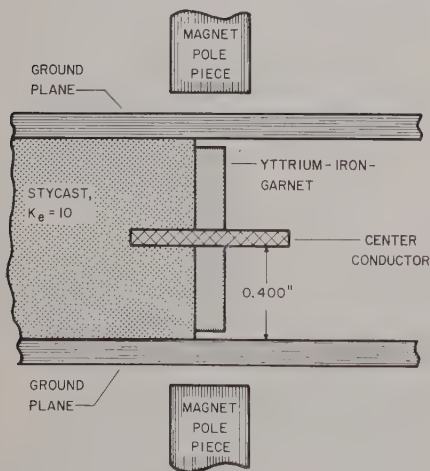


Fig. 2—Cross-sectional view of yttrium-iron-garnet gyrator.

below resonance with a constant magnetic field. Insertion losses were 1.0 db or less from 1.10 to 1.70 Gc/sec and the isolations were greater than 15 db as shown in Fig. 3(a), (b), and (c). The upper frequency limit of the experimental circulator was determined by the stripline hybrids which were designed for the frequency range 0.8 to 1.6 Gc/sec.

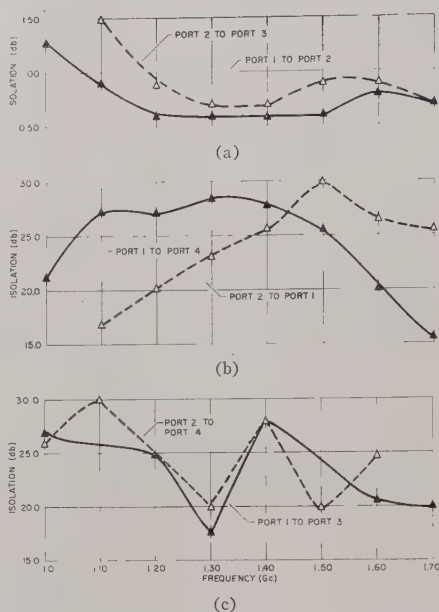


Fig. 3—Performance data for L-band circulator. (a) Insertion loss as a function of frequency. (b) Isolation between adjacent ports as a function of frequency. (c) Isolation between opposite ports as a function of frequency.

W. S. KOOP
A. K. JORDAN
Microwave and Antenna Section
Research Division
Philco Corp.
Blue Bell, Pa.

The stepped-teflon transformer of Fig. 1 fills the entire cross section of the circular guide, thus permitting pressurization for higher peak power capabilities. A curve showing the VSWR for a prototype unit is also shown in Fig. 1. The VSWR increases to 1.20 at frequencies of 7.0 and 9.0 Gc.

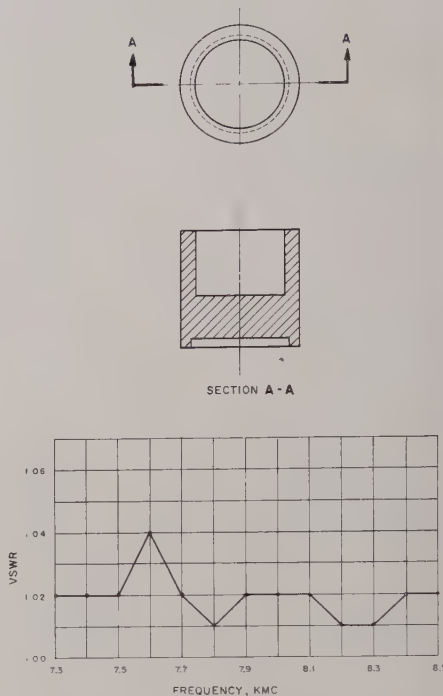


Fig. 1—Stepped-teflon transformer.

In order to choose the diameter of the circular guide the following steps should be considered:

- 1) The TM_{01} is the first higher-order mode which may propagate after the dominant TE_{11} mode. The cutoff wavelength for the TM_{01} mode is

$$\lambda_c = 2.61a, \quad (1)$$

where a is the radius of the circular guide. Therefore, to maintain mode purity, one should choose a guide diameter small enough to stop the propagation of the TM_{01} wave at the highest frequency of concern.

- 2) The characteristic impedance as defined by power and voltage considerations for WR(112) rectangular waveguide is 443 ohms at 8 Gc. For a circular guide of one inch diameter the characteristic impedance is 1508 ohms at the same frequency.

It is seen then, a one inch diameter guide has an impedance several times greater than the impedance of WR(112) rectangular waveguide. The characteristic impedance of circular guide for TE_{11} mode is given by³

$$Z_{wv} = \frac{754}{\sqrt{1 - \left(\frac{\lambda}{3.41a}\right)^2}} \quad (2)$$

* Received by the PGM-TT, July 21, 1961.
¹ I. D. Olin, "Dielectric transformers for X-band waveguide," *Electronics*, pp. 146-147; December, 1955.
² R. A. Whiteman, *et al.*, "A low reflection dielectric waveguide stepped taper," *Proc. National Electronics Conf.*, vol. 14, pp. 393-412; 1958.

³ G. C. Southworth, "Principles and Applications of Waveguide Transmission," D. Van Nostrand Co., Inc., New York, N. Y., p. 125; 1950.

¹ F. Arams, *et al.*, "Octave-bandwidth UHF/L-band circulator," *IRE TRANS. ON MICROWAVE THEORY AND TECHNIQUES*, vol. MTT-9, pp. 212-216; May, 1961.

where λ is the free space wavelength. Eq. (2) shows that an increase in the radius of the guide will decrease the characteristic impedance. It is desirable to minimize the change in the impedances at the junction. Therefore, a larger diameter is preferred for matching the circular guide to the rectangular waveguide.

From condition 1) above it is seen that the necessary and sufficient condition for propagation of the dominant TE_{11} mode while suppressing all higher order modes is

$$\frac{\lambda_l}{3.41} < a \leq \frac{\lambda_h}{2.61}, \quad (3)$$

where λ_l is the wavelength at the low end of the band and λ_h is the wavelength at the high end of the band.

From condition 2) above it is seen that the optimum transformer design occurs at the maximum permissible radius. Thus

$$\frac{\lambda_l}{3.41} < a = \frac{\lambda_h}{2.61}. \quad (4)$$

The author would like to acknowledge many helpful discussions with S. Lehr, and R. Mohr. He is also indebted to L. Bertan, who supervised the project, and J. Ebert for their many helpful suggestions.

B. MAHER
FXR,

Amphenol-Borg Electronics Corp.
Woodside, N. Y.

The synthesis of the divider to provide n outputs of prescribed values with a given input is straightforward. The various α 's are solved for from the relation

$$\alpha_k = \frac{P_k}{P_i - \sum_{q=1}^{k-1} P_q} \quad 1 \leq k < n \quad (1)$$

since

$$P_i = \sum_{q=1}^n P_q \quad (2)$$

from energy considerations, the choice of all P_q , and hence all α_q from $q=1$ to $q=n-1$, quite determines P_n .

The isolation α_{lm} between output ports l and m is

$$\alpha_{lm} = \alpha_l \alpha_m \alpha_D \quad (3)$$

where all α 's are in power ratios and α_D is the directivity of the coupler nearest the input. This is a minimum isolation, since resistive and coupling losses to intervening couplers are neglected.

The divider proposed is 100 per cent efficient; it is matched looking into any port; the isolation between output ports is infinite (assuming perfect directivity); further, there is no theoretical limit to the number of outputs or relative amplitude of outputs that may be obtained consistent with (2).

RICHARD J. MOHR
Microwave Dynamics Corp.
Plainview, N. Y.

made the system rather frequency sensitive.¹

Several methods have been described for the measurement of the excitation efficiency; most of these depend on some kind of measurement on the reactive surface.^{2,3}

The method for the excitation of surface waves which is described in this paper is essentially an application of the theory and technique of directional couplers.⁴ In our case, however, it is sought to achieve complete power transfer from the primary line onto the reactive surface waveguide. The theoretical treatment will therefore be based on Miller's light coupling theory.⁵ The reader is referred to Miller's paper for a complete and systematic analysis of a system of coupled transmission lines. Here we shall summarize, with the aid of Fig. 1, the most important results of this analysis.

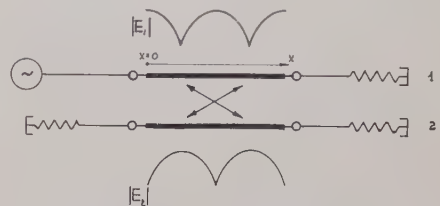


Fig. 1—A system of coupled transmission lines.

1) When two homogeneous transmission lines are coupled along the axis of propagation, power transfer between the lines takes place cyclically.

2) If, and only if, both lines have identical propagation constants, *i.e.*, $\gamma_1 = \gamma_2$ ($\gamma_n = \alpha_n + j\beta_n$), complete power transfer is possible, and the minimum length of the coupling aperture necessary is given by $2cx_{\min} = \pi$ where c is the coupling coefficient in nepers per unit length.

Complete power transfer is also possible when $\gamma_1 - \gamma_2 = \alpha_1 - \alpha_2 > 0$, but in this case x_{\min} will be different from the value given above, and generally, in the presence of losses, the term *complete power transfer* will mean only that values of x exist for which no power is present in line 1.

3) When $\gamma_1 \neq \gamma_2$, and in particular when $\beta_1 \neq \beta_2$, only partial power transfer will take place. The maximum possible wave amplitude in line 2 is, in this case, a function of $(\beta_1 - \beta_2)/c$ and is defined as the discrimination function of the coupled system. In this case, again, the point of maximum possible power transfer will differ from the value of x given for $\gamma_1 - \gamma_2 = 0$.

¹ Because of the numerous contributions to the subject dealt with in this note the reader is referred to two survey papers which contain exhaustive bibliographies.

a) F. J. Zucker, "The guiding and radiation of surface waves," *Proc. Symp. on Modern Advances in Microwave Techniques*, Polytechnic Institute of Brooklyn, N. Y.; 1954.

b) A. F. Harvey, "Periodic and guiding structures at microwave frequencies," *IRE TRANS. ON MICROWAVE THEORY AND TECHNIQUES*, vol. MTT-8, pp. 30-61; January, 1960.

² G. Goubau, "On the excitation of surface waves," *Proc. IRE*, vol. 40, pp. 865-868; June, 1952.

³ R. H. DuHamel and J. W. Duncan, "Launching efficiency of wires and slots for a dielectric rod waveguide," *IRE TRANS. ON MICROWAVE THEORY AND TECHNIQUES*, vol. MTT-6, pp. 277-284; July, 1958.

⁴ R. J. Hanratty, "An end-fire X-band flush antenna based on the branch-waveguide directional coupler," private communication.

⁵ S. E. Miller, "Coupled wave theory and waveguide applications," *Bell Sys. Tech. J.*, vol. 33, pp. 661-719; May, 1954.

A Microwave Power Divider*

Recent literature has described the theoretical performance of unmatched power dividers.^{1,2}

A proposed multilaterally matched power divider for any number n of equal or unequal

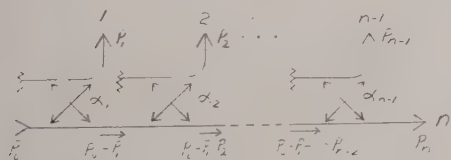


Fig. 1—Directional coupler power divider.

outputs, is shown in Fig. 1, where

P_i = input power to the divider

P_k = output power from the k th output port

α_k = power coupling coefficient of the k th coupler =

$$\frac{P_k}{P_i - \sum_{q=1}^{k-1} P_q}$$

* Received by the PGMTT, July 31, 1961.

¹ E. J. Wilkinson, "An N -way hybrid power divider," *IRE TRANS. ON MICROWAVE THEORY AND TECHNIQUES*, vol. MTT-8, pp. 116-118; January, 1960.

² H. Kagan, "N-way power divider," *IRE TRANS. ON MICROWAVE THEORY AND TECHNIQUES* (Correspondence), vol. MTT-9, pp. 198-199; March, 1961.

On the Efficiency of the Excitation of Surface Waves by Distributed Coupling*

INTRODUCTION

The excitation of surface waves on reactive surfaces is accompanied by loss of power which is radiated directly from the region of the feed. Since a surface wave supported by a surface wave line is a (nonhomogeneous) plane wave, it cannot be excited as the only field of a current distribution of finite size and amplitude.

The excitation efficiency is defined as that fraction of the total power transmitted through the exciting aperture, which is contained in the surface wave field. Excitation efficiencies approaching theoretically computed values have been achieved in practice by using horizontal or annular slots, but these apertures usually presented to the primary line highly reflecting loads, and consequent introduction of matching structures

* Received by the PGMTT, August 3, 1961. This note is a sequel to the author's report on "Improvement of the Excitation Efficiency of Surface Waves," M.S. thesis, Technion, Israel Inst. Tech., Haifa, Israel, January, 1960.

The main difference between this method of surface wave excitation and methods which employ apertures having zero length lies in the absence of a single discontinuity in the primary line. As a result, the bandwidth of such a system is determined almost exclusively by the dependence of $\gamma_1 - \gamma_2$ and of c on frequency.

THEORY

Fig. 2 shows a length of rectangular waveguide which has a series of closely spaced slots cut in one of its broad walls.

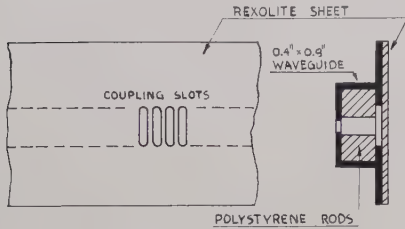


Fig. 2—Section of a waveguide-to-reactive surface directional coupler.

This wall extends on the outside to form the metal base of a dielectric clad reactive surface. We now assume that when a propagating wave is excited in the waveguide, a fraction of the power carried by it is coupled into a surface wave supported by the reactive surface and part of it is radiated into surrounding space. We further assume that the waveguide and reactive surface possess the characteristics of a system of homogeneous coupled transmission lines. With each of these lines, we associate a propagating constant of the lowest-order propagating mode, *viz.*,

$$\gamma_1 = \alpha_1 + j\beta_1 \quad (1a)$$

$$\gamma_2 = \alpha_2 + j\beta_2 \quad (1b)$$

where the subscripts 1 and 2 refer to the waveguide and reactive surface, respectively.

The propagating wave amplitudes in the coupled system satisfy the set of equations

$$\frac{dE_1}{dx} = -(\gamma_1 + jc)E_1 + jcE_2 \quad (2a)$$

$$\frac{dE_2}{dx} = -(\gamma_2 + jc)E_2 + jcE_1 \quad (2b)$$

where

E_1 = complex wave amplitude in the waveguide

E_2 = complex surface wave amplitude

c = coupling coefficient between waveguide and surface wave field.

Only propagating waves in the positive x direction are assumed to exist, and coupling action starts at $x=0$ with the initial conditions

$$E_1(0) = 1; \quad E_2(0) = 0.$$

We now consider the orthogonality relations valid for the surface wave field and radiation field and use these relations in order to postulate the existence of two separately defined coupling coefficients: one for the waveguide-to-surface wave field and another for the waveguide-to-radiation field.

The radiation field is excited by the slots, and the contribution from a particular slot is proportional to $E_1(x)$ at that slot. Hence, in an otherwise lossless system, this coupling coefficient is represented by the attenuation coefficient $\alpha = \alpha_1$ of the primary line. We finally assume that $\beta_1 = \beta_2 = \beta$, and we shall show later that the validity of this assumption can be verified experimentally. Eqs. (2a) and (2b) thus take the form:

$$\frac{dE_1}{dx} = -[\alpha + j(\beta + c)]E_1 + jcE_2 \quad (3a)$$

$$\frac{dE_2}{dx} = -j(\beta + c)E_2 + jcE_1 \quad (3b)$$

and their solution for $E_1(0) = 1; E_2(0) = 0$ is

$$|E_1| = \frac{e^{-cx\xi}}{\sqrt{1-\xi^2}} \cdot \left| \cos \left(cx\sqrt{1-\xi^2} + \arctg \frac{\xi}{\sqrt{1-\xi^2}} \right) \right| \quad (4a)$$

$$|E_2| = \frac{e^{-cx\xi}}{\sqrt{1-\xi^2}} \cdot \left| \sin cx\sqrt{1-\xi^2} \right| \quad (4b)$$

where $\xi = a/2c$.

From 4(a), we find that zero field amplitudes will be detected in the primary line at points x_n given by

$$cx_n\sqrt{1-\xi^2} + \arctg \frac{\xi}{\sqrt{1-\xi^2}} = (2n-1)\frac{\pi}{2} \quad (n = 1, 2, \dots) \quad (5)$$

and, in particular, position coordinates of the first two minima x_1 and x_2 satisfy

$$cx_1\sqrt{1-\xi^2} + \arctg \frac{\xi}{\sqrt{1-\xi^2}} = \frac{\pi}{2} \quad (6a)$$

$$cx_2\sqrt{1-\xi^2} + \arctg \frac{\xi}{\sqrt{1-\xi^2}} = \frac{3\pi}{2} \quad (6b)$$

from which we obtain

$$c = \frac{\frac{\pi}{\alpha_1(\rho-1)}}{\cos \frac{\pi}{2} \frac{\rho-3}{\rho-1}} \quad (7)$$

and

$$\xi = \sin \frac{\pi}{2} \frac{\rho-3}{\rho-1} \quad (8)$$

where $\rho = x_2/x_1$. We now substitute from (7) and (8) into (4b) and put $x = x_1$, which is the point of maximum surface wave amplitude. Thus

$$|E_2|_{\max} = \exp \left\{ -\frac{\pi}{\rho-1} \cdot \tan \frac{\pi}{2} \frac{\rho-3}{\rho-1} \right\}$$

$$= \exp \left\{ -\frac{\pi}{\rho-1} \cdot \tan \frac{\pi}{2} \frac{\rho-3}{\rho-1} \right\} \cdot \frac{\sin \frac{\pi}{\rho-1}}{\cos \frac{\pi}{2} \frac{\rho-3}{\rho-1}} = \exp \left\{ -\frac{\pi}{\rho-1} \cdot \tan \frac{\pi}{2} \frac{\rho-3}{\rho-1} \right\} \quad (9)$$

(The fraction equals unity identically.)

For $E_1(0) = 1$, the surface wave excitation efficiency η is defined by

$$\eta = |E_2|_{\max}^2 \quad (10)$$

and thus

$$\eta = \exp \left\{ -\frac{2\pi}{\rho-1} \cdot \tan \frac{\pi}{2} \frac{\rho-3}{\rho-1} \right\} \quad (11)$$

Eq. (11) is an expression of the excitation efficiency in terms of the distances to the points of maximum power transfer. This can be generalized by stating that in the case of surface wave excitation by distributed coupling it is possible, in principle, to determine the excitation efficiency by measuring the distribution of the absolute value of the wave amplitude in the primary line only.

Fig. 3 shows the plot of η vs ρ for the range $3.01 \leq \rho \leq 4$. For values of ρ in the range $3 \leq \rho \leq 3.01$, the approximation

$$\eta \cong 1 - \frac{\pi}{4} (\rho - 3) \quad (12)$$

can be used and the plot of this function is shown in Fig. 4.

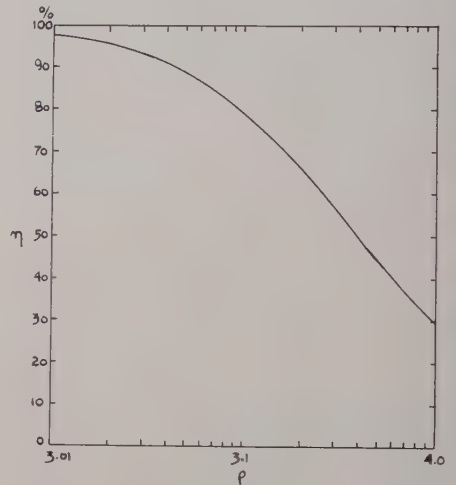


Fig. 3—Plot of excitation efficiency vs displacement of field minima in primary line for $3.01 \leq \rho \leq 4$.

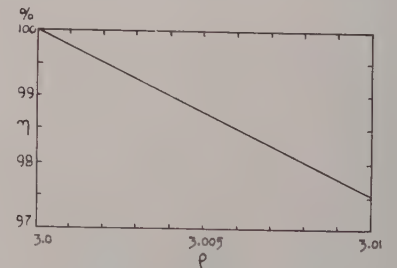


Fig. 4—Plot of excitation efficiency vs displacement of field minima in primary line for $3 \leq \rho \leq 3.01$.

EXPERIMENT

It was pointed out in the Introduction that complete power transfer, in the restricted sense, is possible only if $\beta_1 = \beta_2$. Thus, the detection of zero field amplitude in the primary line can serve, in principle, as an indication of the equality of phase coefficients of the coupled lines.

The initial design of the system called for the insertion of dielectric slabs into the

waveguide, and the resulting value of β_1 was determined with the aid of a method described by the author elsewhere.⁶ The thickness of the dielectric sheet to give the necessary value of $\beta_2 = \beta_1$ was determined from the transverse resonance condition.^{1a} Because of inaccuracies involved in this procedure, the design did not result in the desired situation in which $\beta_2 = \beta_1$ at the design frequency. At this stage, use has been made of the fact that the group velocities in the coupled lines have different values, i.e., $\partial\omega/\partial\beta_1 \neq \partial\omega/\partial\beta_2$, and by searching in the neighborhood of the design frequency, a particular frequency has been found for which $\beta_1 = \beta_2$.

Copper-clad teflon, and later Rexolite, have been used in the construction of the reactive surface. The coupling aperture consisted of a row of 150 slots cut in the wide wall of a 0.4×0.9 -in ID rectangular waveguide (see Fig. 2). The measurement of the field amplitude in the waveguide was performed by cutting in the opposite wide wall a longitudinal slot such as used in a slotted section and mounting the waveguide in a hp809B Universal Probe Carriage from which the original slotted section has been removed. The whole setup has been placed on a surface covered with microwave absorbing material.

In a few experiments conducted up to now, excitation efficiencies of between 92 and 95 per cent have been determined.

EFRAIM RAVID-WEISSBERG
Scientific Dept.
Ministry of Defence
Hakirya, Tel Aviv, Israel

⁶ E. Weissberg, "Experimental determination of wavelength in dielectric-filled periodic structures," IRE TRANS. ON MICROWAVE THEORY AND TECHNIQUES (Correspondence), vol. MTT-7, pp. 480-481; October, 1959.

Higher-Order Mode Resonances in Strip-Line Y-Junction Circulators*

Because of its small physical size, the Y-junction circulator has been the recipient of a great amount of investigation. Various theorists and experimentalists have devoted time to understanding the behavior of this device, both on the far and near side of ferrimagnetic resonance.¹⁻⁴

In our laboratory, we have succeeded in developing units operating at the near

side of resonance from 1.0-8.0 kMc. These units have instantaneous bandwidths providing 20 db of isolation in excess of 20 per cent; some units have bandwidths as high as 40 per cent. One of the limitations on bandwidth that we have discovered are resonances that occur in the insertion loss and isolation characteristics of the device at the HF end of the band. In narrow-band designs, these resonances might never be noticed. Because of their presence, it is necessary to limit the bandwidth specification to exclude them from the operating region. If resonance could be eliminated, we believe bandwidths of 50-60 per cent could be achieved.

Fig. 1 shows some experimental points relating the frequency at which the resonance occurs to the diameter of the ferrimagnetic material used in the design. Various materials were used, and they are labeled with their manufacturer's designation.

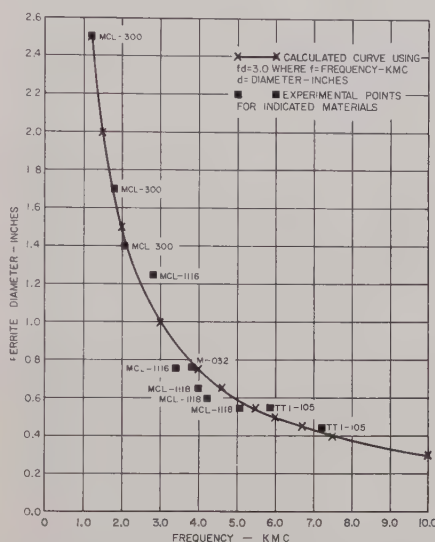


Fig. 1—Diameter at which higher-order mode resonance occurs for strip-line Y-junction circulators on the near side of resonance.

The frequency of these resonances depends upon the value of magnetic field. They occur at lower frequencies for smaller field values. The values of field used in the data presented were sufficient to saturate the disks.

A theoretical curve is plotted using the relationship

$$fd = 3.0$$

where

f = frequency in kMc

d = diameter of material in inches.

This type of expression is typical of propagation in cylindrical waveguide where the mode cutoff frequency is related to the guide diameter and the proper-order Bessel function. It is felt, therefore, that these resonances can be explained by higher-order mode propagation in a direction parallel to the applied magnetic field, even though the dominant mode in the strip line is propagating perpendicular to this direction.

It is hoped that these resonances can be moved to higher frequencies without effect-

ing the basic nonreciprocal scattering of the ferrimagnetic disks. Experiments to determine the feasibility of removing these resonances are now underway and, if successful, will be reported.

ALVIN CLAVIN
Microwave Dept.
Rantec Corp.
Calabasas, Calif.

A Proposed Design to Enhance Microwave-Power-Limiter Characteristics*

A design is proposed for a device which would enhance the properties of presently available microwave power limiters, thereby making their use as crystal protectors in duplexing units of microwave systems more desirable. This design is a combination of a power-sensitive, nonlinear element with a traveling-wave ring resonator.

Several nonlinear elements, such as subsidiary resonance ferrite limiters,¹ and De-Grasse type of ferrimagnetic limiters,² and diode parametric limiters³ have been devised which exhibit an attenuation vs power-level curve such as is depicted in the lower curve of Fig. 1. The nonlinear properties of ferroelectric materials indicate that these materials might also be used to produce limiting action.

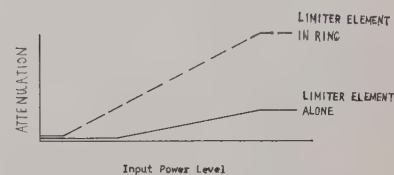


Fig. 1.

However, the referenced limiters are not completely usable as crystal protectors because either their threshold power levels are too high, or their maximum attenuations, slopes of attenuation vs power curve, or their power-handling capabilities are inadequate. Combining any one of the nonlinear elements with the traveling-wave ring resonator would improve upon all of these shortcomings, provided that the low-level insertion loss of the element is sufficiently small.

* Received by the PGMTT, August 21, 1961.

¹ B. A. Auld, "The synthesis of symmetrical waveguide circulators," IRE TRANS. ON MICROWAVE THEORY AND TECHNIQUES, vol. MTT-7, pp. 238-246; April, 1959.

² L. Davis, Jr., et al., "A strip-line L-band compact circulator," PROC. IRE (Correspondence), vol. 48, pp. 115-116; January, 1960.

³ G. V. Buehler and A. F. Eikenberg, "Stripline Y-circulators for the 100 to 400 Mc region," PROC. IRE (Correspondence), pp. 518-519; February, 1961.

⁴ J. Clark and J. Brown, "Miniaturized, temperature stable, coaxial Y-junction circulators," IRE TRANS. ON MICROWAVE THEORY AND TECHNIQUES (Correspondence), vol. MTT-9, pp. 267-269; May, 1961.

¹ G. S. Uebele, "Characteristics of ferrite microwave power limiters," IRE TRANS. ON MICROWAVE THEORY AND TECHNIQUES, vol. MTT-7, pp. 18-23; January, 1959.

² R. W. DeGrasse, "Low-loss gyromagnetic coupling through single crystal garnets," J. Appl. Phys., suppl. to vol. 30, pp. 155S-156S; April, 1959.

³ A. E. Siegman, "Phase-distortionless limiting by a parametric method," PROC. IRE (Correspondence), vol. 47, pp. 447-448; March, 1959.

Much has been written about the traveling-wave ring resonator.⁴⁻⁶ Its properties, particularly the rapidity of the decrease in amplification factor with increasing ring attenuation, are relatively familiar. If a second coupler is added to the ring circuit to couple power out, it may be used as a pass-band-stopband filter for frequency separation and combination.⁷

Consider the microwave circuit in Fig. 2; this is a traveling-wave ring-resonator comprised of two directional couplers. Two ports of each coupler are joined to form an integral wavelength transmission line into which a power-sensitive, nonlinear element, having an attenuation vs power-level characteristic (such as in Fig. 1), has been introduced.

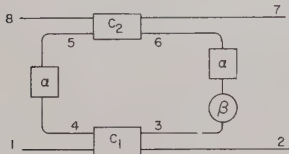


Fig. 2.

where

α = attenuation of one-half of ring circuit
 a = transmission constant corresponding to α , ($a = 10^{-\alpha/20}$)

β = attenuation of limiter element, a function of E_3 , ($\beta = f(E_3)$)

b = transmission constant corresponding to β , ($b = 10^{-\beta/20}$)

C_1 = coupling coefficient of input directional coupler

$$E_3/\theta_3 = C_1 E_1/\theta_1 + 90^\circ$$

$$E_2/\theta_2 = \sqrt{1 - C_1^2} E_1/\theta_1$$

C_2 = coupling coefficient of output directional coupler

$$E_8/\theta_8 = C_2 E_6/\theta_6 + 90^\circ$$

$$E_5/\theta_5 = \sqrt{1 - C_2^2} E_6/\theta_6$$

An analysis has been made which shows that the voltage amplification factor or the ratio of RF voltage in the ring to that in the input transmission line is

$$\frac{E_3}{E_1} = \left| \frac{E_3/\theta_3}{E\theta_{1/1} + 90^\circ} \right|$$

$$= \frac{C_1}{1 - a^2b \sqrt{1 - C_1^2} \sqrt{1 - C_2^2}}, \quad (1)$$

and the transmission through the device, from port 1 to port 8 is

$$\frac{E_8}{E_1} = \left| \frac{E_8/\theta_8}{E_1/\theta_1 + 90^\circ} \right|$$

$$= \frac{abC_1C_2}{1 - a^2b \sqrt{1 - C_1^2} \sqrt{1 - C_2^2}}. \quad (2)$$

For any given value of a^2b_0 , where b_0 is the maximum value of b under low-power level and minimum insertion-loss operation, the condition may be imposed by judicious design that

$$\sqrt{1 - C_1^2} = a^2b_0 \sqrt{1 - C_2^2}. \quad (3)$$

If this condition is met, it may be shown that $E_2 = |E_2/\theta_2| = 0$, due to destructive cancellation in arm 2. Assuming highly directional couplers and matched components are used throughout, all power incident to port 1, less insertion loss in the ring circuit and limiter element, emerges from port 8. For high-power operation, where limiting is desired, b becomes very small. Eq. (3) is no longer satisfied, and most of the incident power goes to the matched load on port 2. It may be shown that the power incident to the limiter element is less than that at port 1 by a factor approaching the decoupling value of directional coupler number 1. This results in an equal increase in the power-handling capability of the device over the limiting element used alone.

For low-power level operation, where b is very nearly unity (leftmost section, Fig. 1) and (3) is satisfied, (1) and (2) reduce to

$$\frac{E_3}{E_1} = \frac{1}{C_1}, \quad (4)$$

and

$$\frac{E_8}{E_1} = \frac{abC_2}{C_1}, \quad (5)$$

respectively.

Under these conditions, the power level in the ring circuit, which is the power incident to the limiter element, is $(1/C_1)^2$ times greater than the power in port 1. The device will reach its threshold at a power level $(1/C_1)^2$ times less than the threshold of the limiter element.

At high-power levels, the isolation between port 1 and port 8 approaches the sum of the isolation of the limiter element and the decoupling factors of both direction couplers [see (6)]. This can be seen intuitively in Fig. 2 by removing the section of the ring circuit opposite the limiter element. This may be done at power levels at which the attenuation of the limiter element is high, since very little power (approaching zero for sufficiently high attenuations) is carried by this transmission line. It is obvious from the circuit, then, that

$$E_8/E_1 = C_1bC_2. \quad (6)$$

An absorptive limiter would be more easily used as a crystal protector since a reflective limiter would necessitate the use of a circulator or isolator to get rid of the unwanted leakage power and to provide transmitter isolation. Since most limiter elements are reflective in nature, the proposed device will provide an additional advantage in that the input VSWR will be reduced from nearly infinity to a value approximately that of a short circuit viewed through an attenuation equal to the decoupling factor of the input directional coupler. This would make the problem of transmitter isolation less severe.

It is felt that 0.1 db is an attainable figure for low-level insertion loss for a crossed-stripline ferrimagnetic limiter at S-band frequencies, which includes limiter-element loss and transmission-line loss. This figure would correspond to $2\alpha + \beta$, making a^2b equal to 0.98953.

Starting with this assumption, typical design figures might be as follows: Choosing a value of 7.0 db for the input coupler, $C_1 = 0.445$ and $\sqrt{1 - C_1^2} = 0.896$. To satisfy (3) and enforce optimum operation at low-power levels, $\sqrt{1 - C_1^2} = a^2b \sqrt{1 - C_2^2}$, $\sqrt{1 - C_2^2} = 0.9053$, $C_2 = 0.424$, and the output directional coupler-decoupling factor is seen to be 7.5 db. For low-power level operation, $E_8/E_1 = abC_2/C_1 = 0.948 = 0.45$ db, which is an increase of 0.35 db over the limiter element alone. The power buildup factor, $P_8/P_1 = (E_8/E_1)^2 = (1/C_1)^2 = 5.05 = 7.0$ db, reduces the effective threshold of the device by 7.0 db below that of the element alone.

For operation above threshold power levels where a^2b is no longer nearly unity, (3) is no longer satisfied, and the isolation through the device becomes

$$\frac{E_8}{E_1} = \frac{abC_1C_2}{1 - a^2b \sqrt{1 - C_1^2} \sqrt{1 - C_2^2}}$$

$$= \frac{0.1877b}{1 - 0.8028b} = \frac{0.1877(10^{-\beta/20})}{1 - 0.8028(10^{-\beta/20})},$$

where β is the attenuation of the limiter element in db. It is seen that a slight change in β has a great effect on transmission loss E_8/E_1 providing effective "amplification" of limiting attenuation. As the attenuation of the limiter element increases and oscillations in the ring circuit are greatly reduced, the power incident to the limiting element is 7.0 db below the input power, raising the power-handling capability of the device 7.0 db above the limiter element alone. The isolation through the device approaches a value of 14.5 db greater than the limiter element isolation for increasing power levels. The maximum input VSWR is 1.50:1, when the limiter element is infinitely mismatched.

The preceding typical design figures could be still further improved by using more strongly decoupled directional couplers, but only at the expense of increased low-level insertion loss.

It is felt that the foregoing proposal has sufficient merit to warrant further investigation, and an experimental study is planned.

WILLIAM H. WRIGHT, JR.
 U. S. Army Signal Res. and Dev. Lab.
 Fort Monmouth, N. J.

⁴ L. J. Milosencic and R. Vautey, "Traveling-wave resonators," IRE TRANS. ON MICROWAVE THEORY AND TECHNIQUES, vol. MTT-6, pp. 136-143; April, 1958.

⁵ P. J. Speranza, "Traveling-wave resonator," Electronics Ind., vol. 14, pp. 84-85; November, 1955.

⁶ J. W. E. Griensman, "Preliminary Design Considerations of Microwave Flywheel," Polytechnic Inst. of Brooklyn, Brooklyn, N. Y., Repts. on Air Force Contract AF-18(600)-1505; 1957.

⁷ S. B. Cohn and F. S. Coale, "Directional channel separation filters," Proc. IRE, vol. 44, pp. 1018-1024; August, 1956.

A High-Power Coaxial Ferrite Phase Shifter*

An L-band, reciprocal, coaxial, ferrite phase shifter with a low insertion loss, excellent high-power stability at peak power levels up to at least 300 kw, and a figure-of-merit in excess of 1000 has been developed. These characteristics were achieved by using longitudinal biasing fields considerably greater than the field required for resonance.

The motivation for this work stems from the need for improving the high-power characteristics of microwave ferrite phase shifters which are used as scanning elements in phased array antennas for radar transmitters.

An ideal phase shifter for this application would combine good high power stability and a high figure-of-merit (ratio of total phase shift in degrees to the peak insertion loss in db over the range of biasing fields employed) with small control power requirements and an ability to be rapidly switched from one phase shift setting to another. A number of designs have been explored in order to effect some compromise among these requirements. In recent years principal emphasis has been placed on light-weight, easily switched devices which produce the required phase shift upon application of only a very small biasing field. Most notable among these is the Reggia-Spencer phase shifter¹ which has been scaled for operation over a very wide range of frequencies.²

But low-field devices, by their nature, suffer from the proximity of the subsidiary absorption.³ To some extent the threshold power can be controlled by a suitable selection of material, but it is generally conceded that the highest possible figure-of-merit is incompatible with a high threshold, at least with materials that are now available. Judging by our own experience, a light-weight ferrite phase shifter having an acceptable figure-of-merit (~several hundred deg/db) will usually have a threshold peak power of the order of a few tens of kilowatts. Higher threshold powers may be obtained by reducing the figure-of-merit. At L-band frequencies the problem is further complicated by the presence, in most materials, of rather excessive low field losses; the low field region thus becomes still less attractive.

The nature of the compromise among the phase shifter characteristics can be greatly altered, and low field losses avoided, by operating on the high-field side of resonance. Here the requirements of low control power and light weight must be relaxed, but one need no longer sacrifice figure-of-merit in order to achieve high power stability. The reason for this lies in the fact that the operating region is now far removed from sub-

sidary resonance and no instability from this source is predicted to within the approximation employed by Suhl,⁴ as long as⁵

$$4\pi\gamma M_s < \omega.$$

The saturation of the main resonance, however, can introduce an appreciable variation in insertion loss with RF power level if the biasing field is not sufficiently great.

In order to explore the possibilities for above-resonance operation at microwave frequencies,⁶ we have designed and constructed a ferrite phase shifter in a fully-loaded coaxial geometry for operation at 1350 Mc over a 10 per cent band. The propagation characteristics of such a structure have been analyzed by Suhl and Walker⁷ to the extent that the coaxial line can be approximated by a pair of parallel planes. Their results show that the transmission line is cut off over the range of biasing fields,

$$\frac{\omega}{\gamma} - 4\pi M_s < H < \frac{\omega}{\gamma}.$$

Thus the region $H > \omega/\gamma$ is our present concern.

The device, shown schematically in Fig. 1, consists essentially of a $\frac{1}{8}$ -in coaxial line fully loaded with TT 1-103, a magnesium manganese ferrite-aluminate.⁸ We have found that a longitudinal magnetic field of 900 oe, well above ω/γ (480 oe), is sufficient to reduce the insertion loss of an 18-in length of line to about 0.2 db. This low loss implies that the material has a low dielectric loss tangent.

We should also note that the matching requirements are less stringent than those encountered in low field operation, because here the effective microwave permeability is greater than unity. The characteristic impedance of the ferrite loaded line is thus brought closer to that of the empty line.

In Fig. 2 the electrical characteristics of the phase shifter are shown vs applied dc field. The phase shift and figure-of-merit are given by the same curve with the 0.2-db insertion loss quoted above being the scale factor between the two sets of ordinates.

It is clear from the figure that two feet of loaded line is sufficient to produce 360° of phase shift with a change in biasing field of about 500 oe. A figure-of-merit of more than 1000 may be obtained without difficulty. Most important, however, is the fact that this figure-of-merit does not deteriorate with the application of high power. In fact, up to

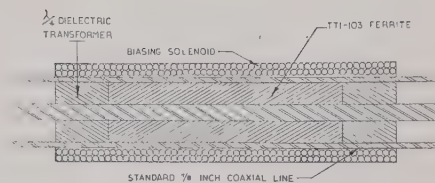


Fig. 1—Diagram of experimental coaxial ferrite phase shifter.

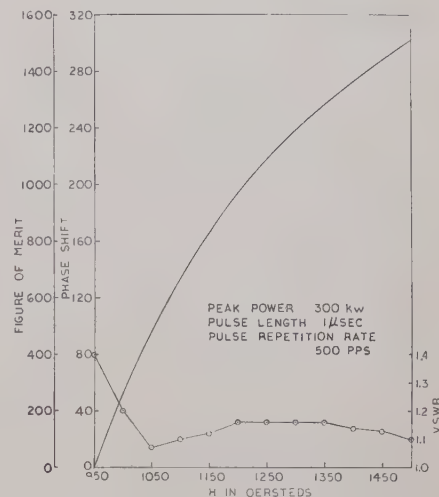


Fig. 2—Phase shift, figure-of-merit and VSWR vs dc field for TT-103 in a $\frac{1}{8}$ -in coaxial geometry. Length = 18-in, frequency = 1.35 kMc.

the highest peak power used (~300 kw),⁹ no instability was observed over the range of biasing fields shown in Fig. 2.

In installations where the large coil weight would not be a major disadvantage and where power and cooling could be provided for the permanent biasing and switching fields, the device described has important advantages. First, the high power stability represents an improvement of at least an order of magnitude over a comparable low-field device. Second, the phase shifter exhibits a very low insertion loss and the RF heating of the ferrite should, as a consequence, be relatively small. Third, the phase shift settings are not disturbed by hysteresis effects, and hysteresis heating by the switching operation is reduced to negligible proportions. In fact, since the magnetization is virtually independent of the biasing field, the presence of the ferrite should have little or no effect on the switching operation.

The authors would like to express their appreciation to W. H. von Aulock for his continuing interest and many helpful discussions. They would also like to express their gratitude to H. E. Noffke for his assistance with the instrumentation and measurements.

A. S. BOXER
S. HERSHENOV
E. F. LANDRY
Bell Telephone Labs.
Whippany, N. J.

* Received by the PGMTT, August 23, 1961. Supported by the Bureau of Ships, Department of the Navy, Contract No. N00br 77570.

¹ F. Reggia and E. G. Spencer, "A new technique in ferrite phase shifting for beam scanning of microwave antennas," *Proc. IRE*, vol. 45, pp. 1510-1517; November, 1957.

² R. S. McCarter and E. F. Landry, "K_a-band ferrite phase shifter," *IRE TRANS. ON MICROWAVE THEORY AND TECHNIQUES*, vol. MTT-9, p. 271; May, 1961.

³ J. F. Ollom and W. H. von Aulock, "Measurement of microwave ferrites at high signal levels," *IRE TRANS. ON INSTRUMENTATION*, vol. I-9, pp. 187-193; September, 1960.

⁴ H. Suhl, "Theory of ferromagnetic resonance at high signal powers," *J. Phys. Chem. Solids*, vol. 1, pp. 209-227; April, 1957.

⁵ P. C. Fletcher and N. Silence, "Subsidiary absorption above ferrimagnetic resonance," *J. Appl. Phys.*, vol. 32, pp. 706-711; April, 1961.

⁶ An above-resonance UHF phase shifter using a stripline geometry was reported on by Johnson (see below) and his results show no instability up to peak powers of 10 kw except in the immediate neighborhood of resonance.

⁷ C. M. Johnson, "Ferrite phase shifter for the UHF region," *IRE TRANS. ON MICROWAVE THEORY AND TECHNIQUES*, vol. MTT-7, pp. 27-31; January, 1959.

⁸ H. Suhl and L. R. Walker, "Topics in guided wave propagation through gyromagnetic media, part III—perturbation theory and miscellaneous results," *Bell Sys. Tech. J.*, vol. 33, pp. 1133-1194; September, 1954.

⁹ Trans.-Tech., Inc., Gaithersburg, Md.

⁹ This power level greatly exceeds the rating for a standard $\frac{1}{8}$ -in coaxial line. However, it was desired that the level be increased until instabilities appeared in the ferrite. In the neighborhood of 300 kw, arcing occurred in the waveguide-coax transitions.

A Duplexer Using the Zero Permeability Characteristics of Ferrite*

It has been shown by Polder¹ and others² that a ferrite material can be made to exhibit an effective zero permeability to a wave that has a positive sense of circular polarization (positive wave) and a corresponding nonzero permeability to a wave with polarization in the negative sense (negative wave). Melchor, *et al.*,³ and Duncan and Swern⁴ have demonstrated that a ferrite material which is magnetically biased such that the real part of its positive wave permeability is zero will largely exclude the positive wave. The negative wave, however, will be concentrated in the ferrite; and, under certain conditions of ferrite geometry and operating frequency, the negative wave will propagate through the ferrite in a dielectric mode.

This note describes a duplexer which utilizes this differential interaction in ferrite when biased to, or in the region of, zero permeability. Fig. 1 shows a diagrammatic sketch of a duplexer which uses these principles.

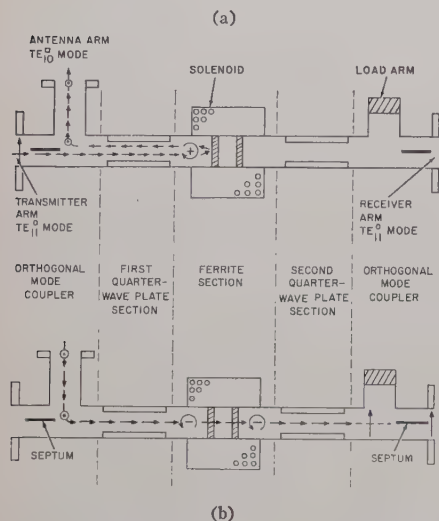


Fig. 1—Diagrammatic sketch of a "zero permeability" duplexer. (a) Transmit case. (b) Receive case.

The design of this structure is such that a linearly polarized wave entering the transmitter arm will propagate through the orthogonal mode coupler with negligible coupling to the antenna arm, and will become circularly polarized in the positive sense before entering the ferrite section of the wave-

guide. The ferrite section consists of one or more ferrite disks which completely fill the cross section of the waveguide as shown in Fig. 1. A solenoid or a cylindrical magnet is used to produce a longitudinal magnetic field to bias the ferrite disks to the region where the real part of the effective ferrite permeability is essentially zero. As discussed in the first paragraph, the positive wave will be almost totally excluded from and, hence, reflected by the ferrite. The reflected wave will propagate through the first quarter-wave plate section which reconverts the wave to linear polarization, oriented 90° with respect to the incident linearly polarized wave. At the orthogonal mode coupler, the wave is then coupled into the antenna arm with negligible losses. The orthogonal mode coupler on the receiver end provides a load for any positive wave energy that is propagated through the ferrite section.

A wave entering the antenna arm will be coupled into the circular waveguide and will propagate into the ferrite section with a negative sense of circular polarization. Since the effective permeability for the negative wave is greater than unity (at the same magnetic bias for zero positive wave permeability), the wave will propagate through the ferrite section if the width and spacing of the disks are such that a proper impedance match is achieved. If the dielectric and magnetic losses of the ferrite material are low, the wave will be only slightly attenuated when it emerges from the ferrite section. The emergent wave, after propagating through the second quarter-wave plate section, will be reconverted to a linearly polarized wave at the receiver arm oriented perpendicular to the septum in the orthogonal mode coupler. Thus, loss to the load arm is negligible.

Fig. 2 shows an experimental X-band "zero permeability" duplexer. Representative data taken on a similar duplexer designed for 9.2 Gc are given in Fig. 3. The ferrimagnetic material used in this particular unit was yttrium-iron garnet. At 9.2 Gc, the transmitter-to-antenna loss was 0.4 db with a corresponding receiver arm isolation of more than 30 db. The transmitter-to-antenna insertion loss remained well below 1.0 db from 9.0 to 9.7 Gc. Subsequent tests have shown that this loss remains below 1.0 db over a 10 per cent bandwidth. Beyond a 10 per cent bandwidth, the higher loss was due primarily to the narrow bandwidth of the quarter-wave plates used in the experimental work.

The antenna-to-receiver insertion loss at 9.2 Gc was also 0.4 db and remained below 1.0 db over a bandwidth of approximately 5 per cent. Increased loss beyond this bandwidth is due principally to the fixed ferrite geometry and spacing with the narrow-band quarter-wave plates contributing to some degree.

A duplexer of this design offers a definite advantage in that high power effects are minimized since the microwave energy associated with high peak power does not propagate through the ferrite. However, there is some magnetic coupling into the ferrite surface; but, by careful selection of ferrite material and geometry, the magnetic biasing field can be kept well below the field which will give rise to subsidiary resonance losses.

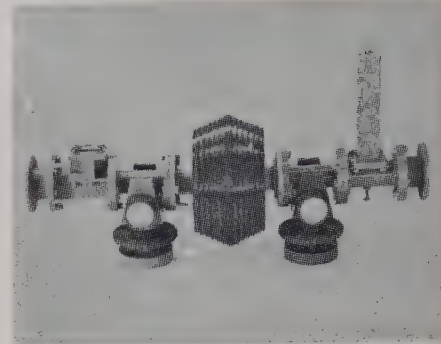


Fig. 2—An experimental X-band zero permeability duplexer.

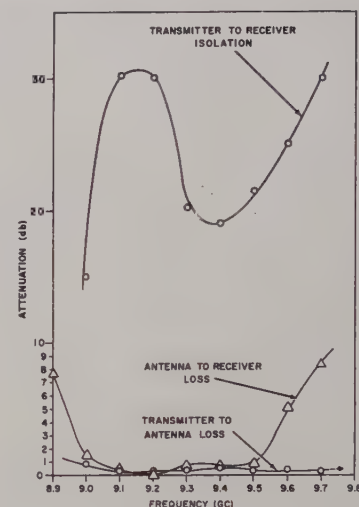


Fig. 3—Characteristics of a zero permeability duplexer using two thin disks of yttrium-iron garnet. $H_{dc} = 925$ gauss.

The duplexer with characteristics shown in Fig. 2 was tested without cooling or pressurization at 250 kw peak (100 w average) at 9.2 Gc with no deleterious effects noted.

Many helpful discussions with Mr. B. J. Duncan, Dr. J. E. Pippin and Dr. G. P. Rodrique, and the help of R. W. Coston in the experimental work presented, are thankfully acknowledged.

L. K. WILSON
G. J. NEUMANN
Solid State and Microwave
Component Dev. Sec.
Sperry Microwave Electronics Co.
Clearwater, Fla.

* Received by the PGMTT, August 25, 1961. This work has been sponsored by the Wright Air Dev. Div., Dayton, Ohio, under Contract Number AF33-(616)6517.

¹ D. Polder, "On the theory of ferromagnetic resonance," *Phil. Mag.*, vol. 40, pp. 99-114; January, 1954.

² See, for example, C. L. Hogan, "The ferromagnetic Faraday effect at microwave frequencies and its applications," *Rev. Mod. Phys.*, vol. 25, pp. 253-263; January, 1953.

³ J. L. Melchor, W. L. Ayres, and P. H. Varian, "Energy concentration effects in ferrite loaded waveguides," *J. Appl. Phys.*, vol. 27, pp. 72-77; January, 1956.

⁴ B. J. Duncan and L. Swern, "Effect of zero ferrite permeability on circularly polarized waves," *Proc. IRE*, vol. 45, pp. 647-655; May, 1957.

A Series-Connected Traveling-Wave Parametric Amplifier*

INTRODUCTION

The conventional parametric amplifier consisting of a single variable element with

* Received by the PGMTT, March 1, 1961; revised manuscript received, September 1, 1961. The work reported here was carried out as part of the Lockheed Research Program.

its accompanying resonant circuits is inherently a narrow-band device. Analysis has also shown that such amplifiers when operating at high gain are extremely sensitive to pump power, *i.e.*, small variations in pump power lead to large variations in gain. Traveling-wave parametric amplifiers, in which not one but many variable elements are involved, have been designed or built to overcome the two limitations mentioned above.¹⁻⁴ This paper is concerned with the analysis of one such amplifier in which the variable elements are placed in series with the signal line as opposed to one in which the elements are placed in shunt. In particular, the variable elements are capacitance diodes.

With the diodes in series with the signal line, it becomes possible to design amplifiers whose structures are considerably simpler than otherwise. Fig. 1 shows one such design, called a "serpentine" amplifier for obvious reasons. The signal to be amplified is carried by the coax line while the pump wave is carried by the waveguide. Note that now a single pump source rather than multiple pump sources is required.³ Considering the diodes as representing capacitances shunting the pump line, it is possible to bias and so space them as to allow only the pump frequency component to exist in the pump line. Note also that such an arrangement allows for more flexibility in that the signal line lengths between diodes can be easily adjusted for optimum operating conditions. Such favorable conditions are easily created in the laboratory and they will be assumed in the following discussion.

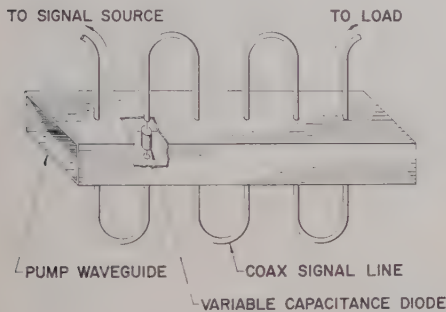


Fig. 1—Serpentine traveling-wave parametric amplifier.

DISCUSSION

The procedure used will follow closely those used by Heffner¹ and Tien.² Consequently, a great deal of the intermediate steps will be omitted.

The signal line in Fig. 1 can be represented by Fig. 2 in which L_0 and C_0 are the equivalent series inductance and shunt capacitance per unit length of the line. The

line carrying the pump wave is not shown but the effect of the pump is reflected in the elastance $S(t, z)$ of the diode by

$$S(t, z) = S_1 e^{j(\omega_p t - \beta_p z)} + S_1^* e^{-j(\omega_p t - \beta_p z)}, \quad (1)$$

where ω_p is the angular frequency of the pump and β_p is the pump, phase constant. As it turns out, consideration of the elastance rather than the capacitance of series elements proves to be more appropriate with such structures. Note that the actual elastance should contain a constant term S_0 representing the average value. In this paper it is assumed that the value of C_0 is such as to include both the inherent line capacitance and the effects of S_0 .

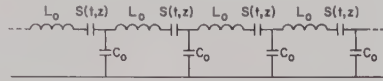


Fig. 2—Signal line.

The differential equations describing the voltage and current relationships over a unit length are

$$\begin{aligned} \frac{\partial V(t, z)}{\partial z} &= -L_0 \frac{\partial I(t, z)}{\partial t} \\ &\quad - \int S(t, z) I(t, z) dz \end{aligned} \quad (2)$$

and

$$\frac{\partial I(t, z)}{\partial z} = -C_0 \frac{\partial V(t, z)}{\partial t}. \quad (3)$$

Except for the term with the integral sign these are the usual transmission line equations. Parametric action of course results from the new term.

Differentiating (2) with respect to time t gives

$$\begin{aligned} \frac{\partial}{\partial t} \frac{\partial V(t, z)}{\partial z} &= -L_0 \frac{\partial^2 I(t, z)}{\partial t^2} - I(t, z) S(t, z). \end{aligned} \quad (4)$$

Differentiating (3) with respect to distance z and interchanging the order of differentiation gives

$$\frac{\partial^2 I(t, z)}{\partial z^2} = -C_0 \frac{\partial}{\partial t} \frac{\partial V(t, z)}{\partial z}. \quad (5)$$

Substituting (4) into (5) leads to

$$\begin{aligned} \frac{\partial^2 I(t, z)}{\partial z^2} &= C_0 L_0 \frac{\partial^2 I(t, z)}{\partial t^2} \\ &\quad + C_0 I(t, z) S(t, z). \end{aligned} \quad (6)$$

It will be assumed that the current $I(t, z)$ consists only of two relevant components; namely, the signal component designated by $I_1(t, z)$ and the idler component designated by $I_2(t, z)$. Appropriate filter networks are placed in the line to eliminate all other frequency components. Thus

$$\begin{aligned} I(t, z) &= I_1(z) e^{j(\omega_1 t - \beta_1 z)} + I_1^*(z) e^{-j(\omega_1 t - \beta_1 z)} \\ &\quad + I_2(z) e^{j(\omega_2 t - \beta_2 z)} + I_2^*(z) e^{-j(\omega_2 t - \beta_2 z)}, \end{aligned} \quad (7)$$

where

$$\beta_1 = \omega_1 \sqrt{L_0 C_0} \quad \text{and} \quad \beta_2 = \omega_2 \sqrt{L_0 C_0}.$$

Consider the case where

$$\omega_p = \omega_1 + \omega_2$$

and the lines are such that

$$\beta_p = \beta_1 + \beta_2.$$

Carrying out the operations indicated in (6) and equating the coefficients of like frequency terms leads to a set of four simultaneous equations, of which two are independent of each other. These are

$$\frac{\partial^2 I_1(z)}{\partial z^2} - j2\beta_1 \frac{\partial I_1(z)}{\partial z} = C_0 S_1 I_2^*(z) \quad (8)$$

$$\frac{\partial^2 I_2^*(z)}{\partial z^2} + j2\beta_2 \frac{\partial I_2^*(z)}{\partial z} = C_0 S_1^* I_1(z). \quad (9)$$

The above equations can be further simplified if it is assumed that

$$\left| \frac{\partial^2 I}{\partial z^2} \right| \ll \left| 2\beta \frac{\partial I}{\partial z} \right|.$$

Thus

$$\frac{\partial I_1(z)}{\partial z} = -\frac{S_1 C_0 I_2^*(z)}{j2\beta_1} \quad (10)$$

and

$$\frac{\partial I_2^*(z)}{\partial z} = \frac{S_1^* C_0 I_1(z)}{j2\beta_2} \quad (11)$$

or

$$\begin{aligned} I_1(z) &= K_1 \exp \left\{ \sqrt{\frac{C_0^2 S_1 S_1^*}{4\beta_1 \beta_2}} z \right\} \\ &\quad + K_2 \exp \left\{ -\sqrt{\frac{C_0^2 S_1 S_1^*}{4\beta_1 \beta_2}} z \right\} \end{aligned} \quad (12)$$

and

$$\begin{aligned} I_2^*(z) &= \frac{jS_1^* K_1}{\sqrt{S_1 S_1^* \beta_2}} \exp \left\{ \sqrt{\frac{C_0^2 S_1 S_1^*}{4\beta_1 \beta_2}} z \right\} \\ &\quad + \frac{jS_1^* K_2}{\sqrt{S_1 S_1^* \beta_2}} \exp \left\{ -\sqrt{\frac{C_0^2 S_1 S_1^*}{4\beta_1 \beta_2}} z \right\}, \end{aligned} \quad (13)$$

where K_1 and K_2 are arbitrary constants. Thus the signal $I_1(z)$ is seen to grow (amplification of the signal) with z . These expressions are similar (but not identical) to those obtained by Heffner¹ and Tien,² as expected.

No attempt will be made to compute the bandwidth and noise because it is felt that the results will be similar to those reported by Heffner and Tien.

CONCLUSIONS

A traveling-wave parametric amplifier of a rather novel design has been presented. Connecting the variable capacitance diodes in series with the signal line leads to structural and operational simplicity. The analysis proves that under certain favorable conditions amplification of the signal can take place.

ACKNOWLEDGMENT

The author wishes to thank V. Counter for his valuable suggestions and Miss J. Hillhouse and K. Fong for checking the mathematics.

TUCK HOP LEE
Missiles and Space Division
Lockheed Aircraft Corp.
Sunnyvale, Calif.

¹ H. Heffner, "Traveling Wave Parametric Amplifier Analysis," class notes, Stanford University, Stanford, Calif.; 1960.

² P. K. Tien, "Parametric amplification and frequency mixing in propagating circuits," *J. Appl. Phys.*, vol. 29, pp. 1347-1357; September, 1958.

³ C. V. Bell and G. Wade, "Circuit considerations in traveling-wave parametric amplifiers," 1959 IRE WESCON CONVENTION RECORD, pt. 2, pp. 75-82.

⁴ R. C. Honey and E. M. T. Jones, "A wide band UHF traveling-wave variable reactance amplifier," *IRE TRANS. ON MICROWAVE THEORY AND TECHNIQUES*, vol. MTT-8, pp. 351-361; May, 1960.

1961 PGMTT National Symposium

The 1961 PGMTT National Symposium was held on May 15, 16, and 17, 1961, at the Sheraton Park Hotel in Washington, D. C. Planning for this Symposium began more than a year before the meeting; the Symposium Committee was formed in March, 1960. The members of the Symposium Committee were:

Symposium Chairman: Robert O. Stone, National Bureau of Standards

Secretary: Charles E. Quigley, Naval Research Laboratory

Technical Program Committee:

Chairman—Gustave Shapiro, National Bureau of Standards

Members—Tore N. Anderson, Microwave Consultant

Alfred C. Beck, Bell Telephone Laboratories

Donald D. King, Electronic Communications, Inc.

William W. Mumford, Bell Telephone Laboratories

Charles E. Quigley, Naval Research Laboratory

Saul W. Rosenthal, Polytechnic Institute of Brooklyn

Theodore S. Saad, Sage Laboratories, Inc.

Leonard Swern, Sperry Gyroscope Company

John E. Tompkins, Diamond Ordnance Fuze Laboratories

Arrangements Committee:

Chairman—Robert V. Garver, Diamond Ordnance Fuze Laboratories

Members—Marshall M. Algor, Diamond Ordnance Fuze Laboratories

Phillip W. Boesch, Weinschel Engineering Company

Julius A. Kaiser, Diamond Ordnance Fuze Laboratories

Mary J. Ronas, National Bureau of Standards

Thelma Southwarth, Diamond Ordnance Fuze Laboratories

Publicity Committee:

Chairman—Benjamin Bernstein, Polytechnic Engineering Company

Members—Elbert (Al) Godfrey, Polytechnic Engineering Company

Edward A. Wolff, Electromagnetic Corp.

Finance Committee:

Chairman—Frank Reggia, Diamond Ordnance Fuze Laboratories

Members—Henry B. Bruns, Diamond Ordnance Fuze Laboratories

Lauren P. Tuttle, Jr., Melpar, Incorporated

Women's Activities Committee:

Chairman—Elisabeth M. Rutz, Emerson Research Company

Members—Marie D. Prytulak, Diamond Ordnance Fuze Laboratories

Kathryn M. Schwarz, National Bureau of Standards

Session Organizers:

Session IV—High-Power Microwave Techniques

Theodore S. Saad, Sage Laboratories, Inc.

Session V—Low-Noise Microwave Amplifiers

Helmut Sommer, Diamond Ordnance Fuze Laboratories

Session VII—System and Receiver Noise Performance

William W. Mumford, Bell Telephone Laboratories

There were seven technical sessions, in which thirty papers were presented. Three of the sessions were panel sessions: Low-Noise Amplifiers, High-Power Microwave Techniques, and System and Receiver Noise Performance Clinic. At these sessions, forty-minute invited papers were presented and then further discussed by the six panel members.

For the first time, a Symposium Digest was available at the Symposium. Charles Quigley, Editor of the Digest, was largely responsible for its quality and excellence. The Digest contains 500-word summaries and five figures for each of the papers presented at the Symposium. Copies of the Digest may be obtained from Frank Reggia, Diamond Ordnance Fuze Laboratories, Washington 25, D. C., for \$3.00 per copy.

On Monday evening, May 15, Mr. Jacob Rabinow, Rabinow Engineering Company, presented a very interesting and informative paper, "The Business of Investing."

A cocktail hour and banquet was held in Sheraton Hall on May 16. The Microwave Prize for the best paper published in the TRANSACTIONS during the previous year was awarded to Dr. A. F. Harvey of the Royal Radar Establishment, Malvern, Worcester, England.

The highlight of the banquet was the perfectly executed hoax by Gustave Shapiro and the guest speaker, Dr. Paul Conroy, U. S. Information Agency. Dr. Conroy, posing as a Russian official, Ivan Serov, disclosed some rather startling Russian advancements in the microwave art and explained why the Russian scientific and economic programs were superior to those of the United States. Everyone was quite surprised, and relieved, to learn that his address was not authentic.

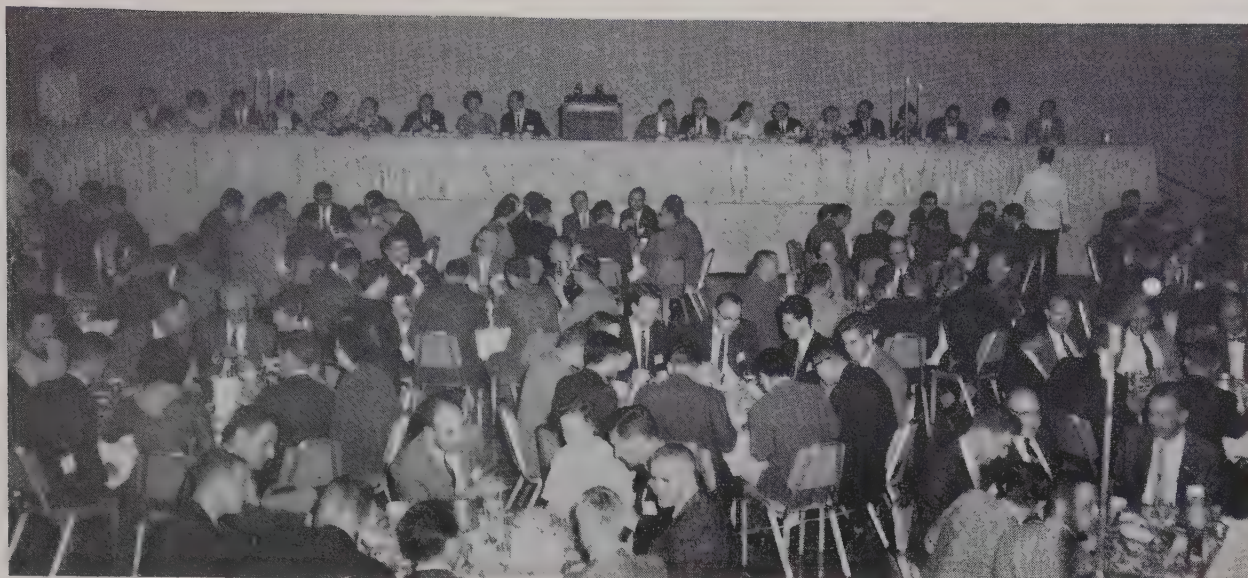
Approximately 600 people attended the Symposium; 500 were IRE members, 95 were nonmembers, and 7 were students.



Left to right: Delmer C. Ports, Dr. Paul Conroy—Banquet Speaker, posing as a Russian official, Ivan Serov—Gustave Shapiro, and Theodore Saad.



Our two honorary life members of PGMTT with their wives. Left to right: Dr. George C. Southworth, Mrs. Southworth, Mrs. Clavier and Andre Clavier—Symposium Keynote Speaker.



Banquet scene before the hoax perpetrated by Paul Conroy and Gustave Shapiro



Left to right: Andre Clavier, Mrs. Clavier, Theodore Saad, Tore Anderson, Mrs. Saad, Frank Klawnsnik, Mrs. Tomiyasu and Kiyo Tomiyasu.



Some of the members of the 1961 Symposium Committee relaxing before the banquet. Left to right: Frank Reggia—Finance Chairman, Mrs. Reggia, Gustave Shapiro—Technical Program Chairman, Robert Garver—Arrangements Chairman, Mrs. Garver, Robert Stone—Symposium Chairman, Mrs. Hepburn, Robert Rivers, Mrs. Rivers, Mrs. McDonley, and W. A. McDonley.



Left to right: Ben Warriner, Andre Clavier, George Southworth, Theodore Saad, Herbert Engelmann, James Hughes, William Culshaw, and Tore Anderson.

Contributors

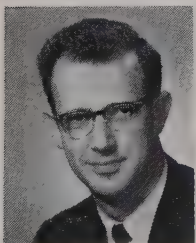
Dean B. Anderson (S'49-M'50) was born in Billings, Mont., on October 22, 1921. He received the B.S. degree in electrical engineering from Montana State College, Bozeman.



D. B. ANDERSON

From 1944 to 1946 he served in the Signal Corps, primarily with the Radio Propagation Unit. Then he joined Hazeltine Electronics Corporation, Little Neck, N. Y., where he contributed to the development of antennas and transmitters for IFF and air navigation systems. Later he was responsible for the microwave aspects of the airborne interrogator and ground stations of the Distance Measuring Equipment for the Civil Aeronautics Administration. Since 1954 he has been associated with the Autonetics, Division of North American Aviation, Inc., Anaheim, Calif., as a Senior Technical Specialist, studying advanced microwave systems and monopulse antennas. His study of parametric amplifiers applied to monopulse systems has recently received major emphasis. He has recently joined the Autonetics Research Center, Anaheim, Calif.

Jerry C. Aukland (S'55-M'59) was born in Macedonia, Ia., on October 7, 1931. He received the B.S. degree in electrical engineering from Iowa State College, Ames, in 1959.



J. C. AUKLAND

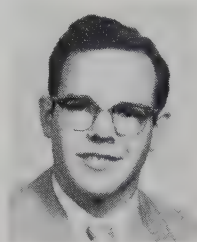
From 1950 to 1954 he was an aviation electronics technician in an Early Warning Radar Squadron (during the Korean conflict). Upon graduation in 1959 he joined the Autonetics Division of North American Aviation, Inc., Anaheim, Calif., where he has been engaged in the study of parametric amplifiers for application to monopulse radars.

Mr. Aukland is a member of Phi Eta Sigma, Eta Kappa Nu, and Tau Beta Pi.

Clare E. Barnes was born in Vassar, Mich., on October 24, 1929. He received the B.S. degree in physics from Michigan State University, East Lansing, in 1956.

From 1948 to 1952 he served in the Air

Force as an aircraft armament instructor. Since 1956 he has been a member of the technical staff of the Bell Telephone Laboratories, Murray Hill, N. J., in the Solid State Device Development Department. He was engaged in the development of ferrite switches and variable attenuators for the Bell System's 6 kmc Radio Relay System while attending the Laboratories' Communications Development Training Program, which he completed in 1959. Subsequently, his work was concerned with ferrite devices at *C* and *X* bands, and at millimeter wavelengths.



C. E. BARNES

ment Training Program, which he completed in 1959. Subsequently, his work was concerned with ferrite devices at *C* and *X* bands, and at millimeter wavelengths.

Keith S. Champlin (S'55-M'59) was born in Minneapolis, Minn., on August 20, 1930. He received the B.S. degree in 1954, the M.S.E.E. degree in 1955, and the Ph.D. degree in electrical engineering in 1958, all from the University of Minnesota, Minneapolis.



K. S. CHAMPLIN

After serving in the U. S. Army Signal Corps in 1951 and 1952, he was briefly associated with the Physics Department of the University of Minnesota and with Remington Rand Univac. Both positions dealt with applications of radio telemetry to high altitude research. As a graduate student, he was engaged in research on noise in semiconductors; first as Research Assistant and later as Research Fellow. His thesis work was in the field of fluctuations in *p-n* junction devices.

At present, he is Associate Professor of electrical engineering at the University of Minnesota. He is in charge of a research group employing microwave techniques to study electronic processes in semiconductors.

Dr. Champlin is a member of Tau Beta Pi, Eta Kappa Nu, Gamma Alpha, and Sigma Xi.

William J. Getsinger (S'48-A'50-M'55) was born in Waterbury, Conn., on January 24, 1924. He received the B.S. degree from the University of Connecticut, Storrs,

in 1949; the M.S. degree from Stanford University, Stanford, Calif., in 1959, and the degree of Engineer, also from Stanford, in 1961, all in electrical engineering.



W. J. GETSINGER

Between 1950 and 1957 he worked at Technicraft Laboratories, Thomaston, Conn., and the Westinghouse Electric Company, Baltimore, Md., on the design and development of waveguide components and assemblies. In 1957 he joined the staff of Stanford Research Institute, where he has been working on strip-line components and antennas.

Mr. Getsinger is a member of Tau Beta Pi and Eta Kappa Nu.

Meyer Gilden (S'47-A'48-M'55) was born in Chicago, Ill., on June 21, 1924. He received the B.S. and M.S. degrees in electrical engineering from the Illinois Institute of Technology, Chicago, in 1946 and 1948, respectively, and the Ph.D. degree from the University of Illinois, Urbana, in 1955.



M. GILDEN

From 1948 to 1956 he was on the staff at the University of Illinois where he attained the rank of Assistant Professor. At the University he taught in the Electrical Engineering Department and was engaged in plasma research in the Gaseous Electronics Laboratory under Dr. L. Goldstein. While at the University he also worked in the Control Systems Laboratory on communication problems.

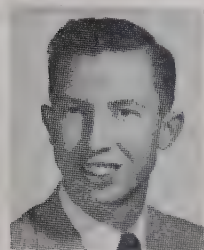
In 1956 he became a member of the staff of the General Electric Microwave Laboratory in Palo Alto, Calif., where he was active in research and development concerned with microwave switches using gas and vacuum discharges, phase shifters using gas discharge plasmas, microwave filters and shock tube instrumentation. From 1959 to 1961 he was a Research Engineer in the Electromagnetics Laboratory at Stanford Research Institute where he became involved in parametric amplifier work. Presently he is a Senior Engineer in the Electron Tube and Device Division of Microwave Associates, Burlington, Mass., where he is engaged in plasma physics research.

Dr. Gilden is a member of the American Physical Society, Sigma Xi, and Kappa Nu.

Thomas S. Hartwick was born in Vandalia, Ill., on March 19, 1934. He received the B.S. degree in engineering physics from the University of Illinois, Urbana, in 1956, and the M.S. degree from the University of California at Los Angeles in 1958, under a Howard Hughes Master of Science Fellowship.

From 1956 to 1961 he was associated with the Solid-State Applications Section, Electro-Physics Laboratory, Hughes Aircraft Company, Culver City, Calif., where he was Head of the Ferrites Research Group, and where he was principally engaged in research on the nonlinear behavior of ferromagnetic materials at microwave frequencies. In early 1961 he joined the Aerospace Corporation, El Segundo, Calif.

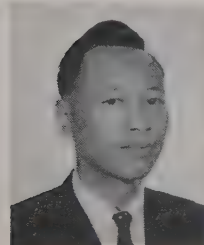
Mr. Hartwick is a member of the American Physical Society.



T. S. HARTWICK

❖

Irving T. Ho was born in Fukien, China, on March 26, 1921. He received the B.S.E.E. degree from Amoy University, Fukien, China, in 1944, and the M.S. and Ph.D. degrees from Stanford University, Stanford, Calif., in 1957 and 1961, respectively.



I. T. HO

From 1952 to 1955 he was a Lecturer in electrical engineering at the Taipei Institute of Technology, Taipei, Taiwan. From 1957 to 1959 he was employed by the Boeing Airplane Company, Seattle, Wash., as a research engineer. During that time, he was also a part-time graduate student at the University of Washington, Seattle, under the Boeing graduate program. In 1959 Boeing granted him a scholarship to continue his studies at Stanford University. At present, he is a research associate with the Electronics Research Laboratories of Stanford University.

Dr. Ho is a member of Sigma Xi.

❖

Ann Yung Hu (S'56-M'58) was born in Hunan, China, on October 6, 1921. She received the B.S.E.E. degree from the National Hunan University, China, in 1944, and the M.S.E.E. degree from the Illinois Institute of Technology, Chicago, in 1957. Currently she is studying at the University of Washington, Seattle.

From 1944 to 1952 she was on the staff

of the Nationalist Chinese Air Force Communication School and the Taipei Institute of Technology as a radio, radar, and loran instructor; and the following two years she worked as a research engineer for the Radio Wave Propagation Research Laboratory of Taiwan, China. In 1956 she joined the Admiral Radio Company, Chicago, Ill., as a research engineer, studying radiation effects of micro-



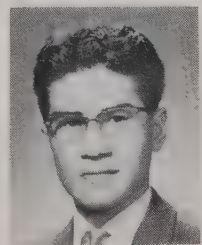
A. Y. HU

wave components, and the following year she was with the Electronics Research Laboratory of the Illinois Institute of Technology. Since 1958 she has been with the Boeing Company, Renton, Wash.

Miss Hu is an associate member of Sigma Xi.

❖

Akira Ishimaru (M'58) was born in Fukuoka, Japan, on March 16, 1928. He received the B.S. degree from Tokyo University in 1951, and the Ph.D. degree in electrical engineering from the University of Washington, Seattle, in 1958.



A. ISHIMARU

In 1951 he worked for the Electrotechnical Laboratories, Tokyo, Japan, until his arrival in the U. S. in 1952 as a graduate student. From 1954 to 1958 he was an Instructor at the University of Washington, and in the summer of 1956 he was employed by the Bell Telephone Laboratories, Holmdel, N. J., where he worked on antenna problems. He was an Assistant Professor of electrical engineering at the University of Washington from 1954 to 1961, and became Associate Professor in 1961. He has also been a consultant to the Boeing Airplane Company, Seattle, Wash., in microwave antennas and propagation. He has been engaged in research on antenna pattern synthesis, propagation, and diffraction and scattering.

Dr. Ishimaru is a member of Sigma Xi.

❖

Irving Kaufman (S'45-A'50-M'55) was born in Geinsheim, Hessen, Germany, on January 11, 1925. He received the B.E. degree in electrical engineering from Vanderbilt University, Nashville, Tenn., in 1945, and the M.S. and the Ph.D. degrees from the University of Illinois, Urbana, Ill., in 1948 and 1957, respectively.

From 1945 to 1948 he worked as development engineer for the RCA Victor Di-

vision, Indianapolis, Ind., and Camden, N. J. Since 1957, he has been with the Research Laboratory of Ramo-Wooldridge, which is now the Research Laboratory of Space Technology Laboratories, Inc., Canoga Park, Calif., working in the field of Microwave Electronics.



I. KAUFMAN

Society.

❖

Robert R. Krongard was born in Montevideo, Minn., on June 10, 1932. He received the B.S. degree in 1959 and the M.S.



R. R. KRONGARD

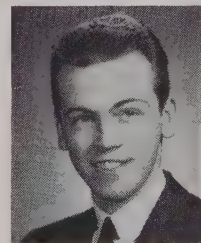
degree in 1961, both in electrical engineering from the University of Minnesota, Minneapolis.

He is presently doing research on the microwave properties of semiconductors at the University of Minnesota while working toward the Ph.D. degree.

Mr. Krongard is a member of Eta Kappa Nu and Gamma Alpha.

❖

William F. Krupke was born in Springfield, Mass., on January 30, 1937. He received the B.S. degree in physics from Rensselaer Polytechnic Institute, Troy, N. Y., in 1958, and the M.A. degree in physics from the University of California, Los Angeles, in 1960, under a Howard Hughes Master of Science Fellowship.



W. F. KRUPKE

From 1958 to 1961 he was associated with the Solid-State Applications Section, Electro-Physics Laboratory, Hughes Aircraft Company, Culver City, Calif., engaged principally in research and development work utilizing the nonlinear properties of ferromagnetic and semiconductor materials at microwave frequencies. Since early in 1961 he has been associated with Minneapolis-Honeywell Regulator Company, Los Angeles, Calif., where he is engaged in electro-optical research and development.

Mr. Krupke is a member of the American Physical Society.

Charles E. Muehe, Jr., was born in Seattle, Wash., on September 27, 1924. He received the B.S. degree in electrical engineering from Seattle University in 1950, and the M.S. degree in electrical engineering from the Massachusetts Institute of Technology, Cambridge, in 1952.



C. E. MUEHE, JR.

From 1952 to 1956 he was a member of the electrical engineering staff of Seattle University. In 1956 he joined the Lincoln Laboratory of M.I.T. where he has been working on microwave components and gaseous discharges.

Mr. Muehe is a member of Sigma Xi.



Melvin E. Pedinoff was born in New York City, N. Y., on June 21, 1930. He received the B.A. and M.A. degrees in physics in 1953, and 1954, respectively, and the Ph.D. degree in ultrasonic physics in 1959, all from the University of California at Los Angeles.



M. E. PEDINOFF

In 1954 he worked for the Naval Ordnance Test Station, Pasadena, Calif., on acoustic guidance systems. From 1954 to 1958 he was employed as a research physicist at U.C.L.A. where he performed research on the propagation of sound in fluids and on the structure of molecules. From 1956 to 1959 he worked at Hoffman Laboratories Division, Los Angeles, Calif., on noise suppression, broad-band low-frequency antennas and radar anti-jam equipment. In 1959 he accepted a position with Hughes Aircraft Company, Culver City, Calif., where he was concerned with the application of communication theory to data processing antennas and later with the investigation of the role of solid-state phenomena in antenna systems. He recently joined the staff of Hughes Research Laboratories, Malibu, Calif., where he will be concerned with quantum electronic problems.

Dr. Pedinoff is a member of Sigma Pi Sigma and Sigma Xi.

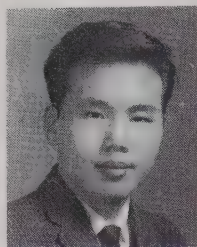


Chuck Y. Pon (S'58-M'61) was born in Canton, China, on April 27, 1935. He received the B.S. and the M.S. degrees in electrical engineering from the University

of California, Berkeley, in 1959 and 1960, respectively.

During the summer of 1959, he was employed as an electronics engineer at the Lawrence Radiation Laboratories, Livermore, Calif., where he was engaged in research on harmonic generations. In 1960 he joined the Dalmo Victor Company, Division of Textron Inc., Belmont, Calif., as a microwave engineer in the Microwave and Propagation Department, where he is doing research on stripline components, high-power strip-line duplexer and nanosecond duplexing circuits.

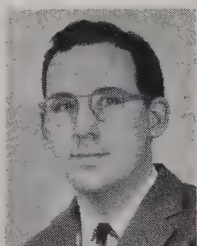
Mr. Pon is a member of Tau Beta Pi and Eta Kappa Nu.



C. Y. PON



Albert E. Sanderson (A'50-M'54) was born in Bethlehem, Pa., on August 8, 1928. He received the A.B. degree in 1949 and the A.M. degree in 1950, both from Harvard University, Cambridge, Mass.



A. E. SANDERSON

From 1950 to 1957 he was with Aircraft Radio Corporation, Boonton, N. J., working on the development of airborne communication receivers, transmitter and antennas.

In 1957 he joined the Impedance Group of General Radio Company, West Concord, Mass., and has been engaged in the design of coaxial microwave components and test equipment.



Anthony Siegman (S'54-M'56) was born in Detroit, Mich., on November 23, 1931. He received the A.B. degree from Harvard College, Cambridge, Mass., in 1952, the M.S. degree in applied physics from the University of California at Los Angeles, Calif., in 1954, and the Ph.D. degree in electrical engineering from Stanford University, Stanford, Calif., in 1957.



A. SIEGMAN

He worked with the Hughes Aircraft Company, Culver City, Calif., from 1952 to 1954, and is now Associate Professor in electrical engineering at Stanford University. He has worked on

traveling-wave tubes, noise fluctuations in electron beams, solid-state masers, and parametric devices.

Mr. Siegman is a member of Phi Beta Kappa, Sigma Xi, and the American Physical Society.



Frederick Sobel was born in Philadelphia, Pa., on February 20, 1927. He received the B.A. degree in physics from Columbia College, New York, N. Y., in 1948, and the M.A. degree in physics from Columbia University, New York, N. Y., in 1949.



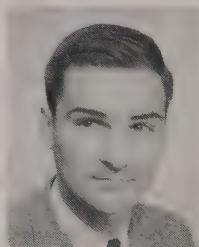
F. SOBEL

From 1949 to 1950 he was employed by Dorne and Margolin, Bethpage, N. Y., in aircraft antenna design and development. He joined the Friez Instrument Division of the Bendix Corporation, Baltimore, Md., in 1951 and was engaged in meteorological instrumentation. From 1952 to 1956 his work as a research associate at the Radiation Laboratory of The Johns Hopkins University, Baltimore, Md., was concerned with military applications of infrared physics and included studies in infrared emission and reflection, the development of calibrated radiation sources, and problems in optical instrumentation. Since 1956 he has been employed by Electronic Communications, Inc., Timonium, Md., where he is responsible for research and development in infrared and optical devices and systems. He has recently been exploring quasi-optical techniques and devices for application at millimeter and submillimeter wavelengths.

Mr. Sobel is a member of the American Physical Society, the Optical Society of America, and the Instrument Society of America.



William H. Steier was born in Kendallville, Ind., May 25, 1933. He received the B.S. degree in electronic engineering from Evansville College, Evansville, Ind., in 1955, and the M.S. and Ph.D. degrees, both in electrical engineering, from the University of Illinois, Urbana, in 1957 and 1960, respectively.



W. H. STEIER

Since 1956 he has been engaged in millimeter wave and electron beam research at the University of Illinois. His areas of investigation have included ferrite

modes, Cerenkov radiation from a plasma, and optical transmission lines. He has been a consultant with Ramo-Wooldridge Research Laboratories and with Space Technology Laboratories, Inc., Los Angeles, Calif. While consulting for these firms he investigated the use of plasmas as microwave variable attenuators and switches. Currently he holds the position of Assistant Professor of electrical engineering at the University of Illinois.

Dr. Steier is a member of the American Physical Society and Sigma Xi.



Kiyo Tomiyasu (S'41-A'42-M'49-SM'52) was born in Las Vegas, Nev., on September 25, 1919. He received the B.S. degree in electrical engineering from the California Institute of Technology, Pasadena, in 1940, and the M.S. degree in communication engineering from Columbia University, New York, N. Y., in 1941. With a Low Scholarship, he studied at Stanford University, Stanford, Calif., and



K. TOMIYASU

then entered Harvard University, Cambridge, Mass., to continue graduate work on a Gordon McKay Scholarship. He served as a Teaching Fellow and Research Assistant at Harvard, and, after receiving the Ph.D. degree in 1948, he served as Instructor.

In September, 1949, he joined the Sperry Gyroscope Company, Great Neck, N. Y., as project engineer, and in 1952 was promoted to the position of Engineering Section Head for Microwave Research in the Microwave Components Department. In August, 1955, he became a Consulting Engineer at the General Electric Microwave Laboratory, Palo Alto, Calif. Five years

later he transferred to the General Engineering Laboratory, General Electric Company, Schenectady, N. Y.

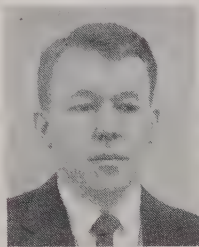
Dr. Tomiyasu is a member of the American Physical Society and Sigma Xi.



Max T. Weiss (S'43-A'45-M'55-SM'57), for a photograph and biography, please see page 370 of the July, 1961, issue of these TRANSACTIONS.



Frederick L. Wentworth (S'54-A'55-M'60) was born in Cumberland, Md., on July 30, 1924. He received the B.S. degree in electrical engineering from The Johns Hopkins University, Baltimore, Md., in 1955, and the M.S. degree in electrical engineering from Drexel Institute of Technology, Philadelphia, Pa., in 1960.



F. L. WENTWORTH

In 1952 he joined the Radiation Laboratory of The Johns Hopkins University where he helped develop experimental circuitry on a proximity fuze program for the U. S. Navy. From 1954 to 1957 he was employed by The Martin Company, Baltimore, Md., where he was engaged in design and development of antennas and microwave components. He also served as acting group engineer for development of the antennas and associated RF equipment on the Vanguard project. In 1957 he joined Electronic Communications, Inc., Timonium, Md., as a project engineer in the Microwave and Applied Physics Section. He has been engaged in research on electromagnetic propagation and scattering in soil, mutual coupl-

ing and phasing problems with large antenna arrays, millimeter wave generation, propagation and detection, solid-state parametric amplifiers, and harmonic generators. He is presently engaged in development of a high-sensitivity radiometer in the 1-2 mm region for the U. S. Army.



James C. Wiltse (S'48-A'53-SM'59) was born in Tannersville, N. Y., on March 16, 1926. He received the B.E.E. degree in 1946 and the M.E.E. degree in 1951 from Rensselaer Polytechnic Institute, Troy, N. Y., and the Dr.Eng. degree from The Johns Hopkins University, Baltimore, Md., in 1959.



J. C. WILTSE

From 1946 to 1947 he was an electronics officer in the U. S. Navy, and from 1947 to 1948 he was employed by the General Electric Company, Schenectady, N. Y. He then taught in the Department of Electrical Engineering at Rensselaer while he completed the requirements for the M.E.E. degree. From 1951 to 1958 he was associated with The Johns Hopkins University where he taught in the Department of Electrical Engineering and later was a staff member of the Radiation Laboratory. He became Microwave Group Leader and was responsible for the millimeter-wave and physical electronics groups. Since 1958 he has been employed at the Research Division of Electronic Communications, Inc., Timonium, Md., where he is now the Research Manager in charge of the Antenna, Microwave, and Infrared Sections.

Dr. Wiltse is a member of Sigma Xi, Tau Beta Pi, and Eta Kappa Nu.

IRE Transactions on Microwave Theory and Techniques

Index to Volume MTT-9, 1961

Contents

Volume MTT-9, Number 1, January, 1961

Frontispiece, 1959 Microwave Prize, <i>Bert A. Auld</i>	2
Contributions from the 1960 National Microwave Symposium	
UHF Strip Transmission Line Hybrid Junction, <i>I. Tatsuguchi</i>	3
Gallium-Arsenide Point-Contact Diodes, <i>W. M. Sharpless</i>	6
Characterization of Microwave Variable Capacitance Diodes, <i>Sverre T. Eng</i>	11
Correction to "Scattering of a Plane Wave on a Ferrite Cylinder and Normal Incidence," <i>Wilhelm H. Eggmann</i>	22
A Study of the Optimum Design of Wide-Band Parametric Amplifiers and Up-Converters, <i>George L. Matthaei</i>	23
Correction to "Impedances of an Elliptic Waveguide (for the H ₁ Mode)," <i>G. R. Valenzuela</i>	38
A Low-Noise X-Band Parametric Amplifier Using a Silicon Mesa Diode, <i>R. D. Weglein and F. Keywell</i>	39
Design and Operation of Four-Frequency Parametric Up-Con- verters, <i>J. A. Luksch, E. W. Matthews and G. A. VerWys</i> ...	44
Ferrites with Planar Anisotropy at Microwave Frequencies, <i>Isidore Bady</i>	52
Wide-Band Resonance Isolator, <i>W. H. Anderson and M. E. Hines</i>	63
Maser Operation at Signal Frequencies Higher than Pump Frequency, <i>Frank R. Arams</i>	68
A Solid-State Microwave Source from Reactance-Diode Har- monic Generators, <i>T. M. Hyltin and K. L. Kotzebue</i>	73
Propagation of Waves in a Plasma in a Magnetic Field, <i>William P. Allis</i>	79
Magnetoplasma Effects in Solids, <i>Benjamin Lax</i>	83
Coherent Excitation of Plasma Oscillations in Solids, <i>David Pines</i>	89
Pulsed Millimeter-Wave Generation Using Ferrites, <i>B. J. Elliott, T. Schaug-Pettersen and H. J. Shaw</i>	92
Correspondence	
Tuning Range of the Backward Traveling-Wave Parametric Amplifier, <i>Thomas M. Straus</i>	95
Size Effect in the Measurement of Microwave Permeability of Ferrites, <i>B. Maher and L. Silber</i>	96
Cutoff Variable Reactor, <i>Koryu Ishii</i>	96
Single-Mode Cavity Maser at 2200 Mc, <i>D. W. Hanson and J. J. Rowley</i>	97
Higher-Order Evaluation of Dipole Moments of a Small Circular Disk for Arbitrary Incident Fields, <i>Wilhelm H. Egg- mann</i>	98
Capacitance Definitions for Parametric Operation, <i>Hubert Heffner</i>	98
A Tunnel-Diode Amplifying Converter, <i>L. E. Dickens and C. R. Gneiting</i>	99
Impedance Matching by Charts, <i>Michael R. Leibowitz</i>	101
Theoretical Evaluation of Resonance Frequencies in a Cylind- rical Cavity with Radial Vanes, <i>A. Singh and R. A. Rao</i> ...	101
PGMTT News, 1960 National Microwave Symposium.....	103
Contributors.....	105

Volume MTT-9, Number 2, March, 1961

Dynamic Interaction Fields in a Two-Dimensional Lattice, <i>R. E. Collin and W. H. Eggmann</i>	110
TEM Impedance and Cross Coupling for Small Circular Center Conductors in a Double Ridged Waveguide, <i>J. E. Storer and T. W. Thompson</i>	116
Design of a Coaxial Hybrid Junction, <i>L. Stark</i>	124
Step-Twist-Junction Waveguide Filters, <i>B. C. DeLoach, Jr.</i> ...	130
Resonators for Millimeter and Submillimeter Wavelengths, <i>William Culshaw</i>	135

A Recording Microwave Spectrograph, <i>D. Ilias and G. Bou- douris</i>	144
A Cavity-Type Parametric Circuit as a Phase-Distortionless Limiter, <i>F. A. Olson and G. Wade</i>	153
A Stripline Frequency Translator, <i>Elisabeth M. Rutz</i>	158
An Approximate Solution to Some Ferrite Filled Waveguide Problems with Longitudinal Magnetization, <i>Sheldon S. Sandler</i>	162
Synthesis of Low-Reflection Waveguide Joint Systems, <i>P. Foldes and N. Gothard</i>	169
A Channel-Dropping Filter in the Millimeter Region Using Circular Electric Modes, <i>E. A. J. Marcatili</i>	176
Coupled-Mode Description of Crossed-Field Interaction, <i>J. E. Rowe and R. Y. Lee</i>	182
Broad-Band Cavity-Type Parametric Amplifier Design, <i>Kenneth M. Johnson</i>	187
Correspondence	
Dependence of the Resonance Linewidth of Microwave Ferro- magnetic Materials on Incident RF Power, <i>J. L. Carter, S. Dixon, Jr., and I. Reingold</i>	195
Green's Function Techniques for Inhomogeneous Anisotropic Media, <i>Alfred T. Villeneuve</i>	197
N-Way Power Divider, <i>Herman Kagan</i>	198
Microwave Absorption Modulation by Electron Mobility Variation in n-Type Germanium, <i>Milton Harmatz</i>	199
Coaxial to Strip Transmission Line Adapter, <i>J. H. Craven</i>	200
A Note on Loaded Line Synthesis, <i>John Reed</i>	201
X-Band Diode Limiting, <i>R. V. Garver and D. Y. Tseng</i>	202
A Note on the Difference Between Equiangular and Archi- medes Spiral Antennas, <i>P. E. Mayes, J. D. Dyson, R. Bawer, and J. I. Wolfe</i>	203
Contributors.....	206
PGMTT National Symposium.....	209

Volume MTT-9, Number 3, May, 1961

Octave-Bandwidth UHF/L-Band Circulator, <i>F. Arams, B. Kaplan, and B. Peyton</i>	212
A Five-Port Matched Pseudo-Magic Tee, <i>Akira Okaya</i>	216
Theory of Dielectric-Loaded and Tapered-Field Ferrite De- vices, <i>R. F. Soohoo</i>	220
Theory of TEM Diode Switching, <i>Robert V. Garver</i>	224
Measurement of Small Dielectric Losses in Material with a Large Dielectric Constant at Microwave Frequencies, <i>R. O. Bell and G. Rupprecht</i>	239
On the Existence of Leaky Waves Due to a Line Source Above a Grounded Dielectric Slab, <i>E. S. Cossedy and M. Cohn</i>	243
A Broad-Band Glass-to-Metal Coaxial Vacuum Seal, <i>W. M. Nunn, Jr., and L. E. Paul</i>	248
Magnetically-Tunable Microwave Filters Using Single-Crystal Yttrium-Iron-Garnet Resonators, <i>P. S. Carter, Jr.</i>	252
Correspondence	
Linear Tapers in Rectangular Waveguides, <i>R. C. Johnson and D. J. Bryant</i>	261
The Unloaded Q of a YIG Resonator from X-Band to 4 MM, <i>D. Douthett and I. Kaufman</i>	261
Z ₀ of Rectangular Coax, <i>R. V. Garver</i>	262
An Easy Method of Matching Microstrip Loads and Attenua- tors, <i>G. H. B. Thompson</i>	263
An Empirical Design Method for Multisection Ridge-Guide Transducers of Large-Impedance Transformation, <i>G. H. B. Thompson</i>	263
Pulse-Operated Circular Switch, <i>L. Freiberg</i>	266
Polishing Technique for Garnet Spheres, <i>Arvia L. Pierce</i>	266
Miniaturized, Temperature Stable, Coaxial Y-Junction Circu- lators, <i>J. Clark and J. Brown</i>	267

K-Band Reciprocal Ferrite Phase Modulator, <i>Frank Reggia</i> . . .	269
K _a -Band Ferrite Phase Shifter, <i>R. S. McCarter and E. F. Landry</i> . . .	271
Low-Temperature Microwave Power Limiter, <i>F. J. Sansalone and E. G. Spencer</i> . . .	272
New Coaxial-to-Stripline Transformers Using Rectangular Lines, <i>R. Levy</i> . . .	273
Contributors . . .	275

Volume MTT-9, Number 4, July, 1961

Report on Advances in Microwave Theory and Techniques—1960, <i>R. C. Hansen and M. T. Weiss</i> . . .	278
The Short Pulse Behavior of Lossy Tapered Transmission Lines, <i>R. Stapelfeldt and F. J. Young</i> . . .	290
A Waveguide Quadruplexer System, <i>P. Foldes and T. B. Thomson</i> . . .	297
Some Recent Findings in Microwave Storage, <i>J. D. Kellett</i> . . .	306
Excess Noise in Microwave Detector Diodes, <i>J. J. Faris and J. M. Richardson</i> . . .	312
Quantum Fluctuations in Microwave Radiometry, <i>L. P. Bolgiano, Jr.</i> . . .	315
On the Resolution of a Class of Waveguide Discontinuity Problems by the Use of Singular Integral Equations, <i>L. Lewin</i> . . .	321
A Dielectric Surface-Wave Structure: the V-Line, <i>P. Diamant, S. P. Schlesinger, and A. Vigants</i> . . .	332
Wave Propagation in a Medium with a Progressive Sinusoidal Disturbance, <i>A. Hessel and A. A. Oliner</i> . . .	337
A New Broad-Band Absorption Modulator for Rapid Switching of Microwave Power, <i>Frank Reggia</i> . . .	343
Rectangular Waveguide Theoretical CW Average Power Rating, <i>H. E. King</i> . . .	349
Correspondence	
Wave Propagation in Coaxial-Cylindrical Slow-Wave Systems, <i>W. M. Nunn, Jr.</i> . . .	358
Ring Network Filter, <i>J. A. Kaiser</i> . . .	359
A Technique for Obtaining DC Isolation in Coaxial Cable RF Transmission Lines, <i>R. A. Sparks</i> . . .	360
Push-Pull Tunnel Diodes, <i>L. E. Dickens</i> . . .	361
Effects of Ferrite Strip Mounting Positions on Millimeter Wave Isolator Characteristics, <i>K. Ishii, J. B. Y. Tsui, and F. F. Y. Wang</i> . . .	362
An L-Band Loop-Type Coupler, <i>B. Maher</i> . . .	362
The Cutoff Wavelengths of Composite Waveguides, <i>G. R. Valenzuela</i> . . .	363
A Mechanical Waveguide Hybrid Phase Shifter, <i>J. Y. Wong</i> . .	364
Rectangular Waveguide Switches, <i>A. Clavin</i> . . .	365
Comments on "Stepped Transformers for Partially-Filled Transmission Lines," <i>M. R. Leibowitz, D. J. Sullivan, and D. A. Parkes</i> . . .	366
Contributors . . .	368
PGMTT News . . .	371

Volume MTT-9, Number 5, September, 1961

Microwaves—A Review of Progress in Great Britain During 1960, <i>A. E. Karbowiak</i> . . .	374
A New Type of Circular Polarizer Using Crossed Dipoles, <i>M. F. Bolster</i> . . .	385
Rounded Corners in Microwave High-Power Filters and Other Components, <i>Seymour B. Cohn</i> . . .	389
A Periodic Structure of Cylindrical Posts in a Rectangular Waveguide, <i>Edward E. Altshuler</i> . . .	398
Modes in Rectangular Guides Loaded with a Transversely Magnetized Slab of Ferrite away from the Side Walls, <i>G. Barziloi and G. Gerosa</i> . . .	403
Higher-Order Evaluation of Electromagnetic Diffraction by Circular Disks, <i>W. H. Eggimann</i> . . .	408
Low-Noise Properties of Microwave Backward Diodes, <i>Sverre T. Eng</i> . . .	419
Design Theory of Up-Converters for Use as Electronically-Tunable Filters, <i>George L. Matthari</i> . . .	425
Anisotropic Properties of Strip-Type Artificial Dielectric, <i>N. J. Kolettis and R. E. Collin</i> . . .	436
Optimization of Waveguide Tapers Capable of Multimode	

Propagation, <i>C. C. H. Tang</i> . . .	442
Correspondence	
A Broad-Band Coaxial Ferrite Switch, <i>R. L. Booth</i> . . .	452
Conditions for Maximum Power Transfer, <i>Carl Shulman</i> . . .	453
A Comment on the Scattering Matrix of Cascaded 2n-Ports, <i>D. J. R. Stock and L. J. Kaplan</i> . . .	454
Use of Flow Graphs to Evaluate Mismatch Errors in Loss and Phase Measurements, <i>Daniel Leed</i> . . .	454
Contributors . . .	455

Volume MTT-9, Number 6, November, 1961

1960 Microwave Prize, <i>Dr. A. F. Harvey</i> . . .	458
1961 National Symposium Papers	
Passive Phase-Distortionless Parametric Limiting with Varactor Diodes, <i>I. T. Ho and A. E. Siegman</i> . . .	459
Solid-State X-Band Power Limiter, <i>W. R. Krupke, T. S. Hartwick and M. T. Weiss</i> . . .	472
On Spurious Outputs from High-Power Pulsed Microwave Tubes, and Their Control, <i>K. Tomiyasu</i> . . .	480
Practical Design and Performance of Nearly Optimum Wide-Band Degenerate Parametric Amplifiers, <i>M. Gilden and G. L. Matthaet</i> . . .	484
Transmission Phase Relations of Four-Frequency Parametric Devices, <i>D. B. Anderson and J. C. Aukland</i> . . .	491
A Plasma Guide Microwave Selective Coupler, <i>W. H. Steier and I. Kaufman</i> . . .	499
High-Power Duplexers, <i>C. E. Muehe</i> . . .	506
Quasi-Optical Surface Waveguide and Other Components for the 100- to 300-Gc Region, <i>F. Sobel, J. C. Wiltse and F. L. Wentworth</i> . . .	512
Broad-Band Isolators and Variable Attenuators for Millimeter Wavelengths, <i>C. E. Barnes</i> . . .	519
A New High-Precision Method for the Measurement of the VSWR of Coaxial Connectors, <i>A. E. Sanderson</i> . . .	524
Hybrid-Ring Directional Coupler for Arbitrary Power Divisions, <i>Chuck Y. Pon</i> . . .	529
A Coupled Strip-Line Configuration Using Printed-Circuit Construction that Allows Very Close Coupling, <i>William J. Getsinger</i> . . .	535
The Measurement of Conductivity and Permittivity of Semiconductor Spheres by an Extension of the Cavity Perturbation Method, <i>K. S. Champlin and R. R. Krongard</i> . . .	545
The Dominant Cutoff Wavelength of a Lunar Line, <i>A. Y. Hu and A. Ishimaru</i> . . .	552
The Negative-Conductance Slot Amplifier, <i>M. E. Pedinoff</i> . .	557
Correspondence	
Measurement of the Conversion Conductances of Esaki Mixer Diodes, <i>R. A. Pucel</i> . . .	567
A Versatile Phase Measurement Method for Transmission-Line Networks, <i>Peter Lacy</i> . . .	568
A VHF High-Power Y-Circulator, <i>G. V. Buehler and A. F. Eikenberg</i> . . .	569
N-Terminal Power Divider, <i>R. W. Peterson</i> . . .	571
10-DB X _L Cross Guide Coupler, <i>Richard Z. Gerlack</i> . . .	571
Design Note on an L-Band Strip-Line Circulator, <i>W. S. Koop and A. K. Jordan</i> . . .	571
A Stepped-Dielectric Transformer for Rectangular-to-Circular Waveguide, <i>B. Maher</i> . . .	572
A Microwave Power Divider, <i>Richard J. Mohr</i> . . .	573
On the Efficiency of Excitation of Surface Waves by Distributed Coupling, <i>Efraim Ravid-Weissberg</i> . . .	573
Higher-Order Mode Resonances in Strip-Line Y-Junction Circulators, <i>Alvin Clavin</i> . . .	575
A Proposed Design to Enhance Microwave Power Limiter Characteristics, <i>William H. Wright, Jr.</i> . . .	575
A High-Power Coaxial Ferrite Phase Shifter, <i>A. S. Boxer, S. Hershenov, and E. F. Landry</i> . . .	577
A Duplexer Using the Zero Permeability Characteristics of Ferrite, <i>L. K. Wilson and G. J. Neumann</i> . . .	578
A Series-Connected Traveling-Wave Parametric Amplifier, <i>Tuck Hop Lee</i> . . .	578
1961 National Symposium . . .	580
Contributors . . .	582
Annual Index, 1961 . . .	585

Follows page 585

Index to Authors

- A**
Allis, W. P.: Jan 79
Altshuler, E. E.: Sep 398
Anderson, D. B.: Nov 491
Anderson, W. W.: Jan 63
Arams, F. R.: Jan 68, May 212
Aukland, J. C.: Nov 491
- B**
Bady, I.: Jan 52
Barnes, C. E.: Nov 519
Barzilai, G.: Sep 403
Bawer, R.: Mar 203
Bell, R. O.: May 239
Bolgiano, L. P., Jr.: Jul 315
Bolster, M. F.: Sep 385
Booth, R. L.: Sep 452
Boudouris, G.: Mar 144
Boxer, A. S.: Nov 577
Brown, J.: May 267
Bryant, D. J.: May 261
Buehler, G. V.: Nov 569
- C**
Carter, J. L.: Mar 195
Carter, P. S., Jr.: May 252
Cassedy, E. S.: May 243
Champlin, K. S.: Nov 545
Clark, J.: May 267
Clavin, A.: Jul 365; Nov 575
Cohn, M.: May 243
Cohn, S. B.: Sep 389
Collin, R. E.: Mar 110; Sep 436
Craven, J. H.: Mar 200
Culshaw, W.: Mar 135
- D**
DeLoach, B. C., Jr.: Mar 130
Diamant, P.: Jul 332
Dickens, L. E.: Jan 99; Jul 361
Dixon, S., Jr.: Mar 195
Douthett, D.: May 261
Dyson, J. D.: Mar 203
- E**
Eggmann, W. H.: Jan 22, 98; Mar 110; Sep 408
Eikenberg, A. F.: Nov 569
Elliott, B. J.: Jan 92
Eng, S. T.: Jan 11; Sep 419
- F**
Faris, J. J.: Jul 312
Foldes, P.: Mar 169; Jul 297
Freiberg, L.: May 266
- G**
Garver, R. V.: Mar 202; May 224, 262
Gerlack, R. Z.: Nov 571
Gerosa, G.: Sep 403
Getsinger, W. J.: Nov 535
Gilden, M.: Nov 484
Gneiting, C. R.: Jan 99
Gothard, N.: Mar 169
- H**
Hansen, R. C.: Jul 278
Hanson, D. W.: Jan 97
Harmatz, M.: Mar 199
Hartwick, T. S.: Nov 472
Heffner, H.: Jan 98
Hershenov, S.: Nov 577
Hessel, A.: Jul 337
Hines, M. E.: Jan 63
Ho, I. T.: Nov 459
Hu, A. Y.: Nov 552
Hyltin, T. M.: Jan 73
- I**
Ilias, D.: Mar 144
Ishii, K.: Jan 96; Jul 362
Ishimaru, A.: Nov 552
- J**
Johnson, K. M.: Mar 187
Johnson, R. C.: May 261
Jordan, A. K.: Nov 571
- K**
Kagan, H.: Mar 198
Kaiser, J. A.: Jul 359
Kaplan, B.: May 212
Kaplan, L. J.: Sep 454
Karbowiak, A. E.: Sep 374
Kaufman, I.: May 261; Nov 499
Koop, W. S.: Nov 571
Kellett, J. D.: Jul 306
Keywell, F.: Jan 39
King, H. E.: Jul 349
Kolettis, N. J.: Sep 436
Kotzebue, K. L.: Jan 73
Krongard, R. R.: Nov 545
Krupke, W. R.: Nov 472
- L**
Lacy, P.: Nov 568
Landry, E. F.: May 271; Nov 577
Lax, B.: Jan 83
Lee, R. Y.: Mar 182
- Lee, T. H.:** Nov 578
Leed, D.: Sep 454
Leibowitz, M. R.: Jan 101; Jul 366
Levy, R.: May 273
Lewin, L.: Jul 321
Luksch, J. A.: Jan 44
- M**
Maher, B.: Jan 96; Jul 362; Nov 572
Marcatili, E. A. J.: Mar 176
Matthaei, G. L.: Jan 23; Sep 425; Nov 484
Matthews, E. W.: Jan 44
Mayes, P. E.: Mar 203
McCarter, R. S.: May 271
Mohr, R. J.: Nov 573
Muehe, C. E.: Nov 506
- N**
Neumann, G. J.: Nov 578
Nunn, W. M., Jr.: May 248; Jul 358
- O**
Okaya, A.: May 216
Oliner, A. A.: Jul 337
Olson, F. A.: Mar 153
- P**
Parkes, D. A.: Jul 366
Paul, L. E.: May 248
Pedinoff, M. E.: Nov 557
Peterson, R. W.: Nov 571
Peyton, B.: May 212
Pierce, A. L.: May 266
Pines, D.: Jan 89
Pon, C. Y.: Nov 529
Pucel, R. A.: Nov 567
- R**
Rao, R. A.: Jan 101
Ravid-Weissberg, E.: Nov 573
Reed, J.: Mar 201
Reggia, F.: May 269; Jul 343
Reingold, I.: Mar 195
Richardson, J. M.: Jul 312
Rowe, J. E.: Mar 182
Rowley, J. J.: Jan 97
Rupprecht, G.: May 239
Rutz, E. M.: Mar 158
- S**
Sanderson, A. E.: Nov 524
- Sandler, S. S.:** Mar 162
Sansalone, F. J.: May 272
Schaug-Pettersen, T.: Jan 92
Schlesinger, S. P.: Jul 332
Sharpless, W. M.: Jan 6
Shaw, H. J.: Jan 92
Shulman, C.: Sep 452
Siegmán, A. E.: Nov 459
Silber, L.: Jan 96
Singh, A.: Jan 101
Sobel, F.: Nov 512
Soohoo, R. F.: May 220
Sparks, R. A. P.: Jul 360
Spencer, E. G.: May 272
Stapelfeldt, R.: Jul 290
Stark, L.: Mar 124
Steier, W. H.: Nov 499
Stock, D. J. R.: Sep 454
Storer, J. E.: Mar 116
Straus, T. M.: Jan 95
Sullivan, D. J.: Jul 366
- T**
Tang, C. C. H.: Sep 442
Tatsuguchi, I.: Jan 3
Thompson, G. H. B.: May 263
Thompson, T. W.: Mar 116
Thomson, T. B.: Jul 297
Tomiya, K.: Nov 480
Tseng, D. Y.: Mar 202
Tsui, J. B. Y.: Jul 362
- V**
Valenzuela, G. R.: Jan 38; Jul 363
VerWys, G. A.: Jan 44
Vigants, A.: Jul 332
Villeneuve, A. T.: Mar 197
- W**
Wade, G.: Mar 153
Wang, F. F. Y.: Jul 362
Weglein, R. D.: Jan 39
Weiss, M. T.: Jul 278; Nov 472
Wentworth, F. L.: Nov 512
Wilson, L. K.: Nov 578
Wiltse, J. C.: Nov 512
Wolfe, J. I.: Mar 203
Wong, J. Y.: Jul 364
Wright, W. H., Jr.: Nov 575
- Y**
Young, F. J.: Jul 290

Index to Subjects

- A**
Absorption Modulation, Microwave, by Electron Mobility Variation in *n*-Type Germanium: Mar 199
Absorption Modulator, Broad-Band, for Rapid Switching: Jul 343
Antennas, Equiangular and Archimedes Spiral: Mar 203
Attenuators, Microstrip Loads, and Matching: May 263
Attenuators, Variable, Broad-Band Isolators and, for Millimeter Wavelengths: Nov 519
- C**
Capacitance Definitions for Parametric Operation: Jan 98
Cavity, Cylindrical, Evaluation of Resonance Frequencies in: Jan 101
Circulators:
 L-Band Strip-Line, Design Note on: Nov 571
- Miniaturized, Temperature Stable, Coaxial Y-Junction: May 267
Octave-Bandwidth UHF/L-Band: May 212
Strip-Line Y-Junction, Higher-Order Mode Resonances in: Nov 575
Switch, Pulse-Operated: May 266
VHF High-Power Y: Nov 569
Coax, Rectangular, Z_0 of: May 262
Coherent Excitation of Plasma Oscillations in Solids: Jan 89

Conductances, Conversion, of Esaki Mixer Diodes, Measurement of: Nov 567
 Conductivity and Permittivity of Semiconductor Spheres, Measurement by Extension of the Cavity Perturbation Method: Nov 545
 Converter, Tunnel-Diode Amplifying: Jan 99
 Corners, Rounded, in Microwave High-Power Filters and Other Components: Sep 389
 Coupled-Mode Description of Crossed-Field Interaction: Mar 182
 Couplers:
 Hybrid-Ring Directional, for Arbitrary Power Divisions: Nov 529
 L-Band Loop-Type: Jul 362
 Plasma Guide Microwave Selective: Nov 499
 10-DB X_L Cross Guide: Nov 571
 Crossed-Field Interaction, Coupled-Mode Description of: Mar 182
 Cutoff Wavelength of a Lunar Line, Dominant: Nov 552
 Cutoff Wavelengths of Composite Waveguides: Jul 363

D

Dielectric Losses, Small, in Material with Large Dielectric Constant: May 239
 Dielectric Slab, Grounded, Leaky Waves Due to Line Source Above: May 243
 Dielectric, Strip-Type Artificial, Anisotropic Properties of: Sep 436
 Dielectric Surface-Wave Structure: the V-Line: Jul 332
 Diffraction, Electromagnetic, by Circular Disks, Higher-Order Evaluation of: Sep 408
 Diodes:
 Esaki Mixer, Measurement of Conversion Conductances of: Nov 567
 Gallium-Arsenide Point-Contact: Jan 6
 Microwave Backward, Low-Noise Properties of: Sep 419
 Microwave Detector, Excess Noise in: Jul 312
 Microwave Variable Capacitance, Characteristics of: Jan 11
 Push-Pull Tunnel: Jul 361
 Varactor, Passive Phase-Distortionless Parametric Limiting with: Nov 459
 Dipole Moments of Small Circular Disk, Higher-Order Evaluation of: Jan 98
 Divider, Microwave Power: Nov 573
 Divider, N -Terminal Power: Nov 571
 Duplexer Using Zero Permeability Characteristics of Ferrite: Nov 578
 Duplexers, High-Power: Nov 506

F

Ferrites:
 Devices, Dielectric-Loaded and Tapered-Field: May 220
 Filled Waveguide Problems, Solution: Mar 162
 Phase Modulator, K -Band Reciprocal: May 269
 Phase Shifter, High-Power Coaxial: Nov 577
 Phase Shifter, K_a -Band: May 271
 Pulsed Millimeter-Wave Generation Using: Jan 92
 Size Effect in Measurement of Microwave Permeability of: Jan 96
 Strip Mounting Positions, Effects of: Jul 362

Switch, Broad-Band Coaxial: Sep 452
 Transversely Magnetized Slab, Modes in Rectangular Guides Loaded with: Sep 403
 with Planar Anisotropy: Jan 52
 Zero Permeability Characteristics, Duplexer Using: Nov 578
 Ferromagnetic Materials, Microwave, Resonance Linewidth of, Dependence on Incident RF Power: Mar 195
 Fields, Dynamic Interaction, in Two-Dimensional Lattice: Mar 110
 Filters:
 Channel-Dropping, in Millimeter Region Using Circular Electric Modes: Mar 176
 Electronically-Tunable, Up-Converters for Use as: Sep 425
 Magnetically-Tunable Microwave, Using Single-Crystal Yttrium-Iron-Garnet Resonators: May 252
 Microwave High-Power, and Other Components, Rounded Corners in: Sep 389
 Ring Network of: Jul 359
 Step-Twist-Junction Waveguide: Mar 130
 Five-Port Matched Pseudo-Magic Tee: May 216
 Flow Graphs to Evaluate Mismatch Errors in Loss and Phase Measurements: Sep 454
 Frequency Translator, Stripline: Mar 158

G

Garnet Spheres, Polishing Technique for: May 266
 Green's Function Techniques for Inhomogeneous Anisotropic Media: Mar 197

H

Hybrid Junction, Coaxial, Design: Mar 124
 Hybrid-Ring Directional Coupler for Arbitrary Power Divisions: Nov 529

I

Impedance and Cross Coupling for Small Circular Center Conductors in Double Ridged Waveguide: Mar 116
 Impedance Matching by Charts: Jan 101
 Integral Equations, Singular, Resolution of Class of Waveguide Discontinuity Problems by: Jul 321
 Isolator, Wide-Band Resonance: Jan 63
 Isolators, Broad-Band, and Variable Attenuators for Millimeter Wavelengths: Nov 519

L

Lattice, Two-Dimensional, Dynamic Interaction Fields in: Mar 110
 Leaky Waves Due to Line Source Above Grounded Dielectric Slab: May 243
 Limiters:
 Low-Temperature Microwave Power: May 272
 Microwave Power, Design to Enhance Characteristics: Nov 575
 Phase-Distortionless, Cavity-Type Parametric Circuit as: Mar 153
 Solid-State X-Band Power: Nov 472
 Limiting, X-Band Diode: Mar 202
 Loaded Line Synthesis: Mar 201
 Lunar Line, Dominant Cutoff Wavelength of: Nov 552

M

Magnetoplasma Effects in Solids: Jan 83
 Maser Operation at Signal Frequencies

Higher than Pump Frequency: Jan 68
 Maser, Single-Mode Cavity, at 2200 Mc: Jan 97
 Matching Microstrip Loads and Attenuators: May 263
 Measurements, Loss and Phase, Flow Graphs to Evaluate Mismatch Errors in: Sep 454
 Microwaves:
 Progress in Great Britain During 1960: Sep 374
 Radiometry, Quantum Fluctuations in: Jul 315
 Source, Solid-State, from Reactance-Diode Harmonic Generators: Jan 73
 Storage, Findings in: Jul 306
 Theory and Techniques, 1960, Advances in: Jul 278
 Tubes, High-Power Pulsed, Spurious Outputs from: Nov 480
 Modes in Rectangular Guides Loaded with Transversely Magnetized Slab of Ferrite: Sep 403

N

Noise, Excess, in Microwave Detector Diodes: Jul 312
 Noise Properties, Low, of Microwave Backward Diodes: Sep 419

P

Parametric Amplifiers:
 and Up-Converters, Wide-Band, Optimum Design of: Jan 23
 Backward Traveling-Wave, Tuning Range of: Jan 95
 Broad-Band Cavity-Type, Design: Mar 187
 Low-Noise X-Band, Using Silicon Mesa Diode: Jan 39
 Nearly Optimum, Wide-Band Degenerate, Design and Performance of: Nov 484
 Series-Connected Traveling-Wave: Nov 578
 Parametric Circuit, Cavity-Type, as Phase-Distortionless Limiter: Mar 153
 Parametric Devices, Four-Frequency, Transmission Phase Relations of: Nov 491
 Parametric Limiting, Passive Phase-Distortionless, with Varactor Diodes: Nov 459
 Parametric Operation, Capacitance Definitions for: Jan 98
 Parametric Up-Converters, Four-Frequency: Jan 44
 Permeability, Microwave, of Ferrites, Size Effect in Measurement of: Jan 96
 Permittivity of Semiconductor Spheres, Conductivity and, Measurement by Extension of the Cavity Perturbation Method: Nov 545
 Phase Measurement Method, Versatile, for Transmission-Line Networks: Nov 568
 Phase Measurements, Loss and, Flow Graphs to Evaluate Mismatch Errors in: Sep 454
 Phase Modulator, K -Band Reciprocal Ferrite: May 269
 Phase Shifter, High-Power Coaxial Ferrite: Nov 577
 Phase Shifter, K_a -Band Ferrite: May 271
 Phase Shifter, Mechanical Waveguide Hybrid: Jul 364
 Plasma Guide Microwave Selective Coupler: Nov 499

Plasma in a Magnetic Field, Propagation of Waves in: Jan 79
 Plasma Oscillations in Solids, Coherent Excitation: Jan 89
 Polarizer, Circular, Using Crossed Dipoles: Sep 385
 Polishing Technique for Garnet Spheres: May 266
 Posts, Cylindrical, in a Rectangular Waveguide, Periodic Structure of: Sep 398
 Power Divider, *N*-Way: Mar 198
 Power Transfer, Maximum, Conditions for: Sep 453
 Propagation of Waves in a Plasma in a Magnetic Field: Jan 79
 Propagation Wave, in Coaxial-Cylindrical Slow-Wave Systems: Jul 358
 Propagation, Wave, in Medium with Progressive Sinusoidal Disturbance: Jul 337
 Pulsed Millimeter-Wave Generation Using Ferrites: Jan 92

Q

Quantum Fluctuations in Microwave Radiometry: Jul 315

R

Resonance Frequencies in a Cylindrical Cavity, Evaluation of: Jan 101
 Resonance Linewidth of Microwave Ferromagnetic Materials, Dependence on Incident RF Power: Mar 195
 Resonator, YIG, Unloaded *Q* of, from *X*-Band to 4 MM: May 261
 Resonators for Millimeter and Submillimeter Wavelengths: Mar 135
 Resonators, Single-Crystal Yttrium-Iron-Garnet, Magnetically-Tunable Microwave Filters Using: May 252
 Ring Network Filter: Jul 359

S

Scattering Matrix of Cascaded $2n$ -Ports: Sep 454
 Scattering on a Plane Wave on a Ferrite Cylinder, Correction: Jan 22
 Semiconductor Spheres, Conductivity and Permittivity of, Measurement by Extension of the Cavity Perturbation Method: Nov 545

Slot Amplifier, Negative-Conductance: Nov 557
 Slow-Wave Systems, Coaxial-Cylindrical, Wave Propagation in: Jul 358
 Solid-State *X*-Band Power Limiter: Nov 472
 Spectrograph, Recording Microwave: Mar 144
 Spurious Outputs from High-Power Microwave Tubes: Nov 480
 Stepped-Dielectric Transformer for Rectangular-to-Circular Waveguide: Nov 572

Strip-Line Configuration, Coupled, Using Printed-Circuit Construction: Nov 535
 Strip-Line *Y*-Junction Circulators, Higher-Order Mode Resonance in: Nov 575
 Surface Waves, Efficiency of Excitation by Distributed Coupling: Nov 573
 Switch, Broad-Band Coaxial Ferrite: Sep 452
 Switch, Circulator, Pulse-Operated: May 266
 Switches, Rectangular Waveguide: Jul 365
 Switching, TEM Diode: May 224

T

Tee, Five-Port Matched Pseudo-Magic: May 216
 Transducers, Multisection Ridge-Guide, Design Method for: May 263
 Transformer, Stepped-Dielectric, for Rectangular-to-Circular Waveguide: Nov 572
 Transformers, Coaxial-to-Stripline: May 273
 Transformers, Stepped, for Partially-Filled Transmission Lines, Comments on: Jul 366
 Transmission Lines:
 Adapter, Coaxial-to-Strip: Mar 200
 Coaxial Cable RF, Obtaining DC Isolation in: Jul 360
 Hybrid Junction, UHF Strip: Jan 3
 Lossy Tapered, Short Pulse Behavior of: Jul 290
 Networks, Versatile Phase Measurement Method for: Nov 568
 Partially-Filled, Stepped Transformers for, Comments on: Jul 366
 Tuning Range of Backward Traveling-

Wave Parametric Amplifier: Jan 95
 Tunnel-Diode Amplifying Converter: Jan 99
 Tunnel Diodes, Push-Pull: Jul 361

U

Up-Converters for Use as Electronically-Tunable Filters: Sep 425

V

Vacuum Seal, Broad-Band Glass-to-Metal Coaxial: May 248
 Variable Reactor, Cutoff: Jan 96
 VSWR of Coaxial Connectors, High-Precision Method for Measurement of: Nov. 524

W

Waveguides:
 Composite, Cutoff Wavelengths of: Jul 363
 Discontinuity Problems, Class of, Resolution by Use of Singular Integral Equations: Jul 321
 Double Ridged, Impedance and Cross Coupling for Small Circular Center Conductors in: Mar 116
 Elliptic, Impedances of, Correction: Jan 38
 Filters, Step-Twist-Junction: Mar 130
 Hybrid Phase Shifter, Mechanical: Jul 364
 Joint Systems, Low-Reflection: Mar 169
 Problems, Ferrite Filled, Solution: Mar 162
 Quadruplexer System: Jul 297
 Quasi-Optical Surface, and Other Components for 100- to 300-Gc Region: Nov 512
 Rectangular, Linear Tapers in: May 261
 Rectangular, Periodic Structure of Cylindrical Posts in: Sep 398
 Rectangular, Theoretical CW Average Power Rating: Jul 349
 Rectangular-to-Circular, Stepped-Dielectric Transformer for: Nov 572
 Switches, Rectangular: Jul 365
 Tapers Capable of Multimode Propagation, Optimization of: Sep 442

Z

Z_0 of Rectangular Coax: May 262

INSTITUTIONAL LISTINGS

MICROLAB
570 West Mount Pleasant Ave., Livingston, N.J.
Designers and Manufacturers of a Complete Line of
Coaxial Microwave Components and Cavity Filters

SCIENTIFIC-ATLANTA, INC.
2162 Piedmont Rd., N.E., Atlanta 19, Ga.
Complete Antenna Pattern Range Instrumentation,
Special RF and Antenna Systems Development

MICROWAVE ASSOCIATES, INC.
South Avenue, Burlington, Mass.
Waveguide Devices, Microwave Diodes, Magnetrons,
Duplexers, TWT's, Ferrite & Solid-State Devices

STEWART ENGINEERING COMPANY
Santa Cruz, Calif.
Backward Wave Oscillators & Other TW Type Tubes;
Controlled Atmosphere Furnaces & Precision Spot Welder

THE MICROWAVE JOURNAL
1330 Beacon St., Brookline 46, Mass.
A Magazine Devoted to the Interests of Engineers
Working at Microwave Frequencies

SYLVANIA MICROWAVE DEVICE OPERATIONS
Sylvania Electric Products Inc.
500 Evelyn Ave., Mountain View, Calif.
Magnetrons, Klystron, TWT's, BWO's, Ferrite Devices,
Waveguide Windows, Microwave Diodes

NARDA MICROWAVE CORP.
Plainview, L.I., New York
Microwave Test Equipment & Components, Modulators,
Bolometer & Thermistors, Ferrite Devices

TECHNICRAFT DIVISION, Electronic Specialty Co.
Thomaston, Conn.
Designers, Developers and Producers of Microwave
Components, Transmission Lines, and Assemblies

PHELPS DODGE COPPER PRODUCTS CORP.
300 Park Ave., New York 22, N.Y.
Styroflex, Foamflex Air Dielectric Aluminum Sheathed
Coaxial Cables, Connectors and Waveguides

WATKINS-JOHNSON COMPANY
3333 Hillview Ave., Palo Alto, Calif.
Res., Dev., Mfg. Microwave Electron Devices, TWT's,
BWO's, Parametric Amplifiers, Microwave Systems

PRD ELECTRONICS, INC.
202 Tillary St., Brooklyn 1, N.Y.
Complete Line of Microwave and Electronic Test Equipment
Waveguide and Coaxial Components

WEINSCHEL ENGINEERING COMPANY, INC.
10503 Metropolitan Ave., Kensington, Md.
Attenuation Standards, Coax Attenuators, Insertion
Loss Test Sets, Voltage & Power Calibrators

SAGE LABORATORIES, INC.
3 Huron Dr., Natick, Mass.
Microwave Attenuators, Couplers, Crystal Holders,
Filters, Hybrids, Mixers, Rotary Joints

WHEELER LABORATORIES, INC.
Great Neck, N.Y.
Antenna Lab., Smithtown, N.Y.
Consulting Services, Research & Development,
Microwave Antennas & Waveguide Components

INSTITUTIONAL LISTINGS

The IRE Professional Group on Microwave Theory and Techniques is grateful for the assistance given by the firms listed below, and invites application for Institutional Listing from other firms interested in the Microwave field.

AIRBORNE INSTRUMENTS LABORATORY
A Division of Cutler-Hammer, Inc.
Deer Park, Long Island, New York
Research and Development

EIMAC TUBES, EITEL-McCULLOUGH, INC.
301 Industrial Way, San Carlos, Calif.
Microwave Tubes, TWT-VTM-Reflex Klystrons,
Power Grid Tubes, Amplifier Klystrons

AIRTRON, INC.
A Division of Litton Industries
200 East Hanover Ave., Morris Plains, N.J.
Designers and Producers of Complete Line of
Microwave Electronic and Aircraft Components

ELECTRONIC SPECIALTY CO.
5121 San Fernando Rd., Los Angeles 39, Calif.
Airborne and Ground Antennas, Towers, Waveguides,
Microwave Components, Complete Radiating Systems

ALFORD MANUFACTURING COMPANY
299 Atlantic Ave., Boston 10, Mass.
RF Instruments, Coaxial Components,
Antennas and Air Navigation Aids

ITT FEDERAL LABORATORIES
500 Washington Ave., Nutley 10, N.J.
Line-of-Sight and Over-the-Horizon Microwave
Systems; Test Equipment and Components

CASCADE RESEARCH
Div. of Lewis & Kaufman Electronics Corp.
5245 San Fernando Rd., Los Angeles, Calif.
Research, Development, Production: Microwave Ferrite Devices,
Microwave Components & Subsystems

LITTON INDUSTRIES
Electron Tube Division
960 Industrial Rd., San Carlos, Calif.
Magnetrons, Klystron, TWT's, Noise Sources, BWO's,
Display Devices, CFA's, Switch Tubes, MM Wave Tubes

MELABS
3300 Hillview Ave., Palo Alto, Calif.
Microwave Components and Systems for Communications,
Countermeasures, Reconnaissance, Radar, Etc.

(See inside back cover for additional listings.)

The charge for an Institutional Listing is \$50.00 per issue or \$210.00 for six consecutive issues. Applications for Institutional Listings and checks (made out to The Institute of Radio Engineers, Inc.) should be sent to Robert A. Rivers, PGMTT Advertising Editor, Aircom Inc., 354 Main St., Winthrop 52, Mass.